Vol. XI, Issue 40, April 2017 ISSN 1971 - 8993

FRATTURA ED INTEGRITÀ STRUTTURALE

FRACTURE AND STRUCTURAL INTEGRITY

THE INTERNATIONAL JOURNAL OF
GRUPPO ITALIANO FRATTURA (IGF)

www.gruppofrattura.it

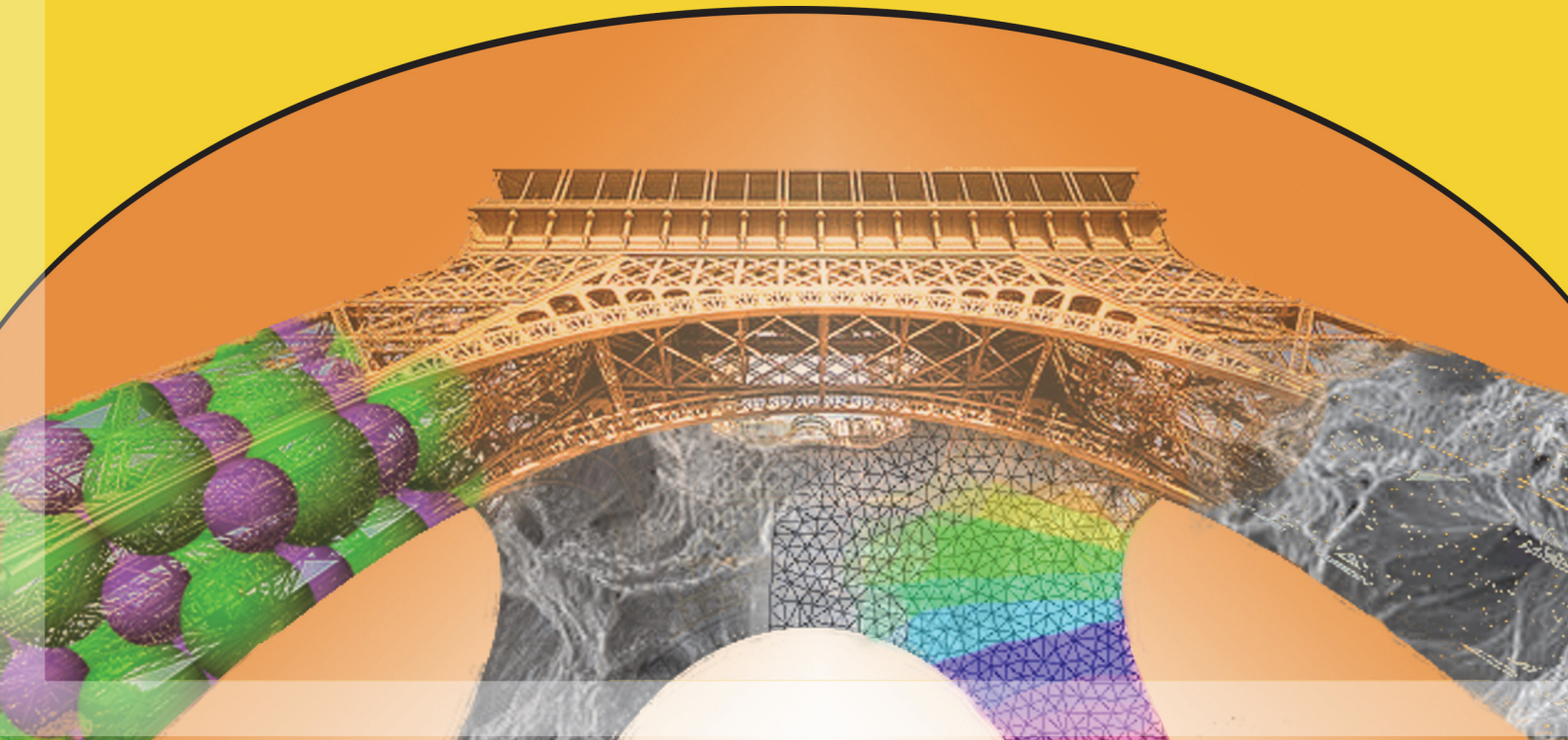

Table of Contents

Journal description and aims

Frattura ed Integrità Strutturale (Fracture and Structural Integrity) is the official Journal of the Italian Group of Fracture. It is an open-access Journal published on-line every three months (July, October, January, April).
Frattura ed Integrità Strutturale encompasses the broad topic of structural integrity, which is based on the mechanics of fatigue and fracture, and is concerned with the reliability and effectiveness of structural components. The aim of the Journal is to promote works and researches on fracture phenomena, as well as the development of new materials and new standards for structural integrity assessment. The Journal is interdisciplinary and accepts contributions from engineers, metallurgists, materials scientists, physicists, chemists, and mathematicians.

Contributions

Frattura ed Integrità Strutturale is a medium for rapid dissemination of original analytical, numerical and experimental contributions on fracture mechanics and structural integrity. Research works which provide improved understanding of the fracture behaviour of conventional and innovative engineering material systems are welcome. Technical notes, letters and review papers may also be accepted depending on their quality. Special issues containing full-length papers presented during selected conferences or symposia are also solicited by the Editorial Board.

Manuscript submission

Manuscripts have to be written using a standard word file without any specific format and submitted via e-mail to gruppofrattura@gmail.com. Papers should be written in English. A confirmation of reception will be sent within 48 hours. The review and the on-line publication process will be concluded within three months from the date of submission.

Peer review process

Frattura ed Integrità Strutturale adopts a single blind reviewing procedure. The Editor in Chief receives the manuscript and, considering the paper's main topics, the paper is remitted to a panel of referees involved in those research areas. They can be either external or members of the Editorial Board. Each paper is reviewed by two referees.
After evaluation, the referees produce reports about the paper, by which the paper can be:
a) accepted without modifications; the Editor in Chief forwards to the corresponding author the result of the reviewing process and the paper is directly submitted to the publishing procedure;
b) accepted with minor modifications or corrections (a second review process of the modified paper is not mandatory); the Editor in Chief returns the manuscript to the corresponding author, together with the referees' reports and all the suggestions, recommendations and comments therein.
c) accepted with major modifications or corrections (a second review process of the modified paper is mandatory); the Editor in Chief returns the manuscript to the corresponding author, together with the referees' reports and all the suggestions, recommendations and comments therein.
d) rejected.
The final decision concerning the papers publication belongs to the Editor in Chief and to the Associate Editors.
The reviewing process is usually completed within three months. The paper is published in the first issue that is available after the end of the reviewing process.

Publisher

Gruppo Italiano Frattura (IGF)
http://www.gruppofrattura.it
ISSN 1971-8993
Reg. Trib. di Cassino n. 729/07, 30/07/2007

Recent advances in "Experimental Mechanics of Materials" in Greece

The present issue of "Fracture and Structural Integrity" contains, among others, a set of papers reporting current research achievements in the field of "Experimental Mechanics of Materials" from a series of Universities and Research Institutes of Greece. The papers were collected within the framework of the activities of the "Greek Society for Experimental Mechanics of Materials" (GSEMM).

GSEMM was founded recently and its mission (as described in its officially Certified Statute) is the production and dissemination of scientific knowledge as well as training, education and know-how transfer in all fields related to "Experimental Mechanics of Materials". The Society is already accepted by the European Structural Integrity Society (ESIS) as the National Committee of Greece. GSEMM plans to organize the "1st Conference of the Greek Society of Experimental Mechanics of Materials" in Athens from 10 to 12 May 2018. GSEMM is already in contact with the Executive Committee of ESIS in order for the conference to be held under the official auspices of ESIS. Moreover, GSEMM is in contact with the Editor-in-Chief of "Procedia Structural Integrity" in order for the proceedings of the conference (after the proper peer review process), to be published in a special issue of the journal.

The papers included in this issue of "Fracture and Structural Integrity" are original contributions concerning recent developments aiming at highlighting critical aspects of the mechanical behaviour and failure of specific building materials and structures. Attention is focused on the application of certain novel experimental sensing techniques (like Acoustic Emissions, Pressure Stimulated Currents and Electrical Resistance Change of embedded PVA-CNT fibers) in the direction of: (i) pumping data from the interior of tested specimens, (ii) detecting proper pre-failure indicators and, finally, (iii) assessing the potential of the as above mentioned techniques to be used as flexible tools for Structural Health Monitoring. The materials considered are characterized by increased brittleness and include marble, soda-glass, various porous stones, cement mortar and cement-paste and bone tissue. Some of these materials, like for example Dionysos marble and Alfas porous stone, are widely used in on-going restoration projects of classical monuments of the Greek Cultural Heritage. The majority of the papers describe experimental research work, while two of them are based on analytical and/or numerical schemes.

The Guest Editors would like to emphasize that it is an honor and privilege for us the fact that we have had the opportunity to edit this issue of "Fracture and Structural Integrity". We wish to sincerely thank the authors who have contributed and also, we would like to express our gratitude to the reviewers of all the papers, since they worked tirelessly to assure the scientific quality and originality of the submitted articles.

Finally, we would like to thank the Editor-in-chief of "Fracture and Structural Integrity" Professor Francesco Iacoviello, who provided us with the 'podium' of the journal and offered us the opportunity to demonstrate the research implemented at various Greek institutes, in the field of "Experimental Mechanics of Materials". We hope that the publication of this issue of "Fracture and Structural Integrity" will be the first step towards the enhancement of the relation between the "Italian Group of Fracture" and the newly founded GSEMM, for the mutual benefit of the members of both societies.

Stavros K. Kourkoulis
School of Applied Mathematical and Physical Sciences, Department of Mechanics,
National Technical University of Athens,
Athens, Greece

Dimos Triantis
Department of Electronics,
Technological Educational Institution of Athens,
Athens, Greece

Using acoustic emissions to enhance fracture toughness calculations for CCNBD marble specimens

K. Kaklis, S. Mavrigiannakis
School of Mineral Resources Eng., Technical Univ. of Crete, Greece
kaklis@mred.tuc.gr, smaurig@mred.tuc.gr

V. Saltas, F. Vallianatos
Dept Environmental and Natural Res. Eng., Tech. Educational Institute of Crete, Greece
vsaltas@chania.teicrete.gr, fvallian@chania.teicrete.gr

Z. Agioutantis
Department of Mining Engineering, University of Kentucky, Lexington, KY, USA
zach.agioutantis@uky.edu

ABSTRACT. Rock fracture mechanics has been widely applied to blasting, hydraulic fracturing, mechanical fragmentation, rock slope analysis, geophysics, earthquake mechanics and many other science and technology fields. Development of failure in brittle materials is associated with microcracks, which release energy in the form of elastic waves called acoustic emissions. In the present study, acoustic emission (AE) measurements were carried out during cracked chevron notched Brazilian disc (CCNBD) tests on Nestos marble specimens. The fracture toughness of different modes of loading (mode-I and –II) is calculated and the results are discussed in conjunction with the AE parameters.

KEYWORDS. Rock fracture toughness; Mode I loading; CCNBD; Acoustic emissions; Marble.

Citation: Kaklis, K., Saltas, V., Mavrigiannakis, S., Valiannatos, F., Agioutantis, Z., Using acoustic emissions to enhance fracture toughness calculations for CCNBD marble specimens, Frattura ed Integrità Strutturale, 40 (2017) 1-17.

Received: 11.07.2016
Accepted: 12.09.2016
Published: 01.04.2017

INTRODUCTION

Fracture mechanics can be applied to many engineering fields including civil and mining engineering, where drilling, excavation, explosion and cutting of rocks are closely related to the strength, stability and fracture of rock materials and structures. Fracture toughness represents the ability of a material to resist the propagation of cracks; it is considered to be an inherent property of each material and should not be related to testing conditions.

Among many different testing methods for rock fracture toughness, the International Society for Rock Mechanics (ISRM) suggests the Chevron Bend (CB) and the Short Rod (SR) specimens [1]. These tests are relevant to mode I (opening mode) fracture toughness calculations, but are not appropriate for testing the fracture toughness of rock under mode II or mixed mode I-II cases [2, 3]. Considering notched circular specimen geometries, Atkinson et al. in 1982 [4] introduced the Cracked Straight Through Brazilian Disc (CSTBD). Shetty et al., in 1985 [5], based on the CSTBD configuration, presented the Cracked Chevron Notched Brazilian Disc (CCNBD) test, by employing the straight through crack assumption. The introduction of the CSTBD and CCNBD tests, allows the determination of rock fracture toughness under mode I (opening mode), mode II (in plane shear mode) and mixed mode I-II loading cases. Both of these tests configurations show great potential for current and future applications and overcome the disadvantages of the CB and SR specimens.

The International Society for Rock Mechanics [6] suggested the cracked chevron notched Brazilian disc (CCNBD) for determining the mode I fracture toughness of rock. There are some unique features characterizing the CCNBD specimen: (a) it is closely related to the Brazilian test which is widely used for tensile strength test for rock and concrete, (b) it can be easily used for mode I, mode II and even mixed mode testing, (c) it can sustain higher critical load than other kinds of specimens with comparable size and (d) it also maintains the merit of convenience for specimen preparation from rock cores. Recent research dealt with the calibration of the minimum (critical) dimensionless stress intensity factor Y^*_{min} [7-9] and with measuring the fracture toughness under mode II and mixed mode I-II loading conditions using CCNBD specimens of different rock types [10, 11].

Regarding AE, it is known that a large number of such signals are generated when a rock specimen is loaded to failure. Since AE signals are caused by the formation, expansion and propagation of microcracks, such signals inherently include information related to the structural changes taking place within a rock sample.

This study focuses on the correlation between the AE signals and the diametrically applied load during CCNBD tests. The acoustic emission activity was monitored using piezoelectric acoustic emission sensors, and the potential for accurate prediction of the fracture load based on acoustic emission data is investigated.

EXPERIMENTS AND ACQUISITION OF ACOUSTIC EMISSIONS

Material

Specimens consisting of Nestos marble were properly prepared and tested. This marble is quarried by surface mines in northern Greece and is mainly used as a building material. It is composed of 93.4% calcite, 6% dolomite and 0.6% quartz. Its density is 2.67 g/cm^3 and its absorption coefficient by weight is 0.09%. It is of white color with a few thin parallel ash-green colored veins containing locally silver areas due to the existence of dolomite [12].

The geometry of the CCNBD specimen

The CCNBD specimen has the same geometry and shape (Fig. 1) as the conventional Brazilian disc used for measuring, indirectly, the tensile strength of rock. Additionally, the CCNBD specimen has a chevron notch. ISRM [6] recommends that the following dimensionless parameters can be used to characterize the geometry of the chevron notch:

$$\alpha_0 = \frac{\alpha_0}{R},\ \alpha_1 = \frac{\alpha_1}{R},\ \alpha_B = \frac{B}{R},\ \alpha_s = \frac{D_s}{D},\ \alpha^* = \frac{\alpha^*}{R} \tag{1}$$

where the diameter D is twice the radius R, B is the thickness of the disc, α_0 is the initial notch length, α_1 is the final notch length, α^* is the intermediate crack length, α^*_m is the critical crack length, and α_0, α_1, α_B, α^*, α^*_m are the relevant dimensionless expressions.

Furthermore, as shown in Fig. 1a, 2b is the crack front width, P is the load applied to the disc and D_s is the diameter of the circular cutting blade. Typical standard ratios for a CCNBD specimen suggested by ISRM [6] are given as:

$$\alpha_0 = 0.2637, \alpha_1 = 0.65,\ \alpha_B = 0.80,\ \alpha^*_m = 0.5149 \tag{2}$$

For crack lengths as presented above, high stress concentrations are generated at the crack tip which eventually lead to crack propagation and failure.

At this point it should be stressed that cracks machined by rotating cutting saws are actually of a rectangular shape thus possessing four critical points, the corners of the rectangular slit, rather than two crack tips [13]. This fact leads to a more complicated failure mechanism in the closed vicinity of the crack crown. Here however, taking also into account the AE instruments available (namely the relatively big size of sensors used), interest is focused to a wider area considering a single dominating singularity, the crack tip.

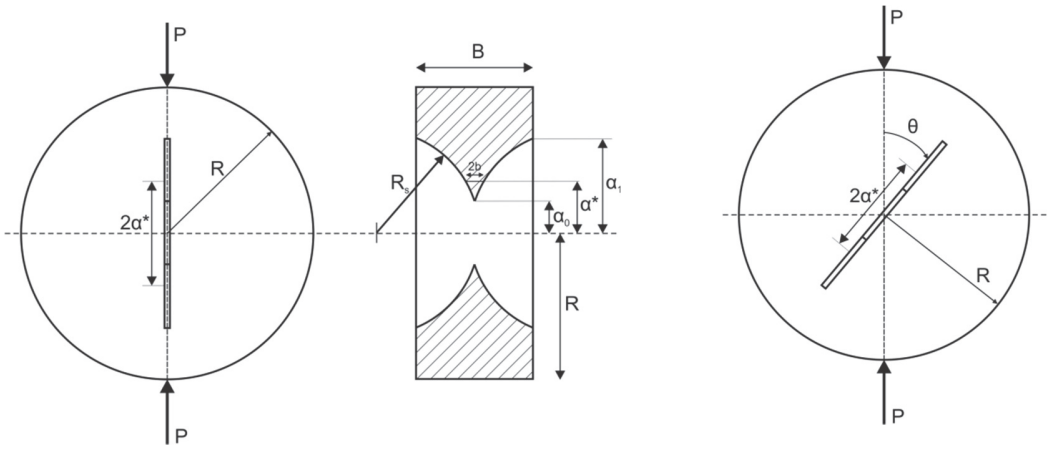

Figure 1: Geometry of CCNBD specimens under (a) pure mode I loading and (b) mixed mode I-II loading.

Fracture toughness calculation for CCNBD tests

The stress intensity factors (SIF), K_I and K_{II} for the Cracked Straight-Through Brazilian Disc (CSTBD) specimen with a through notch length of 2α, can be expressed as [5]:

$$K_I = \frac{P}{\sqrt{\pi \cdot R \cdot B}} \cdot \sqrt{\alpha} \cdot N_I \quad \text{or} \quad K_I = \frac{P}{\sqrt{\pi \cdot R \cdot B}} \cdot Y_I \tag{3a}$$

where

$$Y_I = \sqrt{\alpha} \cdot N_I \tag{3b}$$

$$K_{II} = \frac{P}{\sqrt{\pi \cdot R \cdot B}} \cdot \sqrt{\alpha} \cdot N_{II} \quad \text{or} \quad K_{II} = \frac{P}{\sqrt{\pi \cdot R \cdot B}} \cdot Y_{II} \tag{4a}$$

where

$$Y_{II} = \sqrt{\alpha} \cdot N_{II} \tag{4b}$$

where P is the load applied in compression, $a = \alpha / R$ and N_I, N_{II} are dimensionless coefficients that are functions of a and the notch inclination angle with respect to the loading direction, θ (Fig. 1b). Y_I and Y_{II} are the dimensionless stress intensity factors for CSTBD specimen.

Fig. 2 compares the geometrical terms for CSTBD and CCNBD specimens. The intermediate crack length α^* in CCNBD specimens varies between α_0 and α_1 and is regarded as equivalent of the crack length α in CSTBD specimens.

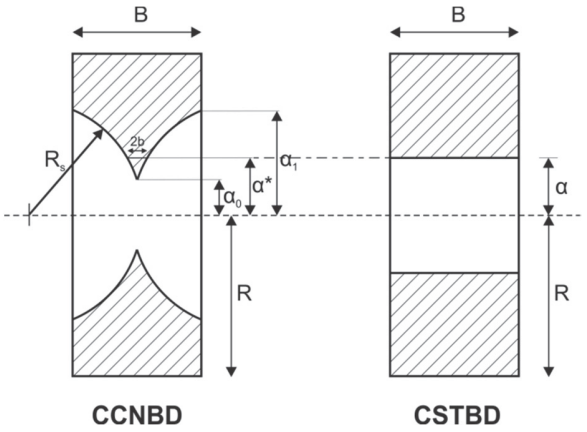

Figure 2: The geometrical definition of crack length α^* (CCNBD) and α (CSTBD).

By applying the Straight Through Crack Assumption (STCA) method [5, 14] to a CCNBD specimen, the relationships (3) and (4) take the form [10]:

$$K_I = \frac{P}{\sqrt{\pi \cdot R} \cdot B} \cdot \sqrt{\alpha^*} \cdot \sqrt{\frac{a_1 - a_0}{\alpha^* - a_0}} N_I \quad \text{or} \quad K_I = \frac{P}{\sqrt{\pi \cdot R} \cdot B} \cdot Y_I^* \tag{5a}$$

where

$$Y_I^* = \sqrt{\alpha^*} \cdot \sqrt{\frac{a_1 - a_0}{\alpha^* - a_0}} N_I \tag{5b}$$

$$K_{II} = \frac{P}{\sqrt{\pi \cdot R} \cdot B} \cdot \sqrt{\alpha^*} \cdot \sqrt{\frac{a_1 - a_0}{\alpha^* - a_0}} N_{II} \quad \text{or} \quad K_{II} = \frac{P}{\sqrt{\pi \cdot R} \cdot B} \cdot Y_{II}^* \tag{6a}$$

where

$$Y_{II}^* = \sqrt{\alpha^*} \cdot \sqrt{\frac{a_1 - a_0}{\alpha^* - a_0}} N_{II} \tag{6b}$$

where Y_I^* and Y_{II}^* are the dimensionless stress intensity factors for CCNBD specimen. Clearly, Y^* of CCNBD and Y of CSTBD are related by the following relationship:

$$Y^* = \sqrt{\frac{a_1 - a_0}{\alpha^* - a_0}} \cdot Y \tag{7}$$

The Eqs. (5) and (6) are employed to calculate fracture toughness values of CCNBD under mixed mode I-II loading. Atkinson et al. [4] provided a solution for N_I and N_{II} given by a five-term approximation (for $0.1 \le \alpha \le 0.6$):

$$N_I = \sum_{i=1}^{n} T_i (\alpha)^{2i-2} \cdot A_i (\theta) \tag{8}$$

$$N_{II} = 2\sin 2\theta \cdot \sum_{i=1}^{n} S_i (\alpha)^{2i-2} \cdot B_i(\theta) \tag{9}$$

where the first five values of T_i, S_i and the corresponding $A_i(\theta)$, $B_i(\theta)$ are given in Tabs. 1 and 2 in Ref. [4], respectively. Fig. 3 presents the variation of the dimensionless coefficients N_I, N_{II} with respect to the inclination angle θ for dimensionless notch lengths $\alpha = 0.1 - 0.6$.

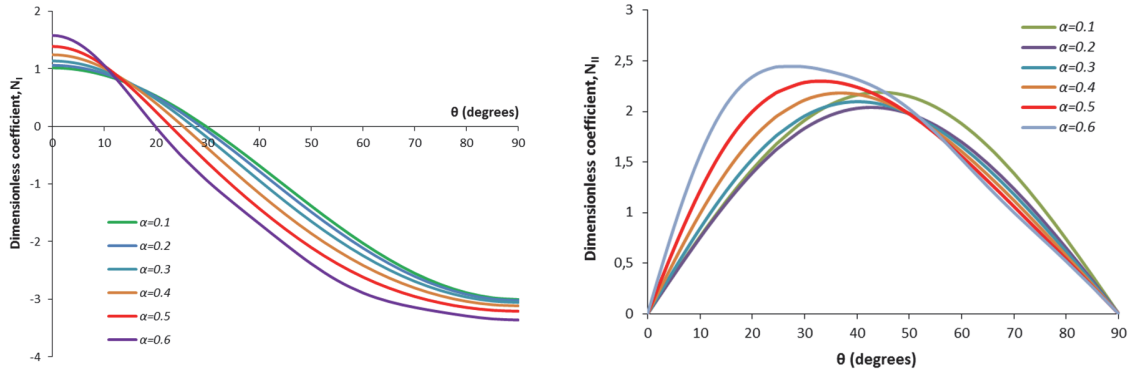

(a) (b)

Figure 3: The dimensionless coefficients (a) N_I and (b) N_{II} for $\alpha = 0.1 - 0.6$.

In the ISRM suggested methods [6] the mode I fracture toughness K_{IC} of CCNBD specimens [6, 14, 15, 16] can be calculated by the following equation:

$$K_{IC} = \frac{P_{max}}{B \cdot \sqrt{D}} \cdot Y^*_{min} \tag{10}$$

where P_{max} is the maximum load that can be sustained by the specimen and Y^*_{min} is the minimum (critical) dimensionless stress intensity factor which is determined by the specimen geometry parameters α_0, α_1 and α_B only, and is given by:

$$Y^*_{min} = u \cdot e^{v \cdot \alpha_1} \tag{11}$$

where u and v are constants determined by α_0 and α_B only [6].

Changing the angle between loading direction and chevron notch orientation (i.e. angle θ in Fig. 1b), fracture toughness tests can be performed under mode II and mixed mode I-II loading conditions. Thus, for pure mode I loading, the crack direction should be exactly along the applied diametral force (i.e., $\theta = 0^o$), while a pure mode II condition in CCNBD specimen is achieved when the dimensionless SIF Y^*_I in relationship (5b), is equal to zero. According to Fig. 3a, $Y^*_I = 0$ when the crack inclination angle θ is about 23^o. Several researchers have also determined this angle to range between 20 and 24 degrees using numerical models [11, 14]. Markides et al. [17] and Markides and Kourkoulis [18] through analytical solutions of short straight through cracks and bigger cracks obtained from elliptic holes respectively, calculated, also, this angle as a function of the dimensionless crack length from a maximum value of about 29 degrees for $\alpha / R = 0.1$ (very short crack) to about 22 degrees for $\alpha / R = 0.5$.

Calculation of the Critical crack length

Different dimensionless values for the critical crack length have been proposed in the literature. In the ISRM Suggested methods [6] it is stated that the critical crack length is $\alpha^*_m = 0.5149$ (for a specimen geometry given by Eq. (2)) without any explanation of how this value was calculated. For the exact same specimen geometry, Wang et al. [7] proposed to use a critical crack length of 0.49, while a value of 0.4915 is derived in the present paper, by minimizing the dimensionless Stress

Intensity Factor Y^*. More specifically, the upper curve shown in Fig. 4 represents the dimensionless stress intensity factor of the CCNBD specimen for various crack lengths as obtained from Eq. (5b) in conjunction with Eq. (8) for mode I, while the lower curve corresponds to the dimensionless SIF of the CSTBD specimen as obtained from Eq. (3b) in conjunction with Eq. (8) also for mode I. It is observed that the SIF for the CSTBD specimen monotonically ascends, while the SIF curve for the CCNBD specimen is convex and reaches a minimum value between the initial and final crack length. The minimum SIF value for the CCNBD specimen $Y^*_{min} = 1.2578$ corresponds to the critical crack length $\alpha^*_m = 0.4915$. When $\alpha^* \geq \alpha_1$, it is assumed that the SIF for the CCNBD specimen is identical to that of the CSTBD specimen as discussed by [7] and [9].

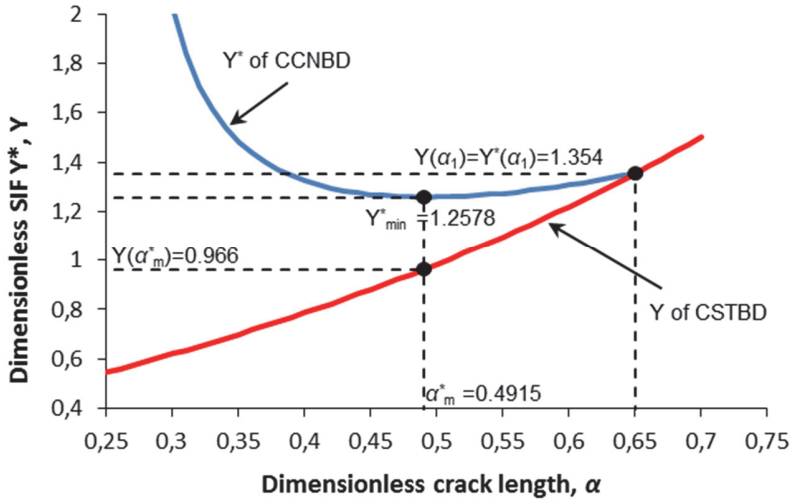

Figure 4: Dimensionless stress intensity factors for straight through and chevron notches in a CCNBD specimen with $\alpha_0 = 0.2637$ and $\alpha_1 = 0.65$.

Specimen preparation and experimental setup

Initially, the circular discs of Nestos marble (D = 52 mm) were prepared by coring specimens out of Nestos cubes with their long axis normal to the plane of transverse isotropy (Fig. 5), in order to avoid large variations in the quality of the stone and ensure similar fracture loads.

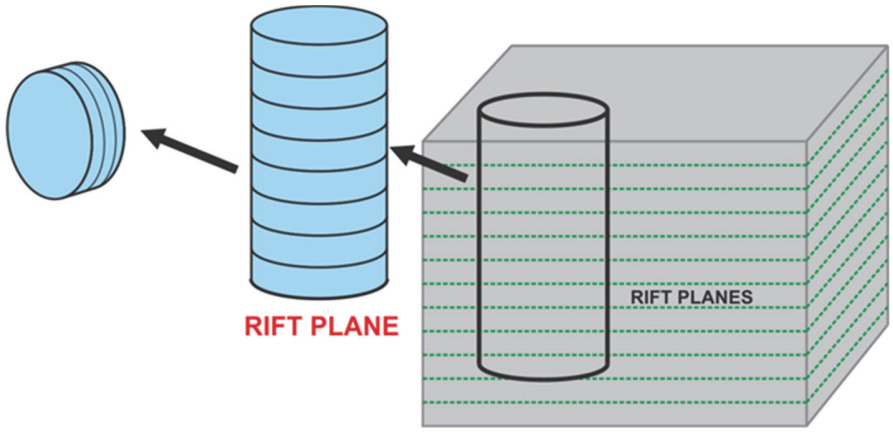

Figure 5: Specimen orientation. The middle plane of the disks is parallel to the plane of transverse isotropy (rift planes).

The CCNBD specimens were prepared according to the standard geometrical dimensionless expressions (2) [6]. Two chevron notches (one in each side) were cut in the center of each disc by using a thin rotary diamond saw with a diameter of D_s = 38 mm and a thickness of t = 1 mm which results in a crack width of less than 1.5 mm (Fig. 6). This satisfies the requirements suggested by [6,9,10,14] that the machined crack width should not exceed 1.5 mm. Wang et al [19]

emphasize that the notch width has an important effect on the stress intensity factors and that the crack width should be adequate to ensure crack propagation. At the same time Shetty et al. [5] indicate that they used a machined slot opening of 250 μm without giving any technical details. The indentation depth of the rotary saw on each side of the disc was about 11.72 mm and thus, two V shape chevron notches were introduced in the circular disc. The diamond saw was cooled by water during the chevron notch cutting process.

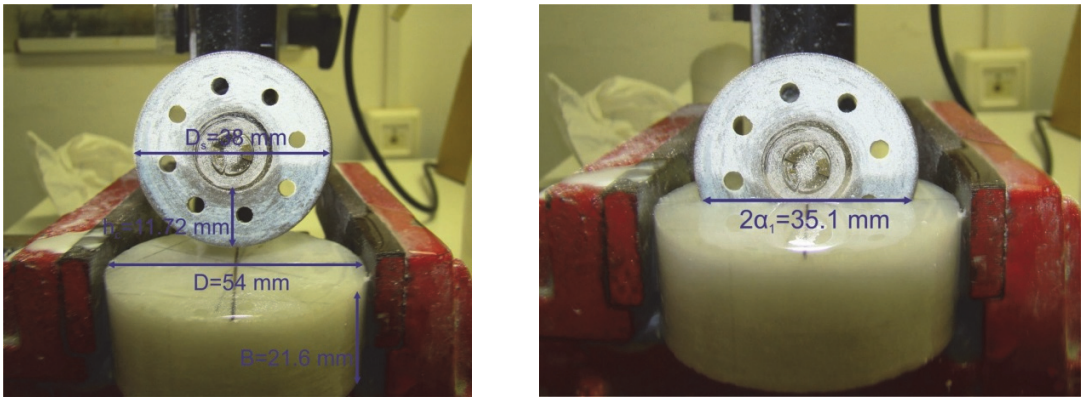

Figure 6: The schematic cutting configuration for preparing CCNBD specimens with some theoretical geometrical parameters.

Fig. 7a presents the final configuration of a CCNBD specimen with the theoretical dimensional parameters α_0 and α_1. In order to obtain consistent test results and to satisfy the plane strain condition, the ISRM [6] prescribes that the range of α_1 and α_B is restricted as shown in Fig. 7b. It is evident that the selected geometric parameters (2) are located within the valid range.

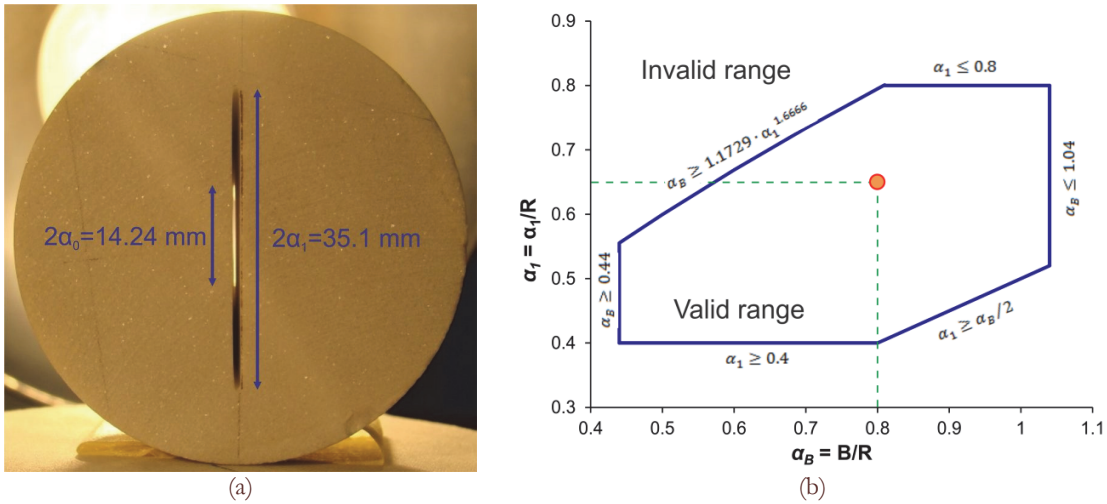

(a) (b)

Figure 7: (a) CCNBD specimen. (b) The valid geometrical range for CCNBD specimen.

The CCNBD specimens (Fig. 7a) were then placed in the Brazilian testing apparatus and loaded by a diametral compressive force P. For pure mode I loading, the crack direction should be exactly along the loading diameter, while for mixed mode I-II loading the chevron notch orientation lies between 0 and 90 degrees. Load was applied using a stiff 1600 kN MTS hydraulic testing machine and a 500 kN load cell, with a loading rate of 200 N/s under load control mode for all experiments.

Monitoring of Acoustic Emissions

The AE activity may be represented in time series of detected signals in each sensor (hits), their amplitudes (signal peak in dB), rise time (RT) which is defined as the time between the first threshold crossing (FTC) and the point of peak amplitude, as well as other acoustic parameters. AE signals were acquired and analyzed using the AE WIN software

package by Enviroacoustics [20]. Acoustic emission signals were detected through 6-8 miniature piezoelectric sensors (PICO sensors, 200 kHz-1 MHz, MISTRAS Group, SA) mounted on the surface of each specimen and recorded through an integrated multi-channel system of Physical Acoustics Corporation. The positions of the sensors on each side of the CCNBD specimens for the determination of the mode I ($\theta=0^o$) and mode II ($\theta=23^o$) fracture toughness are shown in Fig. 8 and Fig. 9, respectively. Usage of such sensors was dictated due to the small size of the specimens. Their high sensitivity over a broad bandwidth ensures the accurate detection of the AE signals. It should be noted that in the case of the specimens subjected to mode I loading, the positions of the AE sensors were symmetrically located with respect to the tips, while in the case of the mode II loading the positions were somewhat arbitrary positioned on the surface of the specimens. In both cases, however, the accurate determination of the events' location is mainly limited by the size of the sensors and to a lesser extent by their positions, as discussed in the next section.
The source location of the AE events on a planar projection was determined by using the arrival times of the hits detected by at least three sensors. This procedure is described in details elsewhere [21].

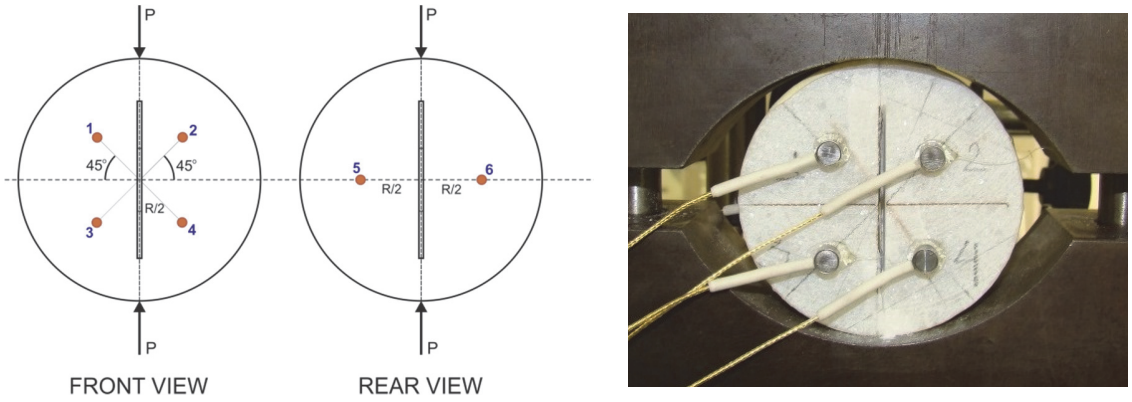

Figure 8: The positions of the sensors for the mode I ($\theta=0^o$) loading CCNBD specimens.

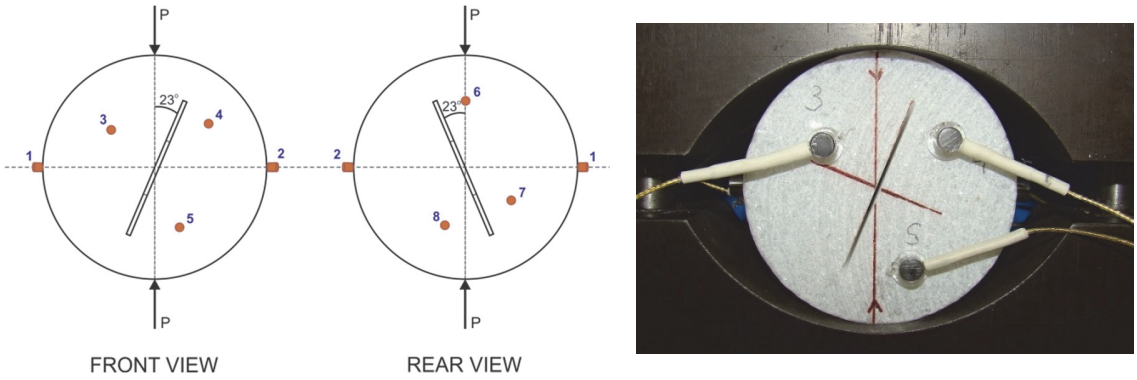

Figure 9: The positions of the sensors for the mode II ($\theta=23^o$) loading CCNBD specimens.

EXPERIMENTAL RESULTS ANS DISCUSSION

Rock fracture toughness for pure mode I

Six CCNBD tests were performed for the determination of mode I fracture toughness (Fig 8). The fracture load was identified using AE records and the specimen fracture toughness was calculated using Eq. (10). The average fracture toughness of these specimens was (0.73±0.08) MPa $m^{1/2}$ (Tab. 1).

The minimum dimensionless stress intensity factor Y^*_{min}, is an important calculation parameter which greatly affects the accuracy of toughness tests. It is calculated using Eq. (11) and the values of parameters u, v, as suggested by the ISRM [6]. In order to improve the fracture toughness tests using CCNBD, recent research [8, 9, 16], based on the slice synthesis method [22] and other numerical methods, presented updated values of the two parameters of the exponential function (Eq. (11)) that cover a wide range of specimen geometries.

Tab. 2 presents the rock fracture toughness calculated by Eq. (11) using parameter values u and v from the original tables of the ISRM [6] and three other publications. It is noteworthy that the difference between the average fracture toughness calculated by the ISRM and the three other publications is about 12%. Note that the K_{IC} values presented in Tab. 2, are calculated using the u and v values proposed by ISRM [6] and those proposed by other researchers [8, 16, 9], while the K_{IC} value for [5] is calculated using $\alpha_m^* = 0.4915$.

Specimen	Thickness (mm)	Diameter (mm)	α_0	Fracture load (kN)	Y_{min}^* [6]	K_{IC} $\left(MPa \cdot m^{1/2}\right)$
2.1	21.00	52.30	0.229	4.35	0.83	0.75
2.2	20.75	52.20	0.234	3.63	0.83	0.64
2.3	20.75	52.20	0.241	4.33	0.83	0.76
3.3	20.80	52.17	0.230	3.72	0.83	0.65
4.2	20.75	52.17	0.264	4.95	0.84	0.88
4.3	20.50	52.23	0.302	3.81	0.85	0.69
Average				4.13	0.83	0.73
St. Dev.				0.46	0.01	0.08

Table 1: Geometrical parameters, fracture loads and fracture toughness of CCNBD specimens under pure mode I loading (the value for Y_{min}^* was calculated based on eq. (11) using the values for u and v given by ISRM [6] in table form).

Specimen	ISRM [6]	Wang et al. [8]	Wang [16]	Wang et al. [9]	Shetty et al. [5]
2.1	0.75	0.85	0.84	0.86	0.91
2.2	0.64	0.72	0.72	0.73	0.77
2.3	0.76	0.86	0.85	0.87	0.91
3.3	0.65	0.73	0.73	0.75	0.78
4.2	0.88	0.99	0.99	1.00	1.05
4.3	0.69	0.78	0.78	0.80	0.81
Average	0.73	0.82	0.82	0.84	0.87
St. Dev.	0.08	0.10	0.10	0.10	0.10

Table 2: Comparison of rock fracture toughness $K_{IC}\left(MPa \cdot m^{1/2}\right)$ for the CCNBD specimens.

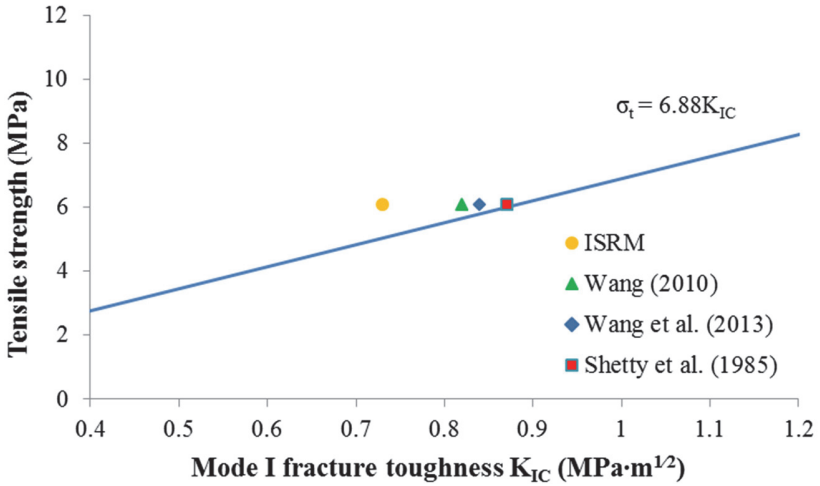

Figure 10: Correlation between the tensile strength and mode I fracture toughness based on different methodologies.

Furthermore, Zhang [23] correlates the mode I fracture toughness and tensile strength of different rock types through the following equation:

$$\sigma_t = 6.88 \cdot K_{IC} \tag{12}$$

For comparison, the average values of mode I fracture toughness obtained for Nestos marble as shown in Tab. 2 were plotted together with Eq. (12). A tensile strength for the Nestos Marble equal to 6.07 MPa (determined experimentally using a traditional Brazilian test) was used for all data points. Experimental results correlate well with the values generated by Eq. (12) except for the value obtained via the ISRM (Fig 10).

Rock fracture toughness for pure mode II

The orientation of the chevron notch crack of the CCNBD specimen, for the determination of the fracture toughness for pure mode II loading was θ=23° from the loading direction. The fracture toughness K_{IIC} values were calculated using Eq. (6a) with the aid of relationship (9) (Tab. 3). Two sets of K_{IIC} values are provided in Tab. 3, calculated for different critical crack lengths. In the first case, K_{IIC} was calculated using a critical crack length calculated by minimizing Y^*_{min} while in the second case the critical crack length was set equal to 0.36 [10].

Specimen	Thickness (mm)	Diameter (mm)	α_0	α_1	Fracture load (kN)	N_{II}	K_{IIC} $\left(MPa \cdot m^{1/2}\right)$ $\left(a^*_m = 0.4915\right)$	K_{IIC} $\left(MPa \cdot m^{1/2}\right)$ $\left(a^*_m = 0.36\right)$
CCNBD 1	20.90	52.30	0.262	0.679	5.10		1.64	1.84
CCNBD 2	20.85	52.35	0.263	0.685	4.89		1.58	1.77
CCNBD 3	21.20	52.30	0.229	0.672	5.90		1.87	2.10
CCNBD 6	21.25	52.25	0.270	0.684	5.98	1.8013	1.89	2.13
CCNBD 7	19.50	52.30	0.350	0.677	4.73		1.63	1.83
CCNBD 8	21.00	52.30	0.281	0.673	4.89		1.57	1.76
CCNBD 9	21.60	52.30	0.242	0.675	4.95		1.54	1.73
Average					5.21		1.67	1.88
St. Dev.					0.51		0.15	0.16

Table 3: Geometrical parameters, fracture loads and fracture toughness of CCNBD specimens under pure mode II loading.

Crack growth and mode of fracture

The crack growth for mode I specimens was along the chevron notch plane and the tensile splitting was the dominant failure mode. Fig. 11 shows a typical CCNBD specimen fractured under pure mode I loading. For mode II loading where the angle between the applied stress and the chevron node direction is 23°, a typical fractured specimen is illustrated in Fig. 12.

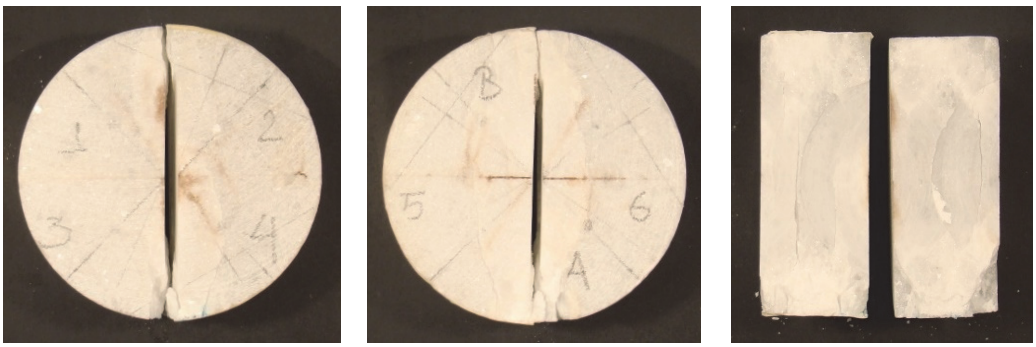

Figure 11: A typical CCNBD specimen fractured under mode I loading.

Figure 12: A typical CCNBD specimen fractured under mode II loading.

At this point it should be mentioned that investigation of the closed vicinity of the 'crack tip', particularly in the case of mode-II loading, reveals that crack growth seems to start from the inner edge of the chevron slit and then propagates towards the corner points of the slit that are nearer to the points of application of the externally applied load (Fig 12).That seems to be the case even for mode-I loading (Fig.11), due, however, to reasonable imperfections detected in the final shape of the chevron slit.

That phenomenon may, in a first approximation, be attributed to the fact that the corner points nearer to the points of application of the externally applied load are under a combined tensile and shearing stress field probably enhancing fracture, while the opposite ones are under a combined compressive and shearing stress field [13], probably not enchasing fracture.

In this context, the SIF concept referring to mathematical cracks, should be considered with extra care, when it comes to slits.

In addition, it should also be mentioned that the fracture patterns detected in the vicinity of the disc-jaw contact region (visible at the bottom areas of contact in Figs. 11, 12) and the possibility of premature fracture in these areas (even in the present case of the pre-CCNBD specimen), are probably attributed to frictional stresses developed at the contact areas to counterbalance the rotation tendency of the disc as a whole due to the presence of the slope slit [24]. This may be an area to be closely monitored in subsequent experiments by potentially using additional piezoelectric sensors at these regions of the specimen.

Acoustic emission results

The time evolution of various acoustic emission parameters during the CCNBD test of a representative specimen (specimen 2.3) subjected to mode I fracture (see Fig. 11) is shown in Fig. 13a-d. Observable AE activity starts at the time t=30 s of the test, i.e., just before the occurrence of the first macroscopic crack at the load of 4.3 kN. The final rupture of the specimen occurs at around 54 s, as it is evident from the corresponding drop in the load which is also accompanied with relatively high amplitudes of the recorded signals in all channels (see Fig. 13a).

It is noteworthy that the first macro-crack is clearly distinguished in the recorded parameters since it is associated with an abrupt increase of recorded hits with high amplitudes (see Fig. 13a, c) and the corresponding observed peak of high hit rate at around 33 s (see Fig. 13b). In contrast, the recorded relatively high mean hit rate and the corresponding uniform increase of cumulative hits after 52 s are not sufficient to correlate them with the final rupture of the specimen. An important AE parameter which has also to be considered is the rise time (RT) of the recorded waveforms that gives us information about the fracture process [25]. It is evident from Fig. 13d that high values of RT are observed at around t = 32.5 s due to the formation of the first macroscopic crack and afterwards during the stage of the final rupture (53 - 54 s). In the intermediate region, the mean value of RT remains almost constant (RT < 250 μs), while the AE activity increases continuously. These low values of RT are related to the formation of tensile micro-cracks while, the high recorded values are due to the formation of mixed mode cracks (tensile and shear) observed either solely during the formation of the macroscopic crack at the initial stage of loading (around 32.5 s), or at the final stage where the coalescence of the existent cracks takes place, leading to the ultimate rupture of the specimen [25]. Notably, during the final rupture of the specimen (at 53-54 s), the load does not decrease abruptly as it could be expected, while, large values of amplitudes are still observed afterwards. This is attributed to the fact that although the specimen was separated into two parts (see Fig. 11), it retained its stability, while considerable AE activity is produced due to the friction between, either the two separated parts of the fractured specimen, or the mounting jaws and the surface of the specimen.

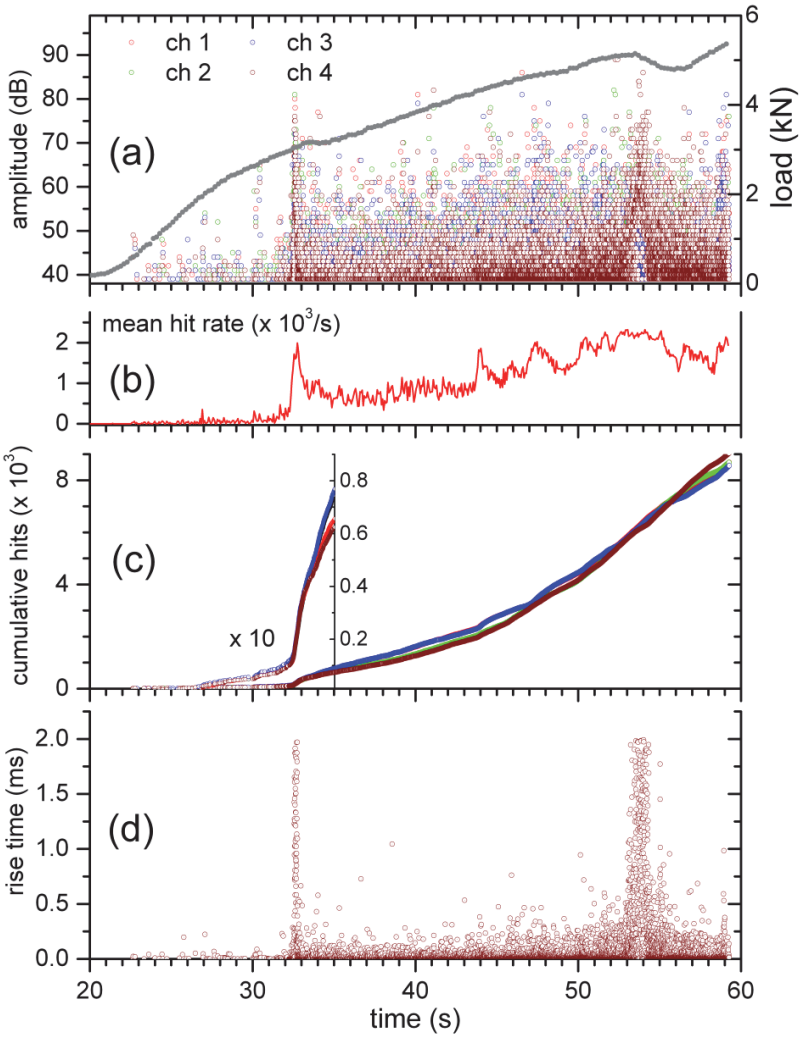

Figure 13: Time evolution of acoustic emission parameters during the CCNBD test of the specimen 2.3 (mode I fracture). (a) The distribution of amplitudes of the 4 sensors located to the front face of the specimen, in conjunction with the applied load. (b) The mean hit rate of all sensors. (c) The cumulative distribution of hits and (d) the rise time of hits recorded in channel 4.

Two-dimensional AE source localization was also conducted in order to gain additional information for the formation of the first macroscopic crack in specimens with mode I fracture.

We have to note here that the small size of the specimens as compared to the size of the sensors (5mm diameter) and the size effect to the acoustic wave velocities result to inevitable large uncertainties to the estimation of the events location, leading to the scattering of the estimated positions. However, the rejection by filtering, of the events with low amplitudes close to the threshold (Amp<44 dB) may improve the overall pattern although it reduces their total number.

A 2D location pattern derived from the signals recorded from the 4 sensors positioned at the front side of specimen 2.3 is illustrated in Fig. 14. From the first snapshot (t = 26 s) we may conclude that the AE activity initiates at the bottom tip of the chevron notch. Afterwards, events with higher amplitudes are observed to the upper tip suggesting that the stress concentration is higher in this region. However, during the formation of the macroscopic crack (t = 34 s) the events are randomly distributed around the two tips of the notch without any preferential orientation or position. Similar patterns were also estimated for the other specimens subjected to mode I fracture.

In the case of the CCNBD tests of the specimens fractured under pure mode II loading, the AE activity exhibits some similar characteristics with the mode I loading, regarding the correlation of the AE parameters with the fracture process. The AE parameters during the test of a representative specimen (specimen 3.23) are shown in Fig. 15a-d. Considerable AE activity starts at around 57% of the fracture load (5.9 kN) as it is indicated from the uniform increase of the mean hit rate in Fig. 15b. However, a small number of hits with relative high amplitudes are also recorded from the beginning of

the test, suggesting a limited formation of isolated micro-cracks. High values of RT are observed at the final stage of the rupture (after t=72 s), as in the case of the specimen 2.3, but there is no indication of any macroscopic crack before the final rupture of the specimen.

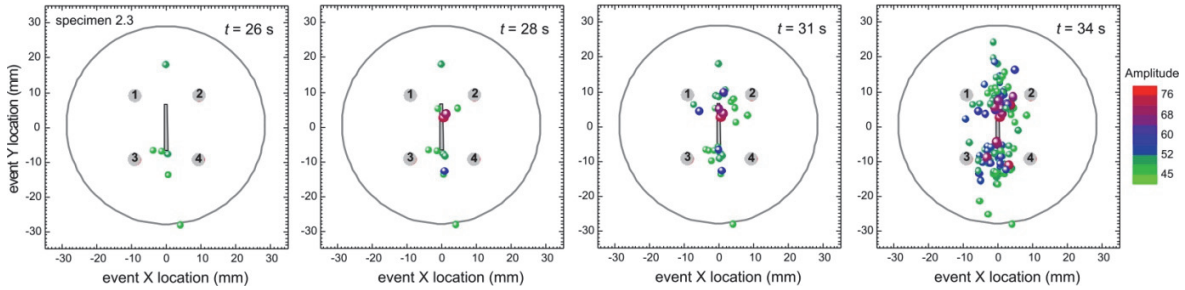

Figure 14: 2D pattern of the location of cumulative events at different selected times, during the CCNBD test of the specimen 2.3 (mode I loading). The positions of the 4 sensors at the front side of the specimen that were used in the location algorithm and the chevron notch are also indicated. The color scale denotes the highest amplitude of the recorded hits in each event and thus is an estimation of the magnitude of the events.

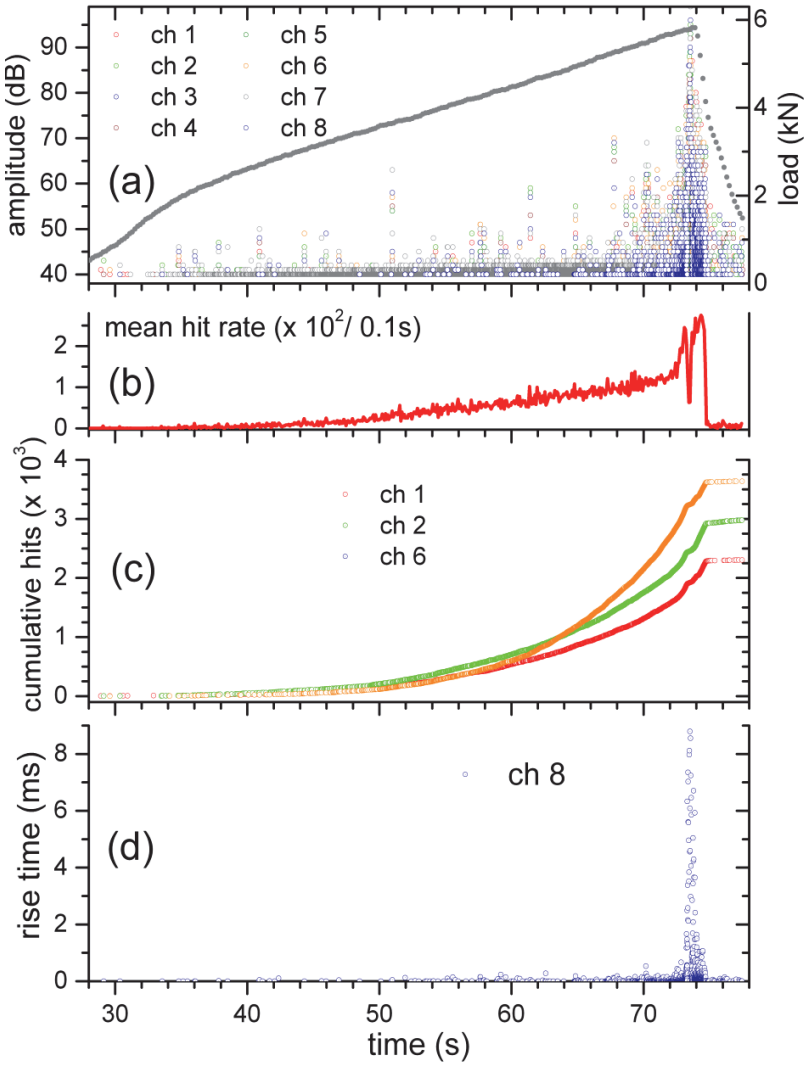

Figure 15: Time evolution of acoustic emission parameters during the CCNBD test of the specimen 3.23 (mode II fracture). (a) The distribution of amplitudes of all sensors located to the surface of the specimen, in conjunction with the applied load (b) The mean hit rate of all sensors. (c) The cumulative distribution of hits from sensors 1, 2 and 6 and (d) the rise time of hits recorded in channel 8.

Finally, a planar projection pattern of the 3D location derived from the signals recorded from all the sensors positioned at the sides of specimen 3.23 is illustrated in Fig. 16. As it is evident from the first snapshot at the early stages of the loading (t=65 s), the stress concentration should be uniform in each side of the specimen during the applied load. At the final rupture of the specimen (t=77.5 s), a rather diffused distribution of the events is observed, while their concentration at the upper tip of the chevron notch is more pronounced. The latter is consistent with the created final macroscopic crack at the upper side of the specimen (see Fig. 12). However, it should be noted that, although the location has been improved considerably by taking into account the filtered hits (Amp >46 dB) as in the case of the specimen 2.3 (Fig. 14), the discontinuity of the specimen due to the chevron notch, in conjunction with the small size of the samples, sufficiently restrict the quality of the location results.

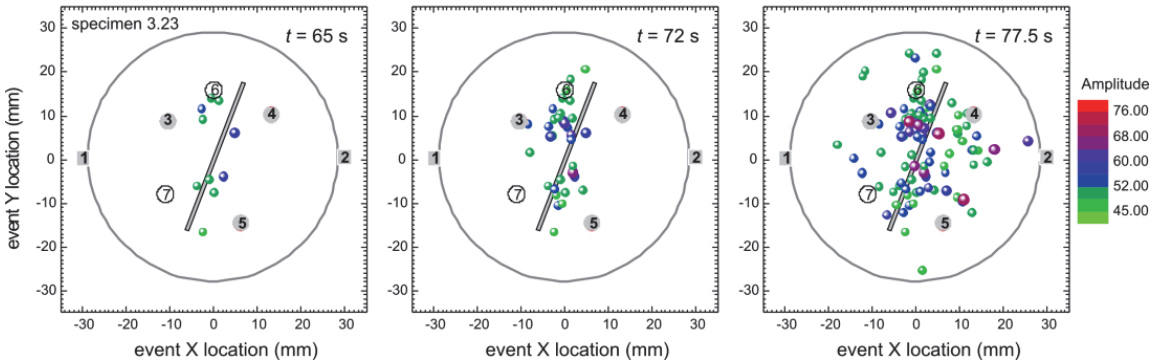

Figure 16: The projection of the 3D location of cumulative events on the circular side of the specimen 3.23 (mode II loading) at different selected times, during the CCNBD test. The positions of the sensors and the chevron notch at 23° are also indicated.

A well-established parameter that is used to determine the stages of fracture has been introduced from the field of seismology and has been modified in order to describe the amplitude distribution in AE analysis. This so-called improved b-value is defined by utilizing statistical values of the amplitude distribution, such as the mean value μ and the standard deviation σ, according to the following relation [26]:

$$I_b = \frac{logN\left(\mu-\alpha_1\sigma\right)-logN\left(\mu+\alpha_2\sigma\right)}{\left(\alpha_1+\alpha_2\right)\sigma} \tag{13}$$

where $N\left(\mu-\alpha_1\sigma\right)$ represents the cumulative number of events with amplitudes greater than $\mu-\alpha_1\sigma$ and $N\left(\mu+\alpha_2\sigma\right)$ is the cumulative number of events with amplitudes greater than $\mu+\alpha_2\sigma$. The empirical constants a_1 and a_2 are user-defined and usually take values equal to unity [26].

Low values of I_b are associated with the generation and propagation of micro-cracks and thus, the characteristic trend of its variation may serve as a qualitative index of damage in the material under investigation. In practice, a window of successive events is predetermined (usually between 50 and 100 events) and then it is shifted in order to calculate the I_b value in each window during the evolution of the experiment. The overlap between successive windows ensures the correlation of the estimated values during the time evolution of the test.

The variation of the calculated I_b values during the CCNBD tests of the specimens 2.3 (mode I loading) and 3.23 (mode II loading) are illustrated in Fig. 17 and Fig. 18, respectively. In each case, values lower than unity are associated with the formation of macroscopic cracks or/and the final failure of the specimens, as it has already been mentioned previously. Thus, in the case of the specimen 2.3, the initially observed macro-crack at around 32.5 s, as well as its final rupture at 54 s, is related with I_b values lower than 0.8 (see Fig. 17). In the case of specimen 3.23 (see Fig. 18), high values of I_b are observed up to the 90% of the failure load but after that, I_b decreases considerable reaching values below unit just before the final rupture.

Furthermore, the results obtained for mode I fracture toughness are similar to experimental results available for a different Greek marble (Dionysos marble) [27, 28, 29]. The interpretation of acoustic data for the later tests [28, 29] shows a higher damage level prior to localization.

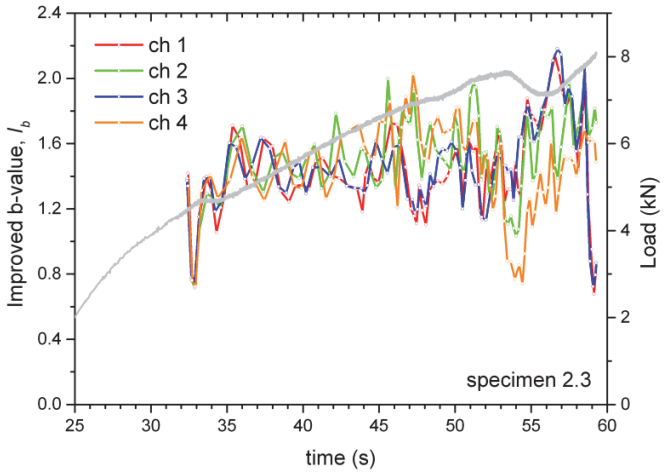

Figure 17: The variation of the improved b-value during the CCNBD test of the specimen 2.3 for each of the 4 sensors positioned in the front face (Number of successive events = 90, 50% overlapping, $a_1 = a_2 = 1$).

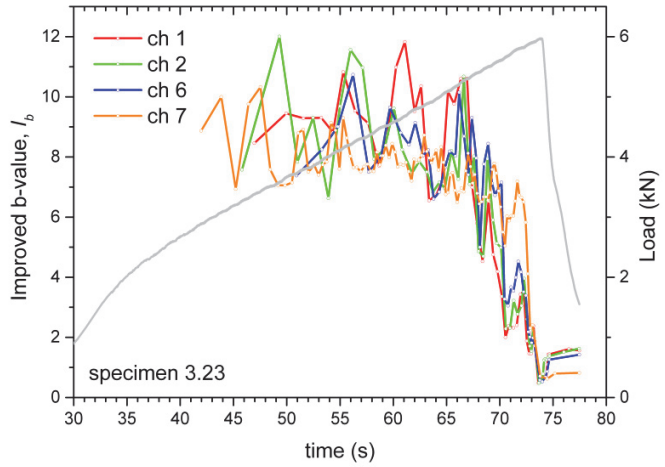

Figure 18: The variation of the improved b-value during the CCNBD test of the specimen 3.23 for 4 selected sensors (Number of successive events = 50, 50% overlapping, $a_1 = a_2 = 1$).

CONCLUSIONS

A number of CCNBD tests were carried out in order to determine the fracture toughness of Nestos marble. Specimens were also instrumented with acoustic sensors in an effort to better determine stress evolution during loading.

The available methodologies for calculating the mode I fracture toughness K_{IC} from CCNBD tests were critically evaluated and compared. In addition, the dimensional stress intensity factor of the CCNBD specimen, Y^*, is calculated with respect to the dimensionless crack length a^* using the dimensionless crack lengths (α_0 and α_1) proposed in the ISRM suggested methods [6]. The calculated minimum SIF value for the CCNBD specimen $Y^*_{min} = 1.2578$ corresponds to the critical crack length $\alpha^*_m = 0.4915$ and is comparable to published critical length values.

In addition, experimental results from the acoustic emissions monitored during the CCNBD tests are evaluated with respect to the load applied to each sample. The localization of the generated events is plotted at different time intervals during the test. Results indicate that during the early loading stages the stress concentration is uniform on both crack edges. As the load increases and the specimen is ready to fail, a rather diffused distribution of the events is observed, while their concentration at the upper tip of the chevron notch is more pronounced. Overall, using acoustic emission signals a

better determination of the failure load can be achieved, as shown in Fig 13 and 15. This failure load can then be used for the fracture toughness calculations.
Using the same experimental data, the mode I fracture toughness is calculated for each one of the different methodologies. Again, these values are comparable to each other and also correlate well with the equation proposed by Zhang [23] relating the tensile strength of rocks to their mode I fracture toughness. The mode II fracture toughness value was only calculated using the methodology proposed by Shetty et al. [5].
Future work could involve the use of an array of several sensors which will be properly positioned on the entire surface of the disc in conjunction with appropriate filtering of AE results, and an investigation of potential correlations with some of the more sophisticated analytic solutions that are available for the entire planar disc, in order to accomplish an overall analysis of the failure mechanism.

REFERENCES

[1] ISRM Testing Commission, (co-ordinator: F. Ouchterlony), Suggested methods for determining the fracture toughness of rock. Int J. Rock Mech Min Sci Geomech Abstr., 25 (1988) 71–96.
[2] Fowell, R.J., Chen, J.F., The third chevron-notch rock fracture specimen - the cracked chevron-notched Brazilian disk. Proc. 31st U.S. Symp. Rock. Balkema, Rotterdam, (1990) 295– 302.
[3] Fowell, R.J., Xu, C., The cracked chevron notched Brazilian disc test - geometrical considerations for practical rock fracture toughness measurement. Int. J. Rock Mech. Mineral Sci. Geomech. Abstr., 30 (7) (1993) 821– 824.
[4] Atkinson, C., Smelser, R.E., Sanchez, J., Combined mode fracture via the cracked Brazilian disk test. Int. J. Fract., 18 (4) (1982) 279– 291.
[5] Shetty, D.K., Rosenfiled, A.R., Duckworth, W.H., Fracture toughness of ceramics measured by a chevron notch diametral compression test. J. Am. Ceram. Soc., 68 (12) (1985) C325– C327.
[6] ISRM Testing Commission (co-ordinator: R.J. Fowell), Suggested method for determining mode I fracture toughness using cracked chevron notched Brazilian disc (CCNBD) specimens. Int J Rock Mech Min Sci Geomech Abstr., 32 (1995) 57–64.
[7] Wang, Q.Z., Jia, X.M., Kou, S.Q., Zhang, Z.X., Lindqvist, P.-A., More accurate stress intensity factor derived by finite element analysis for the ISRM suggested rock fracture toughness specimen – CCNBD. Int J Rock Mech Min Sci., 40 (2003) 233–41.
[8] Wang, Q.Z., JiaX.M., Wu L.Z., Wide-range stress intensity factors for the ISRM suggested method using CCNBD specimens for rock fracture toughness tests. Int J Rock Mech Min Sci., 41 (2004) 709–716.
[9] Wang, Q.Z., Fan H., Gou X.P., Zhang S., Recalibration and Clarification of the Formula Applied to the ISRM - Suggested for Testing Rock Fracture Toughness. Rock Mechanics and Rock Engineering, 46 (2013) 303–313.
[10] Amrollahi, H., Baghbanan, A., Hashemolhosseini, H., Measuring fracture toughness of crystalline marbles under modes I and II and mixed mode I-II loading conditions using CCNBD and HCCD specimens. Int. J. Rock Mech. Min. Sci., 48 (2011) 1123–1134.
[11] Aliha, M.R.M., Ayatollahi, M.R., Rock fracture toughness study using cracked chevron notched Brazilian disc specimen under pure modes I and II loading – A statistical approach. Theoretical and Applied Fracture Mechanics, 69 (2014) 17-25.
[12] Kaklis, K., Mavrigiannakis, S., Agioutantis Z. Bazdanis, G., An investigation of the mechanical characteristics of Nestos Marble. In: Volume in Honor of the late Professor K. Kavouridis, Technical University of Crete Publications, (2010) 57-68 (in Greek).
[13] Markides, Ch.F., Kourkoulis S.K., 'Mathematical' Cracks Versus Artificial Slits: Implications in the Determination of Fracture Toughness. Rock Mech Rock Eng., 49(3) (2016) 707–729.
[14] Chang S-H, Lee C-I, Jeon S., Measurement of rock fracture toughness under modes I and II and mixed-mode conditions by using disc-type specimens. Eng Geol., 66 (2002) 79–97.
[15] Wang, Q.Z., Stress intensity factors of the ISRM suggested CCNBD specimen used for mode-I fracture toughness determination. Int J Rock Mech Min Sci., 35 (1998) 977–982.
[16] Wang, Q.Z., Formula for calculating the critical stress intensity factor in rock fracture toughness tests using cracked chevron notched Brazilian disc (CCNBD) specimens. Int J Rock Mech Min Sci., 47 (2010) 1006–1011.
[17] Markides, C.F., Pazis D.N., Kourkoulis S.K., Stress intensity factors for the Brazilian disc with a short central crack: Opening versus closing cracks. Applied Mathematical Modelling, 35 (2011) 5636–5651.

[18] Markides, Ch.F., Kourkoulis S.K., The finite circular disc with a central elliptic hole under parabolic pressure. Acta Mechanica, 226(6) (2015) 1929–1955.
[19] Wang, Q.Z., Gou, X.P., Fan, H., The minimum dimensionless stress intensity factor and its upper bound for CCNBD fracture toughness specimen analyzed with straight through crack assumption. Engineering Fracture Mechanics, 82 (2012) 1–8.
[20] Enviroacoustics S.A., Noesis, User's manual, (2009).
[21] Agioutantis, Z., Kaklis, K., Mavrigiannakis, S., Verigakis, M., Vallianatos, F., Saltas, V., Potential of acoustic emissions from three point bending tests as rock failure precursors. Int. J. Min. Sci. Tech., 26 (2016) 155-160.
[22] Bluhm, J.I., Slice synthesis of a three-dimensional "work of fracture" specimen. Eng Fract Mech, 7 (1975) 593–604.
[23] Zhang, Z.X., An empirical relation between mode I fracture toughness and the tensile strength of rock. Int J Rock Mech Min Sci., 39 (2002) 401–406.
[24] Markides, Ch.F., Kourkoulis S.K., The circular disc under rotational moment and friction: application to the cracked Brazilian disc test. Archive of Applied Mechanics, 85(12) (2015) 1869–1897.
[25] Shiotani, T., Ohtsu, M., Ikeda, K., Detection and evaluation of AE waves due to rock deformation. Construction and Building Materials, 15 (2001) 235-246.
[26] Shiotani, T., Fujii, K., Aoki, T., Amou, K., Evaluation of progressive failure using AE sources and improved b-value on slope model tests. Progress in Acoustic Emission VII, JSNDI 7 (1994) 529-534.
[27] Dai, S. Labuz, J., Damage and failure analysis of brittle materials by acoustic emission. Journal of Materials in Civil Engineering, 9 (4) (1997) 200-205.
[28] Kaklis K., Mavrigiannakis S., Agioutantis Z., Comparison of acoustic signatures of rock specimens under uniaxial compression. ICCES'12: International Conference on Computational & Experimental Engineering and Sciences, Crete, Greece, (2012).
[29] Nomikos, P.P., Katsikogianni, P., Sakkas, K.M., Sofianos, A.I., Acoustic Emission during Flexural Loading of Two Greek Marbles. Rock Mechanics in Civil and Environmental Engineering, Zhao, Labiouse, Dudt and Mathier (eds), Taylor & Francis Group, London, (2010) 95-98.

Experimental investigation of the mechanical properties of Alfas stone

Konstas N. Kaklis, Stelios P. Mavrigiannakis
School Mineral Resources Eng., Technical Univ. of Crete, Greece
kaklis@mred.tuc.gr, smaurig@mred.tuc.gr

Zach G. Agioutantis
Department of Mining Engineering, University of Kentucky, Lexington, KY University, USA
zach.agioutantis@uky.edu

Emmanouil K. Steiakakis, Foteini K. Stathogianni
School of Mineral Resources Eng., Technical Univ. of Crete, Greece
stiakaki@mred.tuc.gr, stathof@hotmail.com

ABSTRACT. This paper focuses on the experimental investigation of the mechanical properties of the Alfas natural building stone. Two series of uniaxial compression tests and indirect tensile tests (Brazilian tests) were performed in order to determine the uniaxial compressive strength and the indirect tensile strength respectively. Different sets of cylindrical specimens and circular discs were prepared by varying their geometry in order to examine the size effect on the respective strength values. Also, the size effect was investigated with respect to the calculated intact rock modulus and Poisson's ratio. All specimens were prepared by following the ISRM suggested methods and the load was applied using a stiff 1600 kN MTS hydraulic testing machine and a 500 kN load cell. Strain was measured using biaxial 0/90 stacked rosettes appropriately attached on each specimen.

KEYWORDS. Alfas; Building stones; Uniaxial compressive strength; Indirect tensile strength; Size effect.

Citation: Kaklis, K., Mavrigiannakis, S., Agioutantis, Z., Steiakakis, E., Stathogianni, F., Experimental investigation of the mechanical properties of Alfas stone, Frattura ed Integrità Strutturale, 40 (2017) 18-31.

Received: 03.12.2016
Accepted: 09.01.2017
Published: 01.04.2017

INTRODUCTION

Scaling is a major issue for the analysis of large structures made of geomaterials (including rock and soil masses) studied and tested at a smaller scale. In laboratories the researchers are capable to measure the strength of a small specimen and need a scaling law to deduce the strength of a large structure.

The size effect analysis can be dated back to the 15th century when Leonardo da Vinci stated that *among cords of equal thickness, the longest is the least strong* and that a cord *is so much stronger … as it is shorter*. That is the first statement of size effect even though the proportionality between structural size and strength was a bit exaggerated.
In 1638, Galileo when founding the material strength theory rejected da Vinci's rule, but pointed out that large animals have relatively bulkier bones than small ones. He called this statement the weakness of giants.
In 1686, Mariotte conducted several experiments with ropes and deduced that a long rope and a short one always support the same weight unless a long rope happens to have a fault, whereas it will break sooner than in a shorter one. He proposed that this is a consequence of the principle of the inequality of the matter whose absolute resistance may be less in one place than another [1]. At that time, mathematics were not developed enough to properly state the statistical explanation of size effect. This was accomplished two centuries later by Weibull [2].
In rock mechanics and engineering geology, the uniaxial compression and the indirect tension test (Brazilian test) are considered to be the most widely spread methods to obtain rock strength properties and parameters such as the intact rock modulus and Poisson's ratio.
Tensile strength may be measured using the direct tension test. However, this test presents experimental difficulties and is not commonly conducted in rock mechanics laboratories. This is due to both the bending stresses and/or torsion moment caused by the eccentricity of imposed axial loads and the localized concentrated stresses caused by improper gripping of specimens [3,4].
Because of these experimental difficulties, alternative techniques have been developed to determine the tensile strength of rock. In the Brazilian test, a circular solid disc is compressed to failure across the loading diameter. Hondros [5] has analytically solved the Brazilian test configuration in the case of isotropic rocks, while Pinto [6] extended Hondros' method to anisotropic rocks and checked the validity of his methodology on schisteous rock formation. Recent investigations have led to a closed form solution for an anisotropic disc [7,8], a series of charts for the determination of the stress concentration factors at the center of an anisotropic disc [9], and explicit representations of stresses and strains at any point of an anisotropic circular disc compressed diametrically [10].
It should be noted that the so-called "scale effect" is split up into two categories: shape and size effect. The shape effect describes the impact of the height/diameter ratio of a cylindrical specimen on rock strength properties. The size effect is defined by the influence of the absolute size (i.e., volume) of geometrically self-similar specimens. In case of cylindrical specimens this reduces the changes in diameter where the height/diameter ratio remains constant [11].
The scale effect is well known for both the compressive and tensile tests as there are numerous studies in the literature [12,13,14,15] that have investigated the effect of various factors such as size, shape, porosity, density on the uniaxial compressive strength (UCS) and the indirect tensile strength.
This paper presents the effect of the size on UCS, indirect tensile strength, intact rock modulus and Poisson's ratio for the Alfas building stone. The term "intact rock modulus" is used here instead of elastic modulus, in order to differentiate the modulus of intact rock with respect to the deformation modulus of the rock mass.

TESTING MATERIAL

In order to experimentally examine the size effect on the uniaxial compressive and indirect tensile strength, specimens of Alfas building stone were tested. The Alfas stone is a micritic (microcrystalline) homogeneous limestone. X-ray diffraction (XRD) and Rietveld quantitative method [16] results, indicate that it is composed by 91% of calcite ($CaCO_3$), 2% of quartz (SiO_2) and 7% aragonite ($CaCO_3$).
The determination of water absorption at atmospheric pressure is based on standard BS EN 13755 (2008) [17], while the determination of open (effective) porosity and bulk (apparent) density is based on standard BS EN 1936 (2006) [18]. The average results for Alfas stone are shown in Tab. 1.

Water Absorption (%)	Open Porosity (%)	Bulk Density (kg/m^3)
12.19 (±0.61)	31.48 (±3.20)	2870 (±355)

Table 1: Physical properties of the Alfas stone.

THEORETICAL CONSIDERATIONS

Uniaxial compression test

In uniaxial compression test a cylindrical specimen of diameter D and height h is subjected to a uniformly applied stress σ_y, acting on the ends of the specimen (Fig. 1a), following the ISRM suggested method [19]. In addition to the peak stress value, the complete stress-strain curve is recorded in order to calculate the tangent intact rock modulus E_{50} (Fig. 1b).

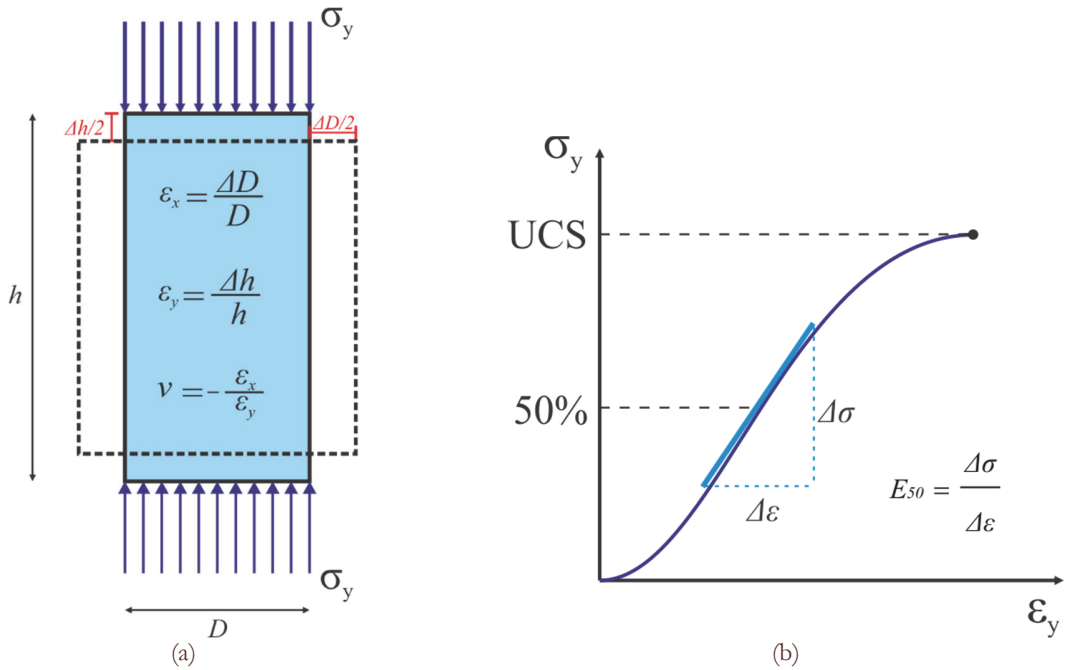

Figure 1: (a) Uniaxial compression test and calculation of axial and lateral strains and Poisson's ratio. (b) Stress-strain curve and the calculation of the tangent intact rock modulus.

Indirect tensile test (Brazilian test)

In the Brazilian test a cylindrical specimen of diameter D and thickness t is subjected to a uniform radial pressure $-p$, acting along an arc of length b at each end of the diameter (Fig. 2a). The angle subtended at the center of the disc by the loaded section of the rim is equal to $2a$. If the material behavior is assumed to be linear elastic, this geometry and loading procedure ensures a nearly uniform tensile stress state in the center plane of the specimen (Fig. 2b). According to this distribution, the expected failure mode is the splitting of the specimen in two halves across the plane of loading. For brittle elastic materials, the maximum tensile stress (f_{st}) is a material property called splitting tensile strength and is linearly related to the failure load (P_f):

$$f_{st} = \frac{2P_f}{\pi D t} \tag{1}$$

Using measurements from electrical strain gages (ε_{xx}, ε_{yy}) that are attached to the center of a specimen, the elastic parameters can be calculated for an isotropic material using the following relationships [20]:

$$E = \frac{16P}{\pi D t} \frac{1}{\varepsilon_{yy}\left(3 + \frac{\varepsilon_{xx}}{\varepsilon_{yy}}\right)} \tag{2}$$

$$\nu = \frac{1+3\left(\frac{\varepsilon_{xx}}{\varepsilon_{yy}}\right)}{3+\left(\frac{\varepsilon_{xx}}{\varepsilon_{yy}}\right)} \tag{3}$$

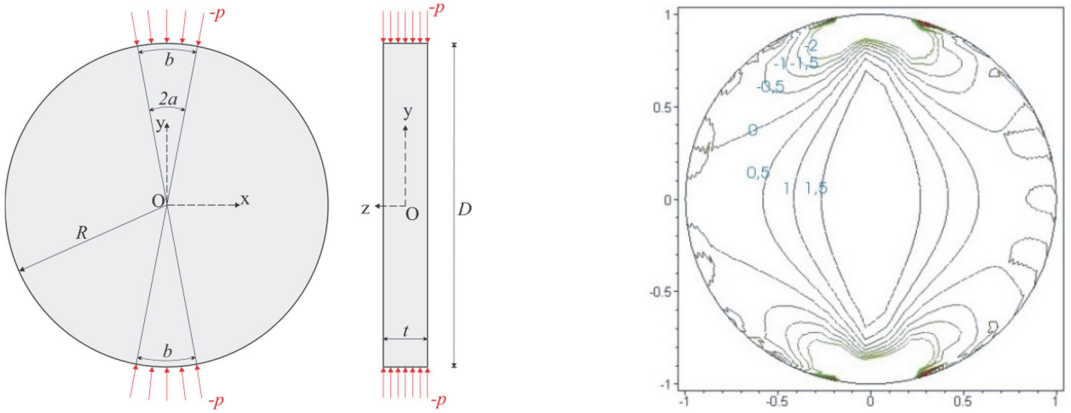

(a) (b)

Figure 2: (a) Load configuration of the Brazilian test, (b) Distribution of the horizontal Stress Concentration factor $q_{xx}=\sigma_{xx}/(p\alpha/\pi)$ calculated according to the theory of elasticity [21].

EXPERIMENTAL PROCEDURE

A sufficient number of block samples for the Alfas stone was collected from the quarry near the Alfas village in Rethymnon, Crete, Greece, and subsequently carefully checked to ensure the homogeneity of the materials. The size of these blocks was 25x30x30 cm. Specimens were prepared for uniaxial compression and indirect tension testing as detailed below. In all testing, load was applied by a stiff 1600 kN MTS-815 hydraulic testing frame and a 500 kN load cell using a load control mode.

Uniaxial compression test

Using the freshly quarried Alfas stone, three sets of cylindrical specimens were prepared according to the ISRM specifications [19] for the uniaxial compression test (Fig. 3a). In order to investigate the size effect, specimens were prepared with diameters D=54, 75 and 100 mm. The height h to diameter D ratio for the uniaxial compression test remained constant and equal to 2. Special care was taken to ensure that the two bases of the cylinders were parallel to each other and perpendicular to the longitudinal axis of the specimens. All experiments were carried out using a very thin film of vaseline jelly as lubrication between the bases of the specimens and the loading platens. The loading rate was 3 kN/s.
In order to measure the axial and lateral strain during the UCS test, three biaxial 0/90 strain gages were appropriately attached at 120^o to each other on the curved surface of the cylindrical specimens, midway between the cylinder bases (Fig. 3b). The use of three strain gages per specimen was deemed appropriate (especially for the larger specimens) in order to check the symmetry of the generated surface strains on the specimen during loading.

Indirect tensile test

Three sets of circular discs were prepared according to the ISRM specifications [22] for the Brazilian test (Fig. 4a). The ratio of the diameter D to thickness t for the Brazilian test remained constant and equal to 2. In order to investigate the size effect, specimens were prepared with diameters D=54, 75 and 100 mm. Subsequently, two strain gages were attached on the center of each flat surface of the circular discs used for the Brazilian tests (Fig. 4b).
The specimens were placed between two steel loading jaws designed to contact diametrically opposed surfaces over an arc of approximately 0.1 radians, (as suggested by ISRM [22]), and the test was conducted with a loading rate of 200 N/s.

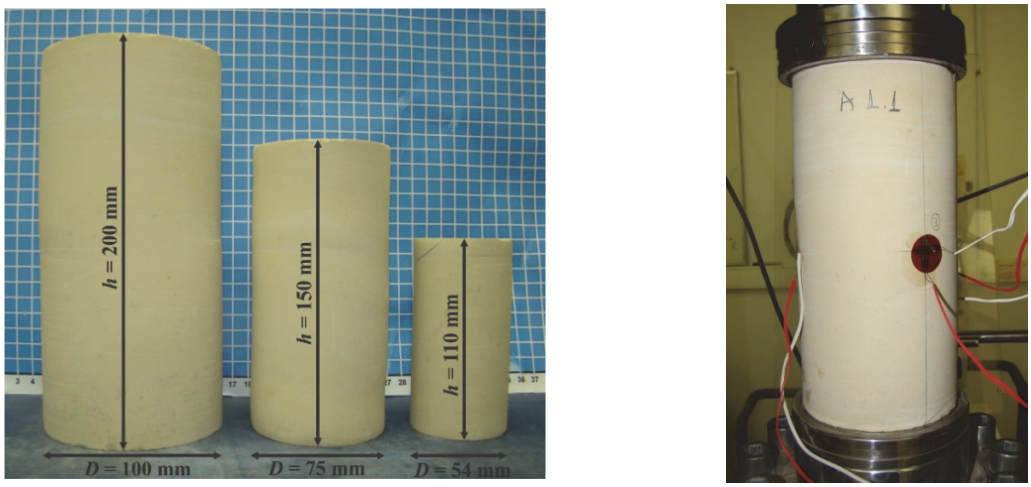

(a) (b)

Figure 3: (a) A series of cylindrical specimens with different diameters and constant ratio $h/D = 2$ for Alfas stone. (b) The position of the strain gages for cylindrical specimens.

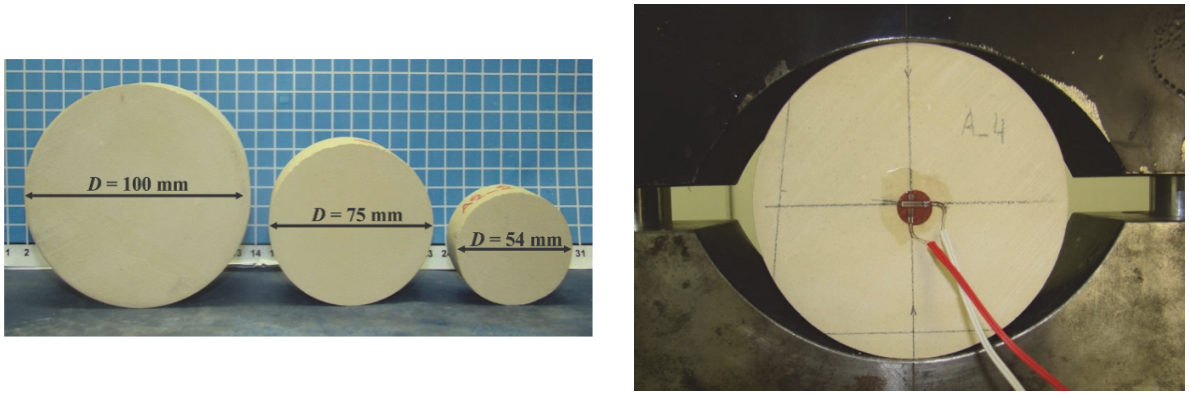

(a) (b)

Figure 4: (a) A series of circular discs with different diameters and constant ratio $D/t = 2$ for Alfas stone. (b) The position of the strain gages attached to the circular discs.

EXPERIMENTAL RESULTS AND DISCUSSION

Uniaxial compression tests

By processing the experimental data, the basic mechanical properties of the material were determined. The uniaxial compressive strength, intact rock modulus and Poisson's ratio are presented in Tab. 2 for the three different sizes of the cylindrical specimens. Note that the intact rock modulus and Poisson's ratio for each specimen was calculated at 50% of the UCS of that specimen. Furthermore, the lateral and axial peak strains and the strain energy density up to the peak load were calculated.

Results from a typical cylindrical specimen with diameter D=100 mm are presented in Fig. 5a, b. It is observed that the strain values measured by the three strain gages are similar (Fig. 5a). It can also be observed that for small strains the constitutive law is almost linearly elastic.

Fig. 5c, d present the variation with the uniaxial stress of the intact rock modulus and Poisson's ratio respectively, for three specimens with diameter D=54 mm. The similarity of these results with respect to the trend and repeatability of the intact rock modulus is evident, at a region where stresses are about 50% of the strength. The variation of Poisson's ratio with stress is consistent along the full stress path for all three specimens.

h [mm]	*D* [mm]	*Number of tests*	*Number of specimens with strain gages*	*Uniaxial compressive strength* [MPa]		*Intact rock modulus* *E* [MPa]		*Poisson's ratio* ν	
				Average [MPa]	*St. Dev.* [MPa]	*Average* [MPa]	*St. Dev.* [MPa]	*Average*	*St. Dev.*
110	54	6	6	35.56	0.51	13575	193	0.221	0.007
150	75	6	6	33.81	0.73	13318	733	0.238	0.022
200	100	6	6	32.09	1.82	13735	1272	0.242	0.015

Table 2: The experimental results of the uniaxial compression tests for Alfas stone.

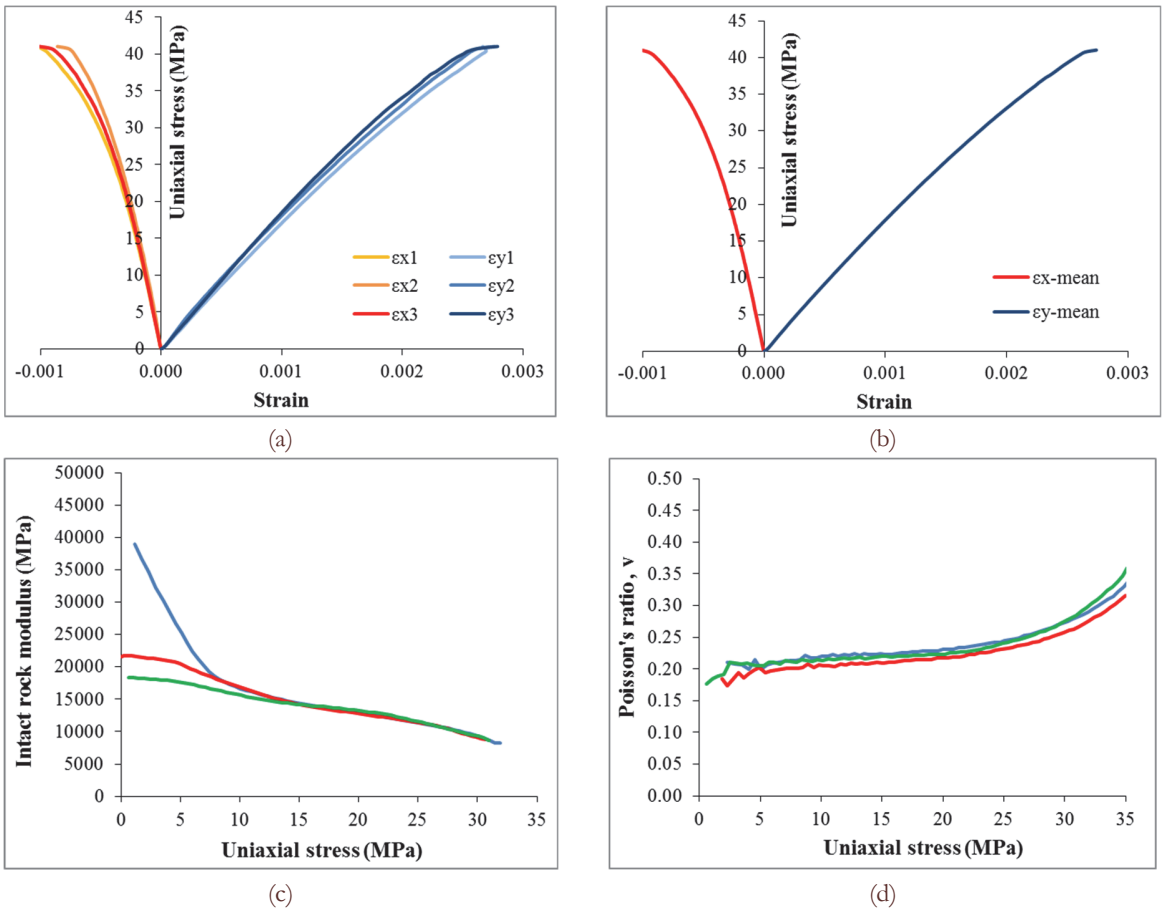

Figure 5: Typical diagrams for uniaxial compression tests. (a) Stress-strain curves from the three biaxial strain-gages, (b) Mean value stress-strain curves, (c) Intact rock modulus and (d) Poisson's ratio in correlation with the uniaxial stress.

Three different failure modes were observed during the uniaxial compression tests of Alfas stone. Some specimens failed along single shear planes (Fig. 6a), others failed in axial splitting (Fig. 6b) and a third group failed along conjugate shear planes (Fig. 6c). It should be noted that in all cases specimens exhibit extensive spalling before failure.

Size effect for uniaxial compression tests

A total of 18 uniaxial compression tests were completed in order to investigate the size effect for the Alfas natural building stone under uniaxial compression. Initially, the mean curves of intact rock modulus and Poisson's ratio, for each set of cylindrical specimens, are plotted in correlation with the uniaxial stress (Fig. 7). For the case of Poisson's ratio (Fig.7b) the trend of these curves is similar for all diameters, while for the intact rock modulus (Fig.7a) this similarity is only observed for stresses greater than 50% of specimen strength.

(a) (b) (c)

Figure 6: Typical crack patterns in Alfas cylindrical specimens. (a) Shear plane failure (D=75 mm); (b) Axial splitting failure (D=100 mm); (c) Failure on conjugates shear planes (D=54 mm).

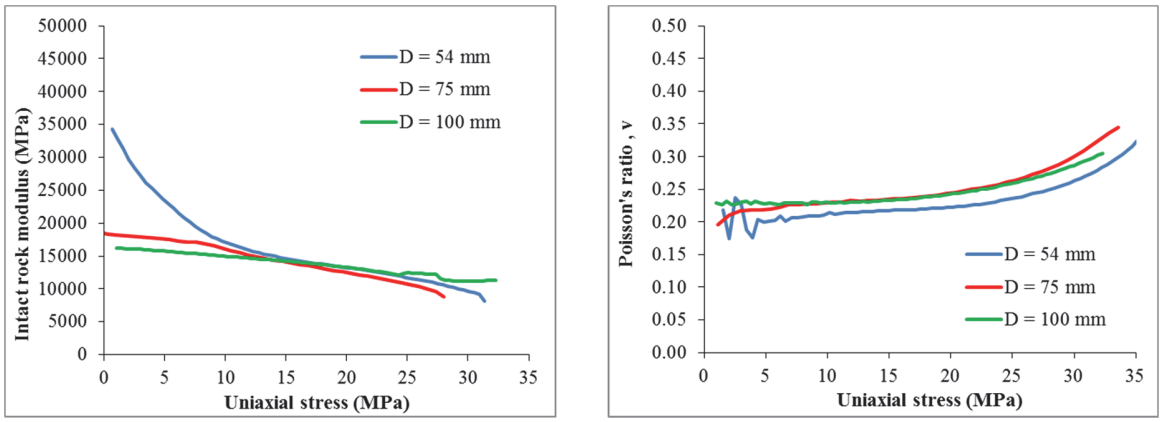

(a) (b)

Figure 7: The mean curves of (a) Intact rock modulus and (b) Poisson's ratio of Alfas stone for each of the three diameters in correlation with the uniaxial stress.

Mean values of rock properties are plotted against the diameter together with their standard deviation values (Fig. 8). Fig. 8a clearly shows that UCS decreases as the diameter increases for a constant height to diameter ratio. A difference between the UCS for specimens with D=54 mm and D=100 mm is observed, which is up to 11%. Also, the same trend is observed for the strain energy density (Fig. 8d). Fig. 8b and Fig. 8c present the variation of the intact rock modulus and Poisson's ratio, as derived from the uniaxial compression test using strain gages. Experimental results show that these parameters remain almost constant for different specimen diameters, with mean values of E=13543 MPa and ν=0.234, respectively. The dependence of the lateral and axial peak strains on the diameter of specimens is presented in Fig. 8e and Fig. 8f respectively. The variation of the peak strains is not a monotonic function versus the diameter. A clear maximum exists and corresponds to the specimens with D=75 mm. The high standard deviation values calculated for some experiments series can be attributed to the small number of specimens used for this analysis.

Indirect tensile tests

The results obtained from the diametral compression tests for the three different circular disc specimen sizes are presented in Tab. 3. Results include values for the splitting tensile strength, the intact rock modulus, Poisson's ratio and the shear modulus. Note that the intact rock modulus, Poisson's ratio and shear modulus for each specimen was calculated at 50% of the indirect tensile strength of that specimen. Furthermore, the lateral and axial peak strains up to the peak load were calculated. Note that the intact rock modulus, Poisson's ratio and shear modulus values calculated for the circular discs with D=54 mm, correspond to only one specimen, because strain gage measurements failed in other specimens of this series.

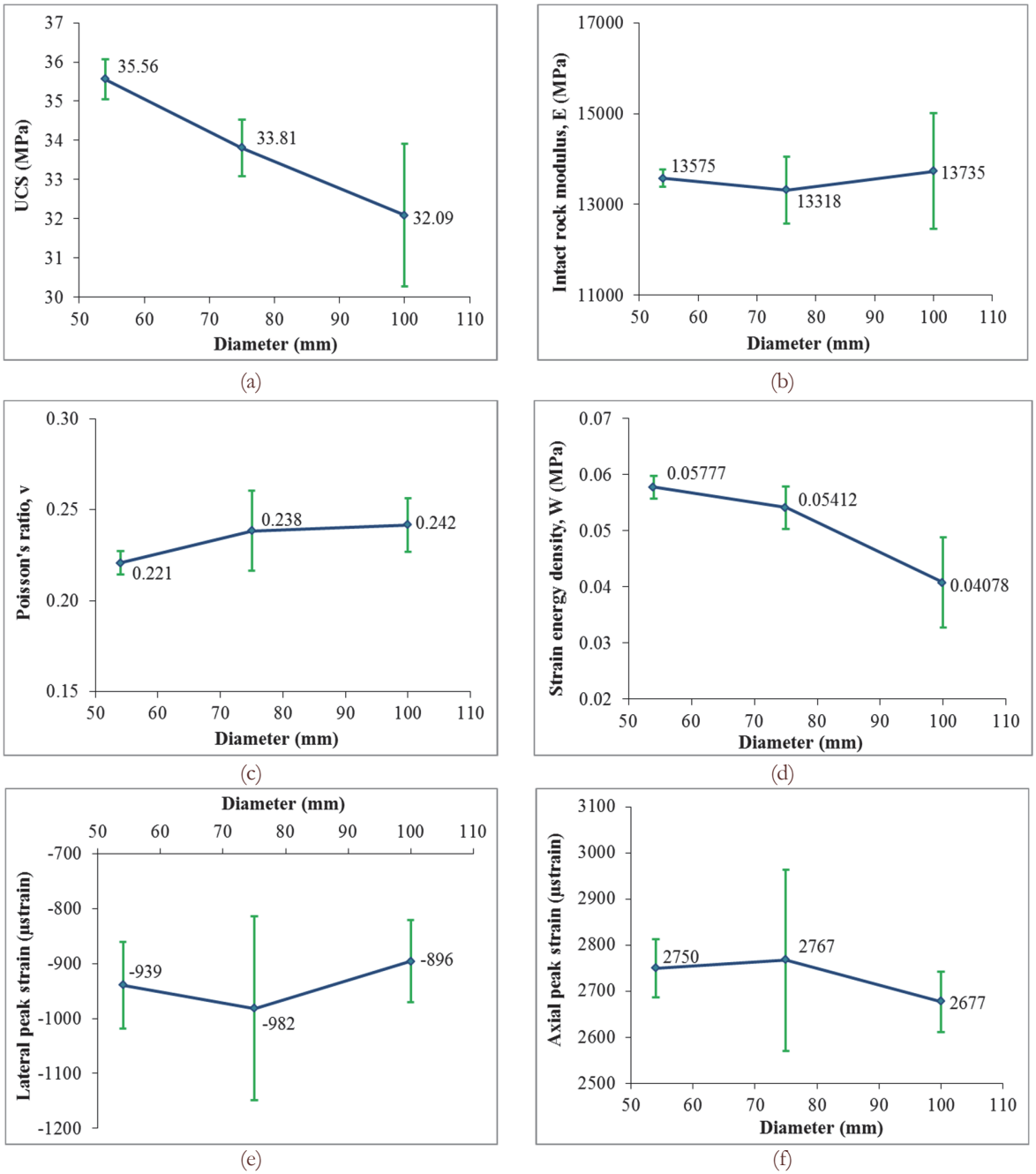

Figure 8: (a) Uniaxial compression strength, (b) Intact rock modulus, (c) Poisson's ratio, (d) Strain energy density, (e) Lateral peak strain and (f) Axial peak strain with respect to the diameters of the specimens.

Results from a typical circular disc specimen with diameter D=100 mm are presented in Fig. 9a-e. The difference between the strain values measured by the strain rosettes on opposite sides of the specimen is shown in Fig. 9b. This has also been observed in other experimental unpublished data by the authors and, currently, it is attributed to a number of experimental difficulties such as: material inhomogeneity, imperfections in the geometry of the disc specimens, which may result in eccentric loading of the discs through the steel jaws, as well as minute differences in the orientation and location of the strain gages with respect to the vertical axis and the center of the specimen respectively. Fig. 9c presents the curves constructed by averaging the respective curves in Fig. 9a; these are the values used in subsequent calculations. Fig. 9 d, e present the variation of the intact rock modulus and Poisson's ratio respectively (as calculated by eq. 2 and 3) with respect

to the indirect tensile stress for the same specimen. Experimental values represented by these curves remain almost constant at about 50% of the indirect tensile strength.

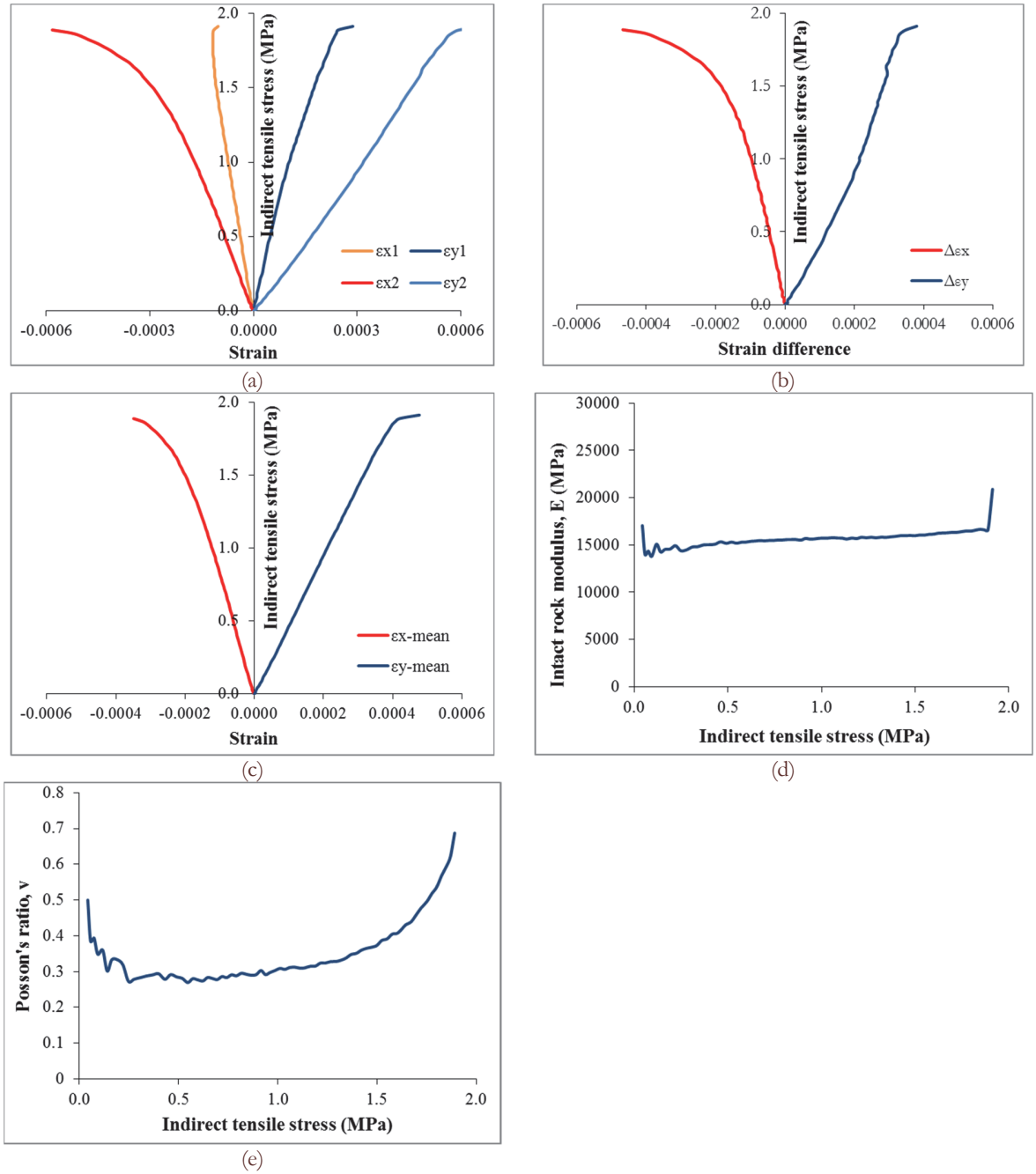

Figure 9: Typical diagrams for Brazilian tests. (a) Stress-strain curves from the two biaxial strain-gages, (b) Stress-difference strain curves from the two biaxial strain-gages, (c) Mean values stress-strain curves, (d) Intact rock modulus and (e) Poisson's ratio in correlation with the indirect tensile stress.

The issue of the different strain values measured on the opposite sides of the disc specimens is intriguing and a number of experimental options are currently being studied / explored by the authors in order to investigation this discrepancy. One way to reduce experimental errors due to utilization of strain gages is to use optical techniques such as the procedure of Digital Image Correlation (DIC) [23, 24] which does not depend on the accurate placement of measuring devices on each specimen. In order to investigate this issue, both sides of a specimen need to be monitored at the same time. An approach

that would reduce specimen seating errors would be to conduct Brazilian tests where the disc specimens will be directly loaded by the loading platens of the compression testing frame (as specified by ASTM – D3967) where eccentric loading can be directly alleviated by the spherical seating of the upper compression platen.

D [mm]	*t* [mm]	*Number of tests*	*Number of specimens with strain gages*	*Splitting tensile strength* f_{st} [MPa]		*Intact rock modulus* E [MPa]		*Poisson's ratio* ν		*Shear modulus* G [MPa]	
				Average [MPa]	*St. Dev.* [MPa]	*Average* [MPa]	*St. Dev.* [MPa]	*Average*	*St. Dev.*	*Average* [MPa]	*St. Dev.* [MPa]
54	27	8	1	2.88	0.38	19100	-	0.333	-	7163	-
75	37.5	7	3	3.34	0.13	21300	7938	0.293	0.019	8269	3179
100	50	6	3	2.28	0.35	14422	713	0.290	0.033	5588	245

Table 3: The experimental results of the Brazilian tests for Alfas stone specimens loaded diametrically.

All specimens, for the Alfas stone, subjected to the Brazilian test, failed as expected by the underlying theory, i.e. by developing an extension fracture along the loaded diametral plane which is assumed to be the result of the induced tensile stress normal to the loaded plane (Fig. 10a). Furthermore, it was observed that in addition to the central primary crack, two symmetrical secondary cracks were developed (Fig. 10b). This behavior is in full agreement with the ideal fracture propagation according to Colback [25].

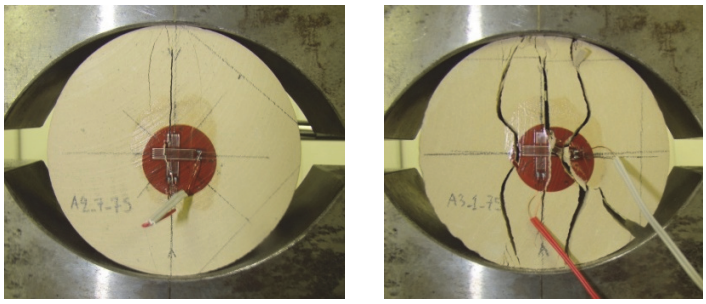

(a) (b)

Figure 10: (a) Center primary fracture plane. (b) Center primary fracture plane with typical secondary fractures.

Size effect for indirect tensile tests

A total of 21 Brazilian tests were completed in order to investigate the size effect for the Alfas natural building stone under diametral compression. The mean values of rock properties are plotted against the diameter together with their standard deviation values (Fig. 11).

The variation of the splitting tensile strength with respect to specimen diameter is not a monotonic function. A clear maximum exists and corresponds to the specimens with D=75 mm (Fig.11a). A similar non-monotonic behavior has been observed by Kourkoulis [12] for the UCS of "Conchyliates" shell-stone, where the maximum value appears for the specimens with diameter D=100 mm. The author attributed this anomaly to the fact that "the specimen starts behaving as a structure rather than as a homogeneous material, since the size of the conches becomes well comparable to the characteristic size of the specimen". This non monotonic dependence of the UCS and the splitting tensile strength with respect to the diameter of the specimens is also mentioned by Vardoulakis et al. [26, 27] and Kaklis and Vardoulakis [21] for a more homogeneous stone, the Dionysos marble.

Although, both the Alfas building stone (investigated in this study) and Dionysos marble (investigated in previous studies) can be considered almost homogeneous materials and their typical grain size cannot be compared to the size of the specimens, nevertheless, they present this non-monotonic behavior. It is clear that additional research needs to be performed to reach definite conclusions regarding this non-monotonic behavior.

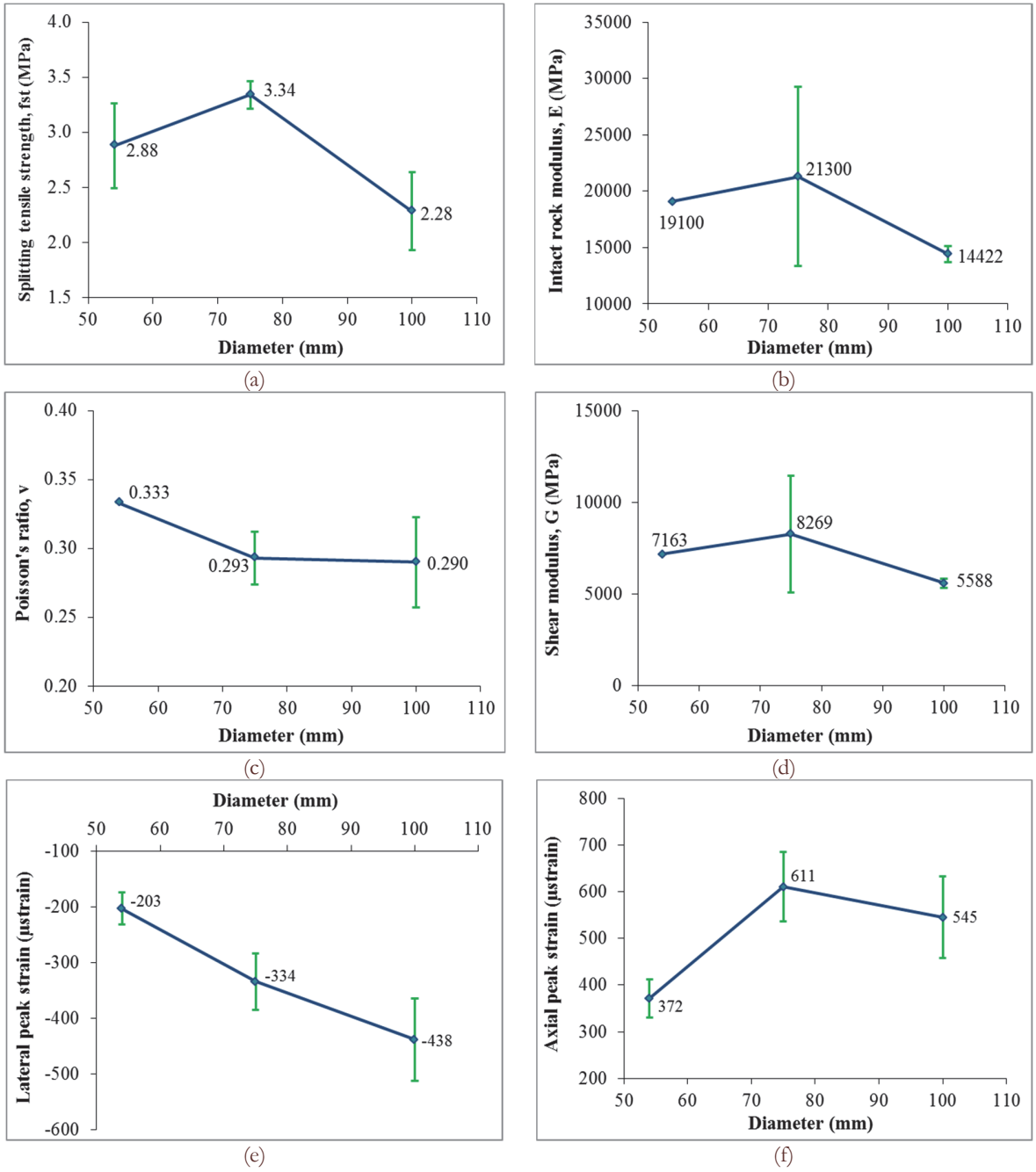

Figure 11: The dependence of (a) the splitting tensile strength, (b) the intact rock modulus, (c) Poisson's ratio, (d) the shear modulus, (e) the lateral peak strain and (f) the axial peak strain on the diameter of the specimens.

Discussion and Additional Considerations

As previously mentioned the so called "size effect" must depend on the bulk material (volume) of the specimen and its limits (external surface) that are exposed to different stress/strain states (plane-stress, plane-strain or triaxial) as well as other factors such as environmental, specimen machining factors, etc. It implies that comparisons must be performed in classes of geometrically self-similar specimens. Consequently, different "shapes" of specimens cannot be compared. This is demonstrated from Fig. 8a and 11a where a qualitatively different behavior of strength is obtained. At the same time, it seems that the size effect may not a material property, but a specimen characteristic and the "law of 3/2", i.e. the ratio (volume)/(external surface), which in the present case reduces to specimen diameter *D*, may be an over-simplification.

This issue requires a long discussion which is outside the scope of this paper.
For comparison, the obtained Alfas stone UCS data were plotted on the diagram published by Hoek and Brown [28] as shown in Fig. 12. Although the range of specimen diameters does not cover a very wide range, the selected core diameters represent typical core sizes using in geotechnical testing practice.

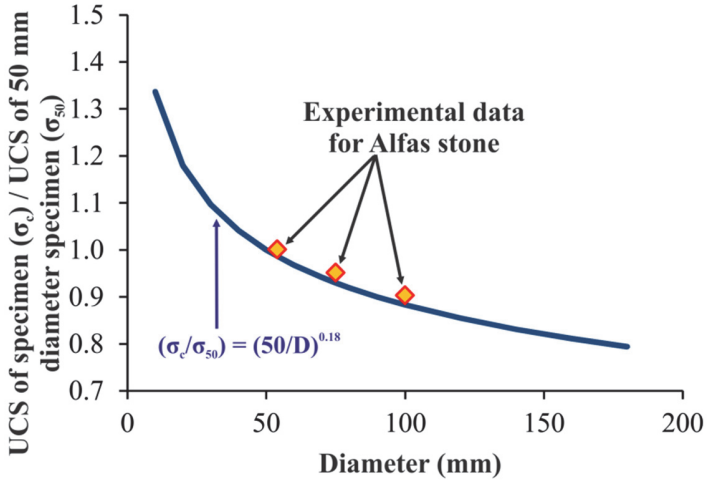

Figure 12: Relationship between UCS and specimen size plotted as dimensionless values [28].

The values of UCS for the Alfas stone that were determined experimentally, are in full agreement with the following formula published by Hoek and Brown [28]:

$$\frac{\sigma_c}{\sigma_{50}} = \left(\frac{50}{D}\right)^{0.18} \tag{4}$$

where σ_c is the calculated UCS measured on the specimen and σ_{50} is the calculated UCS of a 50 mm diameter specimen.
Furthermore, Kaklis and Vardoulakis [21] suggest that for Dionysos marble the dependence of the splitting tensile strength to specimen size, seems to follow Carpinteri's fractal law [29] which advocates the formation of a fractal fracture manifold.
By observing typical crack patterns generated during specimen failure in the current investigation (see examples in Fig. 6) it is evident that specimen spalling and axial splitting rather than specimen shearing may be the predominant failure modes for the Alfas stone. Both axial splitting and spalling failure modes are related to indirect tensile failure. Fig. 13 presents the variation of the uniaxial compressive strength with the specimen diameter of Alfas stone in a double logarithmic plot. The correlation coefficient of the trend line presented in Fig. 13 is almost 100% which suggests that a similar fractal law may apply for uniaxial compression, when splitting can be considered a predominant failure mechanism. The exponent n in the scaling law for the case of Alfas stone is $n = 2.668$, based on the procedure detailed in [21]. A similar correlation for the Brazilian tests is not attempted since the variation of the indirect tensile strength with specimen diameter exhibits a non-monotonic behavior.

CONCLUSIONS

This paper presents experimental results and correlations on the mechanical behavior of the Alfas stone for a range of uniaxial compression and indirect tension tests. A total of 18 cylindrical specimens and 21 Brazilian disc specimens were tested for three different diameters (D=54, 75 and 100 mm). Many specimens where fully instrumented with strain gages to fully capture the deformational characteristics of each test. In addition, the dependence of the mechanical parameters on the size of the specimens was investigated.

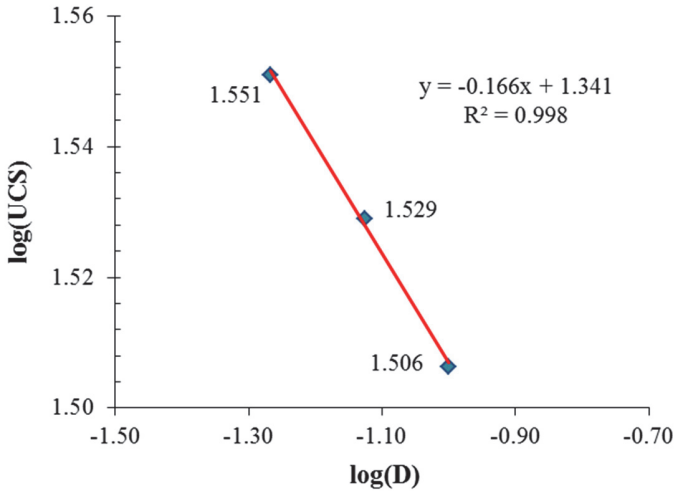

Figure 13: Variation of the UCS with the specimen diameter.

Results show that almost all the mechanical parameters used to describe the behavior of the building stone depend on the size of the specimens, with the exception of the intact rock modulus and Poisson's ratio which appear to be constant with varying specimen diameters. The values of UCS for the Alfas stone that were experimentally determined are in full agreement with the formula published by Hoek and Brown [28]. In addition, an almost perfect linear correlation between UCS and diameters in a double logarithmic chart was developed, which indicates that when specimen spalling and axial splitting rather than specimen shearing is the predominant failure mode, the dependence of UCS to specimen size may follow Carpinteri's fractal law [29].

Furthermore, experimental results indicate that the splitting tensile strength of Alfas stone is not a linear function of the specimen diameter, but it exhibits a non-monotonic pattern. Although this non-monotonic behavior has also been previously presented in the literature [12], it is clear that additional research needs to be performed to reach definite conclusions regarding the dependence of the splitting tensile strength to specimen diameter.

ACKNOWLEDGEMENTS

This research has been co-financed by the European Union (European Social Fund-ESF) and Greek national funds through the Operational Program "Education and Lifelong Learning" of the National Strategic Reference Framework (NSRF) - Research Funding Program: THALES: Reinforcement of the interdisciplinary and/or inter-institutional research and innovation. The authors would also like to thank the anonymous reviewers of this paper for their constructive comments and recommendations.

REFERENCES

[1] Dufour, F., Size effect in geomaterials. Revue Européenne de Génie Civil., 11 (7-8) (2007) 963-975.
[2] Weibull, W., A statistical theory of the strength of materials. Royal Swedish Academy of Eng. Sci. Proc., 151 (1939) 1-45.
[3] Barla, G., Goffi, L., Direct tensile testing of anisotropic rocks. Proceedings of the Third International Congress of Rock Mechanics, 2, Part A (1974) 93-98.
[4] Nova, R., Zaninetti, A., An investigation into the tensile behavior of a schistose rock. International Journal of Rock Mechanics and Mining Sciences & Geomechanics Abstracts, 27 (1990) 231-242.
[5] Hondros, G., The evaluation of Poisson's ratio and the modulus of materials of a low Tensile resistance by the Brazilian (indirect tensile) test with particular reference to concrete. Australian Journal of Applied Science, 10 (1959) 243-264.
[6] Pinto, J.L., Determination of the elastic constants of anisotropic bodies by diametral compression tests. Proceedings of the Fourth ISRM Congress, Montreux, 2 (1979) 359-363.

[7] Amadei, B., Rogers, J.D., Goodman, R.E., Elastic constants and tensile strength of anisotropic rocks. Proceedings of the Fifth ISRM Congress, Melbourne, A189-A196 (1983).
[8] Amadei, B., Importance of anisotropy when estimating and measuring in situ stresses in rock. International Journal of Rock Mechanics and Mining Sciences & Geomechanics Abstracts, 33 (1996) 293-325.
[9] Chen, C.S., Pan, E., Amadei, B., Determination of deformability and tensile strength of anisotropic rock using Brazilian tests. International Journal of Rock Mechanics and Mining Sciences & Geomechanics Abstracts, 35 (1998) 43-61.
[10] Exadaktylos, G.E., Kaklis, K.N., Applications of an explicit solution of the transversely isotropic circular disc compressed diametrically. International Journal of Rock Mechanics and Mining Sciences, 38(2) (2001) 227-243.
[11] Thuro, K., Plinninger, R.J., Zah, S., Schutz, S., Scale effects in rock strength properties. Part 1: Unconfined compressive test and Brazilian test. ISRM Regional Symposium, EUROCK 2001, Rock Mechanics - a Challenge for Society, Espoo, Finland, (2001) 169-174.
[12] Kourkoulis, S.K., An experimental study of the mechanical behaviour of the 'Conchyliates' shell-stone: some irregularities of the size effects. Strain, An International Journal for Experimental Mechanics, 47(1) (2011) e344-e356.
[13] Kourkoulis, S.K., Ganniari-Papageorgiou E., Experimental study of the size- and shape-effects of natural building stones. Construction and Building Materials, 24(5) (2010) 803-810.
[14] Viso, J.R., Carmona, J.R., Ruiz, G., Shape and size effects on the compressive strength of high-strength concrete. Cement and Concrete Research, 38 (2008) 386-395.
[15] Yi, S.T., Yang, E.I., Choi, J.C., Effect of specimen sizes, specimen shapes, and placement directions on compressive strength of concrete. Nuclear Engineering and Design, 236 (2006)115-127.
[16] Rietveld, H.M., A profile refinement method for nuclear and magnetic structures. Journal of applied crystallography, 2 (1969) 65-67.
[17] BS EN 13755, Natural stone test methods. Determination of water absorption at atmospheric pressure, British Standards Institution, (2008).
[18] BS EN 1936, Natural stone test methods. Determination of real density and apparent density, and of total and open porosity, British Standards Institution, (2006).
[19] Bieniawski, Z.T., Bernede, M.J., Suggested methods for determining the uniaxial compressive strength and deformability of rock materials. International Journal of Rock Mechanics and Mining Sciences & Geomechanics Abstracts, 16(5) (1979) 135-140.
[20] Kaklis, K.N., Exadaktylos, G.E., A strain gage method for the determination of the elastic parameters in a transversely isotropic disc on Dionysos marble. 5th Hellenic Conference on Geotechnical and Geoenviromental Engineering, Xanthi, Greece, 1 (2006) 103-110.
[21] Kaklis, K.N., Vardoulakis, I., An experimental investigation of the size effect in indirect tensile test on Dionysos marble. Proceedings of the 7th National Congress on Mechanics, Chania, Greece, 2 (2004) 151-157.
[22] Bieniawski, Z.T., Hawkes, I., Suggested methods for determining tensile strength of rock materials. International Journal of Rock Mechanics and Mining Sciences & Geomechanics Abstracts, 15(3) (1978) 99-103.
[23] Stirling, R.A., Simpson, D.J., Davie, C.T., The application of digital image correlation to Brazilian testing of sandstone. International Journal of Rock Mechanics & Mining Sciences, 60 (2013) 1-11.
[24] Fourmeau, M., Gomon, D., Vacher, R., Hokka, M., Kane, A., Kuokkala, V.T., Application of DIC technique for studies of Kuru Granite rock under static and dynamic loading. Procedia Materials Science, 3 (2014) 691-697.
[25] Colback P.S.B., An Analysis of Brittle Fracture Initiation and Propagation in the Brazilian Test. Proc. First Congress International Society of Rock Mechanics, (1967) 385-391.
[26] Vardoulakis, I., Kourkoulis, S. K., Mechanical Properties of Dionysos Marble. Final Report of the Environment Project EV5V - CT93-0300. Department of Mechanics, National Technical University of Athens, Athens, Greece, (1997).
[27] Vardoulakis, I., Kourkoulis, S. K., Exadaktylos, G. E., Rosakis, A., Mechanical properties and compatibility of natural building stones of ancient monuments: Dionysos marble. In: Proc. of the Interdisciplinary Workshop: The Building Stone in Monuments (M. Varti-Mataranga and Y. Katsikis, Eds). IGME Publishing, Athens, (2002) 187–210.
[28] Hoek, E., Brown, E.T., Underground excavations in rock, Inst. Min. Metall., Chapman & Hall, London, (1980).
[29] Carpinteri, A., Ferro, G., Size effects on tensile fracture properties: a unified explanation based on disorder and fractality of concrete microstructure. Materials & Structures (RILEM), 27 (1994) 563-571.

Acoustic emissions and pressure stimulated currents experimental techniques used to verify Kaiser effect during compression tests of Dionysos marble

Ilias Stavrakas
Laboratory of Electronic Devices and Materials, Technological Educational Institute of Athens, 12210, Athens, Greece
ilias@ee.teiath.gr, http://research.ee.teiath.gr/

ABSTRACT. The damage development due to externally applied mechanical stress is a hot topic of interest involving several applications of everyday life, like civil engineering, monument restoration, construction evaluation and health monitoring. Repetitive loadings of brittle materials cause internal damages that gradually extend, leading to inevitable failures. Such processes are studied under the concept of the materials' mechanical memory effect that is widely known as Kaiser effect. The Kaiser effect states that a structure will only suffer further internal damaging when exposed to applied stresses higher than previously encountered. Certain conditions lead to a violation of the Kaiser effect, known as the Felicity effect, quantitatively measured using the Felicity Ratio. This work presents the experimental results when repetitive mechanical load loops are applied on marble specimens, while concurrent Acoustic Emission (AE) and Pressure Stimulated Currents (PSC) measurements are conducted. The collected AE and PSC data are studied in combination with the mechanical data, like mechanical stress and strain, under the frame of the Kaiser effect. It is clearly seen that the Felicity ratio strongly depends on the stress range the material is subjected to, with regard to the elastic or plastic deformation region.

KEYWORDS. Acoustic Emissions; Pressure Stimulated Currents; Dionysos marble; Kaiser effect; Felicity Ratio.

OPEN ACCESS

Citation: Stavrakas, I., Acoustic emissions and pressure stimulated currents experimental techniques used to verify Kaiser effect during compression tests of Dionysos marble., Frattura ed Integrità Strutturale, 40 (2017) 32-40.

Received: 05.01.2017
Accepted: 06.02.2017
Published: 01.04.2017

INTRODUCTION

The scientific literature reports several studies and recordings of AE that are attributed to mechanical stresses adequate to cause microcracking phenomena in rocks [1]. Towards this direction, the experimental technique of AE detection has been evaluated and developed in order to constitute a valuable tool for the monitoring and

interpretation of the underlying physical mechanisms of mechanical dynamic processes and the detection of an upcoming event of mechanical failure [2]. Further than the AE, the detection and recording of low-level electric signals provide reliable information, regarding the development of damage processes. Such electric signals are detected due to fracture processes in quasi-brittle materials following microcracks formation and growth. It is known that transient electric phenomena are often appearing when solid materials are subjected to stress and mechanical effects are taking place [3, 4].
Since 2000, the detection of the electric signals that are related to weak electric current emissions is conducted through an innovative experimental technique rendered under the term Pressure Stimulated Currents technique, while the recorded electrical currents are known as Pressure Stimulated Currents (PSC) [5]. The PSC are detected through the recording of a weak (low-level) electric current using a sensitive electrometer, when a pair of electrodes is attached properly on the specimen that is subjected to mechanical tests. The above-described experimental technique was initially applied when marble materials were subjected to axial compressive mechanical stress [6, 7].
The Kaiser effect is an AE phenomenon briefly defined as the absence of detectable acoustic emissions until the previously applied stress level is exceeded. This effect is based on the experimental discovery by Kaiser (1950), that metallic materials had the capability to remember the previous maximum stress level. The existence and the experimental verification of the Kaiser effect was also discovered in rocks and described in other works [8-10] and since then, the Kaiser effect is used to detect and assess the amount of damage that has been developed in rocks [11, 12].
The breakdown of the Kaiser effect can be represented quantitatively by the felicity ratio (FR) that is defined as the ratio of the AE-onset stress to the maximum stress of the previous cycle. It may be taken as a measure of the quality of the rock [13]. A high felicity ratio means that the rock is of good quality.
Regarding the PSC emissions, several works in the past demonstrate the ability of a marble specimen to "remember" previous mechanical loadings [5, 6, 14-16]. Specifically, the main properties of the PSC signal, which are affected by the existence of memory, converge to an inertial attitude of the material to the same stimuli and they are quite common with the properties of other fracture induced signals (i.e. AE). Namely, they are the following: (a) The PSC peak evolution over loading cycles is a changing signal property, with respect to the time interval between loadings, (b) The decrease of the dissipated electric energy during cyclic loading tests, (c) The PSC slower relaxation in each loading, quantified by the relaxation process parameters evolution, (d) The PSC signal initiates to show up at higher stress level after each next loading cycle.
The aim of this work is to conduct a laboratory experimental investigation and verification of the Kaiser effect on Dionysos marble specimens combining the AE and PSC recordings. The specimens are subjected to compressive loading loops where the first loading is in the region where the material leaves the elastic region and enters the plastic deformation i.e., the stress-strain curve deviates from linearity.

TEST FACILITIES AND ARRANGEMENT

The marble specimens were subjected to three loading-unloading loops (see Fig. 1). The maximum stress level during the 1st and the 2nd loading was approximately 60 MPa, a value that corresponds to the 70% of the ultimate compressive strength of the material and leads to a Young's modulus of 72 GPa (see Fig. 2). This stress level, according to preliminary tests on similar specimens, corresponds to the region that the material gradually enters the non-linear region regarding its stress-strain behaviour and initial plasticity effects take place, which is in accordance, also, to previously published data [17-19]. During the unloading processes the stress level was maintained at a value of 15 MPa, approximately. A third loading was attempted during which the specimen failed at a stress level of 82.7 MPa. The compressive stress was applied following load control at a rate of 320 kPa/s.
Fig. 1 shows the temporal variation of the loading path until the failure of the specimen and Fig. 2 shows the stress-strain curve during the complete cyclic loading. It must be noted that during the 1st loading the linear region was estimated to last up to a stress level of 58 MPa approximately.
The specimens (i.e. Dionysos marble) were prismatic with dimensions 35mm×35mm×75mm. The physical and chemical properties of this kind of marble have already been presented in bibliography [6, 20, 21]. The strain was measured using Kyowa strain gauges attached on the Microlink-770, 120Ω resistor bridge (see Fig. 3).
During the tests the AE events were monitored using a Physical Acoustic Corporation (PAC) Mistras Systems. The AEs transducer was the model R6 sensor provided from the Mistras S.A. that obtains a wide frequency range and was attached in the middle of the specimen's height (see Fig. 3). The AE threshold for detecting acoustic events was set at 40 dB.
Concerning the PSC technique, the measuring system consisted of an ultra-sensitive programmable electrometer (Keithley, 6517A) resolving currents ranging from 0.1 fA to 20 mA in 11 ranges. The data of the electrometer were stored

in a computer using a GPIB interface. The sensing system consisted of a pair of gold plated electrodes, installed in the middle of the specimen's height (see Fig. 3), enabling the collection of electric emissions as close as possible to any potential source of electric current (or equivalently to any point where damage occurs). Further details on the monitoring of the AE and PSC are described in earlier papers [22, 23].

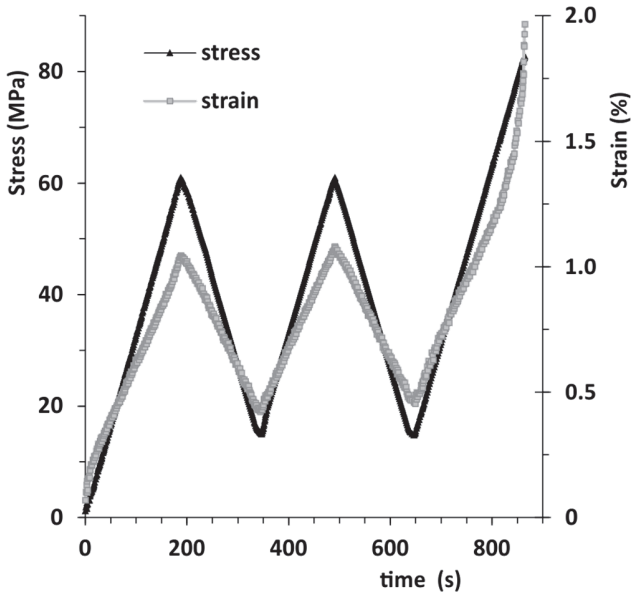

Figure 1: Temporal variation of the mechanical stress (black line), and the corresponding behaviour of the mechanical strain (gray line) during the complete cyclic loading.

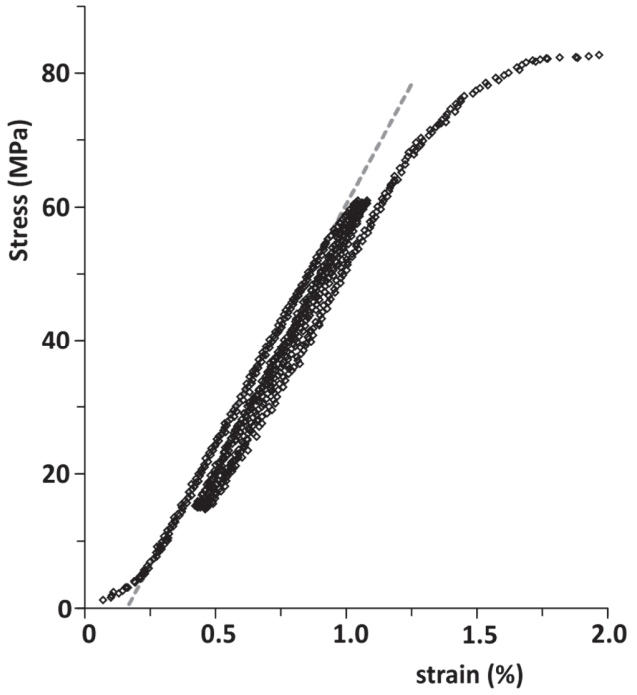

Figure 2: The stress-strain behaviour during the two loading / unloading loops as well as the final loading during which the specimen failed.

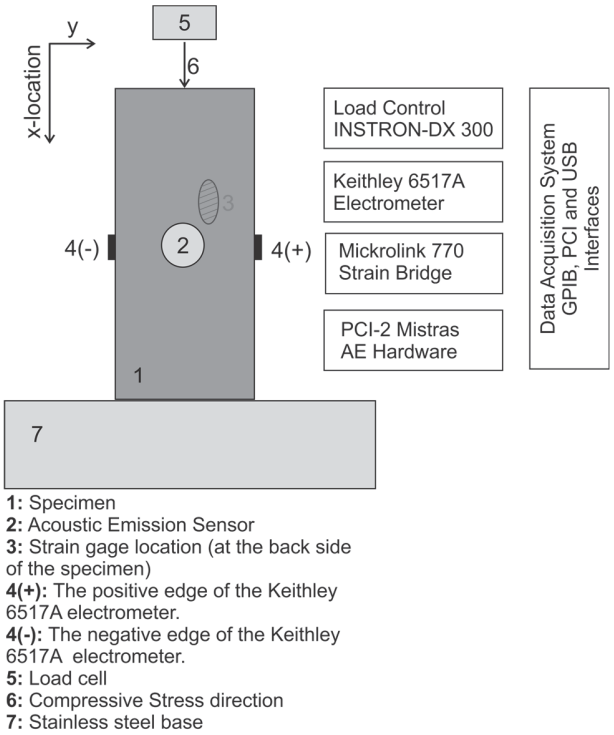

Figure 3: The schematic diagram of the experimental setup showing the physical locations of the sensors on the specimen, the geometry as well as the data communication interfaces.

VERIFICATION OF THE KAISER EFFECT

Acoustic Emission (AE) recordings

The AE activity during the complete experimental procedure is illustrated in Fig. 4. Specifically, the AE events per second are shown with respect to time. In the same figure, the temporal variation of the normalized applied mechanical stress is also presented. It may be clearly seen that AE were continuously detected during the entire process. Specifically, high AE rate is observed during the loading procedures while low AE rate is observed during the unloadings. It must be noted that despite the fact that the experimental apparatus is well isolated from external AE noise and the configuration of the AE hardware system significantly reduces the probability to record noise as AE events (i. preamplifier filters were applied and ii. background noise was continuously recorded and subtracted) the low values of AE rate may be attributed to such an external influence. During the first loading loop, a total number of 978 AE events is recorded while a significantly smaller number of AE events (289 AE events) were recorded during the second loading loop. It is noticeable that during the second loading of the specimen, practically no AE events were recorded until the load reached the 68% of the compressive strength (i.e. only 24 low amplitude AE events were recorded). The most of the AE events (i.e. 90% of the detected AE events) were recorded in the region between 68% and 73% of the compressive strength. This region corresponds to the upper limit of the linear behaviour of the material regarding its stress-strain curve. During the 3rd loading and before the stress reached the level of the previously applied stress, only 45 AE events were recorded while the 36 of them were recorded when the applied stress was in the region between 71% and 73% of the compressive strength. When the stress exceeded these values, 1237 AE events were recorded until the failure of the specimen. The AE records of the entire experimental procedure are plotted in a cumulative form, as shown in Fig. 5. These experimental results are in good agreement with the existing literature and specifically works published in [8-12].
During the 2nd and the 3rd loading-unloading loops the Felicity Ratio (FR) can be calculated to be equal to 0.66 and 0.8 approximately, correspondingly (see Fig. 5). The FR values were calculated according to the following formula:

$$FR = \frac{load\ at\ onset\ of\ significant\ AE\ event}{previous\ maximum\ load}$$

The deviation from the optimum value of FR=1, may be justified due to the fact that the maximum stress values of the 1st and 2nd loading loops was selected to lay in the limits of the linear and non-linear region, regarding the stress-strain behaviour of the marble, and additionally to the quality of the used marble. It must be noted that during each loading loop the FR clearly depends on the maximum stress of the previous loop and decreases as the value of the maximum stress increases [13]. This fact clearly is not the case for the described loading protocol of this work since the FR seems to increase rather than decrease during each next loading. Such a behaviour may be attributed to two main reasons. Firstly, the two initial loadings were performed up to the same stress value, a fact that is not typical for the FR development and secondly the selected stress value of 60 MP lays in the limits between the linear and non-linear region of the stress-strain curve, so no further damages may be caused during the second loading leading, as expected at a higher FR value.

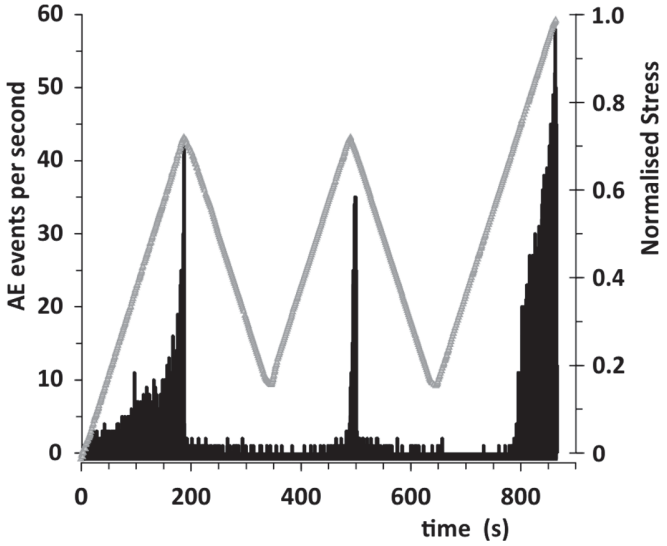

Figure 4: The mechanical stress temporal development during the complete experimental procedure (gray line) and the corresponding per second AE event rate (black bars).

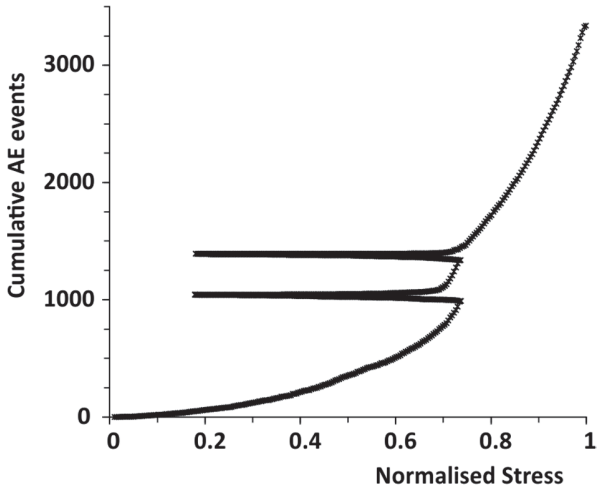

Figure 5: The behaviour of the cumulative number of the AE events with respect to the normalized value of the mechanical stress applied on a typical specimen.

Pressure Stimulated Current (PSC) recordings

Concurrently to the above described observations, PSC emission recordings were conducted. Fig. 6 shows the temporal variation of the recorded PSC with respect to the temporal variation of the mechanical stress. Observing the behaviour of the PSC, it may be clearly seen that during the first loading, where the mechanical stress reached a maximum value of 60MPa approximately, a strong PSC emission was recorded reaching a maximum value of 40pA approximately, while a

gradual decay back to the background level occurs when the mechanical stress is relieved. It must be noted that the maximum value of the applied stress (i.e. 70% of the maximum stress) enters the specimen into the early nonlinear region regarding its stress-strain behaviour. During the second loading the applied mechanical stress reached approximately the level of the mechanical stress of the 1st loading (i.e. 60MPa) while the recorded PSC reached a maximum of 10pA which is significantly lower than the recorded PSC of the first loading. Such a behaviour may be attributed to the underlying physical mechanisms of the PSC generation and specifically the Moving Charged Dislocations model [4]. Since the PSC variation is attributed to the damage generation and extension it is expected that when a brittle specimen, like marble, is subjected to a mechanical stress in sequential loading cycles new damages occur only during the initial application of the stress. During each following stress application only minor extension of the already created damages is produced and consequently only weak PSC emissions are expected. The third loading was scheduled to lead the specimens to failure, and the mechanical stress was applied at the same rate of the two initial loadings. During this third loading a strong PSC emission was detected reaching a peak PSC value of the order of 100pA. It is worth noticing that a short time (i.e. 5 seconds) before the stress drop (due to the specimen's failure) the characteristic PSC decrease [5, 6] was observed clearly indicating the upcoming failure. The above experimental results are in good agreement with the corresponding results presented in other works [5, 6, 14-16].

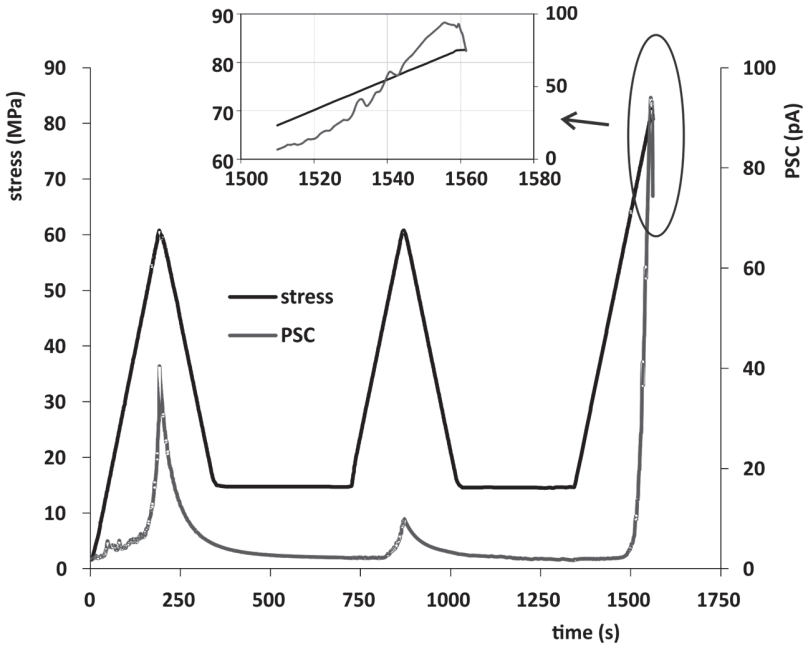

Figure 6: The temporal variation of the mechanical stress during the complete experimental procedure and the corresponding behaviour of the PSC emission. The inset figure constitutes a zoom in at the final stage before fracture making clear the characteristic PSC drop before the failure of the specimen.

Fig. 7 demonstrates the behaviour of the PSC emission in logarithmic scale with respect to the mechanical stress during each loading cycle. Specifically, the blue, the green and the light grey lines correspond to the load increase from 0 MPa to 60 MPa of the first, the second and the third loading, respectively. The black line shows the behaviour of the PSC with respect to the mechanical load during the third loading, when the applied stress becomes higher than 60 MPa exceeding this way any previously applied level of stress. Observing Fig. 7 it is clear that during the three loadings and while the stress is below 60 MPa, the recorded PSC becomes significantly lower for each next loading. When the mechanical stress exceeded 60 MPa during the third loading, the PSC emission significantly increases reaching a peak of 100 pA, few seconds before fracture. The black line in Fig. 7 supports the dominance of the Kaiser effect during the experimental procedure and in addition that PSC may also be used to detect that a sample has suffered significant mechanical stress at earlier times and it "remembers" such a fact. Another observation is that during the second and the third loading the detected PSC and the corresponding PSC energy are both at the same low levels up to a stress value of 45 MPa. Beyond that point of stress and during the third loading the recorded PSC is maintained at a very low level. During the third loading and when stress becomes higher than 60 MPa strong PSC emissions and rapid increase is detected.

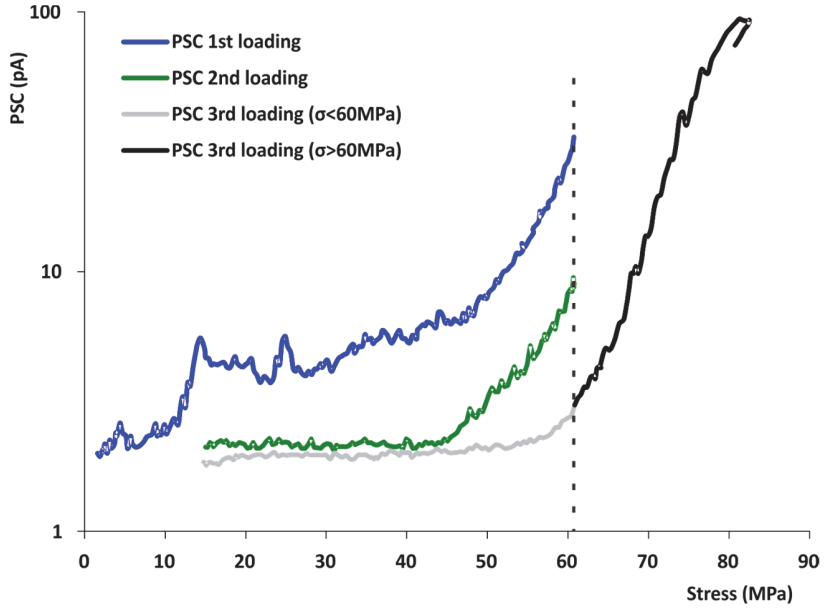

Figure 7: The behaviour of the PSC, shown in logarithmic scale, with respect to the value of the mechanical stress.

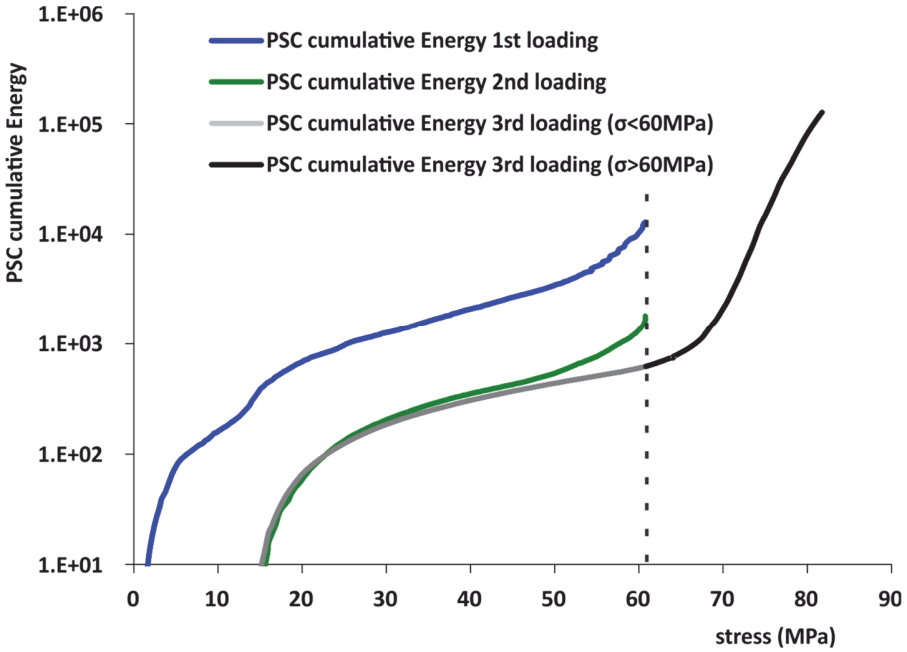

Figure 8: The behaviour of the PSC cumulative energy, shown in logarithmic scale, with respect to the value of the mechanical stress.

Fig. 8 shows the behaviour of the released cumulative energy of the PSC in logarithmic scale with respect to the mechanical loading during the experimental procedure.
The square of PSC adjusted amplitude PSC(t), expresses an energy quantity [24] and may be calculated according to:

$$E_{PSC}(t_i) = PSC^2(t_i)$$

where t_i corresponds to the time instance of each PSC recorded sample.
The cumulative PSC energy CE_{PSC} during each loading is calculated according to the following formula:

$$CE_{PSC} = \sum_{i=1}^{n} E_{PSC}(t_i)$$

where n corresponds to the number of the recorded PSC values in the examined mechanical stress region.
It may be clearly seen that during the first loading a significant amount of energy is released (blue line). Additionally it is clear that the PSC emission initiated from early mechanical stress levels which means that the PSC is emitted even in low stress levels. During the second and the third loadings (green and gray lines respectively) the PSC energy initiates only when stress becomes higher than 15MPa approximately, while their cumulative energy levels are significantly lower than the corresponding of the first loading. Finally, during the third loading and when the mechanical stress became higher than the 60 MPa a significant increase of the released cumulative energy is recorded. This fact that also manifests Kaiser effect dominates the PSC emissions and the corresponding PSC cumulative energy.

CONCLUDING REMARKS

During the present experimental protocol two sequential compressive loadings and unloadings were applied on marble prismatic specimens up to a stress level that corresponds to early non-linear region regarding the stress-strain behaviour. During the third loading, the stress was not relieved but instead it was further increased until the sample mechanically failed. Concurrently to the loading AE and PSC emissions were recorded. The aim was to investigate and correlate the fingerprint of the Kaiser effect on the AE recordings and the PSC emissions as well as the corresponding cumulative energy. The tests were performed on series of marble prismatic specimens and representative experimental results of the carried out tests are presented herein.
Additionally, regarding the AE recordings, it is experimentally verified that for marble specimens the Felicity Ratio (FR) obtains high values (i.e. 0.66 and 0.8 approximately) during the two loading/unlading cycles when the applied stress lays in the region where the material is still near the limits of linear region regarding its stress-strain behaviour.
Regarding the behaviour of the AE events the number recorded is significantly large during the first loading while the number of AE events becomes fewer during the second load. AE events practically disappear during the third loading and more specific when the applied stress is in the range of the two previous loadings. When the stress was further increased significant AE events are recorded until the fracture of the sample.
Regarding the PSC emissions it is observed that the maximum value of the PSC emission becomes significantly lower during each next loading while the applied mechanical stress varies in the same stress limits. It is also important to notice that detectable PSC emissions show up at higher stress levels during the second and the third loading. During the third loading and while the applied mechanical stress becomes higher than the corresponding values of the previous loadings, intense PSC emissions are detected. The characteristic drop of the PSC is detected when the sample approaches failure.
All the above manifest that both AE and PSC emissions may be used to detect and qualitatively approach the Kaiser effect phenomena when Dionysos marble samples are subjected to mechanical stress.
Combining the experimental findings after applying the AE and the PSC experimental techniques when marble specimens are subjected to compressive mechanical stress it is observed that both experimental techniques may be used in order to detect an upcoming specimen failure. Further on qualitative comparison shows that the use of PSC and AE provide similar information regarding the existence of the Kaiser effect. Specifically, it was seen that when applying sequential loadings and unloadings on marble specimens the emitted PSC becomes lower during each loading cycle and the recorded AE events rate start to increase only when the applied mechanical stress gets values higher than the corresponding stress values during the previous loadings. Quantitative comparison is not yet possible and further experimental work is required in order to attempt such an approach.

REFERENCES

[1] Tonolini, F., Sala, A., Villa, G., General review of developments in acoustic emission methods, International Journal of Pressure Vessels and Piping, 28(1)(1987) 179–201.
[2] Rao, M.V.M.S., Lakschmi, P.K.J., Analysis of b-value and improved b-value of acoustic emissions accompanying rock fracture. Current Science, 89 (2005) 1577-1582.
[3] Enomoto, J., Hashimoto, H., Emission of charged particles from indentation fracture of rocks, Nature, 346 (1990) 641–643.

[4] Vallianatos, F., Triantis, D., Tzanis, A., Anastasiadis, C., Stavrakas, I., Electric Earthquake Precursors: From Laboratory Results to Field Observations, Physics and Chemistry of the Earth, 29 (2004) 339-351.
[5] Stavrakas, I., Triantis, D., Agioutantis, Z., Maurigiannakis, S., Saltas, V., Vallianatos, F., Pressure Stimulated Currents in rocks and their correlations with mechanical properties, Natural Hazards and Earth System Sciences, 4 (2004) 563-567.
[6] Stavrakas, I., Anastasiadis, C., Triantis, D., Vallianatos, F., Piezo Stimulated currents in marble samples: Precursory and concurrent – with – failure signals, Natural Hazards and Earth System Sciences, 3 (2003) 243-247.
[7] Triantis, D., Stavrakas, I., Anastasiadis, C., Kyriazopoulos, A., Vallianatos, F., An analysis of Pressure Stimulated Currents (PSC), in marble samples under mechanical stress, Physics and Chemistry of the Earth, 31 (2006) 234-239.
[8] Lavrov, A., The Kaiser effect in rocks: principles and stress estimation techniques, International Journal of Rock Mechanics & Mining Sciences, 40 (2003) 151–171.
[9] Lavrov, A., Kaiser effect observation in brittle rock cyclically loaded with different loading rates, Mechanics of Materials, 33 (2001) 669-677
[10] Kurita, K., Fuji, N., Stress memory of crystalline rocks in acoustic emission, Geophys. Res. Lett., 6(1) (1979) 9-12.
[11] Holcomb, D.J., Costin, L.S., Detection damage surfaces in brittle materials using acoustic emissions. Trans, ASME., 53 (1986) 536-544.
[12] Holcomb, D.J., Stone, C.M., Costin, L.S., Combining acoustic emission locations and a microcrack damage model to study development of damage in brittle materials. In: Hustrulid, W.A., Johnson, G.S. (eds) Proc., 31st U.S. Symposium, Rock Mechanics Contributions and Challenges, Balkema, Rotterdam, (1990) 645-651.
[13] Li, C., Nordlund, E., Experimental verification of the Kaiser Effect in Rocks. Rock Mech. Eng., 26-4(1993) 333-351.
[14] Anastasiadis, C., Triantis, D., Hogarth, C.A., Comments on the phenomena underlying pressure stimulated currents in dielectric rock materials, J Mater Sci., 42-8 (2007) 2538-2542. doi:10.1007/s10853-006-0690-7.
[15] Kyriazis, P., Anastasiadis, C., Triantis, D., Vallianatos, F., Wavelet analysis on pressure stimulated currents emitted by marble samples, Nat. Hazards Earth Syst. Sci., 6 (2006) 889–894.
[16] Kyriazis, P., Stavrakas, I., Anastasiadis, C., Triantis, D., Stonham, J., Memory effects on mechanically stimulated electric signal; diversification of stimuli impact on material memory and comments on the observed features, Geophysical Research Abstracts, EGU2010-12994, 12 (2010). http://meetingorganizer.copernicus. org/EGU2010/EGU2010-12994.pdf.
[17] Kourkoulis, S.K., Exadaktylos, G.E., Vardoulakis, I., Unotched Dionysos-Pentelicon marble beams in three point bending: The effect of nonlinearity, anisotropy and microstructure, Int. J. Fracture, 98 (1999) 369–392.
[18] Exadaktylos, G.E., Vardoulakis, I., Kourkoulis, S.K., Influence of nonlinearity and double elasticity on flexure of rock beams - I. Technical theory, International Journal of Solids and Structures, 38(22-23) (2001) 4091-4117.
[19] Exadaktylos, G.E., Vardoulakis, I., Kourkoulis, S.K., Influence of nonlinearity and double elasticity on flexure of rock beams - II. Characterization of Dionysos marble, International Journal of Solids and Structures, 38(22-23) (2001) 4119-4145.
[20] Kourkoulis, S.K., Prassianakis, I., Agioutantis, Z., Exadaktylos, G.E., Reliability assessment of the NDT results for the internal damage of marble specimens, International Journal of Material and Product Technology, 26(1/2) (2006) 35-56.
[21] Kourkoulis, S.K., Ganniari-Papageorgiou, E., Mentzini, M., Dionysos marble under bending: A contribution towards understanding the fracture of the Parthenon architraves, Engineering Geology, 115(3-4) (2010) 246-256.
[22] Stergiopoulos, C., Stavrakas, I., Hloupis, G., Kyriazopoulos, A., Triantis, D., Anastasiadis, C., Stonham, J., Monitoring Acoustic Emissions and Electrical Signals during Three-Point Bending tests performed on cement mortar specimens, VIII International Conference on Fracture Mechanics of Concrete and Concrete Structures, FraMCoS-8, Toledo (Spain), 2013. http://www.framcos.org/FraMCoS-8/p591.pdf
[23] Stergiopoulos, C., Stavrakas, I., Hloupis, G., Triantis, D., Vallianatos, F., Electrical and acoustic emissions in cement mortar beams subjected to mechanical loading up to fracture, Engineering Failure Analysis, 35 (2013) 454–461.
[24] Vallianatos, F., Triantis, D., Scaling in pressure stimulated currents related with rock fracture, Physica A, 387 (2008) 4940-4946.

Correlation between the electric and acoustic signals emitted during compression of brittle materials

Ermioni D. Pasiou
National Technical University of Athens, Department of Mechanics, Laboratory for Testing and Materials, 5 Heroes of Polytechnion Avenue, Theocaris Building, 157 73, Athens, Greece
epasiou@teemail.gr

Dimos Triantis
Technological Educational Institution of Athens, Department of Electronics, Laboratory of Electronic Devices and Materials, Ag. Spiridonos Street, 122 10, Athens, Greece
triantis@teiath.gr

ABSTRACT. An experimental protocol is described including a series of uniaxial compression tests of three brittle materials (marble, mortar and glass). The Acoustic Emission (AE) technique and the Pressure Stimulated Currents (PSC) one are used since the recordings of both techniques are strongly related to the formation of cracking in brittle materials. In the present paper, the correlation of these techniques is investigated, which is finally proven to be very satisfactory.

KEYWORDS. Pressure stimulated currents (PSC); Acoustic emission (AE); Compression; Brittle materials.

Citation: Pasiou, E.D., Triantis, D., Correlation between the electric and acoustic signals emitted during compression of brittle materials, Frattura ed Integrità Strutturale, 40 (2017) 41-51.

Received: 23.12.2016
Accepted: 07.02.2017
Published: 01.04.2017

INTRODUCTION

Monitoring the mechanical response of various brittle materials under compressive loading is of great interest in a range of application fields. Especially, monitoring their damage evolution is crucial since actions can be taken in time in order to preserve the integrity of structures. In this context, a series of diagnostic methods have been developed in order to assess damage and also to detect impending failure of the materials.

Acoustic emission (AE) technique is among the as above techniques [1]. When a material is loaded, transient elastic waves are generated within the material (which are mainly depended on the material's irreversible deformations) and travel along the specimen. These waves are called acoustic emissions and they are recorded by sensors which are attached on the specimen. The first studies of acoustic emissions in geomaterials were carried out in 1938. Monitoring a specimen/structure during its whole loading history is one of the advantages of this technique since in general the increase of acoustic activity, which is observed as the specimen approaches failure, is strongly correlated to the decay of the

mechanical properties of the material. The improved b-value (Ib-value) is one of the acoustic characteristics which is related to the impending failure [1-2] since its value changes during the failure process. Ib-value, firstly introduced by Shiotani et al. [3], is defined as:

$$Ib = \frac{\log N(\mu - \alpha_1\sigma) - \log N(\mu + \alpha_2\sigma)}{(\alpha_1 + \alpha_2)\cdot\sigma} \quad (1)$$

where μ is the mean amplitude, σ the standard deviation and α_1, α_2 constants (which are usually equal to 1 [1]).
Damage process is also well detected by the Pressure Stimulated Currents (PSC) technique [4] and more specific by the weak electric signals emitted during the generation of micro-cracks in brittle materials when they are subjected to mechanical loading [5-6]. More than ten years ago, electric signals were recorded by Stavrakas et al. [6] during mechanical loading of marble. A few years later, electric signals were also recorded when specimens of rock materials and cement based materials were tested [7-10]. The signal was captured by a pair of gold plated electrodes and it was recorded using a sensitive electrometer. In all cases, when the applied stress was above 80% of the maximum stress, PSC increased rapidly reaching a maximum value just before the specimen's fracture [4, 10]. PSC technique is also used by other researchers [11-14] while similar techniques are used [15-16] to detect cracking of rocks and concrete specimens. Some of the advantages of the PSC technique are the low cost of the sensors and the easiness of sensors' production as well as the fact that electrodes don't affect the specimens' structure or the stress and strain fields.
The qualitative correlation of the aforementioned techniques has already been mentioned in previous studies during trivial tests [17-18] as well as in more complex specimens (i.e. made of more than one material [19]). In the present experimental protocol, specimens of three brittle materials (marble, mortar and glass) are subjected to uniaxial compression tests in order to confirm and quantify the correlation of PSC and AE techniques.

MATERIALS AND EXPERIMENTAL SET UP

Materials

Dionysos marble is the stone exclusively used for the restoration of the monuments of the Athenian Acropolis. Its chemical composition is 98% of calcite, 0.5% of muscovite, 0.3% of sericite, 0.2% of quartz and 0.1% of chlorite. Its grain size varies from 100 μm to 400 μm and its specific and apparent densities are equal to 2730 kg/m^3 and 2717 kg/m^3, respectively. The absorption coefficient by weight of Dionysos marble is about 0.11% and its thermal expansion coefficient is 9x10^{-6} /^{o}C between 15 ^{o}C and 100 ^{o}C. Its very low porosity varies between 0.3% (virgin state) to 0.7% (superficial porosity) [20].
The mechanical properties of Dionysos marble vary between broad limits [21]. The specific marble is of rather orthotropic nature, i.e. it is characterized by three different anisotropy directions. However, it can be approximately considered as a transversely isotropic material described adequately with the aid of five elastic constants as it was definitely concluded by detailed experimental protocols including direct tension and compression tests as well as three-point bending and Brazilian Disc tests [22-29]. The as above experimental protocols revealed also that Dionysos marble is slightly non-linear (both in the tension and in the compression regime) and slightly bimodular, i.e. the elastic modulus in compression is about 15% higher than the respective one in tension [24, 25].
Three marble specimens were used in the present study of prismatic shape with dimensions 40 mm x 40 mm x 100 mm. The load was applied normal to the material layers, i.e. along the strong direction of Dionysos marble's anisotropy.
The second material tested was a mortar which consisted of three parts of fine sand, one part of ordinary Portland cement and half part of water. The grain size of the sand varied between 3 mm to 6 mm and its fineness modulus was equal to 2.8. In addition, its specific gravity was found equal to 2.6, its density was 2200 kg/m^3 and its porosity was evaluated at approximately 8% [10].
The constituents of the mortar were mixed at a low speed to enable better moisturizing of the cement grains while at the end of the production process the mixture was agitated very fast for 1 min. Mortar was formed in three prismatic blocks using metallic moulds of dimensions 50 mm x 50 mm x 70 mm the inner surfaces of which were oiled. The moulds were mounted on a desktop vibrator in order to enable compaction. The mortar prismatic blocks were demoulded after 24 h and they were cured in a room with constant ambient temperature of 22 °C and 75-80% humidity. The specimens were stored for 100 days to reach 90-95% of their strength [30].
The third material studied in the present experimental protocol was one of the most common types of glass produced, i.e. the soda-lime-silica one (or simply soda glass). One of its most important advantages is that it is nearly chemically inert,

therefore it doesn't react with other chemicals when they come into contact with it. Soda glass in usually used to make windows, bottles, jars, vials and other laboratory equipment. The chemical composition of this type of glass is presented in Tab. 1. In the present experimental protocol three prismatic blocks (30 mm x 30 mm x 80 mm) were used.

Components	SiO_2	Al_2O_3	Na_2O	K_2O	CaO	MgO	Fe_2O_3	TiO_2	P_2O_5	ZrO_2
%	72.4	1.26	13.4	0.24	8.53	3.95	0.16	0.063	0.018	0.05

Table 1: Chemical composition of soda-lime-silica glass [31].

Experimental set up

Before testing, one Kyowa strain gauge (of 5 mm gauge length and of 120 Ω gauge resistance) was glued on the front surface of the specimen (at the middle of its height and of its width as it is seen in Fig.1a) in order to measure the axial strain during the tests. In addition, one acoustic sensor R15α (denoted by number 3 in Fig.1b) was coupled on the opposite surface of the specimen by means of silicone and one preamplifier with 40 dB gain was also used (the equipment and the software used were by Mistras Group, Inc.). Finally, a pair of electrodes was attached on the two side opposite surfaces of each specimen (orange ellipses in Fig.1a and numbers 1,2 in Fig.1b) in such a way so as the imaginary line connecting them to be perpendicular to the loading axis. A sensitive programmable electrometer (Keithley, 6517A), capable of resolving currents as low as 0.1 fA and as high as 20 mA in 11 ranges, was used to record the electric signals. It should be underlined that thin teflon plates were placed between the specimen and the loading platens for the specimen's electrical isolation. All specimens were subjected to compressive loading under load control conditions ($d\sigma/dt$=0.3 MPa/s) simulating quasi-static loading.

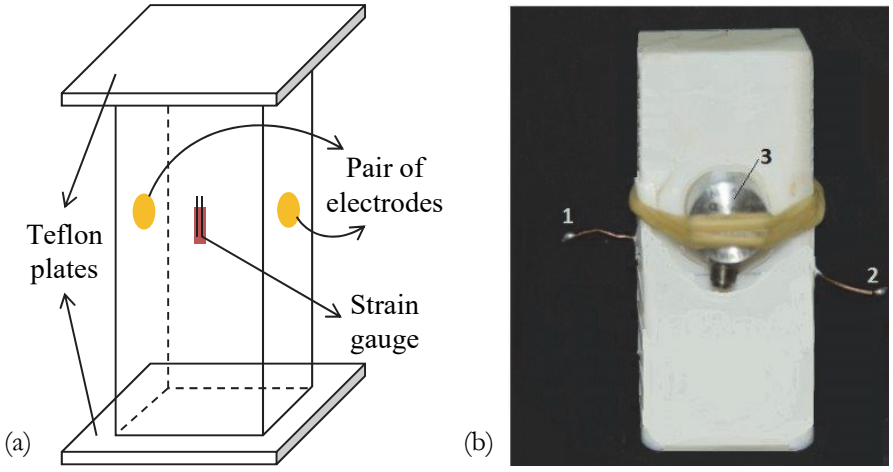

Figure 1: (a) A sketch of the experimental set up, (b) A typical marble specimen. The pair of electrodes (1, 2) and the acoustic sensor (3) are also presented.

RESULTS AND DISCUSSION

Mechanical behaviour

Typical stress-strain curves of each material are presented in Fig.2. The commonly observed "bedding error" during compressive tests is obvious in all three materials. Ignoring this initial part, the curves of both marble and cement mortar are mainly characterized by linearity up to about 80% of their maximum stress (points A and B in Fig.2a,b). The mean value of the fracture stress is ~95 MPa for marble and ~50 MPa for cement mortar. The modulus of elasticity obtained was equal to ~70 GPa and ~20 GPa for marble and mortar, respectively, which are very close to the respective ones from literature [10, 22]. Afterwards both curves deviate from linearity. On the other hand, the stress-strain curve of soda glass is linear almost up to 90% of the maximum stress of the specimens (point C in Fig.2c). Its modulus of elasticity was calculated equal to ~70 GPa as it is also mentioned in [31, 32] and its maximum stress was found to be equal to ~20 MPa. It is also to be noted that ductility of soda glass specimens is one order of magnitude lower than the respective ones of both marble and mortar. The mechanical characteristics obtained from all specimens are recapitulated in Tab. 2.

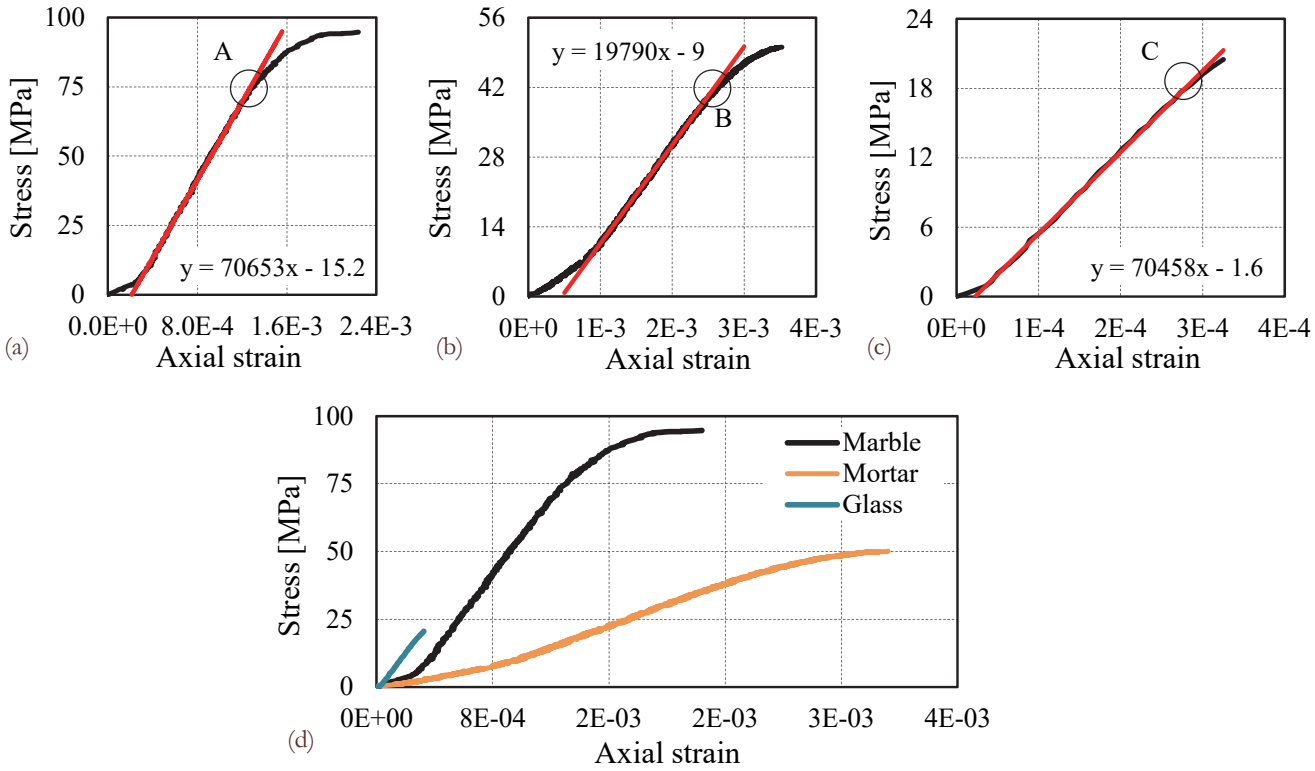

Figure 2: Typical stress-axial strain curves for (a) marble, (b) mortar and (c) glass specimens. (d) The three aforementioned curves together for comparison reasons.

Material	Specimen	Modulus of elasticity [GPa]	Fracture stress [MPa]	Peak axial strain [-]
Dionysos marble	M1	68.8	98.7	$1.7 \cdot 10^{-3}$
	M2	71.2	92.5	$1.9 \cdot 10^{-3}$
	M3	70.7	94.7	$2.2 \cdot 10^{-3}$
	Mean value ± standard deviation	70.2 ± 0.2	95.3 ± 0.5	$1.9 \cdot 10^{-3}$ ± 0.3
Cement mortar	C1	19.8	50.1	$3.5 \cdot 10^{-3}$
	C2	18.1	46.4	$2.4 \cdot 10^{-3}$
	C3	23.3	51.7	$3.1 \cdot 10^{-3}$
	Mean value ± standard deviation	20.4 ± 0.8	49.4 ± 0.5	$3.0 \cdot 10^{-3}$ ± 0.5
Soda glass	G1	68.7	18.8	$2.7 \cdot 10^{-4}$
	G2	70.5	20.5	$3.3 \cdot 10^{-4}$
	G3	70.0	19.4	$3.1 \cdot 10^{-4}$
	Mean value ± standard deviation	69.7 ± 0.2	19.6	$3.0 \cdot 10^{-4}$ ± 0.3

Table 2: The mechanical characteristics of all specimens.

Electric signals

The electric signal produced during a typical compressive test of a marble specimen and the axial strain obtained (normalized over its maximum value) versus the normalized stress are presented in Fig.3. A weak current (from 0.5 pA increases slightly to 2 pA) is initially observed until point A_1 in Fig.3(a1) where the stress level equals ~75% of the maximum stress and strain is ~55% of the fracture strain. This point almost corresponds to point A where the stress-strain curve

deviates from linearity. Afterwards, the electric current starts increasing with higher rate, indicating the onset of micro-cracking. When stress equals about 97% of the maximum applied stress (point A'_1 in Fig.3(a2) where the stress-strain curve tends to become horizontal) and strain equals about 80% of the maximum strain the increase of PSC is remarkable, severe cracking takes place (not yet visible with naked eyes) and the specimen is just before collapse.

In case of mortar specimens, the first noticeable change of the PSC values is observed when strain equals ~55% of the maximum strain and stress is ~60% of the maximum stress, point B_1 in Fig.3b) although the material is still below its proportional limit. The increase of the electric signal starts becoming significantly larger (point B'_1 in Fig.3b) when the respective stress-strain curve deviates from linearity (~75% of the maximum stress and ~70% of the fracture strain, point B in Fig.2b). PSC gets its maximum value slightly before the final fracture (~90% of the maximum strain and ~95% of the maximum stress) indicating the impending failure.

Concerning soda glass, the variation of PSC could be clearly divided in three stages. In the beginning of the test, a weak electric signal is detected until point C_1 in Fig.3c where strain is equal to ~60% of the maximum strain and stress is ~60% of the maximum stress. During the second stage (between points C_1 and C'_1 in Fig.3c), the increase of PSC is considerable while the increase rate becomes even higher during the last stage where the applied stress is ~85% of the maximum stress and strain equals ~80% of the maximum strain. The maximum value of PSC is attained ~96% of both the maximum stress and the maximum strain.

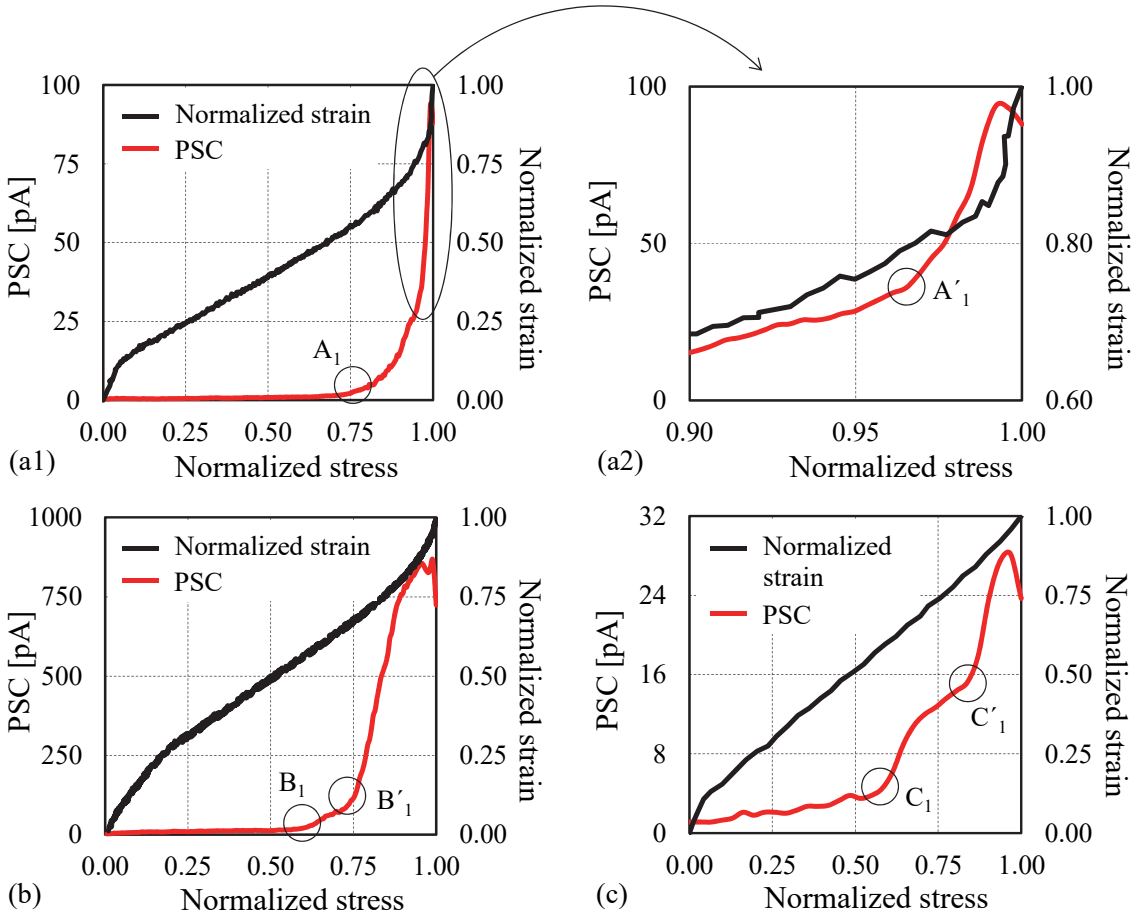

Figure 3: The electric current and the normalized axial strain versus the normalized stress for a typical specimen of (a) marble, (b) mortar and (c) glass.

PCS values in comparison with Ib-values

In all cases, groups of 70 hits were used for the calculation of the Ib-value. The first group included the first 70 hits while each successive group contained 35 hits of the previous one and the next 35 hits. Each Ib-value corresponds to the instant which was calculated as the mean time of the respective hits.

The variation of Ib-value in conjunction with the electric current is shown versus the normalized stress in Fig.4(a1) for a typical marble specimen. In the beginning of the test, until ~30% of the maximum strain and ~35% of the maximum

stress, Ib has high values decreasing from ~2.4 to 1.7. This can be related to the closure of pre-existing micro-cracks of the specimen or/and to rubbing/friction [1]. Afterwards, Ib-value is almost constant with variance around ~2.0 indicating the slow generation of new micro-cracks (until point A_2 in Fig.4(a1) which corresponds to stress level ~80% of the maximum stress and strain ~60% of the maximum strain). This point coincides with the deviation of the stress-strain curve from linearity. Slightly earlier, the first noticeable increase of the electric current was observed. Finally, Ib decreases systematically attaining at the end of the test values close to 1.0 (point A'_2 in Fig.4(a2)). This happens at ~95% of the maximum applied stress and ~75% of the maximum strain and it is related to a large number of cracks. During the decrease of Ib-value, PSC increases further. At the final stage (after point A'_2), Ib slightly decreases further due to the coalescence of cracks which leads the specimen to the final fracture while the electric current increases dramatically reaching its highest value.

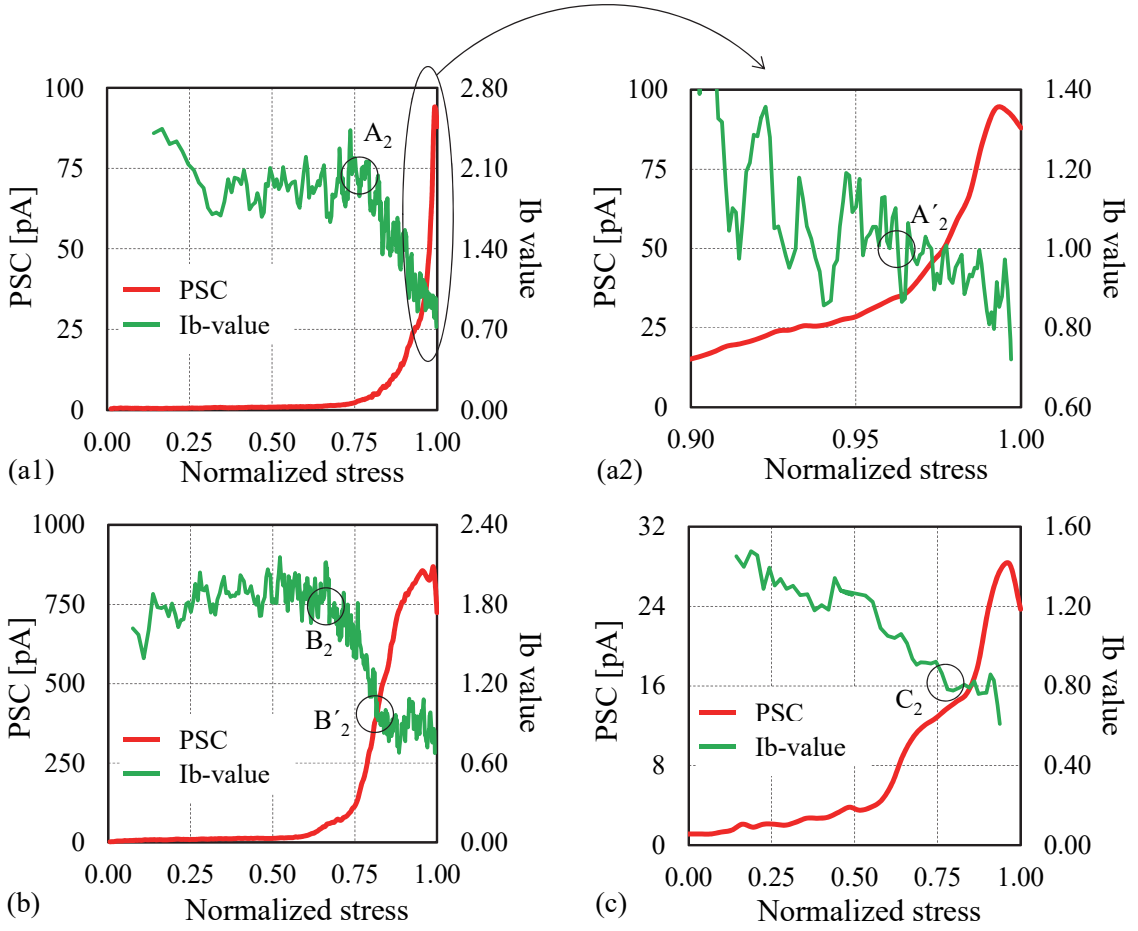

Figure 4: The electric current and the Ib-value against the normalized stress for a typical specimen of (a) marble, (b) mortar and (c) glass.

In case of mortar, Ib-value (Fig.4b) is relatively high from the beginning of the test until ~35% of both the maximum strain and the maximum stress while a period with almost constant Ib-value (~1.8) follows (until point B_2, ~60% of the maximum strain and ~70% of the maximum applied stress). Afterwards, Ib-value decreases (while the increase of PSC becomes significant) reaching the value of 1.0 (point B'_2) when the respective stress-strain curve ceases to be linear (~70% of the maximum strain and ~75% of the maximum stress). Subsequently, the values of Ib become slightly lower than 1.0 remaining almost constant until the fracture of the specimen. During this stage, the electric current attains its peak value indicating the impending failure.

The variation of the Ib-values for a typical soda glass specimen is presented in Fig.4c. Ib-value continuously decreases until point C_2 (~80% of both the maximum strain and the maximum stress), i.e. almost during the first two stages of the PSC variation. The rate of Ib-value decrease is higher between ~40% and ~80% of both the maximum strain and the maximum stress. Afterwards, Ib-value remains almost constant until ~90% of the maximum stress. From this point on and up to the end of the test, Ib-value decreases further. It is worth noticing that in case of soda glass, Ib-value attains the

value of 1.0 when strain is ~65% of the maximum strain and stress is ~65% of the maximum stress, i.e. relatively lower compared to the other two materials.
It should be mentioned at this point that b-value is related, among others, to the heterogeneity of the material. As the degree of nonuniformity of the material increases, b-value also increases [33]. This is consistent with the results of the present study. The material layers of marble and the existence of sand in mortar make these structures quite heterogeneous compared to glass specimens and as a result the Ib-values obtained for marble and mortar are larger than the respective values of glass. In addition, the heterogeneity of both marble and mortar results to the generation of low acoustic activity during the initial load levels leading to an almost constant Ib-value in these first stages of loading. The absence of this constant segment in case of glass makes the variation of the respective Ib-value to be monotonic in contrast to the respective variations of both marble and mortar.

Approach based on energies

Despite the fact that the correlation of PSC and AE techniques became clear in the previous section, an alternative approach based on the released energy was decided to be used in order to quantitatively verify the correlation of the two experimental techniques.
The absolute energy (measured in aJ) produced and recorded by the acoustic sensors characterizes each acoustic hit and it is calculated by the software as the integral of the signal voltage at a power of two over the reference resistance (10 kΩ). In the present study, the sum of the energy released during each second of the tests, E_{AE}, was calculated since it is a measure of the size distribution of micro-cracks in such materials [34]. In case of PSC technique, the energy released was calculated by the familiar expression:

$$E_{PSC}=\int_{t_i}^{t_i+\Delta t} PSC^2(t)dt \qquad (2)$$

where $\Delta t=1$ s and $t_i= 0, 1, \ldots, n-1$ (n is the duration of the experiment). Since PSC is measured in pA, the units of E_{PSC} are $(pA)^2 \cdot s$. Finally, the strain energy density, SED, was calculated as the area below the stress-strain curves of the tests.
All three quantities were normalized over the respective maximum value and the results are presented in logarithmic scale in Fig.5. For all three materials of the present experimental protocol both curves are formed by two almost straight segments with different slope and a knee point is clearly seen corresponding probably to the formation of more severe cracks. In case of marble (Fig.5a), it is quite interesting that PSC technique seems to detect the internal damage of the specimen earlier than AE technique. In case of marble, the $PSC_{knee\ point}$ and the $AE_{knee\ point}$ correspond to about 70% and 80% of the maximum stress, respectively (i.e. about 50% and 60% of the maximum strain, respectively). The same is true for mortar specimens (Fig.5b). The knee point from PSC technique is observed when stress equals about 60% of the maximum stress (~55% of the maximum strain) while $AE_{knee\ point}$ corresponds to ~65% of the maximum stress and ~60% of the maximum strain. In case of glass specimens (Fig.5c), the knee points formed by the two techniques are observed almost simultaneously (~60% of both the maximum stress and strain).

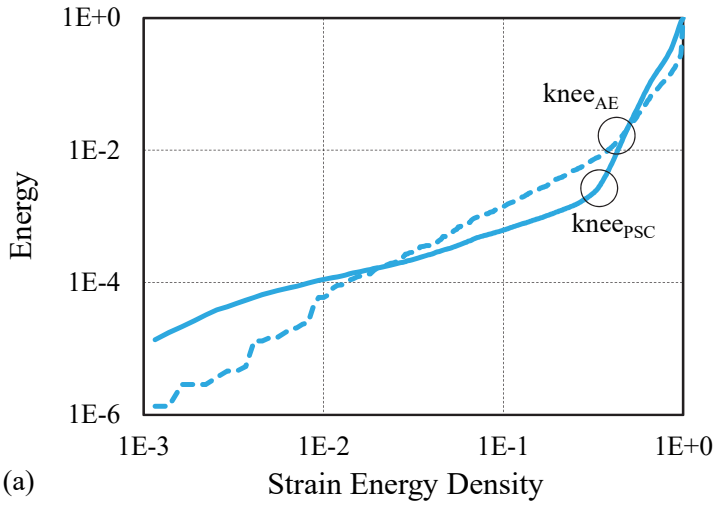

Figure 5: The energy calculated by both PSC and AE techniques versus the strain energy density for a typical specimen of (a) marble.

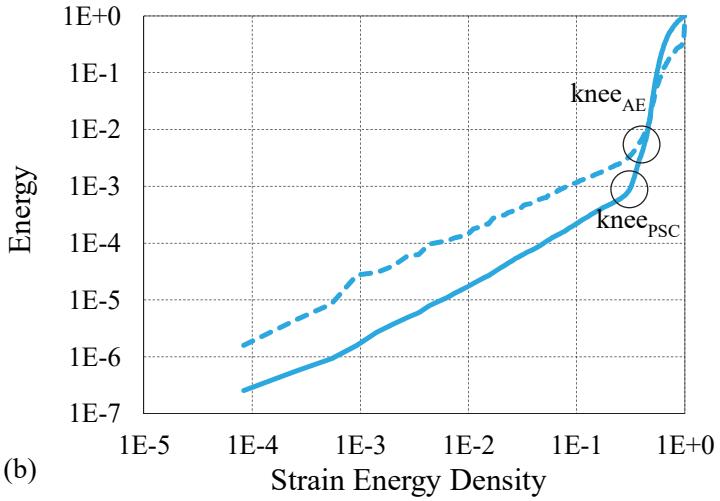

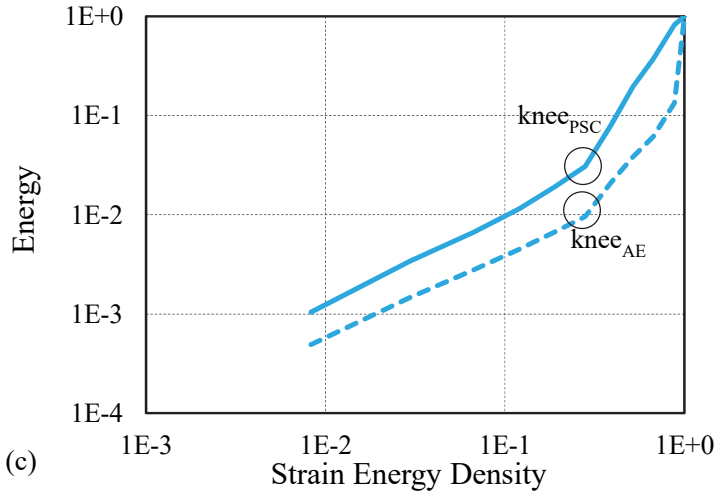

Figure 5 (con't): The energy calculated by both PSC and AE techniques versus the strain energy density for a typical specimen of (b) mortar and (c) glass.

As a next step, an effort was made to investigate any correlation which might exist between the quantities E_{PSC} and E_{AE} calculated by the two experimental techniques. In Figs.6(a-c) both energies are presented in logarithmic scale for a typical specimen for each material studied here. The solid dark blue circles represents the period where the electric current produced is very weak without noticeable changes while the empty symbols corresponds to the increase of the PSC until it reaches its maximum value. It is clear that the correlation is much better when the energy emitted increases considerably (empty dark blue circles). Therefore, ignoring the period where PSC is almost constant or increases very smoothly, it was found that the correlation of the energies calculated based on both experimental techniques obeys a power law, i.e. $E_{AE} \propto (E_{PSC})^m$, where m~0.8 for both marble and glass specimens while m~0.7 for mortar specimens (Figs.6(a-c)).

Conclusions

The correlation of both experimental techniques used in the present experimental protocol is highlighted. More specific, it was found that when the Ib-value decreases, the electric signal detected by the PSC technique starts increasing considerably indicating the formation of cracks. All three materials (marble, mortar and glass) enter a critical state (i.e. Ib-value tends to 1.0) when strain is equal to about 65-75% of the maximum strain (stress level equals to about 95% for marble, about 75% for mortar and about 65% for glass). The same stress level, at which the damage state of Dionysos marble becomes critical, is also obtained by other researchers based on the variation of the b-value [35].
The alternative approach which was based on the energy released during loading of the specimens, although it makes very

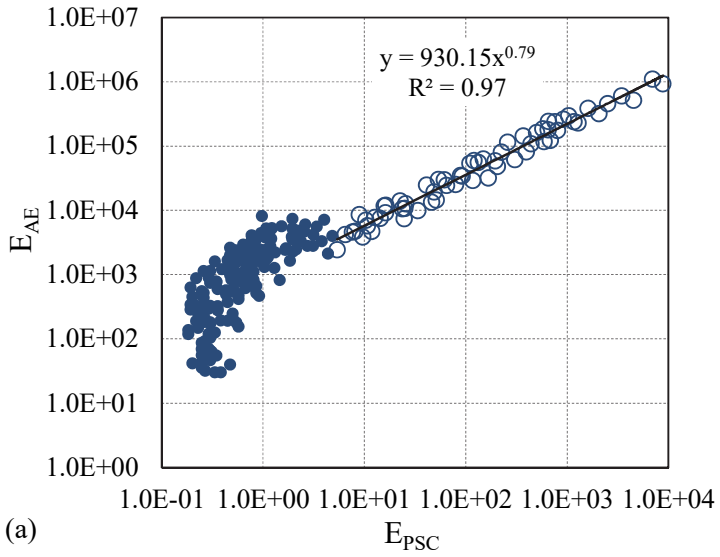

(a)

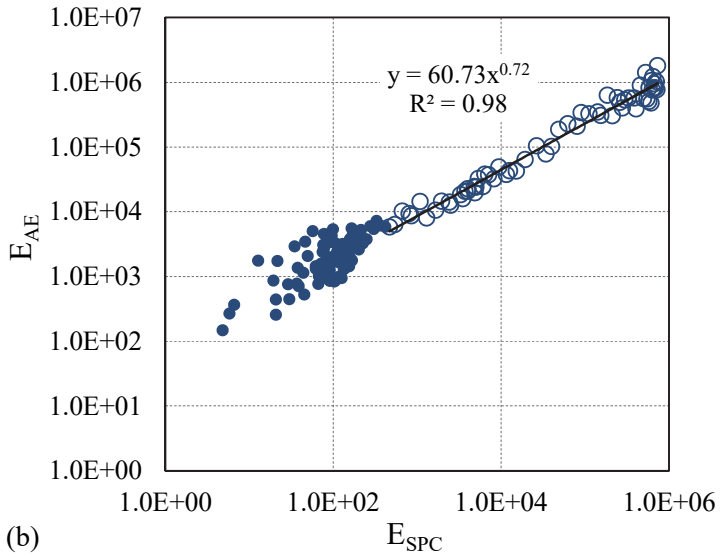

(b)

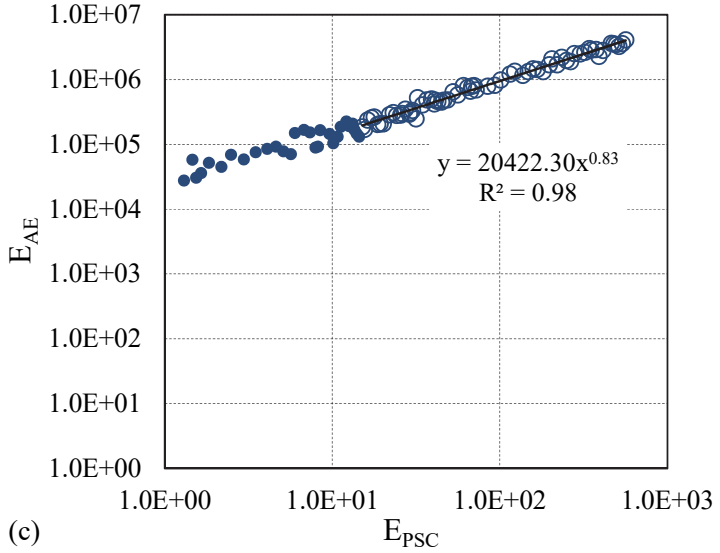

(c)

Figure 6: The correlation of the energy calculated by both PSC and AE techniques for a typical specimen of (a) marble, (b) mortar and (c) glass.

clear the point where cracking becomes more severe, it seems to be more conservative. The knee points are observed when strain equals about 50-60% of the fracture strain for all three materials studied here (while the stress level equals about 70-80% for marble specimens and about 55-65% for mortar and soda glass specimens).
AE technique has already been mentioned as a valuable tool for detecting the impending failure paying attention either to the general acoustic activity or to specific acoustic characteristics in accordance mainly to the stress induced on the specimens [18-19, 35-36].
PSC technique is more recently developed compared to the AE technique and it is not yet fully standardized. It should be mentioned that the specific technique cannot be applied in heavily distorted electromagnetic environments since very low electrical currents (in the order of pA) are measured and the external electrical noise acts as additive electrical noise on the actual signal. In order to minimize such effects special care must be given to the shielding of the experimental apparatus, electrical ground and low noise cabling. Despite the aforementioned limitations, the electric current recorded using the PSC technique has already been related to the mechanical behaviour of the tested material [4, 7].
Concluding, taking into account that strains are much easier to be measured, compared to the stress field developed, the fact that the critical state is detected by both techniques and it is determined at almost the same strain level for all three materials is an interesting finding which could be very useful for monitoring and assessing the integrity of structures.
In addition, in the direction of quantifying the correlation of the AE and the PSC techniques, a successful attempt is made for the very first time in the present paper. Indeed a very good correlation exists between the energies measured by both techniques, which obeys a power law with exponent equal to 0.7-0.8 for the materials studied here.

REFERENCES

[1] Rao, M.V.M.S., Lakschmi, P.K.J., Analysis of b-value and improved b-value of acoustic emissions accompanying rock fracture, Current Science, 89 (2005) 1577-1582.
[2] Colombo, S., Main, I.G., Forde, M.C., Assessing damage of reinforced concrete beam using "b-value" analysis of Acoustic Emission signals, Journal of Materials in Civil Engineering (ASCE), 15 (2003) 280-286.
[3] Shiotani, T., Yuyama S., Li, Z.W., Ohtsu, M., Application of the AE improved b-value to qualitative evaluation of fracture process in concrete materials, Journal of Acoustic Emission, 19 (2001) 118-132.
[4] Stavrakas, I., Triantis, D., Agioutantis, Z., Maurigiannakis, S., Saltas, V., Vallianatos, F., Pressure Stimulated Currents in rocks and their correlations with mechanical properties, Natural Hazards and Earth System Sciences, 4 (2004) 563-567.
[5] Enomoto, J., Hashimoto, H., Emission of charged particles from indentation fracture of rocks, Nature, 346 (1990) 641-643.
[6] Vallianatos, F., Triantis, D., Tzanis, A., Anastasiadis, C., Stavrakas, I., Electric earthquake precursors: From laboratory results to field observations, Physics and Chemistry of the Earth, 29 (2004) 339-351.
[7] Triantis, D., Anastasiadis, C., Vallianatos, F., Kyriazis, P., Nover, G., Electric signal emissions during repeated abrupt uniaxial compressional stress steps in amphibolite from KTB drilling, Natural Hazards and Earth System Sciences, 7 (2007) 149-154.
[8] Vallianatos, F., Triantis, D., Scaling in Pressure Stimulated Currents related with rock fracture, Physica A, 387 (2008) 4940-4946.
[9] Triantis, D., Anastasiadis, C., Stavrakas, I., The correlation of electrical charge with strain on stressed rock samples, Natural Hazards and Earth System Sciences, 8 (2008) 1243-1248.
[10] Kyriazopoulos, A., Anastasiadis, C., Triantis, D., Brown, C.J., Non-destructive evaluation of cement-based materials from pressure-stimulated electrical emission - Preliminary results, Construction and Building Materials, 25 (2011) 1980-1990.
[11] Aydin, A., Prance, R.J., Prance, H., Harland, C.J., Observation of pressure stimulated voltages in rocks using an electric potential sensor, Applied Physics Letters, 95 (2009) art no. 124102.
[12] Freund, F., Pre-earthquake signals: Underlying physical processes, Journal of Asian Earth Sciences, 41 (2011) 383-400.
[13] Cartwright-Taylor, A., Vallianatos, F., Sammonds, P., Superstatistical view of stress-induced electric current fluctuations in rocks, Physica A: Statistical Mechanics and its Applications, 414 (2014) 368-377.
[14] Li, Z., Wang, E., He, M., Laboratory studies of electric current generated during fracture of coal and rock in rock burst coal mine, Journal of Mining, 2015 (2015) article ID 235636.
[15] Archer, J.W., Dobbs, M.R., Aydin, A., Reeves, H.J., Prance, R.J., Measurement and correlation of acoustic emissions and pressure stimulated voltages in rock using an electric potential sensor, International Journal of Rock Mechanics and Mining Sciences, 89 (2016) 26-33.

[16] Dann, D., Demikhova, A., Fursa, T., Kuimova, M., Research of electrical response communication parameters on the pulse mechanical impact with the stress–strain state of concrete under uniaxial compression, IOP Conference Series: Materials Science and Engineering, 66(1) (2014) 012036, doi:10.1088/1757-899X/66/1/012036
[17] Stergiopoulos, C., Stavrakas, I., Hloupis, G., Triantis, D., Vallianatos, F., Electrical and Acoustic Emissions in cement mortar beams subjected to mechanical loading up to fracture, Engineering Failure Analysis, 35 (2013) 454–461.
[18] Stavrakas, I., Pasiou, E.D., Hloupis, G., Malliaros, G.-T., Triantis, D., Kourkoulis, S.K., Exploring the size effect of marble by combined use of Pressure Stimulated Currents and Acoustic Emission, in: Beskos D.E., Stavroulakis G.E. (Eds.), 10th HSTAM International Congress on Mechanics, Chania, Hellas, (2013) 185-186.
[19] Triantis, D., Stavrakas, I., Pasiou, E.D., Hloupis, G., Kourkoulis, S.K., Innovative experimental techniques in the service of restoration of stone monuments - Part II: Marble epistyles under shear, Procedia Engineering, 109C (2015) 276-284.
[20] Tassogiannopoulos, A.G., A contribution to the study of the properties of structural natural stones of Greece (in Greek), Ph.D. Dissertation, National Technical University of Athens, Greece (1986).
[21] Theocaris, P.S., Coroneos, E., Experimental study of the stability of Parthenon, Publications of the Academy of Athens, 44 (1979) 1-80.
[22] Kourkoulis, S.K., Exadaktylos, G.E., Vardoulakis I., U-notched Dionysos-Pentelicon marble in three point bending: The effect of nonlinearity, anisotropy and microstructure, International Journal of Fracture, 98(3-4) (1999) 369-392.
[23] Kourkoulis, S.K., Ganniari-Papageorgiou, E., Mentzini, M., Dionysos marble under bending: A contribution towards understanding the fracture of the Parthenon architraves, Engineering Geology, 115 (3-4) (2010) 246-256.
[24] Exadaktylos, G.E., Vardoulakis, I., Kourkoulis, S.K., Influence of nonlinearity and double elasticity on flexure of rock beams - I. Technical theory, International Journal of Solids and Structures, 38 (22-23) (2001) 4091-4117.
[25] Exadaktylos, G.E., Vardoulakis, I., Kourkoulis, S.K., Influence of nonlinearity and double elasticity on flexure of rock beams - II. Characterization of Dionysos marble, International Journal of Solids and Structures, 38 (22-23), (2001) 4119-4145.
[26] Exadaktylos, G.E., Kaklis, K.N., Applications of an explicit solution of the transversely isotropic circular disc compressed diametrically, International Journal of Rock Mechanics and Mining Sciences, 38(2) (2001) 227-243.
[27] Markides, Ch.F., Pazis, D.N., Kourkoulis, S.K, Influence of friction on the stress field of the Brazilian tensile test, Rock Mechanics and Rock Engineering, 44(1) (2011) 113-119.
[28] Markides, Ch.F., Kourkoulis, S.K., The stress field in a standardized Brazilian disc: The influence of the loading type acting on the actual contact length, Rock Mechanics and Rock Engineering, 45(2) (2012) 145-158.
[29] Kourkoulis, S.K., Prassianakis, I., Agioutantis, Z., Exadaktylos, G.E., Reliability assessment of the NDT results for the internal damage of marble specimens, International Journal of Material and Product Technology, 26(1/2) (2006) 35-56.
[30] Kosmatka, S.H., Kerkhoff, B., Panarese, W.C., Design and control of concrete mixtures (14th ed.), Portland Cement Association (2002).
[31] Chorfa, A., Madjoubi, M.A., Hamidouche, M., Bouras, N., Rubio, J., Rubio, F., Glass hardness and elastic modulus determination by nanoindentation using displacement and energy methods, Ceramics - Silikáty, 54(3) (2010) 225-234.
[32] Sehgal, J., Ito, S., Brittleness of glass, Journal of Non-Crystalline Solids, 253 (1999) 126-132.
[33] Mogi, K., Earthquakes and fractures, Tectonophysics, 5(1) (1967) 35-55.
[34] Rao, M.V.M.S., Lakshmi K.J.P., Rao, G.M.N., Vijayakumar, K., Udayakumar, S., Precursory microcracking and brittle failure of Latur basalt and migmatite gneiss under compressive loading, Current Science, 101(8) (2011) 1053-1059.
[35] Nomikos, P.P., Sakkas, K.M., Sofianos, A.I., Acoustic emission of Dionysos marble specimens in uniaxial compression, Harmonising Rock Engineering and the Environment, Qian and Zhou (eds.), Taylor & Francis Group, London, ISBN 978-0-415-80444-8.
[36] Agioutantis, Z., Kaklis, K., Mavriagiannakis, S., Verigakis, M., Vallianatos, F., Saltas, V., Potential of acoustic emissions from three point bending tests as rock failure precursors, International Journal of Mining Science and Technology, 26 (2016) 155-160.

Acoustic emissions and electric signal recordings, when cement mortar beams are subjected to three-point bending under various loading protocols

A. Kyriazopoulos
Laboratory of Electronic Devices and Materials, Technological Educational Institute of Athens, 12210, Athens, Greece.
akyriazo@teiath.gr

ABSTRACT. Two experimental techniques are used study the response of cement mortar beams subjected to three-point bending under various loading protocols. The techniques used are the detection of weak electric current emissions known as Pressure Stimulated Currents and the Acoustic Emissions (in particular, the cumulative AE energy and the b-value analysis). Patterns are detected that can be used to predict upcoming fracture, regardless of the adopted loading protocol in each experiment. The experimental results of the AE and PSC techniques lead to the conclusion that when the calculated I_b values decrease, the PSC starts increasing strongly.

KEYWORDS. Pressure Stimulated Currents; Acoustic Emissions; Cement mortar; Three point bending; b-value.

Citation: Kyriazopoulos, A., Acoustic emissions and electric signal recordings, when cement mortar beams are subjected to three point bending under various loading protocols, Frattura ed Integrità Strutturale, 40 (2017) 52-60.
Received: 05.01.2017
Accepted: 26.02.2017
Published: 01.04.2017

INTRODUCTION

The mechanical behavior and the evolution of damage in heterogeneous materials under compressive loading are of great interest in a wide range of application fields. Particularly, the Service Life of cement-based structures deteriorates due to heavy loads, fatigue, aging and natural disasters. Accordingly, diagnostic methods for damage assessment have been developed and implemented, aiming to assess the impending failure. To this end, the Acoustic Emissions (AE) technique was developed and is being improved continuously in order to provide a useful tool for monitoring and understanding the mechanisms of dynamic processes, but also for warning of upcoming failure [1]. Acoustic Emission events occur due to sudden release of mechanical energy in the form of short mechanical vibrations due to the fact that a material is under mechanical loading. This mechanical vibration travels in the form of spherical waveforms through the material's bulk. The AE event analysis is used to estimate the damage degree when brittle materials such as concrete and rocks are subjected to mechanical loading [2-5].
Acoustic Emission (AE) due to crack growth in brittle materials is usually observed in the high frequency range, typically between 50 kHz and 800 kHz. AE are recorded even from the early stages of the damage process. During the fracture process in quasi-brittle materials, the micro cracks formation and growth are manifested by a number of AE events released at different amplitudes. It has been shown that as a specimen under mechanical loading approaches failure, there is

an increase in the AE activity rate, as a result of the deterioration of the mechanical properties. Particularly in cement based materials and concrete structures the AE testing is one of the most widely used methods for monitoring crack growth [1].
Another phenomenon related to the micro-crack growth in quasi-brittle nonmetallic materials is the production of electric charges that shape electric dipoles forming a rather complicated charge system [6-8]. Such electric dipoles produce an electric potential across a crack resulting in the appearance of an electric current [9]. Such currents have been measured in both laboratory [7, 10] and at a geodynamic scale [11] and their detection may be useful as a precursor of a fracture.
These electrical signals (weak electrical current emissions) are detected using a novel experimental technique, called Pressure-Stimulated Currents Technique, and the recorded electrical currents are described by the term Pressure Stimulated Currents (PSC) [12]. The PSC's are weak electric currents detected with sensitive electrometers when a pair of electrodes is attached at proper locations on the specimen that is subjected to mechanical stress. Initially, the PSC technique was applied when rock specimens like marble [6, 13] and amphibolite [14] were subjected to compressive axial stress increasing up to failure. Consequently, it was successfully applied to cement-based materials [15, 16]. The PSC technique was also tested during laboratory experiments of three-point bending (3PB) tests on marble [17] and cement-based specimens [5]. The PSC technique has been adopted by several researchers [9, 18], while others use similar techniques [19-21].
Both AE and PSC signals provide important information about the damage processes occurring in specimens under compression or under bending tests. In particular, the PSCs show a considerable increase when the applied load reaches the vicinity of failure and attain their peak value shortly before failure [12, 13, 15, 16].
In Acoustic Emissions one of the statistical parameters, which is often used to estimate a critical situation, is the b-value [1, 22, 23], which exhibits systematic variations during the different stages of fracture processes. The AE based b-value analysis and the variation of the b-value, have attracted researchers working in the engineering field [23, 24]. Other AE statistical parameters that have been used include the event and energy release rates, the cumulative energy and the ring down counts.
In this paper attention is focused on the parallel presentation of AE and PSC detected during 3PB of cement mortar specimens. The main difference between the three experiments is the loading mode. Specifically, one test was conducted under a constant loading rate (i.e. linear load increase) up to fracture while at the other two experiments the load was increasing according to a non-linear mode.

EXPERIMENTAL DETAILS

The specimens used for the experiments were prismatic cement mortar beams with dimensions 250x50x50 mm^3. Their bending strength (L_f) varied from 3.5kN to 4.0kN. Details regarding the specimens, the preparation process and the experimental apparatus can be found in a previous work [25].
Contrary to previous publications [25], the electrodes that were used to capture the PSC emissions were placed as shown in Fig. 1, i.e. on the lower side of the beam (tension zone) and at the left and right sides, symmetrically with respect to the specimen's central cross section where the load is applied. This topology was decided after several experiments conducted in order to estimate the best installation process that ensures the recording of strong PSCs and limits the influence of electric noise. The best electrode distance (ℓ) was also investigated and it was empirically found that for the specific type of experiments it should be $\ell \approx \alpha / 5$, where α is the distance between the two rigid metallic cylindrical rods used to support the cement beam. The PSC was captured by the electrodes and measured using a high sensitivity electrometer (Keithley, model 6517). The data were recorded in real time and stored on a hard disk through a GPIB interface. The mechanical load applied was recorded with the use of an analog-to-digital (A/D DAQ) data acquisition device (Keithley model KUSB-3108). The whole setup was placed in a Faraday shield in order to avoid interference from external electrical noise.
The system that was used to detect and record the AE is the 2-channel PCI-2 AE acquisition system (Physical Acoustics Corp). The R15a sensor (manufactured by PAC, resonant at 75 kHz) was placed in the middle of the beam (see Fig. 1) in order to focus on the region of the crack development processes that take place due to the externally applied bending load. The sensor was coupled to the test specimen using vacuum grease. Preamplifier was used along with the sensor with gain set at 40dB. The signals were band-pass filtered between 20-400 kHz using the software control of the data acquisition system. To set the threshold value for recording and to ensure that sensors were correctly performing, pencil lead breaks (5mm, HB leads) were carried out near the crack tip and the recorded signals were observed. The value of 40dB was selected since it was found to prevent the recording of lower amplitude reflected signals from the pencil lead break tests. For the detected AE data processing the Physical Acoustics Corp. Noesis software was used.

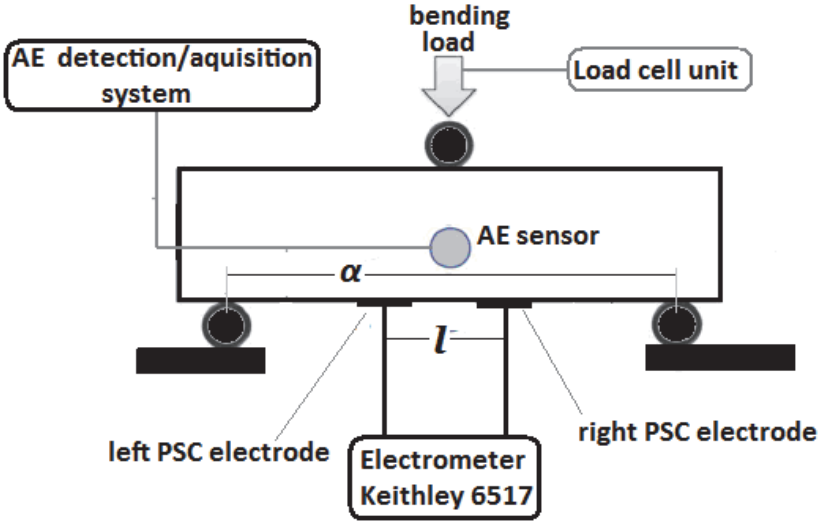

Figure 1: The experimental installation and the location of the AE and PSC sensors.

RESULTS AND DISCUSSION

Tab. 1 includes all the details regarding the loading protocol of each specimen for the three experiments implemented, i.e. load (L) vs. time (t), considering that the function is best described as:

$$L(t) = C_1 \cdot t^2 + C_2 \cdot t \quad (1)$$

where C_1 and C_2 are constants. During the first experiment (i.e. specimen CB01) a linear increase of the load was conducted at a rate of 100N/s while the two following experiments were conducted following a non-linear increase of the mechanical load (see Tab. 1).

Specimen	$L(t) = C_1 \cdot t^2 + C_2 \cdot t$	L_f (kN)	PSC_{peak} (pA)	Q_T (pC)	AE hits	Cum. Energy AE
CB01	C_1=0, C_2=+100N/s	3.6	28.8	294	1062	5.17x10^7 aJ
CB02	C_1=-7.3N/s^2, C_2=+333N/s	3.8	27.2	298	543	4.50x10^7 aJ
CB03	C_1=+0.7N/s^2, C_2=35.4N/s	3.5	29.9	291	893	4.98x10^7 aJ

Table 1. The characteristics of the loading protocol followed during each of the three experiments conducted and the main quantities studied regarding the PSC and AE recordings.

Fig. 2 shows the temporal variation of the emitted PSC from the three experiments, as well as the corresponding behavior of the mechanical load. Shortly before failure of the specimens the emitted PSC tends to show a peak. The recorded peak value (PSC_{peak}) is similar in all three experimental loading protocols (see Tab. 1). The fact that the PSC is maximized before the failure of the cement mortar beam has been systematically observed during compressive stress tests on both cement based [15] and rock [26, 27] materials. This behavior is best demonstrated by the specimen CB02. This is attributed to the fact that the specimen approaches failure at the lowest load rate (see blue lines in Fig. 2). The level of the bending load, for which the PSC signal begins to show an intense and continuous increase, irrespectively of the loading mode, is estimated to be at approximately 60% of the ultimate 3PB strength (L_f) (see Fig. 3), in all three experiments.

As a next step, it is interesting to consider the total electric charge (Q_T), released during the three experiments up to failure. The Q_T was calculated using the relation (t_f is the failure time).

$$Q_T = \int_0^{t_f} PSC(t)\,dt \tag{2}$$

It is worth mentioning that the total electric charge for the three different loading modes reaches almost the same value (see Tab. 1). In a previous work [13], during compressive stress application on marble specimens it was theoretically supported and experimentally proven [28] that the total electric charge value does not depend on the applied mechanical stress rate. This behavior is verified experimentally herein when cement mortar specimens are subjected to 3PB loading.

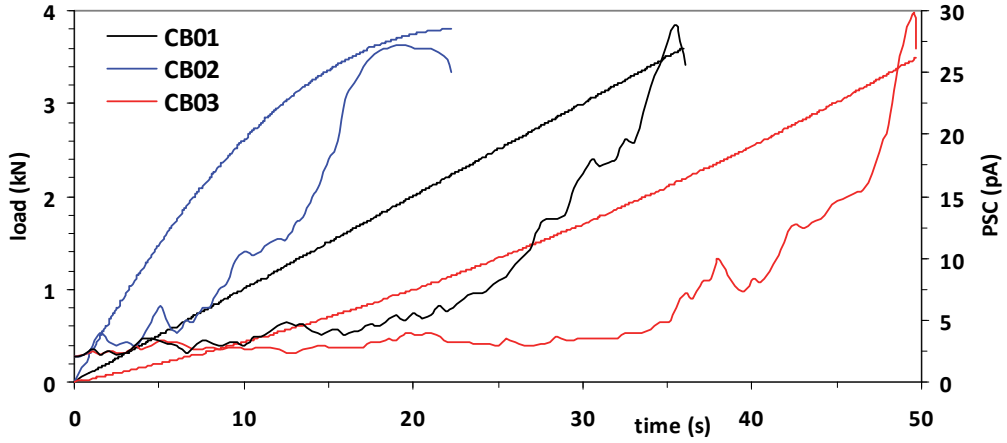

Figure 2: The time variation of the applied 3PB load and the corresponding time variation of the PSC, during all three experiments conducted.

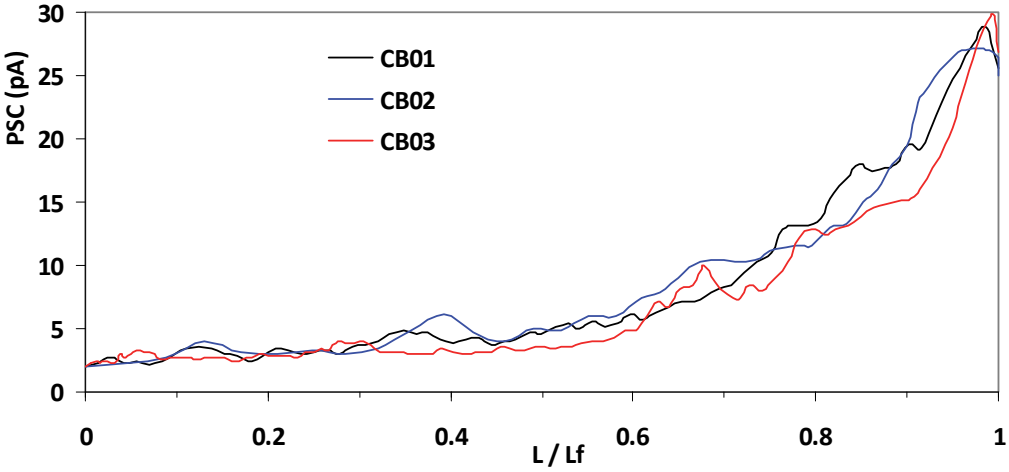

Figure 3: PSC versus normalized load (L/L_f) for all three experiments conducted.

Regarding the AE recordings, during the three experiments, a different number of AE hits was recorded (see Tab. 1). The micro-cracks generated during loading are of different sizes and therefore different AE amplitudes are recorded. A common way of obtaining quantitative information from the above statements is by computing the b-value of AE using the methods adopted in seismology [29, 30]. The b-value is defined as the log-linear slope of the frequency–magnitude distribution of AE [31]. In the present study, the b-values were calculated by applying a method that is known as improved b-value (I_b) analysis after Shiotani et al. [32]. The I_b-value is defined as:

$$I_b = \frac{\log N(\mu - \alpha_1\sigma) - \log N(\mu + \alpha_2\sigma)}{(\alpha_1 + \alpha_2)\cdot\sigma} \tag{3}$$

where, σ is the standard deviation of the magnitude distribution in one group of events, μ is the mean value of the magnitude distribution in the same group of events, and α_1 as well as α_2 are constants, for which usually a value equal to 1 is adopted [1].

In order to highlight the variability of the I_b-value, during the three experiments, the b-value analysis of AE is, in general, applied to a certain number of events, as follows: from event 1 to n, then from event 2 to n+1, and so on. The determination of the value of n has been considered by Shiotani et al. [32] and Colombo et al. [22], since it constitutes a parameter that can influence the results. A value exceeding n=50 is assumed to be a satisfactory one. In the present study, n=70 has been selected. Each value of I_b was calculated from a group of the events 1 to 70, consequently from 2 to 71, and so on. Each calculated I_b value is associated to the time of the 70th event of each group and to that of the corresponding value of normalized (L/L_f) load. The variability of the I_b-value during the three experiments with respect to the normalized (L/L_f) load is shown in Fig. 4. In the same figure the corresponding variation of PSC signals is also presented.

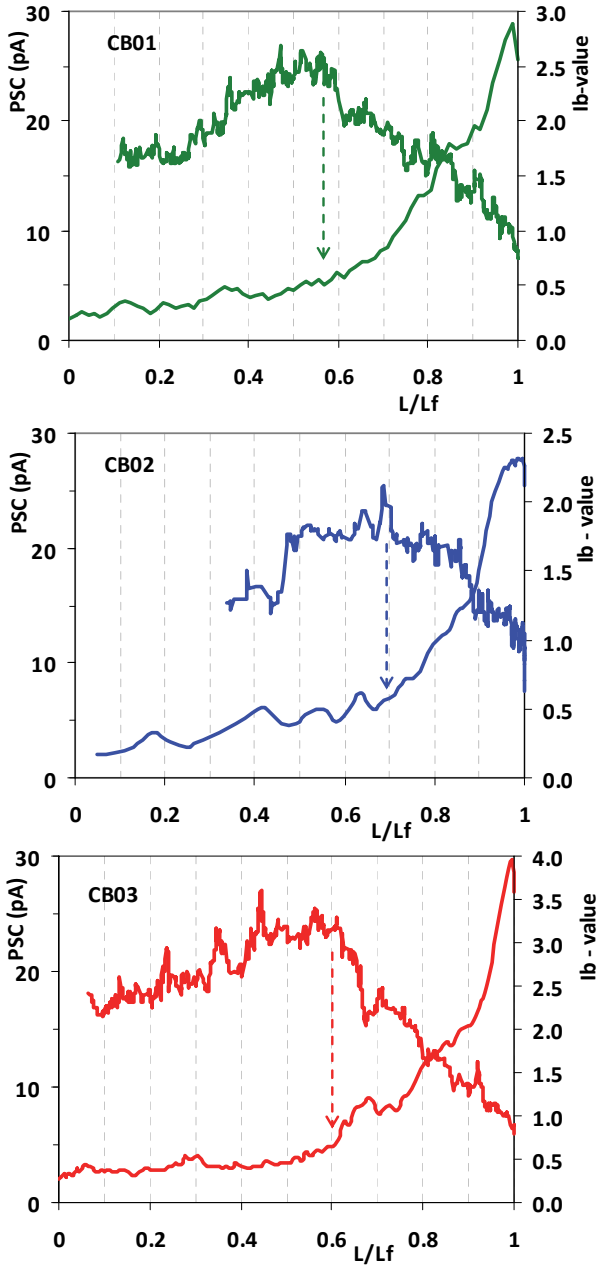

Figure 4: Variation of I_b-values and PSC signals vs. normalized load (L/L_f) for the three conducted experiments.

It is obvious that during the early stages ($L<0.6L_f$ approximately), the I_b-values show an almost constant increase indicating the prevalence of micro-cracking [33]. In these stages the PSC signal is low, showing a slight increase (see Fig. 4). Then, at the following stages ($L>0.6L_f$) I_b-values show an intense reduction combined with a sharp increase of the PSC. This behavioral change in the variability of the I_b-value is observed at a critical normalized load value $[L/L_f]_C \approx 0.6$, for all three experiments. As it is marked in Fig. 4 (dotted arrows), the exact value $[L/L_f]_C$ is 0.55, 0.62 and 0.70 for specimens CB01, CB02 and CB03, respectively. It seems that increasing the rate of the applied bending load the increase of the PSC signal and the corresponding reduction of I_b-values are recorded earlier. It should be pointed out that the I_b-value fluctuation, which is observed in all three experiments at the early stage, is related to the fact that the micro-cracks begin to form randomly. Moreover, in all three experiments, I_b attains values around 1 during the last seconds before the failure of the specimens, which is indicative of the final formation of a localized macro-crack.

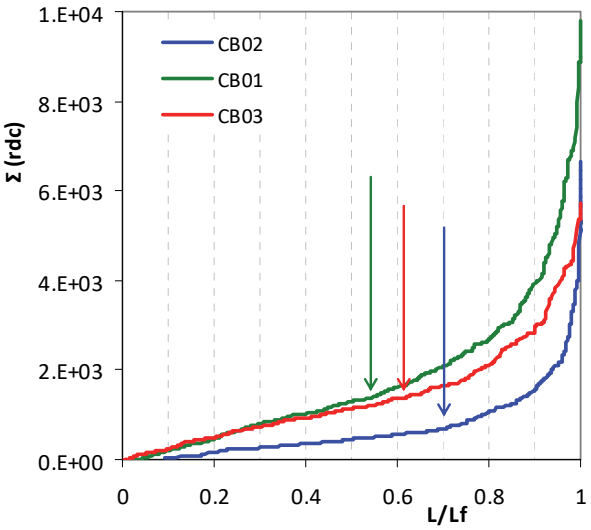

Figure 5: The cumulative ring down count of AE hits vs. normalized load (L/L_f) for the three conducted experiments.

The ring down count (rdc) data was also used, since it is a measure of the number of AE waveform oscillations through a preset voltage threshold [1]. In order to highlight the identification and assessment of important stages of micro-crack damage in a cement mortar material, a common practice has been followed to examine the cumulative ring down count Σ(rdc) and energy (ΣE). These results are illustrated in Figs. 5 and 6 with respect to the normalized load (L/L_f). In all three experiments an almost constant increase in Σ(rdc) was initially observed, related to the initiation of new micro-cracks. For $L/L_f > [L/L_f]_C$ the Σ(rdc) increases at a rate indicating the development of severe damage in the specimen. Concurrently, an abrupt increase of the PSC signal is observed.

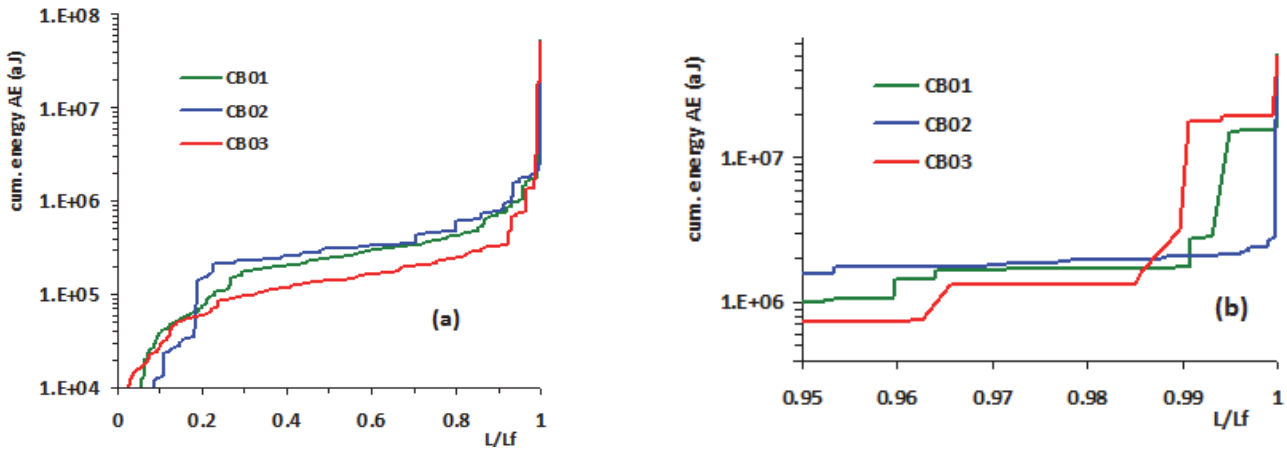

Figure 6: (a) The cumulative AE energy vs. normalized load (L/L_f) for the three experiments and (b) a detailed view close to the fracture load.

Finally, the cumulative energy of the AE hits up to the fracture of the specimens for all three experiments versus the normalized load level (L/L_f) is plotted in Fig. 6a. A significant step-up increase of the cumulative AE energy is observed slightly before the failure of the specimens (see the detailed view in Fig. 6b). The corresponding values of the cumulative energy practically start to converge (see Tab. 1).

CONCLUDING REMARKS

The application of 3PB loading under various protocols regarding the bending load rate on cement mortar beams causes the emission of electric currents (PSC) that show a clearly deterministic behavior. The total electric charge recorded during each experimental procedure is practically of similar value for all three experiments. It may be concluded that the corresponding behavior of the studied AE parameters is also similar.

Micro-cracks generate a sufficient number of weak acoustic emissions leading to a relatively high b-value. When increasing load levels, the fracture process moves from micro- to macro-cracking and the I_b-value decreases.

A distinct correlation between the PSC and the calculated I_b values is observed. Specifically, when I_b-values are relatively high and tend to increase, the PSC signals also exhibit a smooth increase. When I_b-values progressively decrease, the PSC signals show intense increase, indicating that PSC emissions are mainly attributed to crack formation and propagation. The peak of the PSC signals is another clear indication of the upcoming failure. Finally, the damage initiation is also verified by the study of the cumulative ring down count. The qualitative similarity of the results of the present protocol with recently published ones for natural stones and especially for Dionysos marble [17], which is the material extensively used for the restoration of marble monuments in Greece [34-38], supports further the potential use of the PSC technique for in-situ monitoring the response of restored structural elements of masterpieces of Cultural Heritage.

REFERENCES

[1] Rao, M.V.M.S., Lakschmi, P.K.J. Analysis of *b*-value and improved b-value of acoustic emissions accompanying rock fracture. Current Science, 89 (2005) 1577-1582.

[2] Aggelis D.G., Mpalaskas A.C., Matikas T.E., Investigation of different fracture modes in cement-based materials by acoustic emission, Cement and Concrete Research, 48 (2013) 1–8

[3] Stanchits, S., Dresen, G., Vinciguerra, S., Ultrasonic velocities, acoustic emission characteristics and crack damage of basalt and granite, Pure Applied Geophys,163 (2006) 5–6, 975–994

[4] Lockner, D., The role of acoustic emission in the study of rock fracture. Int. J. Rock Mech. Min. Sci. Geomech. Abstr., 30 (1993) 883–899.

[5] Stergiopoulos, C., Stavrakas, I., Hloupis, G., Hloupis, D., Triantis, Vallianatos, F., Electrical and acoustic emissions in cement mortar beams subjected to mechanical loading up to fracture, Engineering Failure Analysis, 35 (2013) 454-461.

[6] Stavrakas, I., Anastasiadis, C., Triantis, D., Vallianatos, F., Piezo Stimulated currents in marble samples: Precursory and concurrent – with – failure signals, Natural Hazards and Earth System Sciences, 3 (2003) 243-247.

[7] Vallianatos, F., Triantis, D., Tzanis, A., Anastasiadis, C., Stavrakas, I., Electric Earthquake Precursors: From Laboratory Results to Field Observations, Physics and Chemistry of the Earth, 29 (2004) 339-351.

[8] Varotsos, P.A., Sarlis, N.V., Skordas, E.S., Long-range correlations in the electric signals that precede rupture, Phys. Rev. E, 66 (2002) 011902.

[9] Cartwright-Taylor, A., Vallianatos, F., Sammonds, P., Superstatistical view of stress-induced electric current fluctuations in rocks, Physica A: Statistical Mechanics and its Applications, 414 (2014) 368–377.

[10] Frid, V., Goldbaum, J., Rabinovitch, A., Bahat, D., Electric polarization induced by mechanical loading of Solnhofen limestone, Phil. Mag. Lett., 89 (7) (2009) 453–463

[11] Varotsos, P.A., The Physics of Seismic Electric Signals, TerraPub (2005)

[12] Stavrakas, I., Triantis, D., Agioutantis, Z., Maurigiannakis, S., Saltas, V., Vallianatos, F., Pressure Stimulated Currents in rocks and their correlations with mechanical properties, Natural Hazards and Earth System Sciences, 4 (2004) 563-567.

[13] Triantis, D., Stavrakas, I., Anastasiadis, C., Kyriazopoulos, A., Vallianatos, F., An analysis of Pressure Stimulated Currents (PSC), in marble samples under mechanical stress, Physics and Chemistry of the Earth, 31 (2006) 234-239.

[14] Triantis, D., Anastasiadis, C., Vallianatos, F., Kyriazis, P., Nover, G., Electric signal emissions during repeated abrupt uniaxial compressional stress steps in amphibolite from KTB drilling, Natural Hazards & Earth System Sciences, 7 (2007) 149-154.
[15] Kyriazopoulos, A., Anastasiadis, C., Triantis, D., Brown, J. C, Non-destructive evaluation of cement-based materials from pressure-stimulated electrical emission - Preliminary results, Construction and Building Materials, 25 (2011) 1980-1990.
[16] Triantis, D., Stavrakas, I., Kyriazopoulos, A., Hloupis, G., Agioutantis, Z., Pressure Stimulated Electrical Emissions from cement mortar used as failure predictors, International Journal of Fracture, 175 (2012) 53-61.
[17] Stavrakas, I., Pasiou, E.D., Hloupis, G., Malliaros, G.-T., Triantis, D., Kourkoulis, S.K., Exploring the size effect of marble by combined use of Pressure Stimulated Currents and Acoustic Emission, in: Beskos D.E., Stavroulakis G.E. (Eds.), 10th HSTAM International Congress on Mechanics, Chania, Hellas, (2013) 185-186.
[18] Li, Z., Enyuan, W., Miao, H., Laboratory Studies of Electric Current Generated during Fracture of Coal and Rock in Rock Burst Coal Mine, Journal of Mining, 2015 (2015) ID 235636.
[19] Sun, M., Liu, Q., Li, Z., Wang, E. Electrical emission in mortar under low compressive loading. Cement and Concrete Research, 32 (2002) 47–50.
[20] Archer, J. W., Dobbs, M. R., Aydin, A., Reeves, H. J., & Prance, R. J., Measurement and correlation of acoustic emissions and pressure stimulated voltages in rock using an electric potential sensor. International Journal of Rock Mechanics and Mining Sciences, 89 (2016) 26-33.
[21] Dann, D., Demikhova, A., Fursa, T., Kuimova, M., Research of Electrical Response Communication Parameters on the Pulse Mechanical Impact with the Stress–Strain State of Concrete Under Uniaxial Compression, IOP Conf. Series: Materials Science and Engineering, 66 (2014) 012036. doi:10.1088/1757-899X/66/1/012036
[22] Colombo, S., Main, I., G., Forde, M. C., Assessing damage of Reinforced Concrete Beam using "*b*-value" Analysis of Acoustic Emission signals. J. Mat. Civil Eng. (ASCE), 15 (2003) 280-286.
[23] Vidya Sagar, R., Prasad, RV., Raghu Prasad, B.K., Rao, M.V.M.S., Microcracking and fracture process in cement mortar and concrete: a comparative study using acoustic emission technique. Experimental Mechanics, 53 (2013) 1161–1175.
[24] Vidya Sagar, R., Raghu Prasad, B.K., Shantha Kumar, S., An experimental study on cracking evolution in concrete and cement mortar by the b-value analysis of acoustic emission technique, Cement and Concrete Research, 42 (2012) 1094-1104.
[25] Stergiopoulos, C., Stavrakas, I., Hloupis, G., Triantis, D., Vallianatos, F., Electrical and acoustic emissions in cement mortar beams subjected to mechanical loading up to fracture, Engineering Failure Analysis, 35 (2013) 454–461.
[26] Anastasiadis, C., Stavrakas, I., Triantis, D., Vallianatos, F., Correlation of pressure stimulated currents in rocks with the damage variable, Annals of Geophysics, 50 (2007) 1-6.
[27] Vallianatos, F., Triantis, D., Scaling in Pressure Stimulated Currents related with Rock Fracture, Physica A, 387 (2008) 4940-4946.
[28] Triantis, D., Anastasiadis, C., Stavrakas, I., The correlation of electric charge with strain on stressed rock samples, Natural Hazards and Earth System Sciences, 8 (2006) 1243-1248.
[29] Scholz, C. H., The frequency–magnitude relation of microcracking in rock and its relation to earthquakes. Bull. Seis. Soc. Am., 58 **(**1968) 399–415.
[30] Aki, K., Maximum likelihood estimates of *b* in the formula log*N* = *a* – *bm* and its confidence limits. Bull. Earthquake Res. Inst., Tokyo Univ., 43 **(**1965) 237–239.
[31] Main, I. G., Meredith, P. G. and Jones, C., A reinterpretation of the precursory seismic *b*-value anomaly from fracture mechanics. Geophys. J., 96 (1989) 131–138.
[32] Shiotani, T., Yuyama S., Li, Z. W., Ohtsu, M. Application of the AE improved b-value to qualitative evaluation of fracture process in concrete materials, J. Acoust. Emission, 19 (2001) 118–132.
[33] Rouchier, S., Foray, G., Godin, N., Woloszyn, M., Roux, J.-J. Damage monitoring in fibre reinforced mortar by combined digital image correlation and acoustic emission, Construction and Building Materials, 38 (2012) 371-380.
[34] Kourkoulis, S.K., Ganniari-Papageorgiou, E., Mentzini, M., Dionysos marble under bending: A contribution towards understanding the fracture of the Parthenon architraves, Engineering Geology, 115 (3-4) (2010) 246-256.
[35] Kourkoulis, S.K., Prassianakis, I., Agioutantis, Z., Exadaktylos, G.E., Reliability assessment of the NDT results for the internal damage of marble specimens, International Journal of Material and Product Technology, 26(1/2) (2006) 35-56.
[36] Kourkoulis, S.K., Exadaktylos, G.E., Vardoulakis I., U-notched Dionysos-Pentelicon marble in three point bending: The effect of nonlinearity, anisotropy and microstructure, International Journal of Fracture, 98(3-4) (1999) 369-392.

[37] Exadaktylos, G.E., Vardoulakis, I., Kourkoulis S.K., Influence of nonlinearity and double elasticity on flexure of rock beams – II. Characterization of Dionysos marble, International Journal of Solids and Structures, 38(22-23) (2001) 4119-4145.
[38] Kourkoulis, S.K., Pasiou, E.D., Interconnected epistyles of marble monuments under axial loads', International Journal of Architectural Heritage, 9(3) (2015) 177–194.

Strain monitoring of cement-based materials with embedded polyvinyl alcohol - carbon nanotube (PVA-CNT) fibers

Zoi S. Metaxa
National Technical University of Athens, Laboratory of Strength and Materials, 9 Heroes Polytechnion Str., 15780 Athens, Greece

Wilfrid Neri, Philippe Poulin
University of Bordeaux, Centre de Recherche Paul Pascal – CNRS, Avenue Schweitzer, 33600 Pessac, France

Nikolaos D. Alexopoulos
University of the Aegean, Department of Financial Engineering, 821 00 Chios, Greece
nalexop@aegean.gr

ABSTRACT. This article investigates the possibility of exploiting innovative polyvinyl alcohol fibers reinforced with carbon nanotubes (PVA-CNT fiber) as a strain sensor in cement mortars used in the restoration of Cultural Heritage Monuments. Two types of PVA-CNT fibers were embedded in the matrix at a short distance from the bottom of the beam and their readings were correlated with traditional sensors, e.g. strain gauges and Fiber Optic Bragg Gratings. The Electrical Resistance Change (ERC) of the embedded PVA-CNT fiber was in-situ monitored during four-point bending mechanical tests. For the case of coated PVA-CNT fiber, a linear correlation of the applied strain at the bottom surface of the specimen along with ERC values of the fiber was noticed for the low strain regime. For the case of incremental increasing loading – unloading loops, the coated and annealed PVA-CNT fiber gave the best results either as embedded or as 'surface attached' sensor that exhibited linear correlation of ERC with applied strain for the low applied strain regime as well as hysteresis loops during unloading. The article discusses their high potential to be exploited as strain/damage sensor in applications of civil engineering as well as in restoration of Monuments of Cultural Heritage.

KEYWORDS. Cement-based materials; Sensing; FOBGs; Monitoring.

Citation: Metaxa, Z.S., Neri, W., Poulin, P., Alexopoulos, N.D., Strain monitoring of cement-based materials with embedded polyvinyl alcohol - carbon nanotube (PVA-CNT) fibers, Frattura ed Integrità Strutturale, 40 (2017) 61-73.

Received: 19.01.2017
Accepted: 10.03.2017
Published: 01.04.2017

INTRODUCTION

The ad-hoc accurate and thorough knowledge of the mechanical behaviour of building materials used in the restoration of Cultural Heritage Monuments is fundamental for the protection of their structural integrity. However, most of the traditional techniques used in the laboratory and in the field, such as strain-gauges, dial-gauges, extensometers, and Linear Variable Differential Transformers (LVDTs), provide data drawn from the materials' external surface. Therefore, gathering information about the internal events, for example local failures and micro-fracture, which precede those detected on the materials' surface, is challenging. The technological need to mine data from the interior of the restored joints and specimens were reported by Kourkoulis et al [1]. In a series of articles, e.g. [2-4] the important role of the interphases of the connecting materials used in the interior of the restored joints are noted. Additionally, several researchers underlined the important aspects of straining of the connecting members of the joint that are well in the interior of the restored Monument of Cultural Heritage, e.g. [5-7]. To cope with this problem, innovative measuring techniques should be used in parallel with the traditional ones for calibrating purposes.

An already mature technique for damage monitoring of cement-based materials is the embedded glass fiber optical sensors. In the areas of local strain change, loss of the transmitted light signal [8] occurs that corresponds to damage within the monitoring region [9]. The detection can be performed with small embedded Bragg grating sensors with nominal diameter of approximate 120 μm, e.g. [10-12]. Nevertheless, this technique has several limitations, e.g. monitoring of the matrix transverse cracking. In addition, a dense network of optical fibers would be needed to fully monitor the complete structure that is economically not sustainable.

Acoustic emission is another technique to monitor damage development in cement-based materials. Initiation of damage mechanisms (tension or shear) induce different crack tip motions, resulting in quite different AE characteristics. These distinct acoustic events can therefore be directly linked to a specific type of failure or can be evaluated in a cumulative manner to characterize the state of damage of the matrix, e.g. [13, 14]. Despite the numerous articles in this scientific field, the provided AE data are usually not sufficient to solely characterize the structural health of the matrix and another technique is required to cross-plot the necessary information [15, 16].

In this study, the exploitation of different types of advanced fibers made from polyvinyl alcohol (PVA) reinforced with carbon nanotubes (CNTs) for sensing the mechanical performance of the cement mortar used for the restoration of Acropolis' Parthenon will be investigated. These new innovative PVA-CNT fibers have small dimensions (d = 40 to 60 μm) and exhibit excellent piezoresistive characteristics and ductility that exceeds 100 % elongation [17]. Manufacturing of the specific fibers can be done by a potentially scalable process already reported [18]. Previous research on epoxy resin composites reinforced with glass fibers showed that the aforementioned PVA-CNT microfibers can be successfully embedded in the composite [19] and can be used for strain/damage monitoring purposes of non-conductive composites under tensile and bending loading tests [20, 21].

EXPERIMENTAL PROCEDURE

Manufacturing of prismatic cement mortar specimens

White cement, Portland type, with the code name AALBORG WHITE and class CEM I 52,5R was used in the present study. The specific cement is manufactured from exceptional pure limestone and fine-grain quartz sand. The mineralogical phases of the white cement used as well as several characteristics of the cement can be seen in Tabs. 1 and 2, respectively. Two different sand types were used: (a) coarse grained quartz sand from 1 to 2 mm as well as (b) fine-grain quartz sand M32 with average grain size of 260 mm. The selection of the above materials has been performed according to several criteria, extensively discussed in [4].

C3S	C2S	C3A	C4AF
77 (wt%)	16 (wt%)	5 (wt%)	1 (wt%)

Table 1: Mineralogical phases of white cement.

In the present work, the following kinds of sensors were used: (a) 2 different types of CNT reinforced PVA fibers (PVA-CNT fibers). The first type will be called in the following as "coated PVA-CNT" fiber, while the second one as "coated and annealed PVA-CNT" fiber, that had different process parameters as discussed in the following. This kind of sensors

utilizes the electrical resistance change method for the damaged areas of the matrix. The second type of sensor used was (b) Fiber Optical Bragg Gratings (FOBG) in order to detect damage on the surrounding medium through the transmission of light within the fiber.

Density (kg/m^3)	3130
Phenomenological density (kg/m^3)	1100
Curing time of cement according EN 196-3	120 min

Table 2: Physical characteristics of white cement.

The PVA-CNT fibers were fabricated at the facilities of University of Bordeaux (CNRS-CRPP). Multi-wall carbon nanotubes (MWCNTs) with 98 % purity were used from Arkema, Lacq in Aquitaine province of France. Typical the fibers have a concentration of approximate 13 wt% MWCNTs. For specific applications, the manufactured fibers can be coated with MWCNTs in order to increase their surface conductivity [18]. In the present case, the coated PVA-CNT fibers had been coated with an immersion technique in an aqueous solution with dispersed MWCNTs. The solution contained 0.5 wt% MWCNTs and 0.7 wt% SDS; the latter is a common surfactant, widely used to stabilize MWCNTs in aqueous solutions. The fibers were dried before use and several images (macro photos as well as cross-sectional) can be seen in [19].
The coated and annealed PVA-CNT fibers were also coated fibers according to the already described procedure that had an additional heat treatment stage. The annealing of the polymer (approximately around 150 ^{o}C) well above the glass temperature transition (T_g) temperature, makes the polymer softer, thus enabling the more efficient attachment of the MWCNTs on the surface of the fiber. Additionally, it improves the crystallinity as well as the mechanical properties of the manufactured fibers.
Two types of cement-based prismatic specimens were manufactured: Type I specimen deals with sensors that were embedded during manufacturing. Type II deals with surface-attached sensors; they were attached on the specimens when the curing process of the cement-based specimens ended and just before mechanical testing.
The same mixing procedure was followed for all the cement-based specimens according to ASTM C305 [22]. Mixing was performed using a standard 5 l mixer made from TECHNOTEST®. Initially, cement and water were placed into the mixing bowl. Mixing started immediately at a slow speed of (140 ± 5 r/min) and lasted for 30 s. Following, both types of sand (course and fine), that were premixed, were slowly added to the paste over a 30 s period, while mixing at slow speed. Next, the materials were mixed for 30 s at medium speed (285 ± 10 r/min). The mixer was stopped for 90 s to let the mortar stand, during the first 30 s of this interval; any mortar that had collected on the side of the bowl was scraped down into the batch. To certify the homogeneity of the mortar, as a final step, the materials were mixed at medium speed for 90 s.

(a) (b)

Figure 1: (a) Mold for the manufacturing of the prismatic specimens with already installed PVA-CNT fiber and specific oil and (b) casted mixture in the mold for two specimen's preparation.

Customized prismatic molds made from aluminum having a length of 80 mm and a cross-section of 20 mm × 20 mm, were used. Very thin holes of approximately 1 mm dimeter, suitable for the placement of PVA-CNT fibers / FOBGs, were drilled at both sides of the molds. Before casting, suitable concrete demolding oil was used to facilitate the specimens' removal. Then the fibers were placed in the molds as shown in Fig. 1a and casting was performed (Fig. 1b).
Immediately after casting, the specimens were covered with plastic wrap and were left to cure for 24 h at room temperature. After demolding, the saturated wet covering method was adopted for further curing of the samples. This was to make sure that specimens were kept in a wet condition during the curing period without damaging/affecting the fibers. The specimens were covered with wet cloths (water saturated with calcium hydroxide) and were sealed with plastic wrap.

According to Nahata et al. [23] mortars cured using the aforementioned procedure demonstrate a slightly lower compressive strength compared to specimens cured in water immersion (specimens cured in water tank at room temperature) demonstrating that the curing procedure adopted in this study does not compromise the mechanical performance of the material. At the age of 28 days the specimens with the embedded sensors were uncovered and were ready for mechanical testing (Fig. 2a and b), while for several specimens the sensor was externally attached (Fig. 2c) before testing.

Mechanical testing

For the execution of the mechanical tests, a number of experimental devices were used (Fig. 3) that will be explained in the following. An MTS Insight loading frame was used to record the changes in crosshead displacement and mechanical load, a multimeter for the electrical resistance of the embedded PVA-CNT fiber, an interrogator for the respective measurements of the FOBG sensor and finally a data logger for the measurements of the strain gauges.

(a) (b) (c)

Figure 2: (a) Prismatic specimen with embedded PVA – CNT fiber (Type I), (b) specimen with embedded PVA – CNT fiber and FOBG fiber and (c) specimen with externally attached PVA – CNT fiber (Type II).

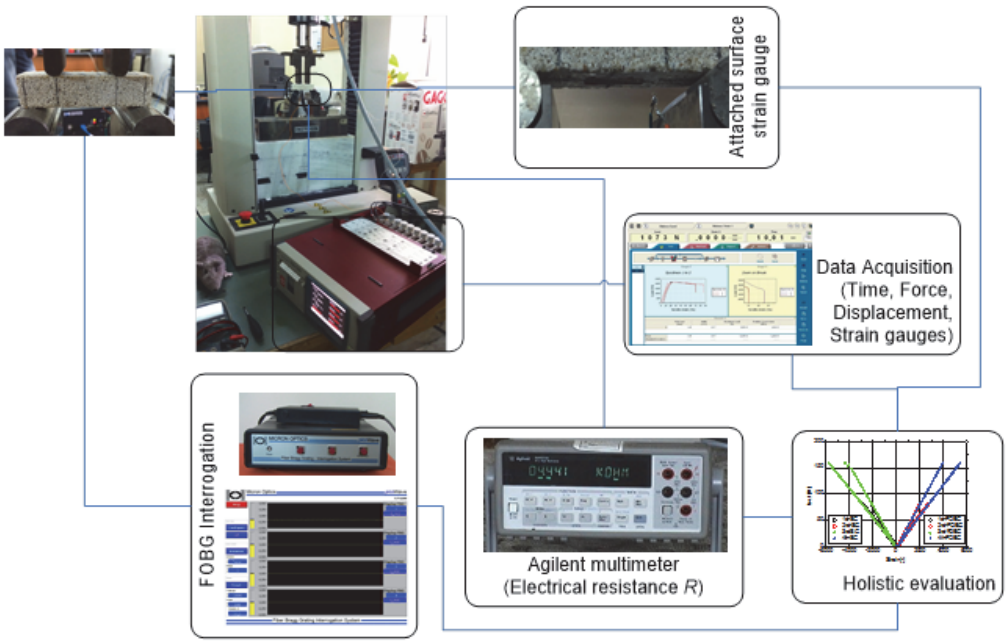

Figure 3: Flow diagram of the experimental procedure.

Two types of prismatic specimens were evaluated. The first one (Type I) has embedded sensors and the second one (Type II) has surface attached sensors. The geometrical dimensions of all specimens can be seen in Fig. 4a (Type I specimen is shown), while the loading supports (four point bending) can be seen in Fig. 4b. The three-point bending tests had been performed on specimens with embedded PVA-CNT fiber on the tensile region (fiber close on bottom surface of the specimen). The correctly adjusted / placed specimen at the jigs of the testing machine can be seen in Fig. 5a, where surface-attached strain gauges were also used to monitor the strain changes at the bottom surface of the prismatic specimens (Fig. 5b). As the incremental loading steps have been made to specific levels of fracture stress of the material,

the testing machine was load-controlled with a crosshead speed of 0.1 mm/min. Evaluation of the four point bending (4pb) mechanical tests have been performed according to ASTM D6272 [24]. During testing, crosshead displacement, load and the strain gauges measurements were continuously recorded and stored in a P/C.
An Agilent multimeter was used to record in situ the electrical resistance data of the specimen's embedded PVA-CNT fiber during mechanical loading. A DC voltage of 10 V was applied to cables connected to the PVA-CNT fiber of the specimens (Fig. 3), the current was measured and the resistance was calculated from these values. The resistance measurements were performed in a two-point measurement set-up in the longitudinal direction. Data acquisition of 1 Hz was also used for the resistance measurements and stored simultaneously in the P/C of the testing machine. Electrical resistance change (ERC) values were post-calculated form the initial resistance values.
The optical fiber sensors used were Bragg gratings of 2 mm nominal length. The reflectivity of these sensors was of the order of 20 %, in order to ensure adequate spectrum reflection and at least 50 cm of free optical fiber should be available at each side for adaptation of connectors. Selected center wavelength was 1540 ± 1 nm, while $\Delta\lambda$ was approximate ~ 0.7 nm. An interrogation system was used to measure the wavelength changes due to the mechanical field loading and evaluate the equivalent strain values. The wavelength data were afterwards converted to axial strains measured in the vicinity of the Bragg grating sensors, based on the fundamental equation for constant temperature for mechanically and optically isotropic optical fibers:

$$\Delta\lambda_B = \lambda_B \cdot (1-\rho_a) \cdot \Delta\varepsilon + \lambda_B \cdot (\alpha+\xi) \cdot \Delta T \quad (1)$$

that relates the wavelength changes to the axial strain of the fiber at the sensor area through the sensitivity coefficient λ_B. Term $\Delta\lambda_B$ is the change in Bragg wavelength, ρ_α, a and ξ are respectively the photoelastic, thermal expansion and thermo-optic coefficients of the fibre, $\Delta\varepsilon$ is the strain and ΔT is the temperature change, respectively. In the present work, λ_B was measured via calibration and for the specific sensor it was found to be equal to 0.89 με / pm or inversely 1.12 pm / με. Using Eq. (1), all wavelength shifts were collected from the interrogator device and the respected axial strains were calculated.

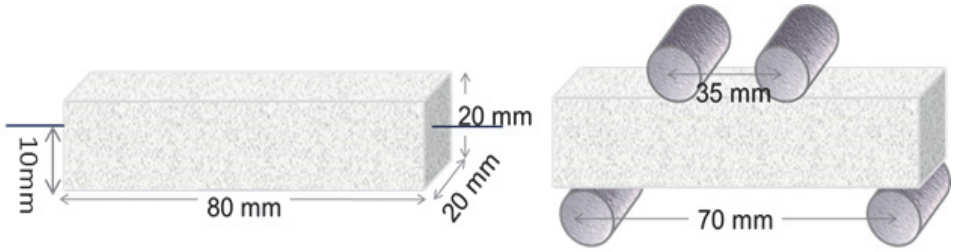

(a) (b)

Figure 4: Sketch of the (a) geometrical dimensions and (b) testing supports of the specimen.

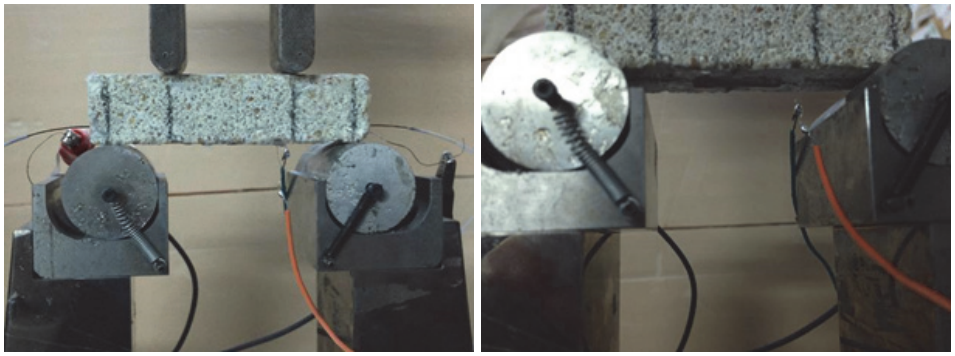

(a) (b)

Figure 5: (a) Installed specimen with embedded PVA-CNT fiber and (b) magnification of the bottom side of the specimen with surface attached strain gauge.

For the Type I specimens (with embedded sensors), the following tests have been performed: (a) monotonic loading till fracture and (b) incrementally increasing loadings - unloadings till fracture. For the Type II specimens (with attached

sensors) constant amplitude loadings - unloadings have been performed to assess the screening of the sensors. In total 11 different test categories were performed that can be seen in Tab. 3.

	Reference	Coated PVA-CNT fiber	Coated and annealed PVA-CNT fiber
(-)	P	-	-
Attached surface strain gauge	P	M, P	M, P
FOBG and attached surface strain gauge	M, P	P	P

NOMENCLATURE: M: Monotonic four point bending (4pb) till fracture
P: Progressive damage accumulation in 4pb (incremental loading-unloadings till fracture)

Table 3: List of the experimental tests.

RESULTS AND DISCUSSION

The experimental bending test results will be presented and discussed in this section in order to establish a useful correlation of the readings of the embedded / attached sensors with the mechanical deformation of the specimen.

Monotonic bending tests

Monotonic tests have been performed on different specimens for the three investigated embedded sensors, (a) coated PVA-CNT fiber, (b) coated and annealed PVA-CNT fiber and (c) FOBG. Fig. 6 shows the comparison of the mechanical response of the each specimen during four-point bending testing. The specimens with the embedded PVA-CNT fiber seem to resolve identical maximum stress values along with axial deformation at the bottom level of the specimen. All four different cases seem to have approximately the same mechanical response and the average fracture stress is around 3 MPa.

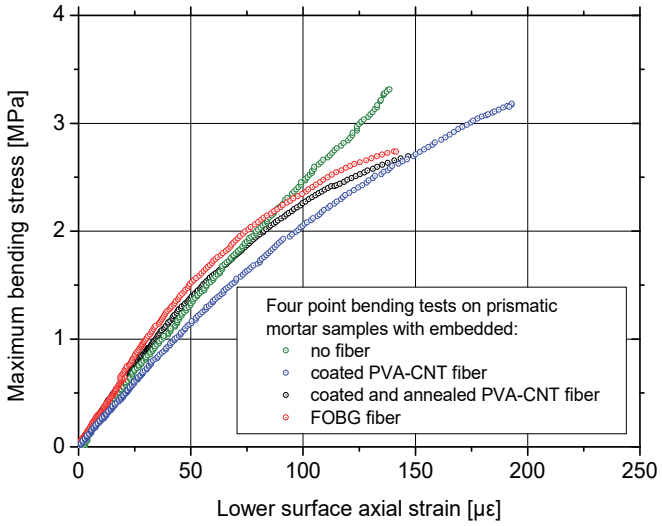

Figure 6: Comparison of the monotonic mechanical response of the specimens with embedded sensors.

Fig. 7 shows the mechanical response of the material along with the simultaneous electrical resistance response of the embedded PVA-CNT fiber for the monotonic loading of the specimen till the macroscopic fracture. Fig. 7a corresponds to the coated PVA-CNT fiber, while the respective results of the coated and annealed PVA-CNT fiber can be seen in Fig. 7b. By comparing the two diagrams, it can be clearly seen that linearity is evident in both types of fibers for the low applied loadings that corresponds to the elastic loading regime. This linearity is no longer evident with increasing the applied bending stresses. Additionally, for the case of the coated PVA-CNT fiber this linear stage ends at higher ERC values that allows for better screening of the results. This loss in linearity is probably due to the partial fracture of the

interphase between the embedded fiber and surrounding matrix [19] that gives a sudden drop in ERC values as the fiber is partially unloaded. This pattern of sudden drops in ERC values can be noticed for even higher stress level and can be additionally due to micro-cracking [20] that approximately starts at the 30 % of the maximum bending stress (around 1 MPa) and fracture for higher applied stresses.

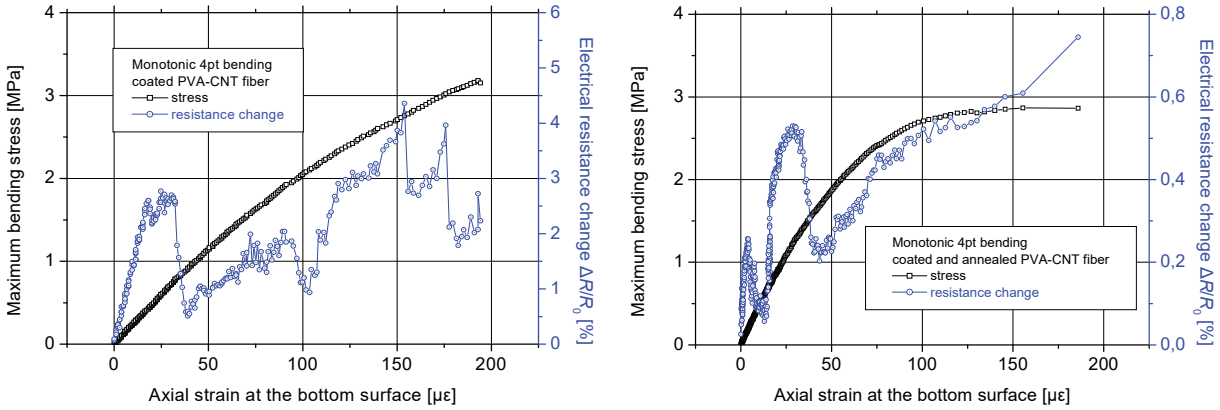

Figure 7: (a) Mechanical response of the prismatic specimens and electrical resistance response of the different embedded PVA-CNT fiber type (a) coated and (b) coated and annealed.

Constant amplitude loading - unloading loops

The test results for the constant amplitude tests will be described in this section. Ten (10) loading – unloading loops were performed with maximum bending load being 80 N that corresponds to approximately 0.5 MPa that is definitely within the elastic loading regime without the presence of micro-cracking. Fig. 8 shows the mechanical response of the type I specimen (stress in red color while strain in black color) as well as the ERC values of the embedded fiber (in blue color) over testing time. Despite the low maximum loading stress, residual strain values can be noticed after several cycles that can be attributed to developed damage inside the specimen. The strain loops seems to take low amplitude values; after the tenth loading loop strain amplitude goes from 1 to 2.5 % axial strain that is almost half when compared with the first loading loop. ERC values show increased scatter values that might be a problem of the high sampling frequency. The peak and valleys of the ERC values can be hardly distinguished in the diagram; however, the trend shows that ERC is continuously increasing with the constant amplitude loadings. Such a trend was also noticed for the case of monitoring glass fiber reinforced plastic with embedded PVA-CNT fiber and ERC was directly compared with the residual strain of the composites that is clearly evidence of induced damage in the matrix of the material [20]. This is obviously the case with the existing test results.

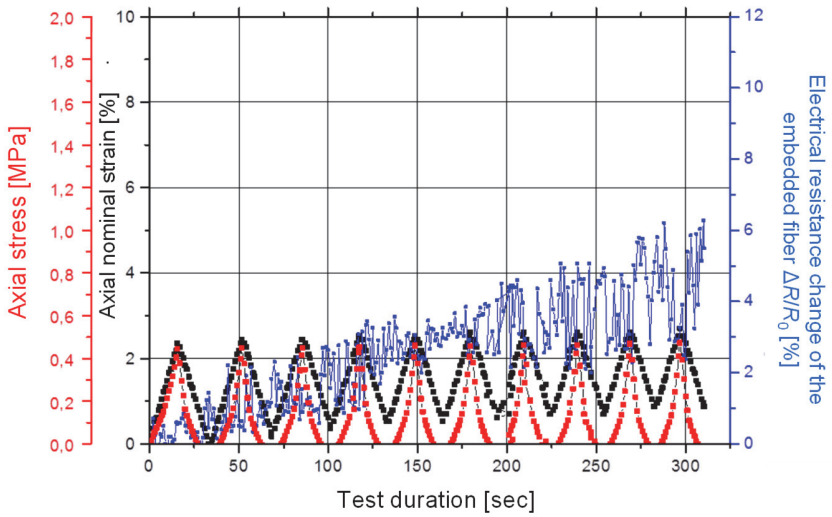

Figure 8: Mechanical response of the type I specimen with embedded coated PVA-CNT fiber under constant amplitude loading – unloading loops and electrical response of the embedded fiber.

Fig. 9 shows the respective test results for the type II specimen with the surface attached fiber. Strain measurements also show a small reduction on the amplitude after some test cycles; ERC measurements seems to be vague and definitely lower sampling rate should have been used. Though the surface-attached fiber gives readings during mechanical testing, optimization will be performed in the near future regarding the preparation of the surface, medium for the proper attachment of the fiber [19], as several vague recordings might be due to local loss of coherency of the interphase of the connecting medium (glue) with the substrate and therefore loading transfer of the specimen to the sensor is not optimal.

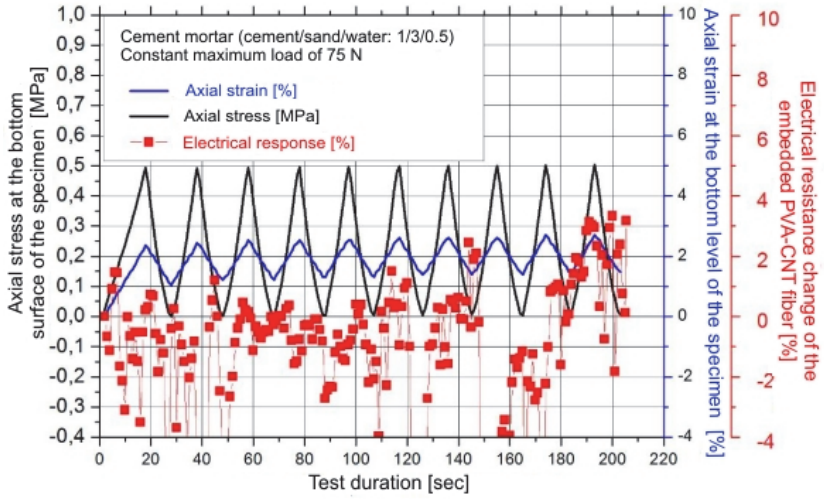

Figure 9: Mechanical response of the Type II specimen with surface attached coated PVA-CNT fiber under constant amplitude loading – unloading loops and electrical response of the attached fiber.

Incrementally increasing loading - unloading loops

In this section the test results of continuous increasing loading – unloading loops will be reported. Tests were performed with continuous increasing maximum load of 40 N after every unloading and hereafter will be called as progressive damage accumulation tests. Typical applied bending force protocol over testing time can be seen in Fig. 10a, while Fig. 10b shows the typical mechanical response (stress-strain) of a specimen for the fourteen cycles till fracture. Residual strain values are noticed every single unloading and the higher the loading value is, the higher the residual axial strain is. Additionally, hysteresis loops are evident for the latest loading cycles.

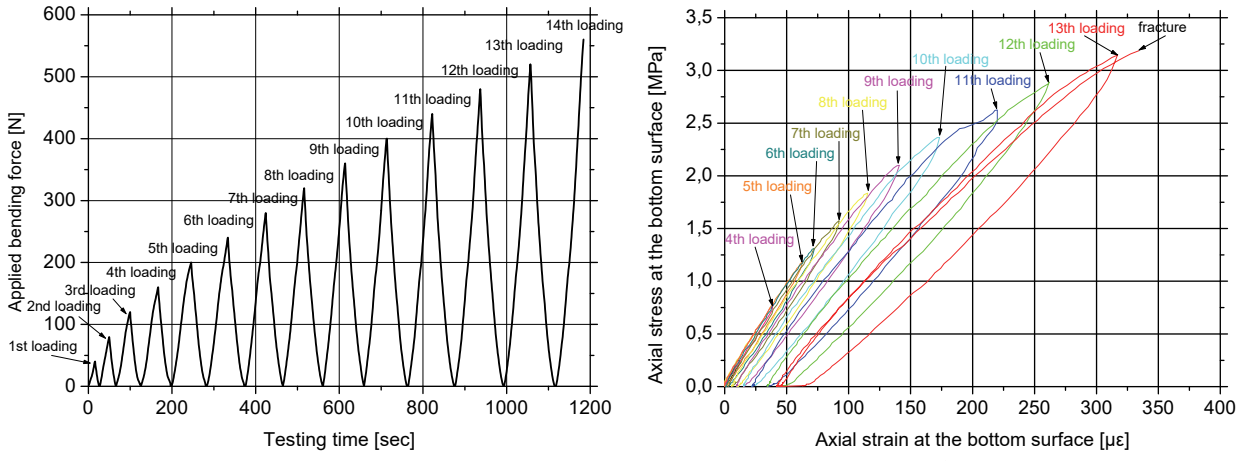

(a) (b)

Figure 10: (a) Applied increasing loading – unloading protocol and (b) mechanical response per different loading loop under four point bending test.

Fig. 11 shows the comparison of the mechanical response from readings of the embedded FOBG (red curves) as well as form the attached surface strain gauge (black curves). For the extremely low loading values (Figs. 11a to c), actually no

discrepancies are noticed when compared the embedded sensor with the traditional, attached strain gauge. With increasing loading loop (Figs. 11d and e), higher discrepancy between the two types of sensors is observed. Similar results were noticed for the same fibers embedded in GFRP under bending loads [20]. Finally, loss in contact of transmitted light was observed in loading branch of the ninth loop (Fig. 11f) and the recording phase of FOBG was terminated after this loop.

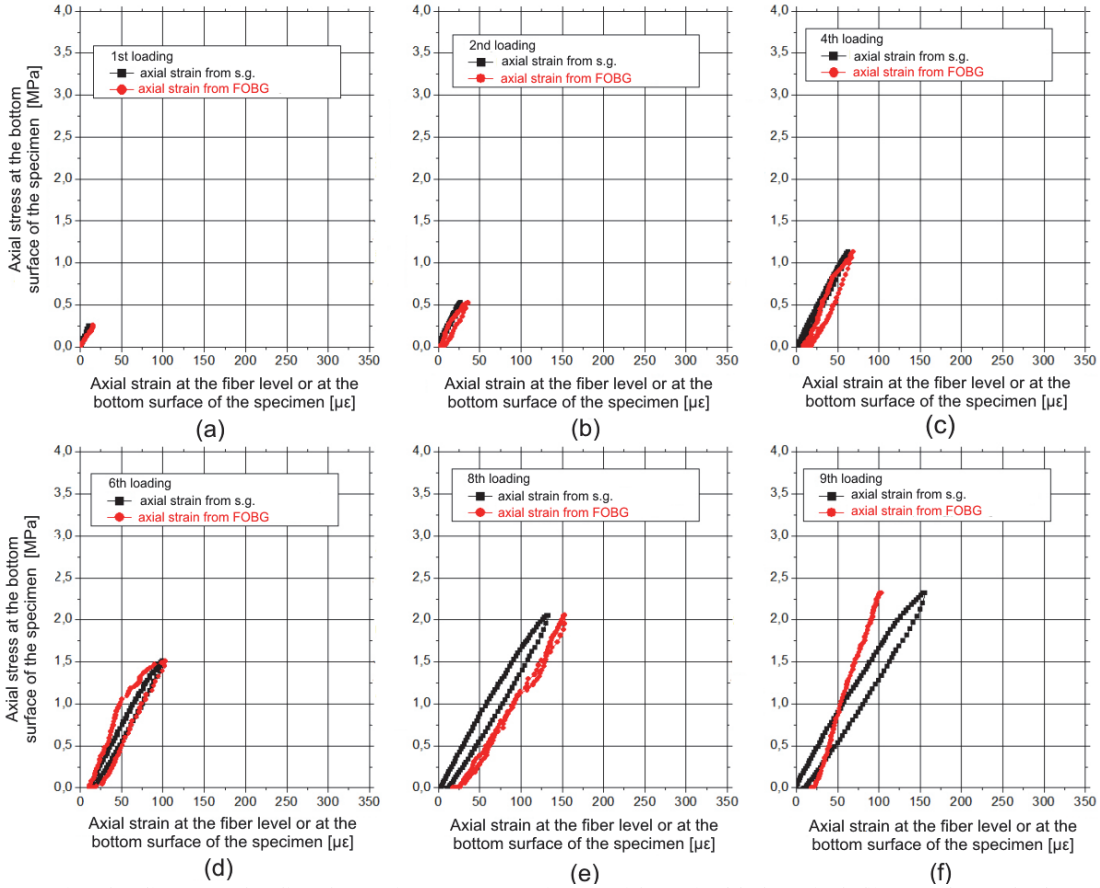

Figure 11: Increasing loading – unloading loops in type I specimen with embedded optical fiber and attached strain gauge for maximum loadings up to: (a) 40 N, (b) 80 N, (c) 160 N, (d) 240 N, (e) 320 N and (f) 360 N.

The same experimental protocol was applied on prismatic cementitious specimens with embedded coated PVA-CNT fiber as well as coated and annealed PVA-CNT fiber, where the test results can be seen in Figs. 12 and 13, respectively. For the case of the embedded coated PVA-CNT fiber, Fig. 12 shows the mechanical response (black curves) as well as the ERC response of the embedded fiber. Regarding the mechanical response of the specimen, it is evident that a linear correlation between stress–strain is observed up till maximum load up till 200 N (Figs. 12a to c). This is actually the elastic limit of the prismatic specimen under bending loads as for increasing applied load (Fig. 12d) hysteresis loop is formulated during unloading branch. Hysteresis loop is even higher noticeable at higher load (Fig. 12e) and finally fracture occurs at 520 N applied load (Fig. 12f). Hysteresis loops are evidence of inelastic mechanical response of the specimen and damage in the matrix (probably matrix cracking) of the specimen. On the contrary, the ERC readings of the embedded fiber seems not to follow the applied loading protocol, losing cohesion with the applied stress / strain variance with the very start mechanical response. This might be due to the insufficient bonding of the fiber with the surrounding matrix [21], as previously documented with the respective monotonic tests. Bonding loss of the specific interphase is probably the best answer to explain the inaccurate ERC values at high applied stress / strain levels.

Fig. 13 shows the respective results of the embedded coated and annealed PVA-CNT fiber in the prismatic specimen under the same experimental loading protocol. Similar to the previous fiber, ERC measurements trend is also noticed for this case. Linearity between stress-strain is noticed for the low applied loadings, while hysteresis loops till fracture is evident as also noticed in [20]. Regarding the ERC measurements, this type of fiber seems to be more promising as it gives not ambiguous, scattered data as noticed for the previous type of fiber. Coated and annealed PVA-CNT fiber gives a linear increase in ERC with the increased stress / strain for the low loading range; loss in coherency for higher applied

loads gives measurements that can be hardly be quantified and processed. To this end, this fiber seems to be more favorable for future research in case that proper interphase will be created with the surrounding matrix.

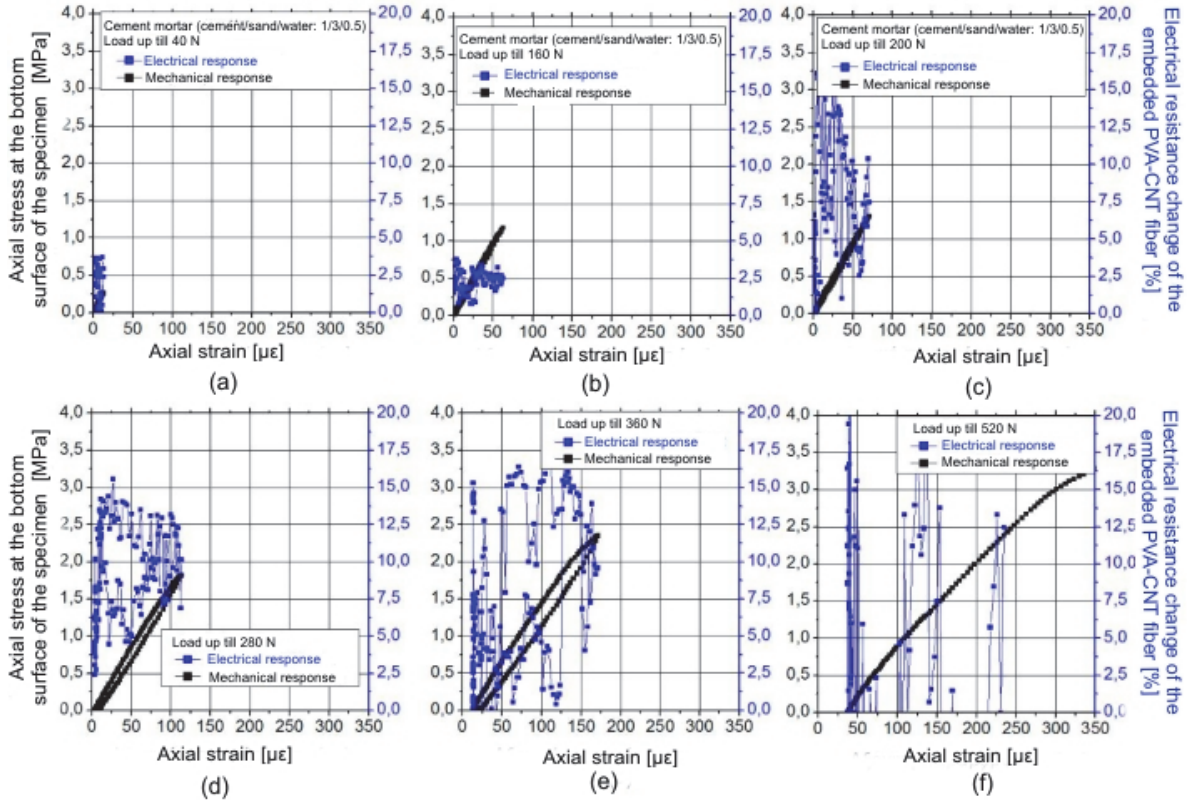

Figure 12: Incremental loading – unloading loops in type I specimen with embedded coated PVA-CNT fiber for applied loadings up till: (a) 40 N, (b) 160 N, (c) 200N, (d) 280 N, (e) 360 N and (f) 520 N (fracture).

Fig. 14 shows the respective test results for the type II specimen with the surface attached fiber. Test results are more encouraging when compared with the respective constant amplitude results, as the screening of the ERC measurements is evident. Linearity between strain and ERC measurements can be justified for low strain values, while hysteresis loops are formed when unloading the specimens, e.g. [20, 21]. Definitely this kind of fiber can be used for sensing applications, provided that optimization on the attaching procedure and loading transfer methodology should be applied.

CONCLUSIONS

- An experimental work has been performed to successfully accomplish the embedding procedure of the sensing fiber without damaging the sensor or the hosting medium.
- Monotonic bending tests with in-situ electrical resistance change of the embedded fiber showed encouraging results. Linearity between bending strain at the bottom of the specimen and electrical resistance change of the embedded fiber for the low applied loading regime was evident. For higher applied monotonic stress, a sudden drop in ERC was noticed that was attributed to the loss of the interphase between the fiber and the specimen as well as micro-cracking formation at the sequence of the test up till fracture.
- The embedded coated PVA-CNT fiber gave satisfactory results on the monotonic bending tests when compared against the coated and annealed PVA-CNT fiber. It enabled the linearity between applied strain and ERC at the low loading regime and generally gave higher ERC values when mechanically stressed that enables for the better screening of the test results.
- For the case of constant amplitude tests, the embedded coated PVA-CNT fiber gave the best results, showing a trend of continuous increasing ERC measurements that can be justified with continuously increasing damage in the

material. On the contrary, the surface attached version of the same fiber gave unsatisfactory results due to possible debonding / loss of coherency with the attaching medium.

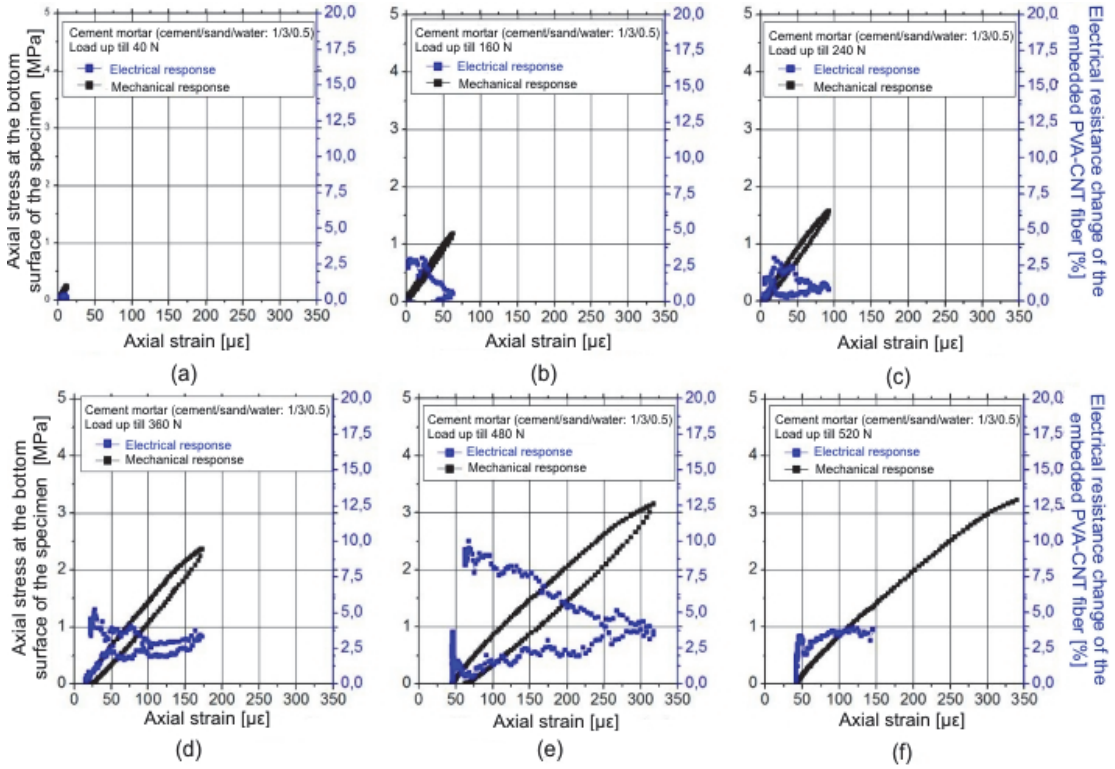

Figure 13: Incremental loading – unloading loops in type I specimen with embedded coated PVA-CNT fiber for applied loadings up till: (a) 40 N, (b) 160 N, (c) 240 N, (d) 360 N, (e) 480 N and (f) 520 N (fracture).

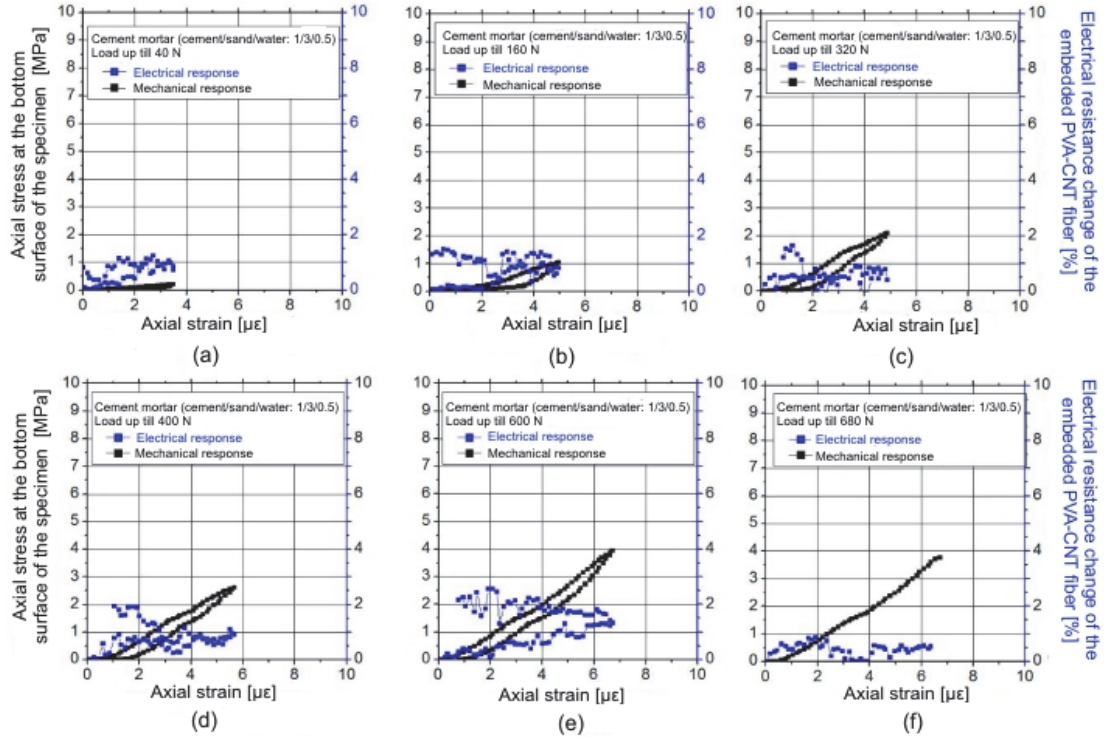

Figure 14: Incremental loading – unloading loops in type II specimen with surface-attached coated and annealed PVA-CNT fiber for applied loadings up till: (a) 40 N, (b) 160 N, (c) 320 N, (d) 400 N, (e) 600 N and (f) 680 N.

- For the case of incremental increasing loading-unloading loops, the FOBGs seems to be the more mature technology for strain sensing of cementitious material for low straining regime. For large displacements/strains damage on the brittle fiber might occur that might terminate the measurements of the sensor. The embedded coated and annealed PVA-CNT fiber gave the best sensing response in the incremental loading – unloading loops, especially at the high loading regime. Linearity between applied strain and ERC measurements was noticed for the low applied loadings while hysteresis loops were formed after every unloading branch.
- Coated and annealed PVA-CNT fiber also gave satisfactory results when surface attached at the bottom surface of the prismatic specimens, showing that annealing plays a significant role on the sensing ability of the fiber, despite lower the screening ability of the fiber itself.

ACKNOWLEDGEMENTS

Dr. Alexopoulos acknowledges the financial support of the European Union (European Social Fund - ESF) and Greek National funds through the Operational Program "Education and Lifelong Learning" of the National Strategic Reference Framework (NSRF) - Research Funding Program: "Thales - National Technical University of Athens - Development and assessment of innovative experimental techniques for the study of the mechanical behaviour of natural building stones: Applications to the conservation and restoration of monuments of Cultural Heritage" (MIS 380147).

REFERENCES

[1] Kourkoulis, S.K., Prassianakis, I., Agioutantis, Z., Exadaktylos, G.E., Reliability assessment of the NDT results for the internal damage of marble specimens, International Journal of Material and Product Technology, 26 (2006) 35-56.
[2] Kourkoulis, S.K., Ganniari-Papageorgiou, E., Bending of fragmented architraves restored with bolted titanium bars: A numerical analysis, Engineering Transactions, 56 (2008) 95-135.
[3] Kourkoulis, S.K., Ganniari-Papageorgiou, E., Mentzini, M., Dionysos marble under bending: A contribution towards understanding the fracture of the Parthenon architraves, Engineering Geology, 115 (2010) 246-256.
[4] Kourkoulis, S.K., Mentzini, M., Ganniari-Papageorgiou, E., Restored marble epistyles under bending: a combined experimental and numerical study, International Journal of Architectural Heritage, 7 (2013) 89-115.
[5] Kourkoulis, S.K, Ganniari-Papageorgiou, E., Restoring fragmented marble epistyles: some critical points, Journal of Cultural Heritage, 11 (2010) 420-429.
[6] Kourkoulis, S.K., Pasiou, E.D., Triantis, D., Stavrakas, I., Hloupis, G., Innovative experimental techniques in the service of restoration of stone monuments - Part I: The experimental set up, Procedia Engineering, 109 (2015) 268-275.
[7] Triantis, D., Stavrakas, I., Pasiou, E.D., Hloupis, G., Kourkoulis, S.K., Innovative experimental techniques in the service of restoration of stone monuments - Part II: Marble epistyles under shear, Procedia Engineering, 109 (2015) 276-284.
[8] Hofer, B., Fibre optic damage detection in composite structures, Composites, 18 (1987) 309-316.
[9] Waite, S.R., Tatam, R.P., Jackson, A., Use of optical fibre for damage and strain detection in composite materials, Composites, 19 (1988) 435-442.
[10] Takeda, S., Okabe, Y., Takeda, N., Delamination detection in CFRP laminates with embedded small-diameter fiber Bragg grating sensors, Composites Part A 33 (2002) 971-980.
[11] Park, J.M., Lee, S.I., Kwon, O.Y., Choi, H.S., Lee, J.H., Delamination detection in CFRP laminates with embedded small-diameter fiber Bragg grating sensors, Composites Part A 34 (2003) 203-216.
[12] Leng, J., Asundi, A., Structural health monitoring of smart composite materials by using EFPI and FBG sensors, Sensors and Actuators A: Physical, 103 (2003) 330-340.
[13] Ohtsu, M., Recommendations of RILEM Technical Committee 212-ACD: acoustic emission and related NDE techniques for crack detection and damage evaluation in concrete: 3. Test method for classification of active cracks in concrete structures by acoustic emission. Materials and Structures, 43 (2010) 1187-1189.

[14] Alver, N., Tanarslan, H.M., Sülün, Ö.Y., Ercan, E., Karcı, M., Selman, E., Ohno, K., Effect of CFRP-spacing on fracture mechanism of CFRP-strengthened reinforced concrete beam identified by AE-SiGMA, Construction and Building Materials, 67 (2014) 146-156.
[15] Mpalaskas, A.C., Vasilakos, I., Matikas, T.E., Chai, H.K., Aggelis, D.G., Monitoring of the fracture mechanisms induced by pull-out and compression in concrete, Engineering Fracture Mechanics, 128 (2014) 219-230.
[16] Sagar, R.V., Raghu Prasad, B.K., A review of recent developments in parametric based acoustic emission techniques applied to concrete structures. Nondestructive Testing and Evaluation, 27 (2012) 47-68.
[17] Vigolo, B., Penicaud, A., Coulon, C., Sauder, C., Pailler, R., Journet, C., Bernier, P., Poulin, P., Macroscopic fibers and ribbons of oriented carbon nanotubes, Science, 290 (2000) 1331-1334.
[18] Mercader, C., Denis-Lutard, V., Jestin, S., Maugey, M., Derré, A., Zakri, C., Poulin, P., Scalable process for the spinning of PVA–carbon nanotube composite fibers, Applied Polymer Science, 125 (2012) 191-196.
[19] Alexopoulos, N.D., Bartholome, C., Poulin, P., Marioli-Riga, Z., Structural health monitoring of glass fiber reinforced composites using embedded carbon nanotube (CNT) fibers, Comp. Sci. Technol., 70 (2010) 260-271.
[20] Alexopoulos, N.D., Bartholome, C., Poulin, P., Marioli-Riga, Z., Damage detection of glass fiber reinforced composites using embedded PVA–carbon nanotube (CNT) fibers, Comp. Sci. Technol., 70 (2010) 1733-1741.
[21] Alexopoulos, N.D., Jaillet, C., Zakri, C., Poulin, P., Kourkoulis, S.K., Improved strain sensing performance of glass fiber polymer composites with embedded pre-stretched polyvinyl alcohol–carbon nanotube fibers, Carbon, 59 (2013) 65-75.
[22] ASTM D305-06 Standard Practice for Mechanical Mixing of Hydraulic Cement Pastes and Mortars of Plastic Consistency, ASTM International, 100 Barr Harbor Drive, PO Box C700, West Conshohocken, United States.
[23] Nahata, Y., Kholia, N., Tank, T.G., Effect of Curing Methods on Efficiency of Curing of Cement Mortar, APCBEE Procedia, 9 (2014) 222-229.
[24] ASTM D6272 Standard Test Method for Flexural Properties of Unreinforced and Reinforced Plastics and Electrical Insulating Materials by Four-Point Bending ASTM International, 100 Barr Harbor Drive, PO Box C700, West Conshohocken, United States.

Focussed on Recent advances in "Experimental Mechanics of Materials" in Greece

Pre-failure indicators detected by Acoustic Emission: Alfas stone, cement-mortar and cement-paste specimens under 3-point bending

Stavros K. Kourkoulis, Ioanna Dakanali

Laboratory of Testing and Materials, Department of Mechanics, School of Applied Mathematical and Physical Sciences, National Technical University of Athens, Zografou Campus, 157 73 Athens, Greece
stakkour@central.ntua.gr, ioannadak@hotmail.com

ABSTRACT. Acoustic Emission (AE) is the technique most widely used nowadays for Structural Health Monitoring (SHM). Application of this technique for continuous SHM of restored elements of stone monuments is a challenging task. The co-existence of different materials creates interfaces rendering "identification" of the signals recorded very complicated. To overcome this difficulty one should have a clear overview of the nature of AE signals recorded when each one of the constituent materials is loaded mechanically. In this direction, an attempt is here described to enlighten the signals recorded, in case a series of structural materials (natural and artificial), extensively used for restoration projects of classic monuments in Greece, are subjected to 3-point bending. It is hoped that obtaining a clear understanding of the nature of AE signals recorded during these elementary tests will provide a valuable tool permitting "identification" and "classification" of signals emitted in case of structural tests. The results appear encouraging. In addition, it is concluded that for all materials tested (in spite their differences in microstructure and composition) clear pre-failure indicators are detected, in good accordance to similar indicators provided by other techniques like the Pressure Stimulated Currents (PSC) one.

KEYWORDS. Alfas stone; Mortar; Cement paste; Three-point bending test; Pre-failure indicators; Acoustic Emission.

OPEN ACCESS

Citation: Kourkoulis, S.K., Dakanali, I., P Pre-failure indicators detected by Acoustic Emission: Alfas stone, cement-mortar and cement-paste specimens under 3-point bending, Frattura ed Integrità Strutturale, 40 (2017) 74-84.

Received: 11.01.2017
Accepted: 07.03.2017
Published: 01.04.2017

INTRODUCTION

For the restoration of fragmented structural elements of stone monuments a pioneering technique has been developed by the scientists working for the restoration of the Acropolis of Athens. According to this technique, the fragmented structural members are rejoined together by inserting threaded titanium bars into pre-drilled holes,

which are then filled by a proper white cement paste [1]. However it has been observed that under specific loading conditions the adhesion between the cement paste and marble is sometimes not adequate permitting gradual or abrupt slip of the reinforcing bar from the body of the restored element, a phenomenon known as "pull-out". Taking into account that the construction of specimens in the form of structural elements of classical monuments is a difficult and costly task, an alternative experimental protocol was recently designed [2, 3], permitting laboratory investigation of the pull-out phenomenon (Fig.1). The specimens were made of Dionysos marble blocks drilled centrally throughout their length. The hole was filled with a cementitious material and a threaded titanium bar was driven into the hole while the filling material was still liquid. The experiments were implemented after a 28-day curing period. Using a properly designed metallic supporting system the marble was fully restricted (Fig.1c) and the bar was pulled-out under displacement-control mode (Fig.1d).

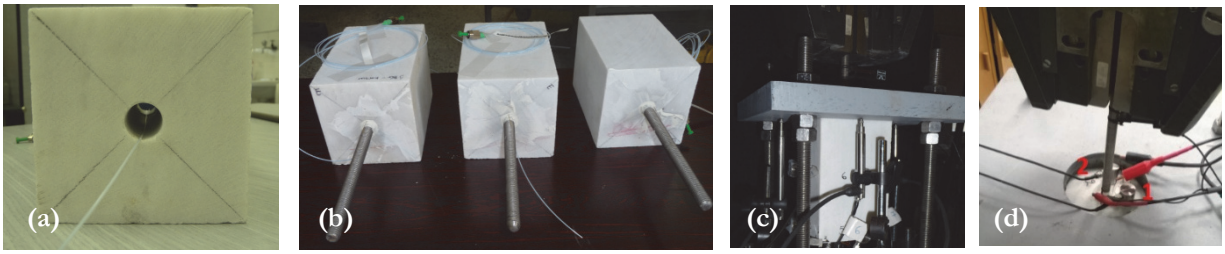

Figure 1: (a), (b) Typical pull out specimens; (c), (d) The experimental set up [2, 3].

The data obtained by the AE sensors during a typical pull-out experiment are somehow "chaotic" as it is seen in Fig. 2, where the AE recordings' duration is plotted (in conjunction to the marble-bar relative slip and also the force imposed by the frame) versus time. A direct interpretation of these data is difficult, especially concerning the sources of the emissions. In the direction of gaining a better insight it was considered that the AE technique should be first applied on specimens of simple geometry made of a single material. The protocol described here has proven that classifying the acoustic sources in such elementary tests is indeed a useful tool for the identification of the sources of acoustic signals in complex structures.

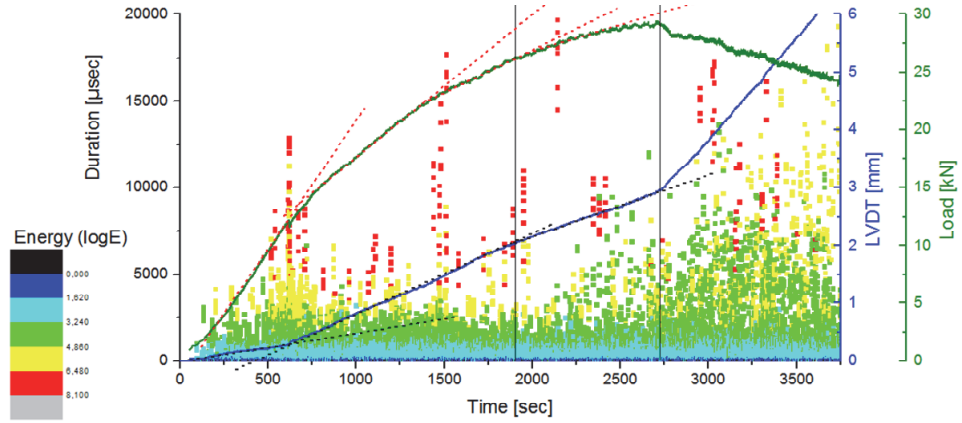

Figure 2: Time variation of the duration of AE recordings, the LVDT (in touch with the bar's lowest end) indications and the load [3].

THE EXPERIMENTAL PROTOCOL

The materials

The Alfas stone is a natural building material, quarried near the village of Alfas in the island of Crete. It was used as building material for quite a few monuments in Crete, both classical and modern, like for example the primary school at Scordilo village, built in 1884 (Fig.3a). Recently, during the construction of the Rethymnon-Ancient Eleutherna road, 128 ancient graves were discovered, all of them sculpted by Alfas stone. Nowadays Alfas stone is extensively used for the restoration of several monuments of great historical and cultural significance such as the

Monastery of Arkadi and the Fortezza fortress in Rethymno. It is also considered as a potential substitute stone for the restoration of the Epidaurus monuments.
When Alfas stone is mined it is relatively soft; however a short while after it is exposed to the sunlight it hardens. It is a compact sub-white stone of low porosity and rather homogeneous structure (Fig.3b). It is composed by 99% of calcite, 0.5% of quartz and 0.5% of aragonite [4]. Its main mechanical properties are recapitulated in Tab. 1 [4-7].

Figure 3: (a) Primary school at Scordilo village made of Alfas stone; (b) The compact texture of Alfas stone.

Modulus of elasticity	2.5-10.0 GPa
Uniaxial Compression Strength	15.0 - 36.8 MPa
Bending strength	7.4 - 10.4 MPa
Absolute density	2.45 g/cm^3
Bulk density	1.73 g/cm^3
Porosity	~30.0 (%)

Table 1: Mechanical properties of Alfas stone [4-7] (The values strongly depend on the point and depth of quarrying).

Two more materials were tested in the present protocol, i.e. a cement-mortar and a cement-paste. The specific materials are used as filling materials of the holes drilled and the grooves sculptured in the marble structural elements of the Acropolis of Athens monuments for the placement of metallic elements which either connect the epistyles to each other or restore the monolithic nature of fragmented structural members. These materials ensure the adhesion between marble and metal while in addition they protect the authentic building stone in case of overload [8]. According to the practice followed by the scientists working for the Parthenon's restoration project these filling materials are composed by coarse quartz sand (grain size: 1mm-2mm), fine quartz sand (grain size: 0.1-0.4 mm) and white Aalborg cement. The ratio for the mortar mix is 2 coarse quartz sand : 1 fine quartz sand : 1 cement. The quartz (silica) sand must be perfectly dry, clean and well graded. The sand's proportion of the containing SiO_2 is a factor of its quality. Quartz is known for its piezoelectric properties. The grains of the sand extracted from rivers are of perfectly spherical shape due to natural friction. Products composed by this sand exhibit excellent workability and elegant finished surfaces. The proper ratio of grain size ratio can provide several advantages to the final product such as the reduction of the gap between the grains, the reduction of the water absorption resulting to high water resistance, increased strength of the mortar and minimized cracking. In addition, quartz sand provides protection against corrosion due to poor environmental conditions. The Aalborg cement is a rapid hardening Portland cement with high early (2 days) and standard (28 days) strengths. It is produced of extremely pure limestone and fine-ground sand. It is characterized by its white color, high consistency, extraordinarily low content of alkali (Na_2O) and high sulphate resistance [9]. The composition for the cement-paste mix is 2.5 cement : 1 water, however it varies according to the needs of its specific application.

Acoustic Emission technique

Fracture is combined with release of stored elastic strain energy, consumed for the generation of new cracks. The elastic waves generated propagate in the material and can be detected by piezoelectric transducers mounted to the structure's surface by means of proper viscous materials [10]. The sensors' output is amplified through a low-noise preamplifier, filtered to remove any extraneous noise and further processed by proper electronic equipment. The AE method includes a wide range of applications such as laboratory experimental studies, field inspections, structural integrity evaluation,

production quality control etc. The major difference between AE and other non-destructive techniques is that AE records signals due to the external application of load to the material. AE relies on energy produced by the material only under stress. The acoustic emission frequencies are in the range of 150-300 kHz, which is above the frequency of audible sound. Usually the sensors used for monitoring the response of structural materials have a recording ability in the 20 kHz -1 MHz range [7]. The basic advantages of the AE method are its high sensitivity, the early detection of defects and cracks and the real time monitoring at a relatively low cost. Several models are proposed to analyze acoustic emissions signals, such as the b-value and the improved b-value, the intensity analysis [11], the Ledeczi et. al. method, etc. Nowadays an alternative approach is widely used for the classification of the acoustic emissions' source based on the relation between the signals' average frequency with the RA (Rise Time/Amplitude) parameter (Fig.4). The results have proven very encouraging [12, 13]. The latter analysis model is adopted in the present study.

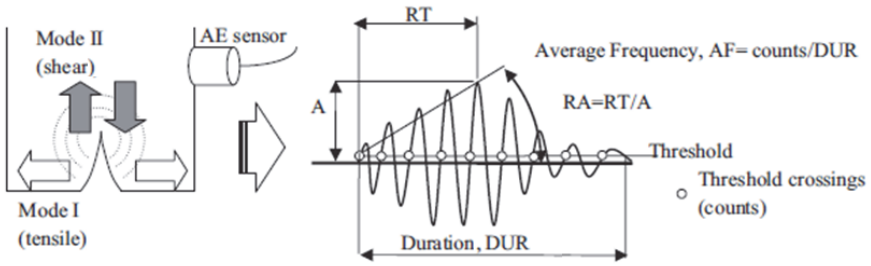

Figure 4: Cracking modes and typical acoustic emission signals [12].

The specimens and the experimental procedure

The specimens made of Alfas stone were of orthogonal parallelepiped shape of dimensions equal 22.5x10x2.2 cm³. The artificial specimens made of mortar and cement paste were also of orthogonal parallelepiped shape and their dimensions were equal to 4 cm x 4 cm x 16 cm according to the ASTM C348 standard. The specimens were subjected to 3-point bending (3PB), under displacement-control mode and quasi-static loading conditions, using an INSTRON (300 kN) servo-hydraulic loading frame, with a 50 kN calibrated load cell. The load was applied monotonically up to the fracture of the specimens. A long series of preliminary experiments highlighted the crucial role of the loading rate on the results and indicated that for the specific materials a rate equal to 0.02 mm/s was the one allowing optimum sampling of the AE data.

For the Alfas stone specimens four acoustic sensors (R15α) were properly arranged around the critical region (Fig.5). For the mortar and cement paste specimens a single acoustic sensor (R15α) was attached in the middle of the specimens' span at their lowest side. The sensors were mounted on the specimen by means of proper silicone paste (Figs.5, 6 and 7).

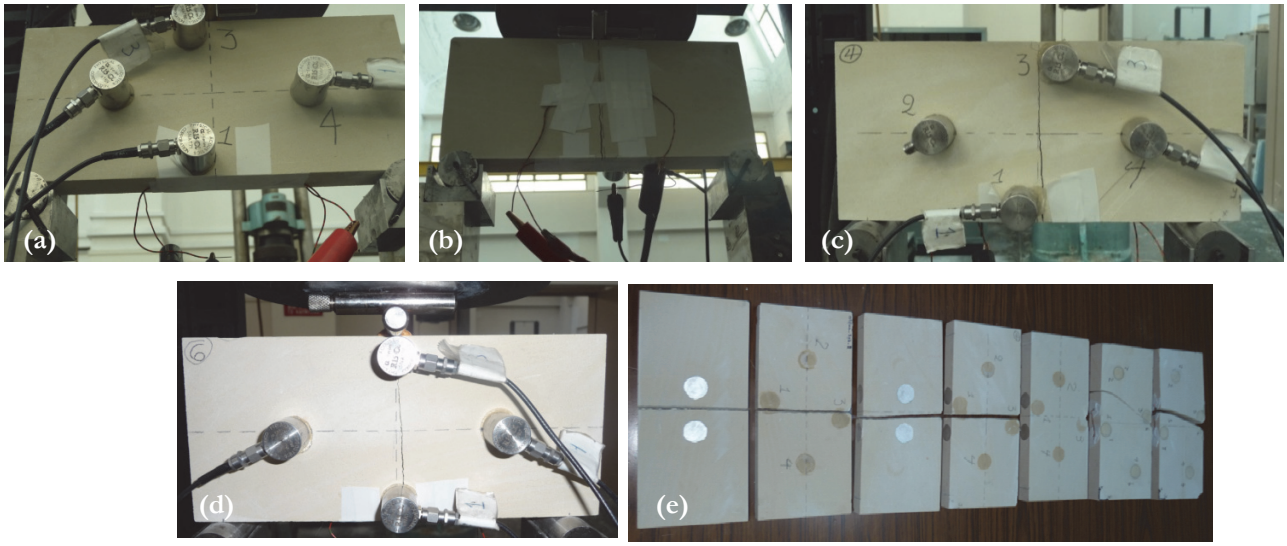

Figure 5: (a)-(d) Experimental set up for the Alfas stone specimens and the position of the AE sensors; (e) typical fractured specimens.

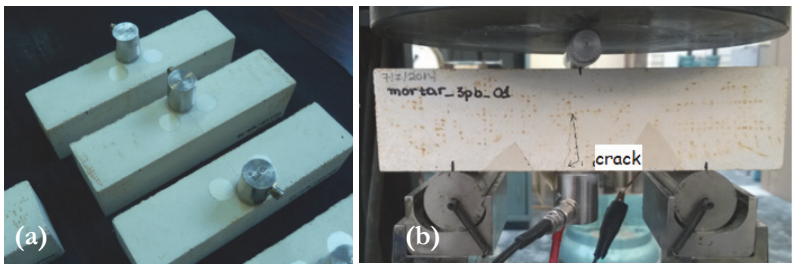

Figure 6: (a) The position of the acoustic sensor; (b) the experimental set up- and the initiation of the crack for a typical test with specimen made of mortar.

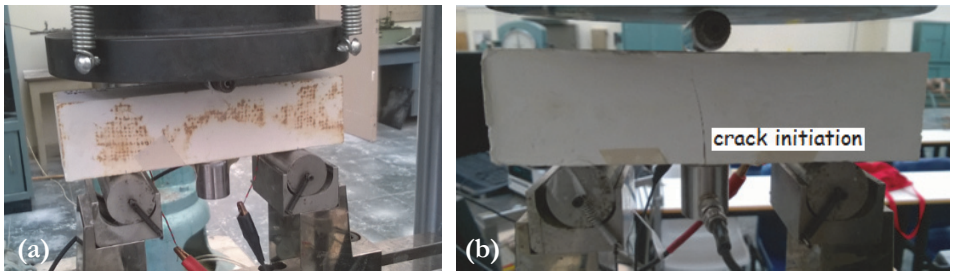

Figure 7: A typical test with a cement paste specimen (a) before and (b) after fracture.

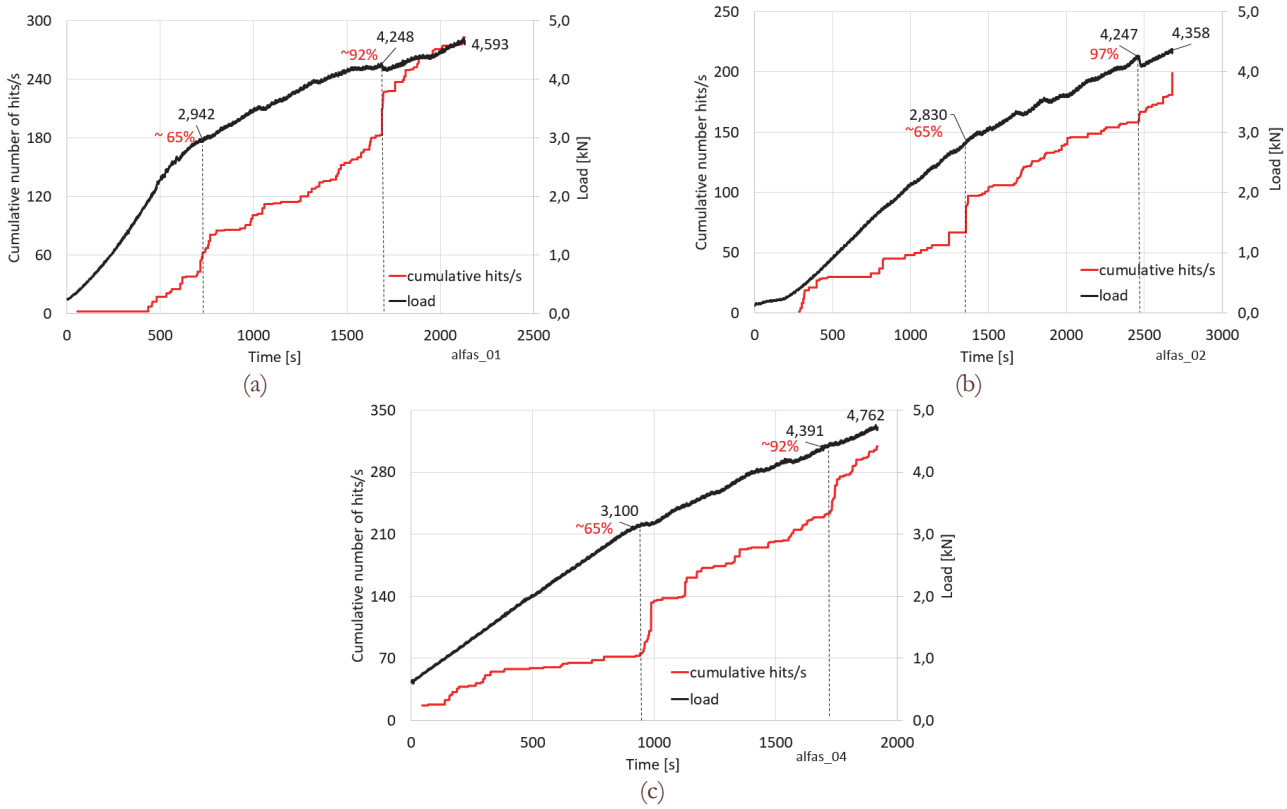

Figure 8: (a)-(c) The time variation of the cumulative hits/s for three characteristic 3-point bending experiments with specimens made of Alfas stone.

EXPERIMENTAL RESULTS

The time variation of the load imposed in conjunction with the respective variation of the cumulative number of hits/s recorded by the AE sensors are plotted in Fig.8 for three characteristic specimens made of Alfas stone. It is worth noticing that at about 65% and 95% of the maximum load abrupt increases of the hits/s appear systematically, in very good correlation with changes (either slope changes or slope discontinuities) of the respective load-time curve.

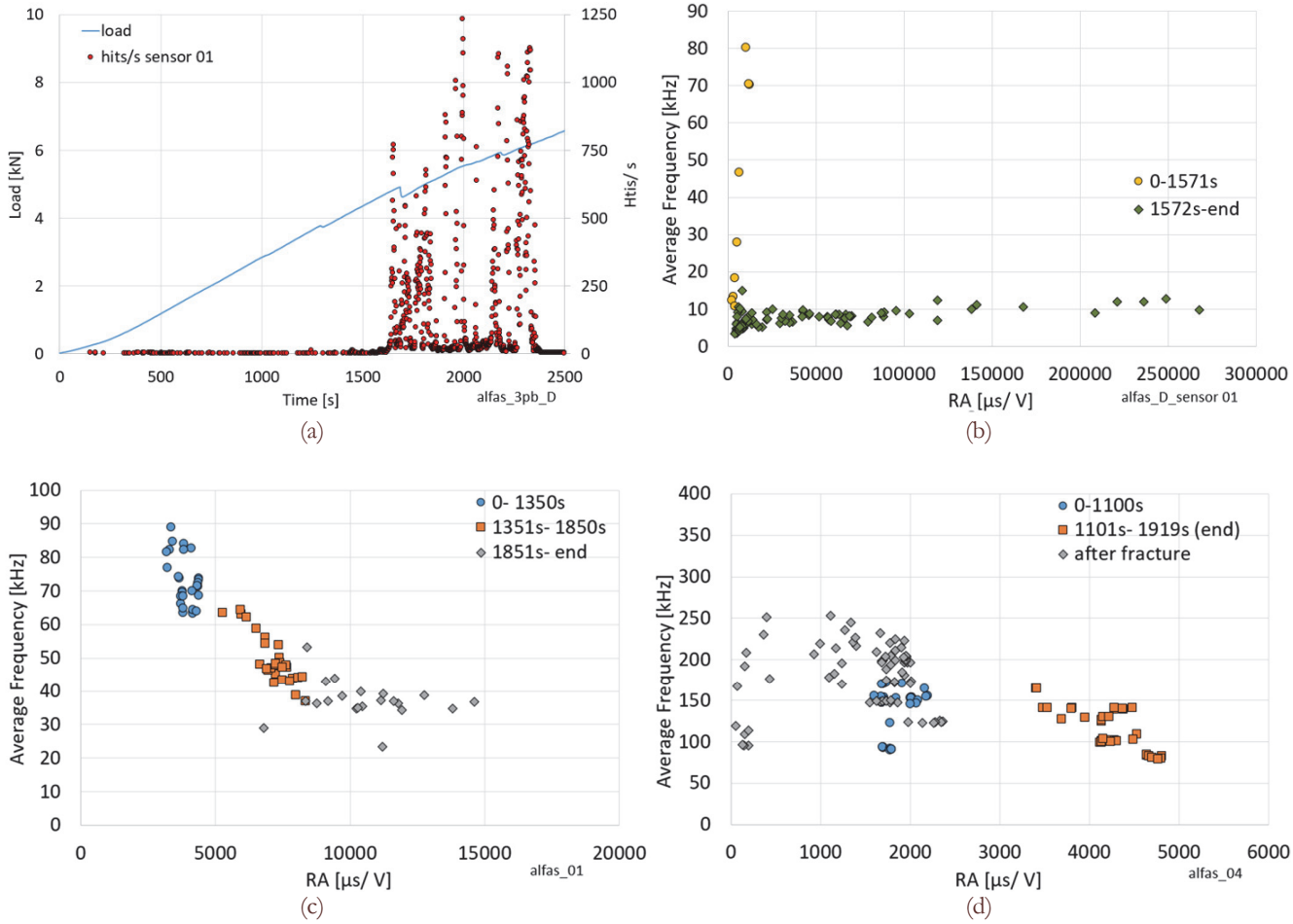

Figure 9: (a) The time variation of the hits/s and the load applied; (b) Average frequency versus the RA parameter (c) and (d) Average frequency versus the RA parameter for two additional characteristic experiments with Alfas stone specimens.

In an attempt to gain a deeper insight of the damage mechanisms activated within the mass of the Alfas stone specimens during loading, the data of sensor 01 (i.e., the one attached at the mid-section of the specimens' supporting length, or in other words the one closest to the critical area where the onset of macroscopic cracking is expected) are here analyzed further: The hits/s recorded by this sensor, are considered for two time intervals, i.e., before and after a critical time instant which, for example, for the specimen studied in Fig.9a is selected equal to $t_{cr}\approx1570$s, for obvious reasons. For these two time intervals average values of the frequency and the RA parameter (Rise Time/Amplitude (μs/V)) are calculated. The mutual dependence of these two quantities is plotted in Fig.9b. A clear qualitative distinction of the acoustic signals recorded before and after the critical time instant is clearly visible. The signals recorded during the first time interval ($0<t<t_{cr}$) are characterized by very high frequency and relatively low RA, while the signals recorded during the second time interval ($t_{cr}<t<t_{fracture}$) are characterized by much lower frequency and extremely higher RA values. This classification of the recorded signals has been a concern of the scientific community for a long time and it is nowadays attributed to different modes of cracking producing elastic waves of different characteristics. According to the dominant explanation, AE with higher frequency and lower RA values are attributed to tensile cracking, while signals with lower frequency and higher RA

are attributed to shear- or mixed-mode cracking [12, 14]. According to this approach, it is concluded that for Alfas stone under 3-point bending the cracks produced before the critical time instant are of tensile nature and are followed by shear- or mixed-mode cracking, which leads eventually to catastrophic macroscopic fracture of the specimen.

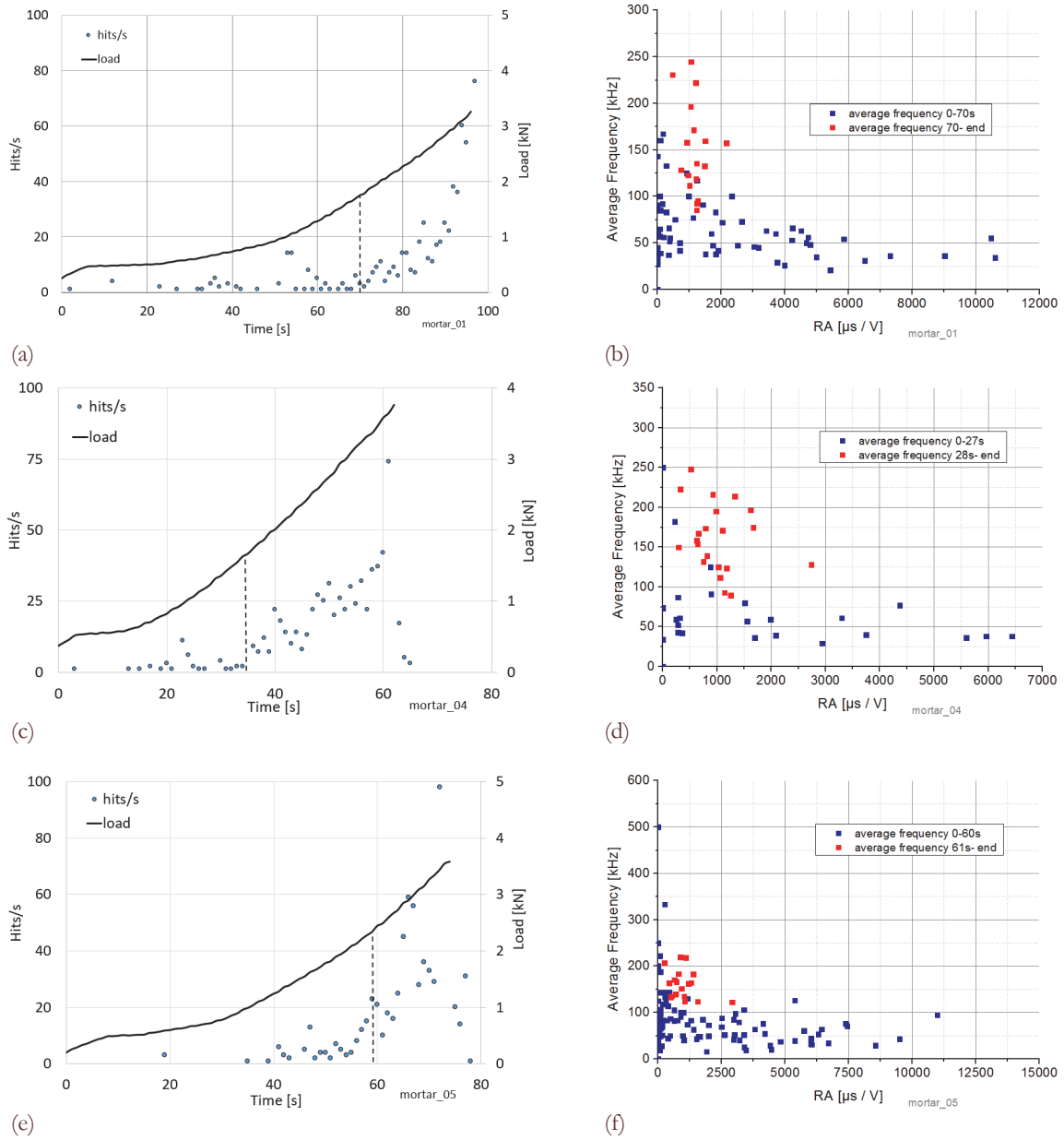

Figure 10: (a), (c), (e) Time variation of the hits/s and the load applied for three characteristic mortar specimens under 3-point bend-ing and (b), (d), (f) the respective average frequency versus the RA parameter.

For the specimens made of mortar and cement paste, the load-displacement curves did not provide any sign at all that the material approaches its critical stage and that catastrophic fracture is impending. In this context the acoustic activity appears to be an extremely valuable tool that can potentially provide clear "warning" of upcoming fracture or that the specimen has entered its critical stage. Along this direction the temporal dependence of the hits/s for three characteristic experiments with mortar specimens are plotted in Figs.10(a,c,e), in juxtaposition to the respective variation of the load applied. It is noticed that in all cases a critical time instant exists after which the number of hits/s starts increasing abruptly, indicating increased internal activity (micro-cracking). Following the procedure described for Alfas stone specimens the average values of the RA parameter and the average frequency of the signals recorded are calculated and plotted in Figs.10(b,d,f)

for the time intervals before and after the respective critical time instant. In all cases considered, the earlier signals ($0<t< t_{cr}$) are characterized by lower frequency and higher RA values (shear or mixed-mode cracking) while the signals recorded after the critical time instant ($t_{cr}<t<t_{fracture}$) are characterized by higher frequency and lower RA values.
The respective diagrams for a typical cement paste specimen are given in Figs.11(a,b). The RA values decrease as the load applied approaches its maximum value while the frequency does not exhibit noticeable changes. What is now much different, however, is that for some specimens (like the one considered in Figs.11(c,d)), after the maximum load is attained the specimen does not disintegrated abruptly but rather a post-peak region follows during which the load decreases gradually and the specimen collapses somehow "smoothly". The overall duration of the experiments of this class of cement paste specimens is divided into three intervals (instead of two). The respective diagram of the average frequency versus RA is plotted in Fig.11d. It can be seen from this figure that the signals recorded during the last time interval (i.e. after the peak load) have the same qualitative characteristics with those before the peak load.

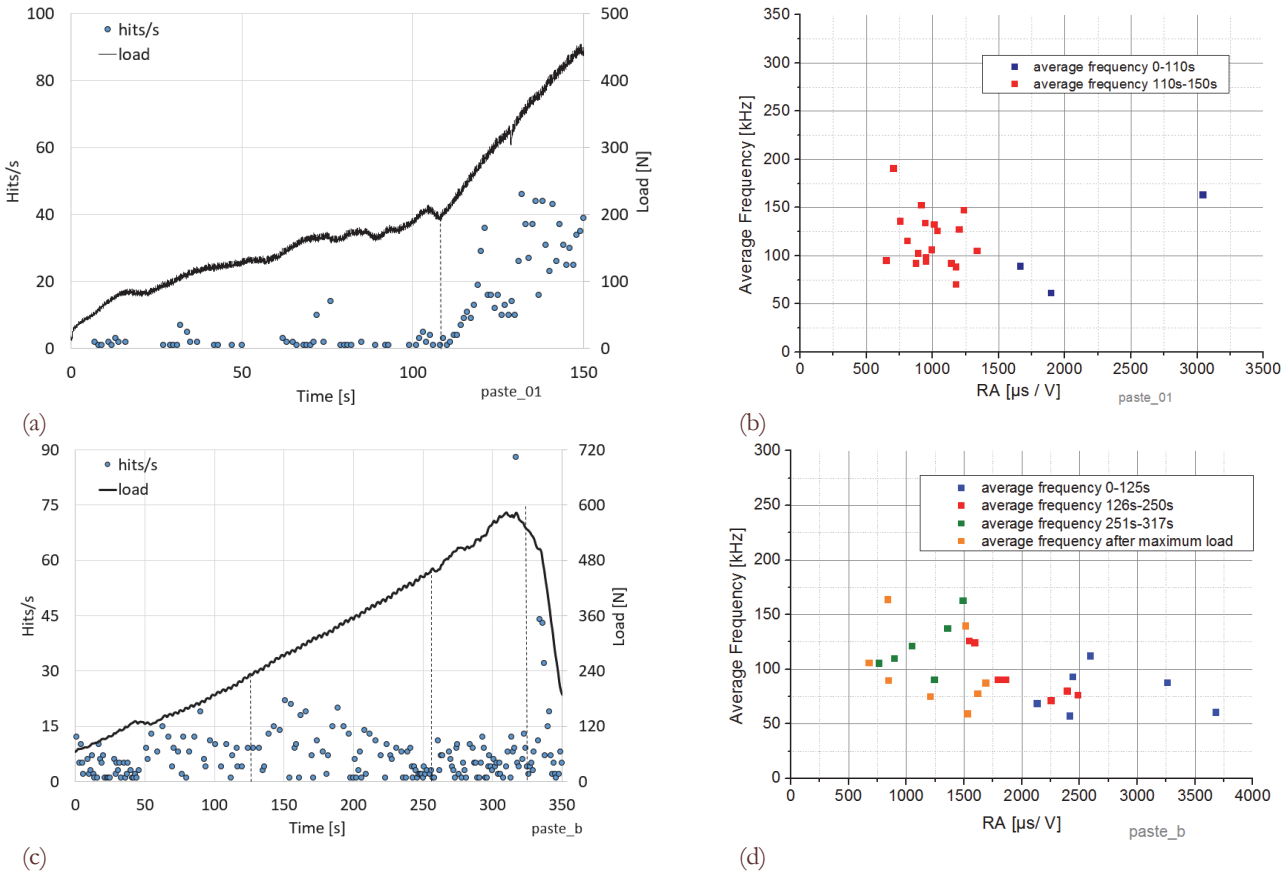

Figure 11: (a) Time variation of the hits /s and the load applied for a cement paste specimen and (b) the respective average frequency versus RA; (c) Time variation of the hits /s and the load applied for a cement paste specimen with a clearly distinguishable post-peak regime and (d) the respective average frequency versus RA.

DISCUSSION AND CONCLUDING REMARKS

Specimens made of either a natural building stone (Alfas stone) or mortar or cement paste were tested under 3-point bending. The main target of the study was to assess the AE signs recorded during the experiments and attempt to classify them according to the nature of the source from which they were emitted. Considering as critical threshold the time instant at which the number of hits/s exhibits an abrupt increase, the duration of the experiments was in general divided into two intervals (excluding the specimens with clear post-peak regime). For each interval the average frequency was plotted against the RA value, in order to apply the classification criterion for the source of the AE emissions [12-14]

according to which the emissions are due to microcracking or friction depending on the combination of frequency and RA values.

It was concluded that a clear difference between specimens made from artificial materials and specimens made from natural stone exists: Indeed, for Alfas stone specimens the failure mechanisms during the primary loading stages are governed by tensile micro-cracking while the last stages before macroscopic fracture are governed by shear- or mixed-mode cracking. On the contrary, for the specimens made of artificial materials the succession of mechanisms is inverted: Shear- or mixed-mode cracking prevails during the primary loading stages and it is then followed by tensile micro-cracking at the loading stages before the final disintegration of the specimens. Differences appear, also, between the mortar and the cement paste specimens concerning mainly the existence or not of a clearly distinguishable post-peak regime which characterized some specimens made of cement paste. This difference can be attributed to their different microstructure, which is clearly visible in Fig.12.

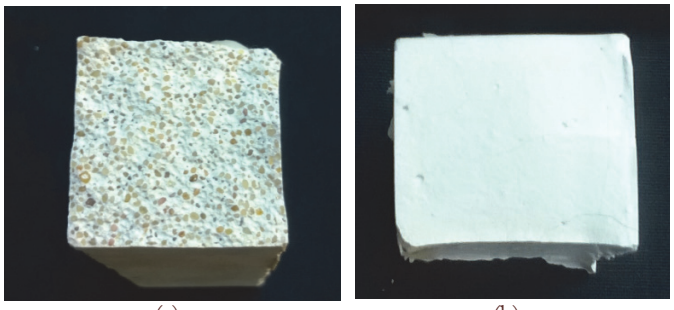

(a) (b)

Figure 12: Cross section of typical specimens made of (a) mortar and (b) cement paste.

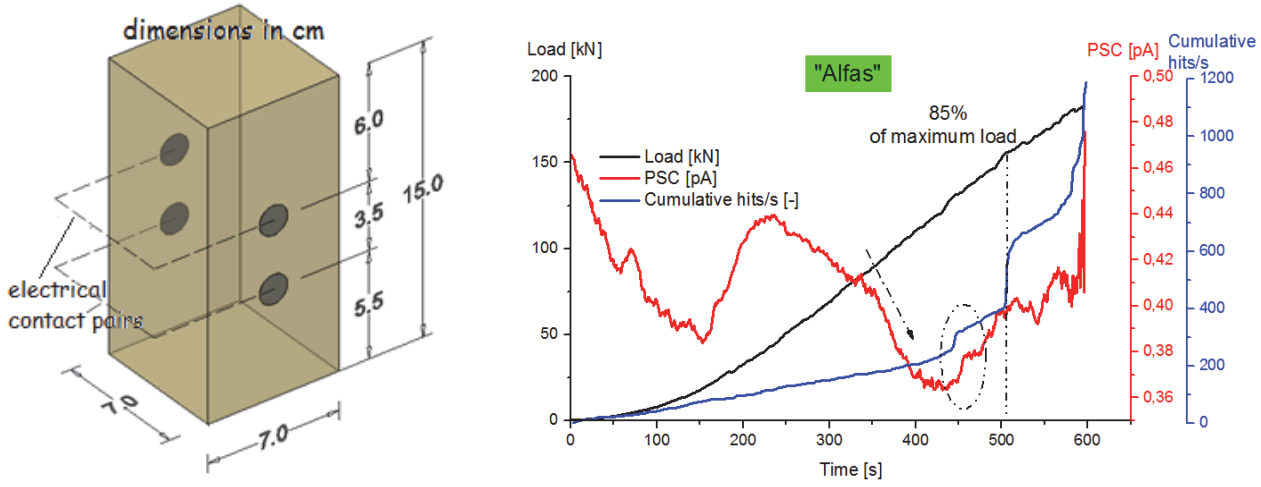

(a) (b)

Figure 13: (a) A typical prismatic specimen made of Alfas stone subjected to uniaxial compression and (b) the respective time variation of load, cumulative hits/s and Pressure Stimulated Currents [15].

Another critical conclusion that can be drawn from the present experimental protocol is that the signals recorded by the AE sensors are characterized by some indicators that can be considered as warnings that the specimens change their state and enter critical stage, well before the peak load is attained. Due to its significance the specific conclusions must be further studied with specimens made of different materials and subjected to other loading modes. In this direction, an experimental protocol is in progress, with Alfas stone specimens subjected to uniaxial compression (Fig.13a) [15]. The results of this protocol are very encouraging. In Fig.13b the data concerning the cumulative hits/s for a typical compression experiment of that protocol are plotted versus time in juxtaposition to the respective variation of the load imposed. It is seen from this figure that at about 85% of the peak-load finally attained the cumulative hits/s exhibit an abrupt jump

equal to about 40% of its value before the sudden jump. This discontinuity can be again considered as a clear indicator that the specimen enters its critical stage and macroscopic fracture is impending.
Another interesting conclusion drawn from Fig.13b is that the pre-failure indicators provided by the AE technique are in very good agreement with similar ones obtained by another sensing technique known as Pressure Stimulated Currents (PSC) [16-20]. Indeed it is seen from Fig.13b that just before the "jump" of the graph of the cumulative hits/s the PSC recorded by a pair of electric contacts starts increasing gradually. The same signal (PSC) exhibits a very steep "jump" just before the macroscopic fracture of the specimens. Considering the data of these two protocols it can be concluded that a combined use of the AE and PSC techniques may be proven valuable in the direction of further enlightening the internal damage process of specimens made of building materials as well as in the direction of providing safe pre-failure indicators.

REFERENCES

[1] Korres, M., Toganides, N., Zambas, C., Skoulikidis, Th., Study for the restoration of the Parthenon, Vol.2a, Athens: Ministry of Culture, Committee for the Preservation of the Acropolis Monuments (in Greek), (1989).
[2] Kourkoulis, S.K., Marinelli A., Dakanali, I., A combined experimental and numerical study of the pull-out mechanism of threaded titanium bars embedded in marble, ECCOMAS Congress 2016-VII European Congress on Computational Methods in Applied Sciences and Engineering, M. Papadrakakis, V. Papadopoulos, G. Stefanou, V. Plevris (eds.), Crete Island, Greece, 5-10 June 2016.
[3] Dakanali, I., Stavrakas, I., Triantis, D., Kourkoulis, S.K., Pull-out of threaded reinforcing bars from marble blocks, Procedia Structural Integrity, 2 (2016) 2865-2872.
[4] PETRES ALFAS M. & D. SARRIS S.A.: http://petresalfas.com
[5] Ninis, L., Kourkoulis, S. K., Sakellariou A., Evaluation Criteria for building stones in the restoration of the Epidaurean Asklepieion, Proceedings of the Interdisciplinary Workshop "The building stone in monuments", Athens, November 2001, IGME Publishing, Eds. M. Varti-Mataranga and Y. Katsikis, , (2002) 235-248 (in Greek).
[6] Kehayas, K., Comparison of results of conventional triaxial- and multilevel triaxial-tests on marly limestone, Diploma Thesis, Technical University of Crete, Supervisor Z. Agioutantis, Chania, Crete, 2012 (in Greek).
[7] Kaklis, K., Agioutantis, Z., Vafidis, A., Mavrigiannakis, S., Kouvela, M., Feggos, G., Characterization of bioclastic limestone of Alfas-Rethymon by laboratory and in-situ tests, 1st National Conference for building materials and elements, Athens, 21-23 May 2008, Technical Chamber of Greece (in Greek).
[8] Aggelakopoulou, E., Design and evaluation of restoration mortars for the Acropolis monuments, The Acropolis Restoration News, 13 (2013) 13-17.
[9] http://www.aalborgwhite.com Aalborg white cement paste
[10] Grosse, C.U., Ohtsu, M., Acoustic Emission testing, Basics for research - Applications in Civil Engineering, Springer-Verlag Berlin Heidelberg, (2008).
[11] Fowler, T.J., Blessing, J.A, Strauser, F.E. Intensity analysis, Proceedings of the 4th International Symposium on Acoustic Emission From Composite Materials AECM-4, Seattle (1992), American Society for Nondestructive Testing, Columbia (1992) 237-246.
[12] Ohno K., Ohtsu, M., Crack classification in concrete based on acoustic emission. Construction and Building Materials, 24(12) (2010) 2339-2346.
[13] AE and Related Nondestructive Evaluation (NDE) Techniques in the fracture mechanics of concrete, Woodhead Publishing Series in Civil and Structural Engineering, editor Masayasu Ohtsu, 57 (2015).
[14] Aggelis, D., Shiotani, T., Momoki, S., Hirama, A., Acoustic emission and ultrasound for damage characterization of concrete elements, ACI Materials. J. 106 (6) (2009) 509-514.
[15] Kourkoulis, S.K., Dakanali, I., Petropoulou, V., Acoustic emission versus pressure stimulated currents in uniaxially compressed natural building stones, Accepted for presentation at the 14th International Conference on Fracture (ICF 14), Rhodes Island, Greece, June 18-23, 2016.
[16] Stavrakas, I., Triantis, D., Agioutantis, Z., Maurigiannakis, S., Saltas, V., Vallianatos, F., Pressure Stimulated Currents in rocks and their correlations with mechanical properties, Natural Hazards and Earth System Sciences, 4 (2004) 563-567.
[17] Vallianatos, F., Tzanis, A., Electric current generation associated with the deformation rate of a solid: Preseismic and coseismic signals, Physics and Chemistry of the Earth, 23 (9-10) (1998) 933-939.
[18] Vallianatos, F., Triantis, D., Tzanis, A., Anastasiadis, C., Stavrakas, I., Electric earthquake precursors: From laboratory results to field observations, Physics &Chemistry of the Earth, 29 (2004) 339-351.

[19] Vallianatos, F.,Triantis, D., Scaling in Pressure Stimulated Currents related with Rock Fracture, Physica A, 387 (2008) 4940-4946.
[20] Cartwright-Taylor, A., Vallianatos, F., Sammonds, P., Superstatistical view of stress-induced electric current fluctuations in rocks, Physica A, 414 (2014) 368-377.

Exercise as a mean to reverse the detrimental effect of high-fat diet on bone's fracture characteristics

Ilias Doulamis, Despina N. Perrea
Laboratory for Experimental Surgery and Surgical Research "N.S. Christeas", National and Kapodistrian Universtiy of Athens, Medical School, Agiou Thoma str. 15B, 11527, Athens, Greece.

Panagiotis E. Chatzistergos
School of Health Sciences and Education, Staffordshire University, Stoke-on-Trent, UK.
Panagiotis.Chatzistergos@staffs.ac.uk

Athanasios S. Mitousoudis, Stavros K. Kourkoulis
Unit of Biomechanics, Department of Mechanics, School of Applied Mathematical and Physical Sciences, National Technical University of Athens, Zografou Campus, 15773, Athens, Greece.

ABSTRACT. The aim of this study is to investigate whether exercise can reverse some of the adverse effects of high-fat-diet-induced obesity on lipid metabolism and bone biomechanical properties. A total of 26 adult male C57bl/6J mice were randomly assigned into three groups: (A) Control group (n=6), (B) High-fat diet group (n=10), (C) High-fat diet and exercise group (n=10). Body mass and relevant biochemical parameters were measured for the duration of the experimental protocol (37 weeks). Mechanical strength of both femurs of each animal was assessed in-vitro based on three point bending tests. It was revealed that exposure to high-fat diet led to significant increase of body mass and cholesterol levels and also to substantial changes in bone morphology and strength. Ultimate stress for the animals exposed to high-fat diet and those exposed to high-fat-diet and exercise was 25% and 24% lower compared to control, respectively. Exercise increased bone thickness by 15% compared to animals that were not exposed to exercise. It was concluded that high-fat-diet appears to have a detrimental effect on bone biomechanics and strength. Exercise reversed the reduction in bone thickness that appears to be induced by high-fat diet. However no statistically significant increase in bone strength was observed.

KEYWORDS. Bone biomechanics; Mice; Femur; High-fat-diet; Three-point bending; Bending strength.

OPEN ACCESS

Citation: Doulamis, I., Chatzistergos, P.E., Mitousoudis, A.S., Kourkoulis, S.K., Perrea, D.N., Exercise as a mean to reverse the detrimental effect of high-fat diet on bone's fracture characteristics, Frattura ed Integrità Strutturale, 40 (2017) 85-94.

Received: 17.02.2017
Accepted: 10.03.2017
Published: 01.04.2017

INTRODUCTION

Obesity's adverse effects on health include increased risk for diabetes (type-2), heart disease and certain types of cancer [1] leading to poor quality of life and ultimately to reduced life expectancy [2]. The continuous rise in its prevalence worldwide has highlighted obesity as one of the major epidemics of our time [3].
With regards to the risk for bone fracture, obesity has been traditionally believed to have a protective role [4,5]. Moreover a significant number of studies reported a positive relation between Body Mass Index (BMI) and bone density [6]. However, the aforementioned classic view on the effect of obesity has been put into question from findings that link obesity to the loss of bone mass and osteopenia [7, 8] and studies highlighting lean body mass as a stronger determinant of bone density in men than BMI [9, 10].
Currently adipose tissue (i.e. body fat) is considered to be hormonally active with a pivotal role with regards to energy homeostasis and metabolism and not just an organ for storing excess energy [11]. More specifically, adipose tissue has been found to produce and secrete numerous substances including the hormone adiponectin. Adiponectin is exclusively secreted by adipose tissue and appears to be linked to increased insulin sensitivity and to have anti-atherogenic and anti-inflammatory properties [12]. The levels of plasma adiponectin are strongly associated with BMI and appear to be higher in obese subjects compared to lean subjects [13, 14].
Animal models have been widely used for the investigation of the effect of obesity, nutrition and exercise. According to these models obesity is induced by subjecting the animals (mainly rats or mice) to a high-fat diet (HFD) [15].
According to literature one of possible ways to prevent bone mass loss is exercise [16, 17]. Besides of its overall positive effect on health, exercise is considered to positively influence bone microstructure [18] and improved strength [19, 20].
In this context the aim of this study is to assess the effect of HFD - induced obesity on bone biomechanics and biochemical measurements and investigate whether exercise can reverse its potentially negative effects.

MATERIALS AND METHODS

Selection and description of animals

A total of 26 male c57bl/6 mice, aged 10-11 weeks, were used. The mice were housed in groups of three in the Animal Housing Facility of the Laboratory of Experimental Surgery and Surgical Research "N.S. Christeas", National and Kapodistrian University of Athens, in a controlled environment. All conditions followed National and European legislation and standards, including cages (Tecniplast S.p.a., Italy) and the environment with 55% relative humidity, central ventilation (15 air changes/h), temperature of 20°C ± 2°C and artificial 12-h light-dark cycle. Access to food and water was ad libitum. The experimental protocol was approved by the Ethics Committee of the local Veterinary Directorate.
Following acclimatization, the rodents were randomized and allocated into three groups: Control group (Group A, n=6), which received a standard chow diet for 37 weeks; High Fat Diet (HFD) group (group B, n=10), which received a high fat diet (standard chow diet enriched with 45% fat) for 37 weeks; High Fat Diet and Exercise (HFDE) group (group C, n=10), which received the same diet as group B for 37 weeks and ran on a treadmill three times a week for the last nine weeks of the experimental protocol.

Treadmill exercise

The duration of the exercise of group C was nine weeks in total. A specially designed treadmill was used (Columbus Instruments, USA, Model: Exer-3/6). An escalation of the vigorousness of exercise was followed. More specifically, the first two weeks were characterized as the adjustment period. Meanwhile, the mice began to run at speed of 5 m/min and gradually (additional 5 m/min per time) reached the speed of 30 m/min at the end of the second week. This was their final running speed until the end of the study. Each exercise session lasted precisely 30 minutes.

Biochemical measurements

Blood samples were collected at baseline, at 12 weeks, at 28 weeks and at the end of the study (37 weeks) prior to euthanasia following a 12-h fast of the animals. Animals were anesthetized with ether and a quantity of approximately 500 μl of blood was collected from the ocular canthus of each mouse. Blood was collected in Vacutainer tubes (BD Diagnostics, NJ, USA). Serum was separated by centrifugation at 3000 rpm for 10 minutes and was stored at -20°C until analysis.

Total serum cholesterol (T-CHOL), high-density lipoprotein cholesterol (HDL-C) serum triglycerides (TG) and serum glucose concentrations were determined enzymatically with commercially available kits (Biosis Biotechnological Applications, Athens, Greece). Due to the nonconfirmed validity of the Friedewald formula for the calculation of low-density lipoprotein (LDL) in rodents this parameter was not included in our study. Moreover, serum adiponectin levels (ADIPO) were estimated with enzyme-linked immunosorbent assay (Mouse Adiponectin ELISA Kit, Intra-assay CV 5.3%, Inter-assay CV 9.9% ABCAM, Cambridge CB4 0FL UK).

Mechanical testing

After euthanasia, both left and right femur of each animal were resected and stored in gauze immersed into N/S 0.9%. The mechanical behaviour and the strength of the specimens was assessed from three point bending tests. All biomechanical tests were performed within four hours from the time the samples were harvested.

Mechanical testing was performed with the use of an electromechanical uniaxial load frame (INSTRON) which was equipped with a high accuracy tension-only load cell (50 N, INSTRON). Because of the use of a tension-only load cell, a custom device had to be used to transform tensional loading to three point bending (Fig. 1). This device comprises two main parts: Part A which was fixed to the load frame's base and B which was attached to its movable crosshead. Part A included the centrally placed cylindrical pin while Part B included the two support pins (Fig. 1). The diameter of all three pins was 2 mm and the distance between the two support pins was 14 mm. To improve the reliability of the testing procedure the distance between the stationary central pin and the movable support pins was directly measured using a lased micrometer (Keyence LS-3000) (Fig. 1). All samples were loaded with a displacement rate of 5 mm/min until failure. The sampling frequency for the distance between the central and the support pins as well as for the force was 3 Hz.

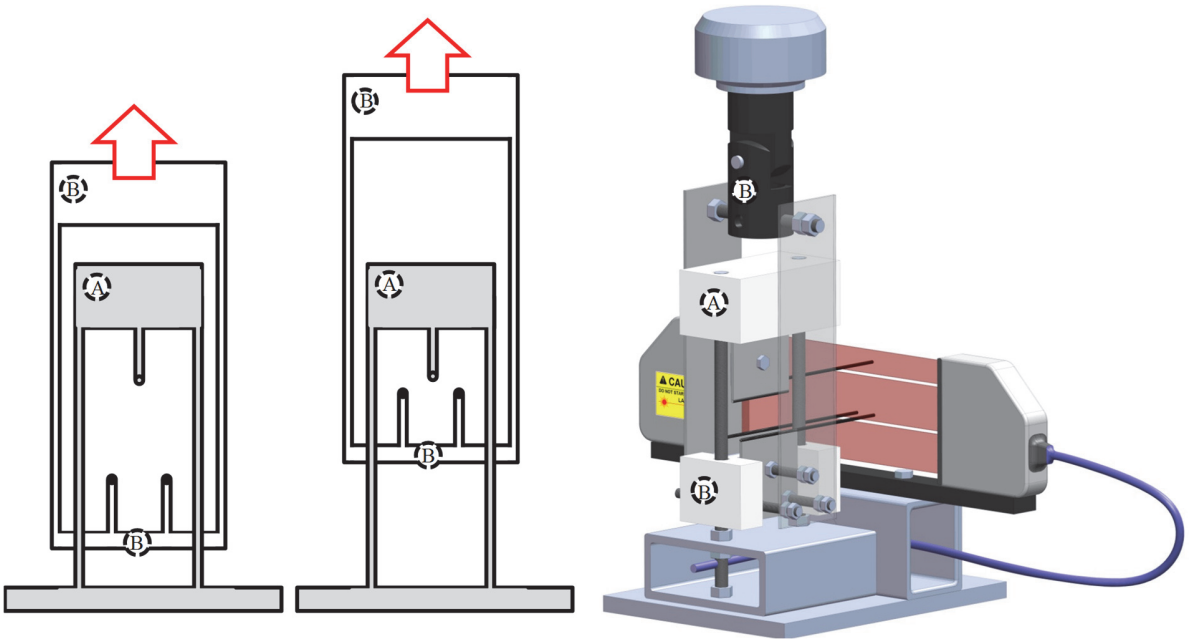

Figure 1: The custom device that was used to perform three point bending tests with a tension only load cell. The device comprises two parts: (A) which was fixed to the load frame's base and (B) which was attached to its movable crosshead.

Before testing, the maximum and minimum external thickness of each sample was measured at the central part of their diaphysis using a digital calliper. Assuming that the cross-section of the diaphysis is elliptical means that the aforementioned maximum and minimum external thickness correspond to the major axis (a) and minor axis (b) of the ellipse respectively (Fig. 2). After the end of the test the actual thickness of the bone cross-section was also measured on the surface of fracture. The measurement of wall thickness was repeated four times for each sample: two at opposite sides of the sample's major axis (t_1,t_2 in Fig. 2) and two at opposite sides of the sample's minor axis (t_3,t_4 in Fig. 2). In the end, these four measurements were used to calculate the average thickness of the sample (t) on the surface of failure.

The recorded data in terms of force were used to find the maximum force that was sustained by each sample, namely the fracture force. The force data combined with the measurements of the distance between the central and support pins were used to draw the force/deflection curve of each test and calculate the stiffness of each sample and also their energy to

failure. Sample stiffness was calculated as the slope of the linear part of the force/deflection curve while energy as the area below the curve. Ultimate stress was also calculated based on the assumption of elliptical cross-section with constant thickness (t) [21].

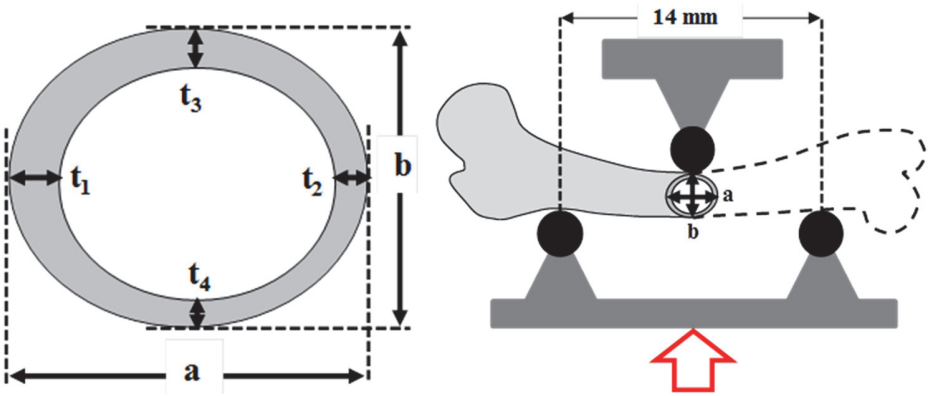

Figure 2: A schematic representation of the three point bending test. The measurement sites for thickness (t_{1-4}) and lengths of the major (right) and minor axis (left) of the samples are also presented.

Statistical analysis

The results for the three groups were compared to each other and the statistical significance of the differences that were observed was evaluated following one way analysis of variance (ANOVA). The level of statistical significance was considered to be equal to 0.05.

The effect of exercise on the biochemical profile and body mass of group C was also investigated. For this purpose one way repeated measures ANOVA (statistical significance level = 0.05) with Bonferroni confidence interval adjustment was used to assess the statistical significance of differences between the measurements that were taken before the start and after the end of the exercise protocol (i.e. week 28 vs 37).

In order to assess the relationship between biomechanical and biochemical parameters and the effect of HFD, the correlation between the average biomechanical measures for each animal (i.e. average for left and right femur) and the biochemical measurements was investigated for groups B and C using Pearson correlation analysis. The correlation between biomechanical measures and body mass was also assessed. All data were tested for linearity, normality and homoscedasticity. The statistical analyses were performed using IBM® SPSS®v.21.

RESULTS

Biochemical measurements

At the beginning of the protocol differences between the three groups were non-significant (Fig. 3), with the exception of TG levels, which were somehow higher in group A (an issue that should be considered further). During week 12, the first changes that can be attributed to HFD are observed in the case of HDL-C, with groups B and C having significantly higher HDL-C levels compared to control (group A). Differences in biochemical parameters become clearer during week 28 when significant differences in terms of body mass are also observed. More specifically, groups B and C appear to have significantly higher body mass and higher levels of HDL-C and T-CHOL compared to control. Group C has significantly higher body mass than group B too (average (±STDEV) body mass for groups A, B and C is equal to 29.3kg (±2.4kg) 35.0kg (±4.2kg) and 39.2kg (±2.3kg), respectively). At the end of the experimental protocol (i.e. week 37) the difference in terms of body mass between control and groups B and C appears to crystallise (average (±STDEV) body mass for groups A, B and C is equal to 27.5kg (±1.4kg) 32.0kg (±3.0kg) and 31.8kg (±3.5kg) respectively). Moreover, groups B and C also have significantly higher levels of T-CHOL compared to control. At the end of the protocol, group C also appears to have significantly higher levels of TG compared to the other two groups (Fig. 3).

At this point it should be highlighted that group C was exposed to exercise only during the last nine weeks of the experimental protocol (i.e. weeks 28-37). Therefore any difference between groups B and C that is observed during the 28th week of the experimental protocol (or earlier than that) cannot be attributed to exercise (Fig. 3).

One way repeated measures ANOVA for group C before and after the introduction of exercise showed statistically significant:

- Decrease in body mass (Wilks' Lambda=0.276, F(1,9)= 23.649, p=0.001)
- Decrease in the levels of T-CHOL (Wilks' Lambda=0.357, F(1,9)= 16.97, p=0.003)
- Decrease in the levels of HDL-C (Wilks' Lambda=0.135, F(1,9)= 57.193, p<0.0005)
- Increase in the level of TG (Wilks' Lambda=0.068, F(1,9)= 124.149, p<0.0005)
- Decrease in the levels of ADIPO (Wilks' Lambda=0.244, F(1,9)= 27.816, p=0.001)

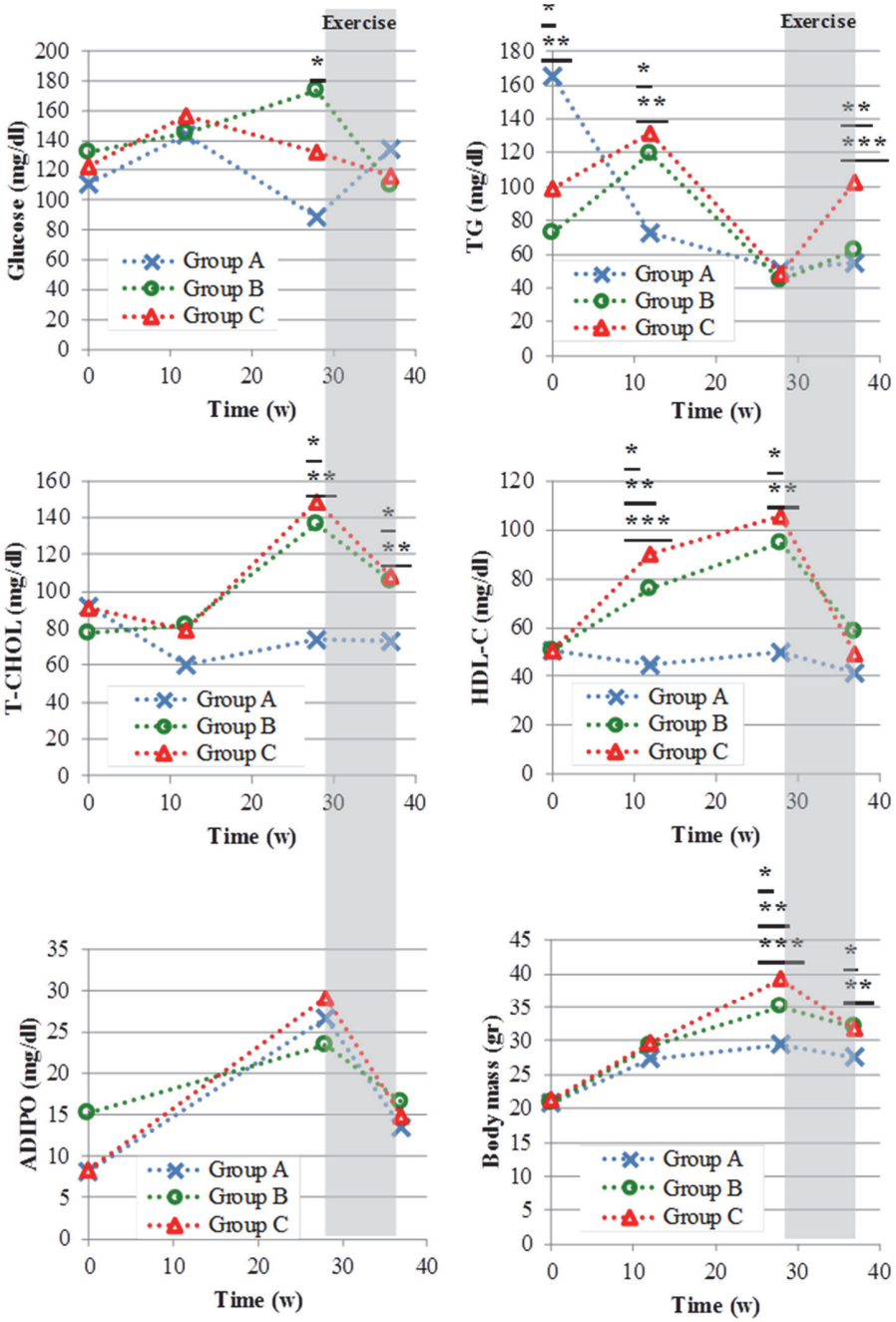

Figure 3: The change in biochemical measures and body mass for the duration of the study. More specifically, biochemical results for the levels of serum glucose, total serum cholesterol (T-CHOL), high-density lipoprotein cholesterol (HDL-C), serum triglycerides (TG) and serum adiponectin levels (ADIPO) are presented. Statistically significant differences (i.e. p<0.05) between groups A and B, A and C and between groups B and C are noted using *, ** or *** respectively. The time period when group C was exposed to exercise (i.e. weeks 28-37) is also highlighted.

Mechanical testing

Some of the samples were damaged before testing during harvesting. In the end, the number of sample pairs (i.e. left and right femurs) that were tested was 3, 6, and 10 for groups A, B and C respectively. The average values and standard deviations for all biomechanical parameters measured in the context of this study are presented in Tab. 1.

Group:	A	B	C
Max Force (N)	16.4 *(2.6)*	14.2 *(2.6)*	15.6 *(2.2)*
Stiffness (N/mm)	77 *(25)*	90 *(34)*	89 *(28)*
Energy (N*mm)	3.16 *(0.85)*	2.64 *(0.92)*	3.36 *(1.20)*
b (mm)	1.42 *(0.06)*	1.59 *(0.07)*	1.53 *(0.11)*
a (mm)	2.05 *(0.04)*	2.19 *(0.10)*	2.16 *(0.11)*
t (mm)	0.24 *(0.03)*	0.22 *(0.03)*	0.25 *(0.04)*
Stress (MPa)	58 *(12)*	43 *(7)*	44 *(11)*

Table 1: The average values for the biomechanical parameters measured. The respective standard deviations are shown in brackets.

One way ANOVA revealed statistically significant differences between the three groups in terms of minor axis length (b), major axis length (a) and thickness of the cross-section (t) and also in terms of ultimate stress (Fig. 4). No statistically significant difference was found in terms of force, stiffness or energy to failure.

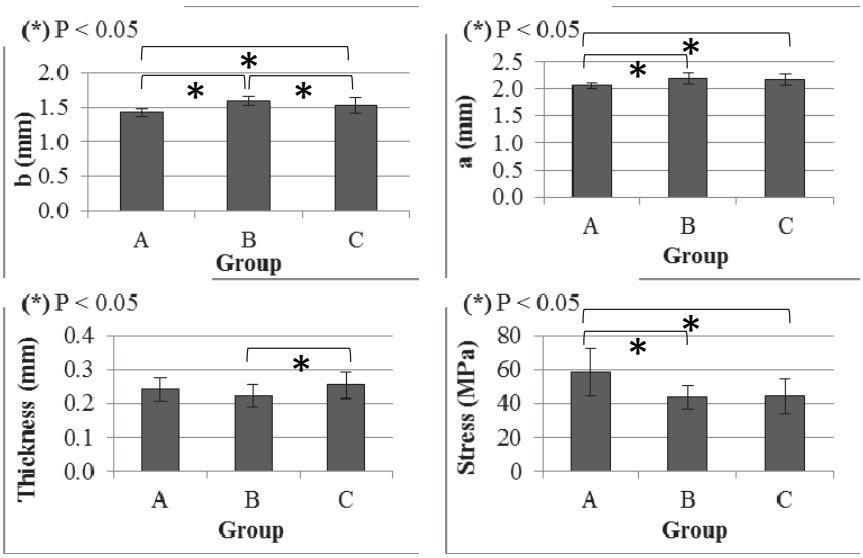

Figure 4: Comparative results in terms of bone morphology and mechanical strength. The lengths of the minor axis (b), of the major axis (a), of cortical shell thickness and of ultimate stress are presented.

More specifically the average minor axis (b) of group A was smaller than group's B and C by 12% (p=0.040) and 7% (p<0.001) respectively. The respective difference between groups B and C was 4% (p=0.041) with the minor axis of group

C being the smallest of the two groups. The major axis of group A was also smaller that group B and C by 7% (p=0.026) and 5% (p=0.004) respectively. The thickness of group C was bigger than group B by 15% (p=0.010). Finally the ultimate stress of group A was higher than B and C by 25% (p=0.021) and 24% (p=0.001) respectively (Fig. 4).

Pearson correlation analysis revealed a strong positive correlation between serum glucose and fracture force (r=0.560, N=18, p=0.016) and between glucose and energy (r=0.660, N=18, p=0.008) (Fig. 5a,b). Body mass was strongly and positively correlated to fracture force (r=0.606, N=18, p=0.008) and negatively correlated to minor axis length (b) (r=-0.644, N=18, p=0.004) (Fig. 5c,d). T-CHOL was negatively correlated to minor axis length (r=-0.644, N=18, p=0.011) (Fig. 5e). The aforementioned correlations indicate that fracture force tends to be higher in animals with higher glucose levels and in animals with higher body mass. Moreover, fracture energy tends also to be higher in animals with higher glucose levels while the minor axis (b) appears to be smaller in animals with higher levels of T-CHOL and in animals with higher body mass.

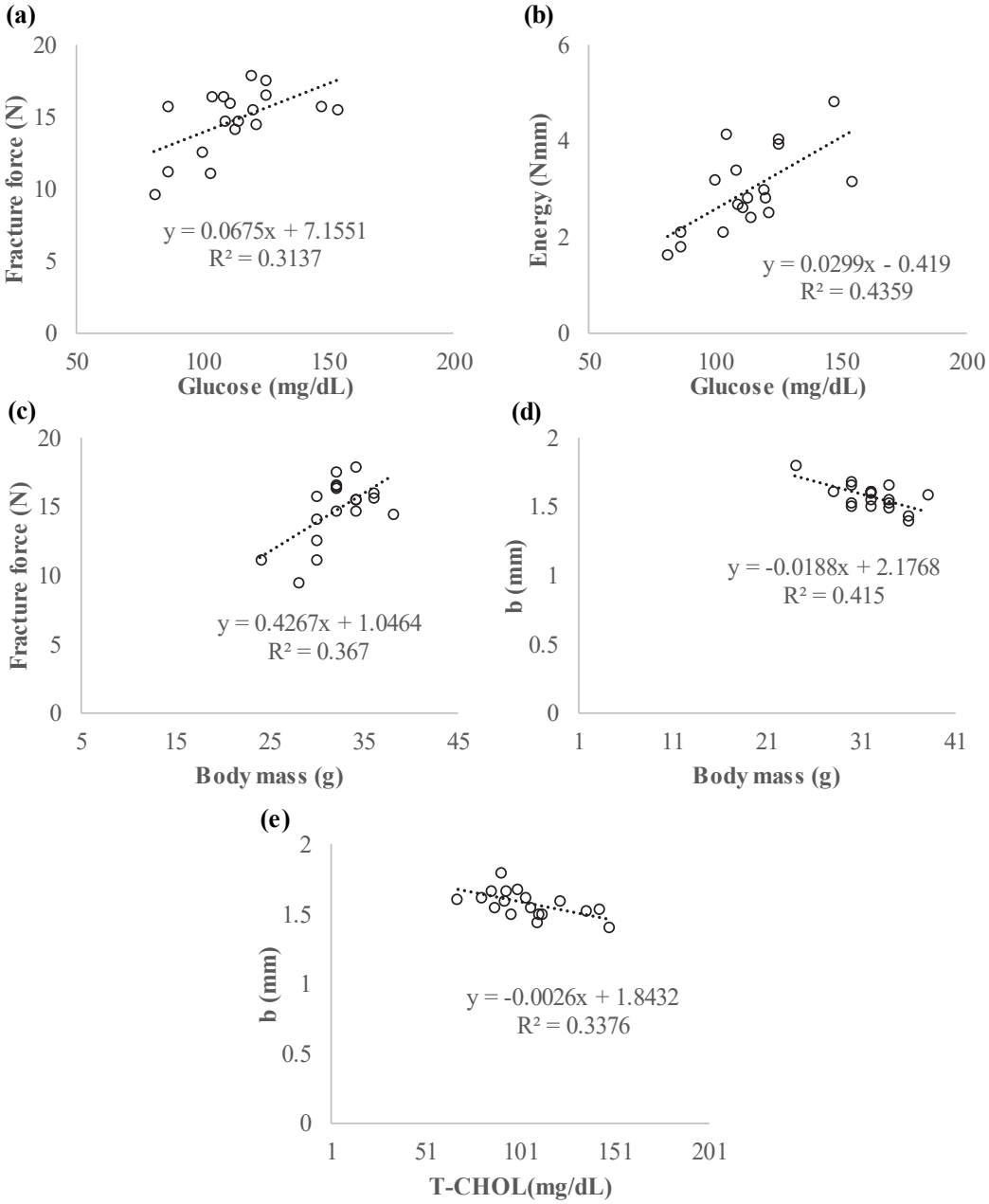

Figure 5: Correlations between biomechanical parameters, body mass and biochemical measurements.

DISCUSSION AND CONCLUSIONS

This study aimed to assess the effect of obesity and exercise on bone biomechanics and biochemical measurements and investigate the potentially beneficial role of exercise. For this purpose, a well-established mouse model of HFD–induced obesity was used [7, 15]. More specifically, mice were randomly assigned in three groups, namely control (group A), HFD with no exercise (group B) and HFD with exercise (group C). Body mass and relevant biochemical parameters were measured for the duration of the study (i.e. 37 weeks).

During the first 28 weeks of the experimental protocol groups B and C were exposed to exactly the same conditions. Indeed, exercise was not introduced to the protocol until the end of the 28th week. This means that analysing the results for the first 28 weeks enables only the assessment of the effect of HFD on body mass and the biochemical profile of the animals. Any difference between groups B and C up to week 28 could be attributed to variations that are inherent in in-vivo testing.

As expected HFD had a significant effect on body mass [15]. More specifically, the animals that received HFD gradually increased their body mass relatively to control with statistically significant differences appearing during the 28th week of the study. With regards to the biochemical measurements, HFD appears to consistently lead to higher levels of cholesterol (T-CHOL and HDL-C).

One way repeated measures ANOVA for group C indicates that the introduction of exercise is followed by some changes, including a drop in body mass, increase in TG levels etc. However, in most cases these changes are not substantial enough to make group C significantly different compared to group B (Fig. 3). The fact that the introduction of exercise didn't appear to lead to substantial changes in body mass and the biochemical profile of group C could be attributed to the specific exercise protocol employed in this study and its relatively limited duration (i.e. 9 weeks). Indeed, there is evidence in literature that exercise of different intensity, frequency and duration can lead to different results in animal HDL-induced obesity models [20].

The levels of adiponectin were also not affected by HFD or exercise. Adiponectin has been reported in literature to have a positive effect on bone properties by activating osteoblastogenesis and suppressing osteoclastogenesis, thus leading to increased bone mass [22]. However, the fact that the results of the present study didn't reveal any statistically significant difference between groups with regards to adiponectin levels means that no relevant conclusion can be drawn.

So far, the effect of exercise and diet on bone strength has been either inferred based on non-invasive measurements and/or computer modelling [23] or directly measured through in-vitro testing [19, 20, 24, 25]. The most commonly used testing techniques are three point bending and torsion which are typically used to measure the maximum sustained force [25] or moment [20], respectively as a measure of strength. These studies have indicated that obesity and exercise can affect both the structure and also the mechanical characteristics of bones [19, 23, 24]. Assessing ultimate stress along with the maximum sustained force enables separating the effect of changes in geometry from changes in the actual material properties of bone tissue [19, 24].

In order to enable the calculation of ultimate stress from the measured fracture force, the cross-section of the specimens was considered to be elliptical with constant thickness [21]. This simplification was deemed to be necessary considering the small size of the samples. Indeed, the longest cross-sectional distance was smaller than 3 mm.

The results from biomechanical testing indicated that the morphology and mechanical strength of femurs was significantly affected by diet and exercise. In terms of morphology, HFD appears to increase the external dimensions of femur regardless of the exposure to exercise. However, the group that received HFD but was not exposed to exercise (group B) also appeared to have significantly lower bone thickness compared to the other two groups. These findings indicate that exercise tends to limit the HFD-induced loss of bone mass by increasing the thickness of the femurs' cortical shell. Interestingly though, this positive effect of exercise was not translated into increased ultimate stress. Hence, both groups that received HFD had significantly lower ultimate stress relatively to control. No statistically significant difference was found in terms of fracture force or total energy.

The aforementioned findings are in agreement with observations linking obesity to the loss of bone mass and osteopenia [7, 8]. High-fat diets in particular have been found to reduce the ability for calcium absorption with possible adverse effects on bone mineralization in growing animals [8].

An investigation of correlations between biomechanical parameters, body mass and biochemical measurements that was focused only on the mice that received HFD (i.e. groups B and C) revealed strong positive associations between fracture force and serum glucose and body mass. More specifically, the femurs of mice that, at the end of the protocol, had higher body mass or glucose levels were found to be stronger compared to mice with lower body mass or glucose levels.

One of the key limitations of the present study is the relatively small number of femurs that were included in the biomechanical testing. Due to the small size of the samples a significant number was damaged during harvesting making it impossible to use them for testing.

In conclusion, the results of this study suggest that exercise can partially reverse the detrimental effects of HFD on bone biomechanics by increasing the thickness of the femurs' cortical shell and thus limiting the HFD-induced loss of bone mass. However, the aforementioned positive effect of exercise was not translated to increased bone strength. Further in vitro/in vivo studies in experimental models and clinical trials are required to unveil the effect of HFD and exercise on bone metabolism and strength.

REFERENCES

[1] Haslam, D.W., James, W.P.T., Obesity, Lancet, London, England, 366 (2005) 1197–209.

[2] Berrington de Gonzalez, A., Hartge, P., Cerhan, J.R., Flint, A.J., Hannan, L., MacInnis, R.J., et al., Body-mass index and mortality among 1.46 million white adults, N Engl J Med, 363 (2010) 2211–2219.

[3] Berghöfer, A., Pischon, T., Reinhold, T., Apovian, C.M., Sharma, A.M., Willich, S.N., Obesity prevalence from a European perspective: a systematic review, BMC Public Health, 8 (2008) 200.

[4] Van Coeverden, S.C., De Ridder, C.M,, Roos, J.C., Van't Hof, M.A., Netelenbos, J.C., Delemarre-Van de Waal, H.A., Pubertal maturation characteristics and the rate of bone mass development longitudinally toward menarche, J Bone Miner Res, 16 (2001) 774–781.

[5] Schwartz, A.V., Diabetes mellitus: Does it affect bone?, Calcif Tissue Int., 73 (2003) 515–519.

[6] Felson, D.T., Zhang, Y., Hannan, M.T., Anderson, J.J., Effects of weight and body mass index on bone mineral density in men and women: the Framingham study, J Bone Miner Res, 8 (1993) 567–573.

[7] Patsch, J.M., Kiefer, F.W., Varga, P., Pail, P., Rauner, M., Stupphann, D., et al., Increased bone resorption and impaired bone microarchitecture in short-term and extended high-fat diet-induced obesity, Metabolism, 60 (2011) 243–249.

[8] Wohl, G.R., Loehrke, L., Watkins, B.A., Zernicke, R.F., Effects of high-fat diet on mature bone mineral content, structure, and mechanical properties, Calcif Tissue Int, 63 (1998) 74–79.

[9] Reid, I.R., Plank, L.D., Evans, M.C., Fat mass is an important determinant of whole body bone density in premenopausal women but not in men, J Clin Endocrinol Metab, 75 (1992) 779–782.

[10] Barondess, D.A., Nelson, D.A., Schlaen, S.E., Whole body bone, fat, and lean mass in black and white men, J Bone Miner Res, 12 (1997) 967–971.

[11] Trayhurn, P., Beattie, J.H., Physiological role of adipose tissue: white adipose tissue as an endocrine and secretory organ, Proc Nutr Soc, 60 (2001) 329–339.

[12] Díez, J.J., Iglesias, P., The role of the novel adipocyte-derived hormone adiponectin in human disease, Eur J Endocrinol, 148 (2003) 293–300.

[13] Lihn, A.S., Pedersen, S.B., Richelsen, B., Adiponectin: Action, regulation and association to insulin sensitivity, Obes Rev, 6 (2005) 13–21.

[14] Gavrila, A., Chan, J.L., Yiannakouris, N., Kontogianni, M., Miller, L.C., Orlova, C., et al. Serum adiponectin levels are inversely associated with overall and central fat distribution but are not directly regulated by acute fasting or leptin administration in humans: Cross-sectional and interventional studies, J Clin Endocrinol Metab, 88 (2003) 4823–4831.

[15] Buettner, R., Schölmerich, J., Bollheimer, L.C., High-fat diets: modeling the metabolic disorders of human obesity in rodents, Obesity (Silver Spring) 15 (2007) 798–808.

[16] Nikander, R., Sievänen, H., Heinonen, A., Daly, R.M., Uusi-Rasi, K., Kannus, P., Targeted exercise against osteoporosis: A systematic review and meta-analysis for optimising bone strength throughout life, BMC Med, 8 (2010) 8:47.

[17] Shimano, R.C., Macedo, A.P., Falcai, M.J., Ervolino, E., Shimano, A.C., Issa, J.P.M., Biomechanical and microstructural benefits of physical exercise associated with risedronate in bones of ovariectomized rats, Microsc Res Tech, 77 (2014) 431–438.

[18] Gerbaix, M., Metz, L., Mac-Way, F., Lavet, C., Guillet, C., Walrand, S., et al., A well-balanced diet combined or not with exercise induces fat mass loss without any decrease of bone mass despite bone micro-architecture alterations in obese rat, Bone, 53 (2013) 382–390.

[19] Miyagawa, K., Kozai, Y., Ito, Y., Furuhama, T., Naruse, K., Nonaka, K., et al., A novel underuse model shows that inactivity but not ovariectomy determines the deteriorated material properties and geometry of cortical bone in the tibia of adult rats, J Bone Miner Metab, 29 (2011) 422–436.

[20] Macedo, A.P., Shimano, R.C., Ferrari, D.T., Issa, J.P.M., Jordão, A.A., Shimano, A.C., Influence of treadmill training on bone structure under osteometabolic alteration in rats subjected to high-fat diet, Scand J Med Sci Sports, 27 (2017) 167–176.
[21] Mandi, J.L., Markel, D.M., Bending tests of bones. In: An, Y., Draughn, R., editors, Mechanical testing of bone and thew bone-implant interface, Boca Raton: CRC PRESS, (2000) 207–217.
[22] Oshima, K., Nampei, A., Matsuda, M., Iwaki, M., Fukuhara, A., Hashimoto, J., et al., Adiponectin increases bone mass by suppressing osteoclast and activating osteoblast, Biochem Biophys Res Commun, 331 (2005) 520–526.
[23] Woo, D.G., Lee, B.Y., Lim, D., Kim, H.S., Relationship between nutrition factors and osteopenia: Effects of experimental diets on immature bone quality, J Biomech, 42 (2009) 1102–1107.
[24] Fried, A., Manske, S.L., Eller, L.K., Lorincz, C., Reimer, R.A., Zernicke, R.F., Skim milk powder enhances trabecular bone architecture compared with casein or whey in diet-induced obese rats, Nutrition, 28 (2012) 331–335.
[25] Lambert, J., Lamothe, J.M., Zernicke, R.F., Auer, R.N., Reimer, R.A., Dietary restriction does not adversely affect bone geometry and mechanics in rapidly growing male wistar rats, Pediatr Res, 57 (2005) 227–231.

Structural interventions on the drums of the Parthenon's north colonnade

Marilena Mentzini
Structural Engineer, Ph.D., Ministry of Culture and Sports, Greece
mmentzini@culture.gr

ABSTRACT. The Acropolis monuments are globally recognized as a cultural heritage and a value belonging not only to Greece but also to Humanity. From 2000 the most recent phase of restoration in their history began by the "Acropolis Restoration Service" (YSMA), introducing new, pioneering methods, recognized now worldwide. Especially the restoration of the Parthenon's North Colonnade is an enormous work-plan to be carried out (extended area of intervention, great number of members to be restored and high degree of damages). Moreover, the structural stability of the Parthenon's north colonnade is among the most important challenges confronted by experts working in this sector. The complexity of this effort (a combination of scientific research and direct field application) makes the implementation of the restoration project difficult, rendering its division into smaller projects (for similar structural members) a necessity. In this direction, characteristic examples of the procedure followed for the structural intervention on the drums are presented in this paper. Each member's report includes a short history of its restoration, the intervention steps, pictures/sketches and the methodology chosen for its structural study, focusing on the particularities of the member and the in-field realization [1].

KEYWORDS. Classical Monuments; Drums; Fracture; Restoration; Titanium reinforcement, Parthenon, Acropolis of Athens

Citation: Mentzini. M., Structural intervention on the drums of the Parthenon's north colonnade, Frattura ed Integrità Strutturale, 40 (2017) 95-107.

Received: 16.01.2017
Accepted: 12.03.2017
Published: 01.04.2017

INTRODUCTION

The determination of the reinforcement required to join together multi-fragmented structural members is a prerequisite for properly restoring the member's structural stability and also for preventing further damages. For the structural restoration of the monuments of the Acropolis of Athens a pioneer method has been developed, already from the early seventies. According to this method fragments of authentic marble or/and supplements of new marble are joined together using titanium bars and suitable cement mortar [2].
The final target is to reach the capacity which corresponds to the maximum load expected to be exerted on the particular member after the completion of the project (taking into account all possible future interventions). This approach is preferred

because usually the reinforcing titanium bars required for reaching the initial carrying capacity can not be fitted due to the shape of the sections of the members, the relatively small size of the remaining authentic parts of the member or the great loss of authentic material [3].
The material used for the erection of the monuments of the Athenian Acropolis was Pentelic marble, well known as the building material of the classical period's masterpieces. The needs of the restoration project in progress (for the construction of "patches" and a few new members) are covered nowadays using Dionysos marble (quarried from mountain Dionysos in Attica), which has similar properties to the authentic one.
In general, the data reported in literature concerning Dionysos marble vary between very broad limits. This scattering can be attributed to the different conditions under which the tests are performed but mainly to the anisotropy of Dionysos marble. There are three different anisotropy directions (parallel to the layers, along the width of the web and along its thickness). After a long series of direct tension and uniaxial compression tests, it was concluded that the mechanical properties along the two of the anisotropy directions are very similar to each other [4-6]. Thus, this marble can be considered as a transversely isotropic material described with the aid of five elastic constants: two elastic moduli, in the plane of transverse isotropy and normal to it, two Poisson's ratios characterizing the lateral strain response in the plane of transverse isotropy to a tensile stress acting parallel and normal to it, and the shear modulus in the planes normal to the plane of isotropy. From these tests it was also concluded that the material appears to be slightly bimodular, i.e. its elastic moduli in tension and in compression are not equal. The combination of these mechanical characteristics with the special internal structure and composition of the material (mainly calcite with very small amounts of muscovite, sericite, quartz, chlorite and areas with imperfections) is responsible for the complicated form of the cracks observed. The shape and extent of the damages are also affected by the particular role of the drums as structural members [7].
In general, the damage of the monument is due to either natural phenomena or human interventions. Among the natural phenomena one could mention aging (and, as already pointed out, the special nature and the imperfections of the material), decay due to physico - chemical/biological actions, freezing, seismic action etc. Catastrophic human interventions include fire, bombing, explosion, vandalism, the problems caused by previous restoration (in the eve of the 20th century) by engineer N. Balanos (thoughtless use of iron elements, which after oxidization expand becoming the origin of a destructive process for the marble surrounding iron elements) and finally the effects of pollution [8, 9].
The first serious damage in Parthenon was caused by the great earthquake of 426 B.C.. The most serious destruction came at 267 A.D., by a German tribe, the Erouli, who burned the place down. During the siege of the Acropolis by the Morosini's Venetians (1687 A.D.) an explosion blew up three of the four walls of the cella, six columns on the south, eight ones on the north (the area of interest in the present paper) and the remains of Pronaos collapsed except one column [9].
Parthenon Temple is a structural system with special characteristics. The form and the stability of the structure are attained by the perfect contact between the members (absence of connecting material) which leads to the development of friction and the use of horizontal (clamps) and vertical (dowels) metallic connectors that resist tensile and shear forces. Thus a complex construction is formed, the dynamic response of which is governed by the sliding and the rocking of the individual stones, either independently or in groups [10].
The process followed to restore the structural integrity of each drum (in order to make it behaving again as an intact member) is based on the principle of avoiding overturning of the fragment (that is to be joined) from the member (in case friction forces are not sufficient) [11, 12]. The method is improved by taking also into account the critical stress state on its surface. It has the advantage of flexibility and therefore it can be applied in many different cases. The reinforcement required is calculated based on the fragment's volume which sustains the load, its position relative to the drum and its height. Therefore the stress field developed can be estimated taking into account the overturning lever arm and the load applied [3].
Dynamic actions, in this case earthquake and explosion, can lead to drums' raising and loss of their proper position, while the rocking effect produces impact phenomena among adjacent members. This impact damages particularly the edges of the contact area between them, which is linear and consists schematically an arc [13, 14]. As a result fragments are produced, which usually form wedges and the presence of converging strata make it easier for fracture to start [7]. To cope with these problems a special procedure was developed, in collaboration with late Pr. I. Vardoulakis, of the Department of Mechanics (National Technical University of Athens) to determine the stress state and therefore the reinforcement required [1, 15].
The restored drums are usually classified with respect to the corresponding column (4th to 11th) with codes representing their original position. Each drum is denoted by two numbers: The first one indicates the column on which they belong (the columns counting starts from East to West; therefore the eight columns of the North's Colonnade Restoration program have codes 4 to 11) and the second number indicates their exact position on the specific column (the drums counting starts from the lowest one, i.e. the one standing on the stylobate). For example the drum with the code "5.8" belongs to the 5th column and stands on the 8th row.

APPLICATION IN THE FIELD

It's very difficult to categorize the Parthenon's North Colonnade's drums failures because they were caused mainly due to their fall after the Morosini's explosion and as a result in many cases the traces of former fractures were covered. The variety of fragments and remains (many of them were carved during N. Balanos' restoration project) offers the challenge to confront unusual structural problems [15]. It is mentioned characteristically that even in a single member, it is possible to deal with one or more of the following cases:

- Join of fragments or supplements which form wedges on the upper or the lower area of the ancient remain.
- Repair a fracture which penetrates all over the height or the width of the drum and at the same time join supplements, which extend all over the height or the width of the drum.
- Join small fragments to the remaining volume of the drum as well as to repair huge cracks by replacing the existing "Π" and double "Ι" iron connectors (a short of clamps) which were placed during the previous restoration by N. Balanos. The proper new ones are made of titanium.
- Create supplements, which include ancient remains.
- Implant ancient fragments in new volumes of marble.
- Join of almost horizontal ancient fragments standing the one above the other.
- Join supplements to the ancient remain core forming the upper or the lower area of the drum.
- Join fragments all-around to a new marble's core.
- Join ancient volumes to a supplement which surrounds all over their height, while at the same time due to the lack of parts of their upper and lower side of the drum, new supplements were also used in these areas.

Due to the irregular shape of the fragments a number of problems often arise during the intervention, which makes it extremely difficult to join the new supplements with ancient sections of the member and to determine a certain direction of the reinforcement bars. In these cases the theoretical approach has to be in situ redesigned.
Attention is paid to avoid crossing of the reinforcement bars coming from different directions, to maintain the proper distance between them, as well as between reinforcement bars and the drum's external surface or the various irregularities /discontinuities in its mass. It is also very important to maintain the proper anchorage length of the reinforcement bars in order for extrusion (or pull-out) to be avoided.

Figure 1: Joining together the ancient fragments A, B, Γ, with the new insert Π to keep them in the right position within the member's volume using cement mortar (left). The joining of this group and the main block of a new marble with "montage" reinforcement bars is presented in the right photo. In the foreground view the opposite fractured surface and the points, where reinforcing bars will be inserted during the next step of intervention, are presented. (Author's note: All pictures in this paper are from the archive of YSMA).

After the intervention, a continuous monitoring and control of the member's response must follow since the work that has been done must provide flexibility to permit future interventions if necessary.
The tactic, complexity and difficulty of the steps' sequence for the intervention of the drums are presented here with a few characteristic examples.

Drum 4.4

The only remains of the member are three ancient pieces (see Figs. 1, 2 and 3).

Figure 2: The aforementioned complex is joined to a new supplement along the height of the drum (depicted in the foreground on the left).

The final join was accomplished by inserting titanium bars which were parallel to the member's upper side from the new fractured area created (for the sake of the volume's formation). This reinforcement is the proper one in order to avoid overturning of each one of the two parts, before the overturning of the drum as a whole. The ancient fragments were captured between the two supplements. Also some of the reinforcement bars penetrate the fragments.

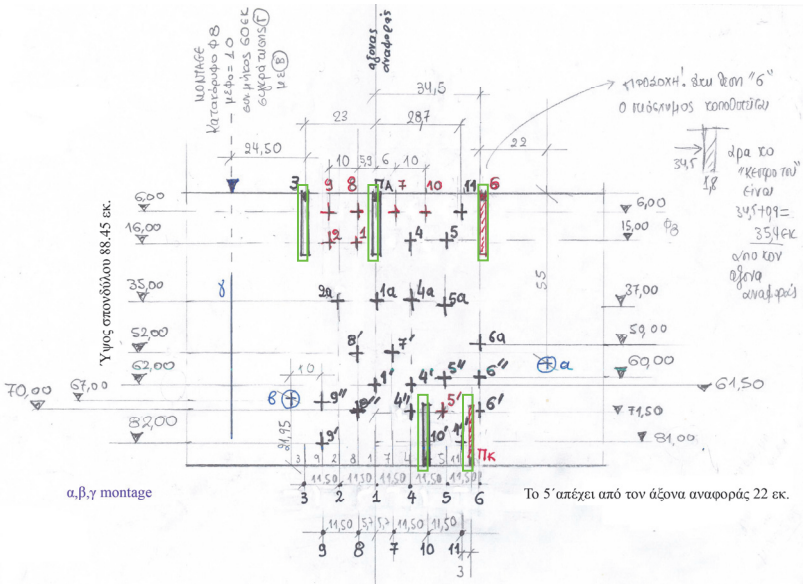

Figure 3: Sketch of the cross-section of the fractured surface of the drum between the two main supplements. The position of the inserted reinforcing bars is fully documented. It is noteworthy that some of the bars determined from the structural study, were replaced by "ΙΙ" shape titanium connectors (highlighted by green colour) to avoid further loss of material. The combination of bars' diameter (i.e. strength) and position provides the required stability moment.

Drum 5.11

Only a part of the drum, less than one quarter of the original volume was maintained (symbolized by the letter B, see Fig.4). To restore the member and form the initial shape two supplements of mew marble were created (A and Γ, see Fig.4). The procedure includes first the join of the supplement A to the ancient volume B (Fig.5 on the left) and afterwards the join of

the unified complex of A+B to the supplement Γ (Fig.5 on the right). During these steps the join of these parts was accomplished by inserting titanium bars parallel to the member's upper side from the fractured - contact areas. This reinforcement is the proper one to avoid overturning of the supplements as well as of the ancient remains, before the overturning of the drum as a whole.

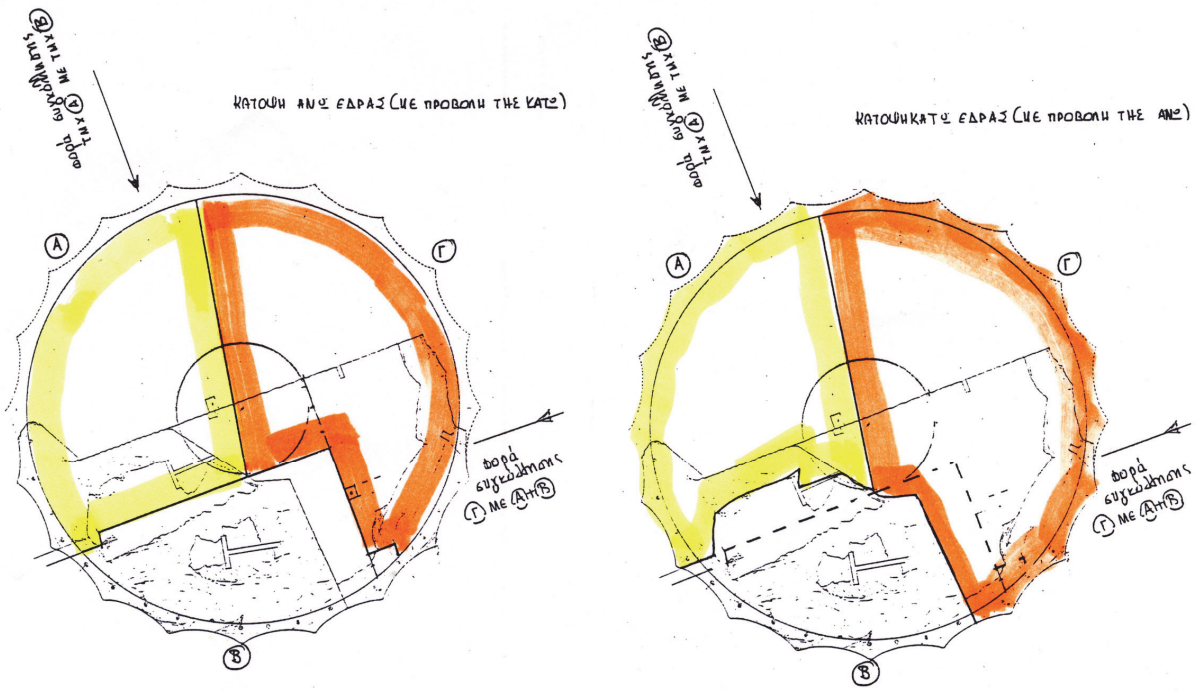

Figure 4: Sketch of the upper (left sketch) and lower (right sketch) side's plan of the drum where the place of the two supplements (A highlighted by yellow and Γ by orange color) and the direction of the required reinforcement are depicted. On the right sketch the dotted lines correspond to the upper side of the ancient part.

Figure 5: Joining the supplement A to the ancient volume (on the left). The supplement Γ with the proper reinforcement on it, is ready to be joined to the rest of the drum (on the right).

Drum 6.3

The ancient member almost maintains its shape, although two parts are missing: one, which forms a gap of wedge's shape in the upper side of the drum and an adjacent one, which extends all over the drum's height. In addition a crack runs across its lower side, which produces, as it was found out, an inclined fracture level (Fig.6a). The supplement used to fill the first mass loss is joined to the main volume by titanium bars which resist shear forces (one horizontal bar - Fig.6b and the remaining ones in different directions after the fitting of the two volumes using suitable cement mortar, from the upper side of the supplement - Fig.7a) to avoid sliding. The supplement used to fill the second gap is joined to the main

volume with horizontal internal titanium bars (Fig.7b). This reinforcement is the proper one to avoid overturning of the supplement. Finally titanium bars are also inserted from the bottom of the drum, vertical to the existent plane of fracture to repair the crack (Fig.8). This reinforcement was determined by zeroing the internal moments from the equilibrium of the fragment which probably will be created by the fracture's completion.

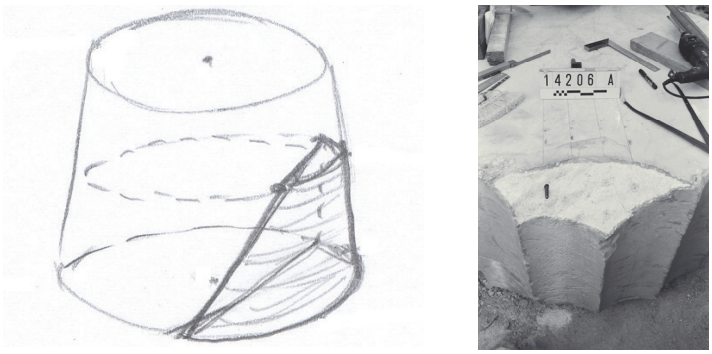

(a) (b)

Figure 6: (a) Sketch of the inclined fracture plane produced by the crack which runs across the lower side of the drum (Drawing: M. Mentzini, YSMA Archive). (b) As a first step, the supplement used to fill the first mass loss is joined to the main volume by one horizontal titanium bar.

(a) (b)

Figure 7: (a) Titanium bars are inserted from the upper side of the supplement used to fill the first mass loss after its fitting with the main volume of the drum. The second fracture is discernible on the left. (b) The supplement used to fill the second mass loss is joined to the main volume with horizontal internal titanium bars.

Figure 8: Titanium bars are inserted to repair the crack. In this picture the drum is upside down.

Drum 7.8

The ancient member was broken in two main fragments (probably due to the Morosini's explosion) which were joined together through iron clamps during the previous restoration of N. Balanos. Nowadays, the two pieces are joined together

using horizontal titanium internal bars as reinforcement and suitable cement mortar to avoid their overturning (Fig.9a). In addition the double "T" iron connectors were replaced by new titanium ones which contributes to the strength required (Fig.9b). Furthermore three supplements of new marble are created to complete the drum's shape. Two supplements fill the gaps in the upper side of the drum and they are joined to the ancient volume only through montage reinforcement because of their balance state due to their shape (Figs.10a,b), while the third supplement was used between the two main fragments, forming a wedge. The reinforcement required for the latter one to resist shear stresses to be developed, was inserted from the drum's lower side, after its fitting with the rest drum's volume using cement mortar (Fig.11). In this way (easier to adjust the pieces) the holes are invisible after the drum will be placed on the column.

(a) (b)

Figure 9: (a) The two main fragments of the drum are joined together using titanium bars. (b) Replacing the double "T" iron connectors by new titanium ones on the upper side of the drum.

(a) (b)

Figure 10: (a) Titanium bars ware inserted from the upper side of the first supplement after its fitting with the rest volume of the drum. (b) Titanium bars were inserted from the upper side of the second supplement after its fitting with the rest volume of the drum.

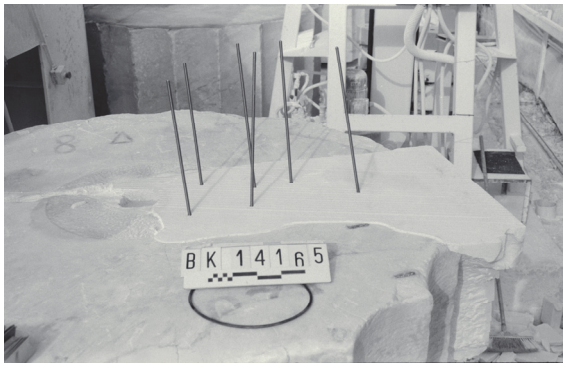

Figure 11: Titanium bars were inserted from the lower side of the third supplement after its fitting with the rest volume of the drum.

Drum 8.8

The ancient member is characterized by two losses of material sited in opposite areas all over its height. To restore the drum's volume two supplements of new marble are created. Their join to the ancient remain core was accomplished by inserting titanium bars which were parallel to the member's upper side from the fractured area (Figs.12a,b). This reinforcement is the proper one to avoid overturning of the supplements, before the overturning of the drum as a whole.

(a) (b)

Figure 12: (a) Joining the first supplement. (b) Joining the second supplement. On the left the first –raw- supplement is already joined.

Drum 9.5

Although the drum seems intact, a fracture plane runs across its upper side and through its mass –allover its height- reaching the center of the lower side. Both upper and lower sides were carved during N. Balanos' restoration and three iron clamps -of double "T" shape- were inserted (two clamps on the upper side and one on the lower one). Nowadays the restoration of the drum requires more reinforcement, therefore the iron clamps were substituted by new ones made of titanium and some extra reinforcement was also added. The additional reinforcement (titanium bars) was inserted in certain areas through both sides of the drum and their direction was 30° with respect to the horizontal level in order to succeed the proper combination of bars' strength and forces lever arm (Figs.13a,b,c). The required moment was calculated so as to avoid the separation of the drum in two fragments i.e. to succeed the stability of each one.

(a) (b) (c)

Figure 13: (a) Inserting reinforcement on the upper side. (b) Inserting reinforcement on the lower side. (c) Inserting reinforcement bar to repair a small crack on the upper side through the Balanos' mortise, before replacing the clamp.

Drum 10.9

Although the drum maintains its shape, a fracture plane runs across its upper side and through its mass - all over its height - reaching the lower side of the drum all over its width (Fig.14a). Three iron clamps - of double "T" shape - were placed in mortises carved on the surface of the drum, during N. Balanos' restoration, to repair the crack only on the upper side. Nowadays the restoration of the specific drum requires more reinforcement. The iron clamps were replaced by new titanium ones and the additional reinforcement (titanium bars) was inserted normal to the fracture plane, from areas of the drum's view which exhibit marks of decay and having lost their original ancient surface (Fig.14b, Fig.15), so as to achieve the

proper combination of bars' strength and forces lever arm in order to avoid the separation of the drum in two fragments i.e. to ensure the stability of each part.

(a) (b)

Figure 14: (a) View of the fracture plane. (b) Inserting the reinforcement on the lower side of the drum. In this picture the drum is upside down.

Figure 15: Inserting the reinforcement on the upper side's area. The red arrow in the left figure points out the crack's tips.

Drum 11.6

Two areas of the ancient member have severe material losses. The first area, which forms a wedge of 45.50cm height, is on the upper side of the drum (depicted schematically in Fig.16 and symbolized by the letters DF). The second one extends all over the drum's height and it is symbolized by the letters D_1F_1 in Fig.16. In addition a crack appears on the upper side, it is symbolized by the letters ΔF_1 in Fig.16, which runs between the aforementioned mass losses, creating a fragment of 34.50cm height (ΔFF_1 top view on the upper side in Fig.16). Finally a severe crack extends allover the height of the drum through the second loss's surface creating a fault (symbolized by the letters df_2 in Fig.16).

The sequence of the actions taken is the following:

1. To restore the drum's volume two supplements of new marble are created. The join of the supplement "DF" to the ancient remain core was accomplished by inserting titanium bars (to resist tensile and compression forces and subsequently to avoid overturning of the main volume or/and separation from the main volume) from its external surface, after the two volumes came into contact using cement mortar and montage reinforcement (Fig.17). In the next step the main reinforcement (titanium bars) was inserted from outside. In order to achieve the proper anchorage length of the bars, because of the thin thickness of the new volume, the end of the bars has been specially threaded to fit a screw nut through a titanium plate anchor (Fig.18 on the left).
2. The join of the fragment "ΔFF_1" to the ancient remain core to avoid separation was accomplished by inserting inclined titanium bars forming 38^0 to the horizontal level, through holes of the drum's view (created from N. Balanos during the intervention). One of the bars used for the join of the supplement "DF", contributes to the strength required (Fig.17).
3. To repair the crack "df_2" (avoid the separation of the possible resulting fragment from the rest of the drum's volume, prohibiting its overturning), titanium bars were inserted from the fracture plane of surface "D_1F_1" on the upper side of the drum, while the extension of two of the bars used for the join of the supplement "DF", contributes to the strength

required. On the lower side of the drum the reinforcement was inserted from outside, from areas of the drum's view, which appeared marks of decay, loosing their original ancient surface (Fig.18 right).

4. Finally, the join of the supplement to the ancient marble to fill the loss "D_1F_1" was accomplished by inserting titanium bars both on the upper and on the lower side of the drum through the fractured area with direction parallel to the member's upper side (Fig.19 left). This reinforcement is the proper one to avoid overturning of the supplement, before the overturning of the drum as a whole. In order to achieve the proper anchorage length of the reinforcement on the supplement's lower area, because of the thin thickness of the new volume there, the end of these bars has also been specially threaded to fit a screw nut through a titanium plate anchor (Fig.19 right).

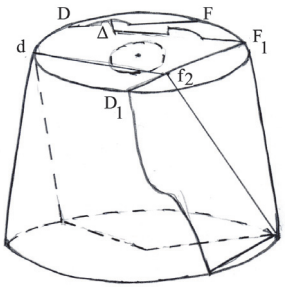

Figure 16: Sketch of the failures of the drum (Drawing: M. Mentzini, YSMA Archive).

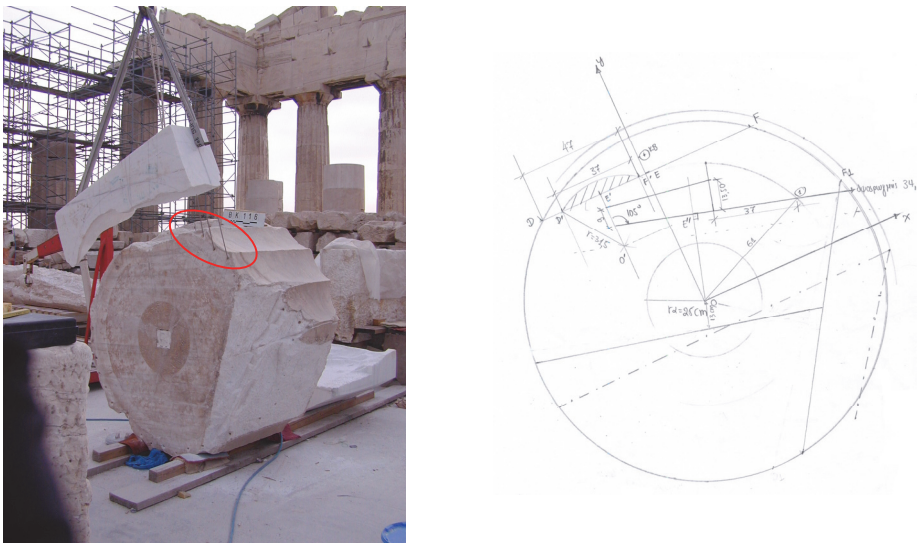

Figure 17: Adjusting a new marble (supplement "DF") onto the upper side of the drum (left). Near by, the reinforcement required to restore the fragment "ΔFF_1" is presented (ellipse in the left figure). Drawing of the parts to be joined together and their geometry for the calculation of the stress field and consequently the reinforcement required (right) (Drawing: M. Mentzini, YSMA Archive).

Figure 18: After joining the supplement "DF" to the main volume of the drum, the holes (in order to adjust the titanium plate anchor) on its surface sealed with the pieces of the extruded new marble (on the left). Repairing the crack "df_2" (on the right).

Figure 19: Inserting titanium bars on the upper side's area of the drum to join the supplement "D_1F_1" to the ancient marble (on the left). After joining the supplement "D_1F_1" to the main volume of the drum, the holes on its surface (in order to adjust the titanium plate anchor) sealed with the pieces of the extruded new marble (on the right).

Fracture detection

During the intervention of the Parthenon's North Colonnade forty-seven (47) drums were structurally restored while the study and the structural intervention for additional fourteen (14) ones have been supervised (in total sixty-one (61) members).

It is noteworthy that although most of the damages were caused from the members' fall due to Morosini's explosion, and many remains were worked out by N. Balanos, changing the shape of the fracture planes of the members as well as their original exact position on the monument, the detailed observation and the data processing succeeded to identify and verify the conclusions of previous research. For example an existing fracture and the consequent loss of mass at drums cause similar failures to the adjacent ones, a kind of imprints. During rocking a severe stress field is developed in the edge of the remaining part of the drum, leading to the creation of cracks at the adjacent members. As a result the bearing capacity and behaviour under seismic loading of the entire structure are drastically deteriorating. Therefore it is necessary to repair the damages and restore them even using new marble supplements [7].

In case of the drums of the Parthenon's North Colonnade, fractures' coincidence has been detected between the following members:

- The upper side of 4.8 in correspondence to the lower side of 4.9
- The upper side of 5.6 in correspondence to the lower side of 5.7
- The upper side of 6.3 in correspondence to the lower side of 6.4
- The upper side of 6.4 in correspondence to the lower side of 6.5
- The upper side of 6.5 in correspondence to the lower side of 6.6
- The upper side of 6.6 in correspondence to the lower side of 6.7
- The upper side of 6.7 in correspondence to the lower side of 6.8
- The upper side of 9.7 in correspondence to the lower side of 9.8
- The upper side of 10.9 in correspondence to the lower side of 10.10

Conclusions

The structural interventions on ancient members during the extensive restoration program of the Parthenon Temple on the Acropolis of Athens, offers to the scientists working in this field an in depth knowledge of the stress and strain fields developed in the structural elements to be restored.

In addition the scientist has to face the challenge of redesigning and adapting the results of the already described theoretical process to achieve the structural integrity of ancient members in a way, which is flexible during its realization.

The shape of the remaining ancient volumes determines the exact geometry of the supplements since their contact areas must be perfectly fitted. As a result the direction of the reinforcement needed is limited.

The present paper reveals the special skill, imagination and creativity of the scientists in order to determine the sequence of actions which must be undertaken to join the pieces forming the drum and to apply the proper reinforcement so as the structural integrity of the drum as a whole to be achieved. In this way in many cases the same reinforcement expands to cover the structural needs of another section.

Moreover, the problems arising due to the irregular shape of fracture's planes or the discontinuities in marble mass, could be solved by changing the number, the diameter or/and the place of the reinforcement bars and keeping in the same time the produced stress field constant. If internal reinforcement bars can not be used (so as to be unseen) because of the inability of the adjustment or the maintenance of the proper anchorage length, alternative solutions are invented, such as: the insert from the sides (which will be covered when the drums will be placed back in their initial position on the column) or from areas of the drum's view, which exhibit marks of decay, having lost their original ancient surface. Even the mortises of N. Balanos' restoration are used to insert bars or to place "Π" and double "T" shape titanium connectors to contribute to the stress required and also to minimize further loss of the authentic material.

As it was pointed out before, the previous restoration by the engineer N. Balanos changed in many cases the original exact position of the drums. During the structural intervention of the dismantled pieces the access to their fractured areas and the verification of coincidence between different members' fractures, reveal their original position and identify whether the certain drum belongs or not to a certain position on the column. Thus by these observations the original exact position of the drums was also confirmed in perfect agreement with the findings of the Architectural study [16].

REFERENCES

[1] Mentzini, M., Report of the project of the Parthenon's North Colonnade restoration, Ancient members' structural intervention: Columns and architraves. The Drums, vol. A, Archives of the General Direction of Antiquities and Cultural Heritage (2015).

[2] Zambas, C., Ioannidou, M., Papanikolaou, A., The use of titanium reinforcements for the restoration of marble architectural members of Acropolis Monuments, Proc. IIC Congress on Case Studies in the Conservation of Stone and Wall Paintings, Bologna: The International Institute for Conservation of Historic and Artistic Works, (1986) 138-143.

[3] Mentzini, M., Joining together architraves and drums of Parthenon using titanium: A new approach, Proc. 5th Int. Symp. for the Restoration of Acropolis Monuments, Athens: Committee for the Preservation of the Acropolis Monuments (2002) 233- 242.

[4] Exadaktylos, G.E., Vardoulakis, I., Kourkoulis S.K., Influence of nonlinearity and double elasticity on flexure of rock beams - II. Characterization of Dionysos marble, International Journal of Solids & Structures, 38 (2001) 4119-4145.

[5] Kourkoulis, S.K., Exadaktylos, G.E., Vardoulakis I., *U*-notched Dionysos-Pentelicon marble in three point bending: The effect of nonlinearity, anisotropy and microstructure, International Journal of Fracture, 98 (1999) 369-392.

[6] Kourkoulis, S.K., Prassianakis, I., Agioutantis, Z., Exadaktylos, G.E., Reliability assessment of the NDT results for the internal damage of marble specimens, International Journal of Material and Product Technology, 26 (2006) 35-56.

[7] Mentzini, M., Drums' fracture-The example of the 6th column of Parthenon's Pronaos, Proc. 8th Int. Sym. on the Conservation of Monuments in the Mediterranean Basin, M. Koui & F. Zezza (eds.), Patras, Greece (2010) 56-57.

[8] Balanos, N., The Restoration of the Acropolis monuments, Editor S.N.Taroussopoulos, Athens, (1940)

[9] Korres, M., Bouras, H., Study for the restoration of the Parthenon, Athens: Ministry of Culture of Greece, Committee for the Preservation of the Acropolis' Monuments (1983).

[10] Mentzini, M., Structural interventions on the Acropolis monuments, Newsletter of the Acropolis restoration service of the Ministry of Culture of Greece, 6 (2006) 15–18.

[11] Zambas, C., Structural problems of the restoration of the Parthenon, Vol.2a, Athens: Committee for the Preservation of the Acropolis Monuments (1989).

[12] Zambas, C., Structural problems of the restoration of the Parthenon, Vol.3b, Athens: Committee for the Preservation of the Acropolis Monuments (1994).

[13] Psycharis, I.N., Lemos, J.V., Papastamatiou, D.Y., Zambas, C., Papantonopoulos, C., Numerical study of the seismic behaviour of a part of the Parthenon Pronaos, Earthquake Engng. Struct. Dyn., 32 (2003) 2063-2084.

[14] Psycharis, I.N., Seismic Response of Classical Monuments with Fractured structural elements, in "Fracture and Failure of Natural Building Stones", Stavros K. Kourkoulis (ed.), Springer, Berlin (2006) 239-255.

[15] Mentzini, M., Columns and architraves: the process of structural intervention, in: Interventions on the Acropolis monuments 2000-2012, The completed programmes, Proc. 6th Int. Symp. for the Restoration of Acropolis Monuments, Athens: Committee for the Preservation of the Acropolis Monuments (2013) 1-24.

[16] Lambrinou L., Resetting of columns and architraves of the North Colonnade, in: Interventions on the Acropolis monuments 2000-2012, The completed programmes, Proc. 6th Int. Symp. for the Restoration of Acropolis Monuments, Athens: Committee for the Preservation of the Acropolis Monuments (2013) 1-27.

The multi-layered ring under parabolic distribution of radial stresses combined with uniform internal and external pressure

Christos F. Markides, Ermioni D. Pasiou, Stavros K. Kourkoulis
National Technical University of Athens, School of Applied Mathematical and Physical Sciences, Department of Mechanics, 5 Heroes of Polytechnion Avenue, Theocaris Bld., Zografou Campus, 157 73 Athens, Greece

ABSTRACT. A recently introduced solution for the stress- and displacement-fields, developed in a multi-layered circular ring, composed of a finite number of linearly elastic concentric layers, subjected to a parabolic distribution of radial stresses, is here extended to encompass a more general loading scheme, closer to actual conditions. The loading scheme includes, besides the parabolic radial stresses, a combination of uniform pressures acting along the outer- and inner-most boundaries of the layered ring. The analytic solution of the problem is achieved by adopting Savin's pioneering approach for an infinite plate with a hole strengthened by rings. Taking advantage of the results provided by the analytic solution, a numerical model, simulating the configuration of a three-layered ring (quite commonly encountered in practical applications) is validated. The numerical model is then used for a parametric analysis enlightening some crucial aspects of the overall response of the ring.

KEYWORDS. Multi-layered ring; Parabolic pressure; Stress and displacement fields; Uniform pressure; Complex potentials.

Citation: Markides Ch.F., Pasiou E.D., Kourkoulis S.K., The multi-layered ring under parabolic distribution of radial stresses combined with uniform internal and external pressure, Frattura ed Integrità Strutturale, 40 (2017) 108-128.

Received: 12.02.2017
Accepted: 12.03.2017
Published: 01.04.2017

INTRODUCTION

In a recently published paper [1] the stress- and displacement-fields developed in a circular multi-layered ring were considered both analytically and numerically. The ring was composed by a finite number of concentric layers made of different linearly elastic materials and it was loaded by a parabolic distribution of radial stresses acting along two finite arcs of the outer boundary of the outer-most layer. In general, the configuration of multi-layered rings is common in quite a few engineering applications of increased interest, ranging from Biomechanics (human aorta) to Fluid Mechanics (insulated pipes). Such composite rings are usually loaded either by uniformly distributed internal or external pressure or by a combination of them.

In the study by Markides et al. [1] a more complicated loading scheme was considered consisting of radial stresses acting along two finite arcs of the external boundary of the outer-most layer (antisymmetric with respect to the geometric centre of the ring) distributed according to a parabolic law. Such a loading scheme appears in case a circular ring is compressed between either plane or curved jaws (as it is for example the jaws of the device introduced by the International Society for Rock Mechanics (ISRM) [2] for the standardized implementation of the Brazilian-disc test).

The solution by Markides et al. [1] is here generalized to confront a more general loading scheme including, besides the parabolic radial stresses, a combination of uniform pressures acting along the outer- and inner-most boundaries of the

layered ring. For the analytic solution of the problem, the procedure proposed by Savin [3] for an infinite plate with a hole strengthened by rings is adopted as it was done also in ref. [1]. The specific procedure is based on the complex potentials technique introduced by Muskhelishvili [4]. The analytic solution achieved provides full-field closed-form expressions for both the stresses and the displacements. However, the specific expressions, in spite of their "elegance" and their numerous advantages (related mainly to their generality and the fact that they are expandable to rings that are made up of any number of concentric layers), are somehow "lengthy" and cumbersome. As a result, detailed parametric analyses of the (quite a few) factors influencing the final outcomes become rather difficult.
To overcome the above mentioned difficulty, the problem is revisited, also, numerically using the Finite Element method and the commercially available software ANSYS. For the validation of the numerical model, the data obtained from the analytic solution for the case of a ring made up of three concentric layers are used. Then the validated numerical model is used for a parametric study of the role of some critical parameters (i.e., the elastic modulus and thickness of the intermediate layer and also the length of the arcs loaded by the parabolic distribution of radial stresses) on the overall stress- and displacement-fields developed in the ring.

THEORETICAL CONSIDERATIONS

The problem and the basic assumptions

Consider a multi-layered hollow cylinder of length w consisting of n concentric hollow cylinders of different thicknesses, perfectly joined together without any gaps at all. The cylinders are assumed to be made of homogeneous, isotropic and linearly elastic materials. The multi-layered cylinder as a whole is in equilibrium under the simultaneous action of three different kinds of loading: inner and outer uniform pressure all along its inner and outer lateral surfaces and a parabolic pressure acting along two finite parts of its outer periphery, antisymmetric with respect to the section's center. All three types of loading act in the body's normal cross-section and remain constant along its length. Ignoring its weight, stresses and displacements are to be determined at any point of the multi-layered cylinder. Clearly, the as above described configuration corresponds to a 1st fundamental problem of plane linear elasticity for the body's cross-section, i.e., the multi-layered circular ring. In this context, Muskhelishvili's method of complex potentials [4] will be employed for the analytic solution.

Mathematical formulation

Under the above assumptions, the multi-layered ring is considered lying in the $z=x+iy=re^{i\theta}$ complex plane, Fig.1. The origin of the Cartesian reference coincides with the center of the ring. The n constituent concentric rings are numbered in such a way so that they are encountered in the order 1, 2,…, n as one moves from the origin towards the outer perimeter of the multi-layered ring. The arbitrary ring is denoted by the index j ($1\leq j\leq n$) and its boundaries are L_j and L_{j+1} corresponding to the radii $r=R_j$ and $r=R_{j+1}$ ($R_{j+1}>R_j$), respectively. In general, it holds that $(R_2-R_1)\neq(R_3-R_2)\neq\ldots(R_{n+1}-R_n)$. Adjacent constituent rings are perfectly joined together along their common interfaces. The inner boundary of the innermost ring, L_1, for $r=R_1$, is subjected to a uniform pressure of magnitude $p_I>0$. The outer boundary of the outermost ring, L_{n+1}, for $r=R_{n+1}$, is under the simultaneous action of a uniform pressure of magnitude $p_E>0$ exerted all over L_{n+1}, and a parabolic pressure of magnitude $p(\theta)>0$ acting along two finite arcs of L_{n+1}, antisymmetric with respect to the ring's center. Each one of these arcs has a length equal to $2\omega_o R_{n+1}$, where ω_o corresponds to the half loaded rim. Particularly, $p(\theta)$ is here considered equal to:

$$p(\theta)=P_c\left[1-\sin^2\left(\phi_o-\theta\right)\Big/\sin^2\omega_o\right],\qquad P_c\equiv\max\left\{p(\theta)\right\}=\frac{2F\sin^2\omega_o}{R_{n+1}\left(\sin 2\omega_o-2\omega_o\cos 2\omega_o\right)w} \tag{1}$$

where ϕ_o is the arbitrary angle formed by the axis of symmetry of the parabolic pressure and x-axis (measured from x-axis in the anticlockwise direction) and F ($F>0$) is the resultant force due to $p(\theta)$. Obviously, for the as above described loading conditions, the multi-layered ring as a whole and each constituent j-ring separately, are in equilibrium and for that configuration the stress- and displacement-fields are to be determined for each j-ring.
According to Muskhelishvili, the latter can be implemented by obtaining on each j-ring two analytic functions of the complex variable z, the complex potentials $\varphi_j(z)$ and $\psi_j(z)$, in terms of which stresses and displacements are expressed as [4]:

$$\sigma_\theta^{(j)} + \sigma_r^{(j)} = 4\Re\left\{\varphi_j'(z)\right\} \tag{2}$$

$$\sigma_r^{(j)} - \mathrm{i}\,\tau_{r\theta}^{(j)} = \varphi_j'(z) + \overline{\varphi_j'(z)} - \mathrm{e}^{\mathrm{i}2\theta}\left[\bar{z}\,\varphi_j''(z) + \psi_j'(z)\right] \tag{3}$$

$$u_r^{(j)} - \mathrm{i}u_\theta^{(j)} = \frac{\mathrm{e}^{\mathrm{i}\theta}}{2\mu_j}\left[\kappa_j\,\overline{\varphi_j(z)} - \bar{z}\,\varphi_j'(z) - \psi_j(z)\right] \tag{4}$$

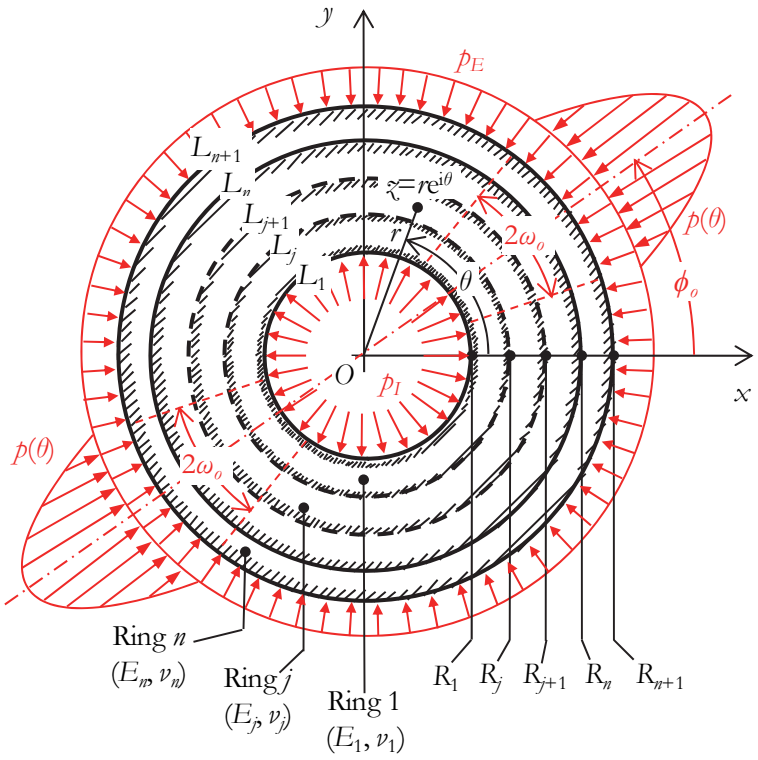

Figure 1: The configuration of the problem and definition of symbols.

In Eqs.(2-4) prime and double prime denote first and second derivative, bar denotes the complex conjugate and $\Re$ is the real part; in addition, μ_j denotes the shear modulus and $\varkappa_j$ is the Muskhelishvili's constant, equal to $3-4\nu_j$ or $(3-\nu_j)/(1+\nu_j)$, for plane strain or plane stress respectively, with ν_j indicating the Poisson's ratio.
Regarding $\varphi_j(z)$ and $\psi_j(z)$, their analytic character on each j-circular ring permits representing them by Laurent series as:

$$\varphi_j(z) = \sum_{-\infty}^{+\infty} a_k^{(j)} z^k, \quad \psi_j(z) = \sum_{-\infty}^{+\infty} b_k^{(j)} z^k, \quad j = 1,2,...,n \tag{5}$$

Therefore the problem reduces to the determination of the coefficients $a_k^{(j)}$ and $b_k^{(j)}$, a task that will be achieved by fulfilling the boundary conditions of the problem. Before implementing this step, however, it is to be mentioned that it is not possible to obtain directly all $a_k^{(j)}$ and $b_k^{(j)}$; namely, for a 1st fundamental problem $\varphi_j(z)$ is determined apart from an arbitrary complex constant and an arbitrary real constant C appearing in a term of the form $\mathrm{i}Cz$. In this context, $a_0^{(j)}$ and the imaginary part, $\Im\left\{a_1^{(j)}\right\}$, of the coefficient $a_1^{(j)}$ remain arbitrary. In the particular problem studied, both are set equal to zero for convenience. What is more, $\psi_j(z)$ is obtained apart from an arbitrary complex constant so $b_0^{(j)}$ remains arbitrary. Actually, it can be seen that for the present problem only one out of all $b_0^{(j)}$ can be arbitrarily fixed while the remaining ones are

subjected to determination. Here it is assumed that $b_0^{(1)}=0$. It is only under these simplifying assumptions that the remaining coefficients $a_k^{(j)}$ and $b_k^{(j)}$ can be determined with the aid of the boundary conditions of the problem.
These conditions are classified into two categories:

i. The boundary values of stresses on the multi-layered ring's boundaries as a whole, reading as:

$$\sigma_r^{(1)}=-p_I,\quad \tau_{r\theta}^{(1)}=0, \qquad \text{for } r=R_1 \quad \text{and} \quad 0\le\theta\le 2\pi \tag{6}$$

$$\sigma_r^{(n+1)}=-p_E-p(\theta),\ \tau_{r\theta}^{(n+1)}=0, \qquad \text{for } r=R_{n+1} \text{ and}$$

$$\phi_o-\omega_o\le\theta\le\phi_o+\omega_o\ \cup\ \pi+\phi_o-\omega_o\le\theta\le\pi+\phi_o+\omega_o \tag{7}$$

$$\sigma_r^{(n+1)}=-p_E,\quad \tau_{r\theta}^{(n+1)}=0, \qquad \text{for } r=R_{n+1} \text{ and}$$

$$\phi_o+\omega_o\le\theta\le\pi+\phi_o-\omega_o\cup\pi+\phi_o+\omega_o\le\theta\le 2\pi+\phi_o-\omega_o \tag{8}$$

ii. The values of stresses and displacements along the interfaces L_{j+1}, j=1,…,n–1, between the j- and (j+1)-ring, due to their firmly joining, reading as:

$$\sigma_r^{(j)}=\sigma_r^{(j+1)},\quad \tau_{r\theta}^{(j)}=\tau_{r\theta}^{(j+1)}, \qquad \text{for } r=R_{j+1} \text{ and } 0\le\theta\le 2\pi \tag{9}$$

$$u_r^{(j)}=u_r^{(j+1)},\quad u_\theta^{(j)}=u_\theta^{(j+1)}, \qquad \text{for } r=R_{j+1} \text{ and } 0\le\theta\le 2\pi \tag{10}$$

Combining Eqs.(3-10) and comparing terms of $e^{ik\theta}$ of the same k-order, in the expressions resulting, the following equations are obtained involving $a_k^{(j)}$ and $b_k^{(j)}$:

Due to the condition of uniform pressure on L_1:

$$\begin{aligned}
&2\alpha_1^{(1)}+R_1^{-2}\overline{b}_{-1}^{(1)}=-p_I\\
&R_1a_2^{(1)}+R_1^{-3}\overline{b}_{-2}^{(1)}=0\\
&3R_1^2a_3^{(1)}+R_1^{-2}\overline{a}_{-1}^{(1)}+b_1^{(1)}=0\\
&R_1^2a_3^{(1)}-R_1^{-2}\overline{a}_{-1}^{(1)}+R_1^{-4}\overline{b}_{-3}^{(1)}=0
\end{aligned} \tag{11}$$

$$\left.\begin{aligned}
&kR_1^{k-1}a_k^{(1)}+R_1^{-(k-1)}\overline{a}_{-(k-2)}^{(1)}+R_1^{k-3}b_{k-2}^{(1)}=0\\
&R_1^{k-1}a_k^{(1)}-(k-2)R_1^{-(k-1)}\overline{a}_{-(k-2)}^{(1)}+R_1^{-(k+1)}\overline{b}_{-k}^{(1)}=0
\end{aligned}\right\},\qquad (k=4,5,\ldots)$$

where $\alpha_1^{(1)}$ is the real part of $a_1^{(1)}$.

Due to the condition of uniform and parabolic pressure on L_{n+1}, (after the factor $p(\theta)$, appearing in the first of Eqs.(1) has been expanded in Fourier series):

$$2\alpha_1^{(n)}+R_{n+1}^{-2}\overline{b}_{-1}^{(n)}=-p_E-\frac{P_c}{\pi}\left(2\omega_o-\frac{2\omega_o-\sin 2\omega_o}{2\sin^2\omega_o}\right)$$

$$R_{n+1}a_2^{(n)}+R_{n+1}^{-3}\overline{b}_{-2}^{(n)}=0$$

$$3R_{n+1}^{2}a_{3}^{(n)}+R_{n+1}^{-2}\overline{a}_{-1}^{(n)}+b_{1}^{(n)}=\frac{P_c}{\pi}\left[\sin 2\omega_o-\frac{1}{2\sin^2\omega_o}\left(\sin 2\omega_o-\omega_o-\frac{\sin 2\omega_o\cos 2\omega_o}{2}\right)\right]\mathrm{e}^{-\mathrm{i}2\phi_o}$$

$$R_{n+1}^{2}a_{3}^{(n)}-R_{n+1}^{-2}\overline{a}_{-1}^{(n)}+R_{n+1}^{-4}\overline{b}_{-3}^{(n)}=\frac{-P_c}{3\pi}\left[\sin 2\omega_o-\frac{1}{2\sin^2\omega_o}\left(\sin 2\omega_o-\omega_o-\frac{\sin 2\omega_o\cos 2\omega_o}{2}\right)\right]\mathrm{e}^{-\mathrm{i}2\phi_o}$$

$$(k-2)\left(kR_{n+1}^{k-1}a_{k}^{(n)}+R_{n+1}^{-(k-1)}\overline{a}_{-(k-2)}^{(n)}+R_{n+1}^{k-3}b_{k-2}^{(n)}\right)=\frac{P_c}{\pi}\left\{\frac{\sin(k-1)\omega_o}{k-1}-\frac{1}{2\sin^2\omega_o}\left[\frac{\sin(k-1)\omega_o}{k-1}\right.\right.$$
$$\left.\left.+\frac{(k-1)\cos 2\omega_o\sin(k-1)\omega_o-2\sin 2\omega_o\cos(k-1)\omega_o}{4-(k-1)^2}\right]\right\}\left(1-\mathrm{e}^{-\mathrm{i}k\pi}\right)\mathrm{e}^{-\mathrm{i}(k-1)\phi_o},\qquad (k=4,5,...)$$

$$k\left[R_{n+1}^{k-1}a_{k}^{(n)}-(k-2)R_{n+1}^{-(k-1)}\overline{a}_{-(k-2)}^{(n)}+R_{n+1}^{-(k+1)}\overline{b}_{-k}^{(n)}\right]=\frac{-P_c}{\pi}\left\{\frac{\sin(k-1)\omega_o}{k-1}-\frac{1}{2\sin^2\omega_o}\left[\frac{\sin(k-1)\omega_o}{k-1}\right.\right.$$
$$\left.\left.+\frac{(k-1)\cos 2\omega_o\sin(k-1)\omega_o-2\sin 2\omega_o\cos(k-1)\omega_o}{4-(k-1)^2}\right]\right\}\left(1-\mathrm{e}^{-\mathrm{i}k\pi}\right)\mathrm{e}^{-\mathrm{i}(k-1)\phi_o},\qquad (k=4,5,...)\qquad (12)$$

where $\alpha_1^{(n)}$ is the real part of $a_1^{(n)}$.

Due to the condition for equal action-reaction at facing points of the *j*- and (*j*+1)-ring, because of perfect matching of the layers:

$$2\alpha_1^{(j)}+R_{j+1}^{-2}\overline{b}_{-1}^{(j)}-2\alpha_1^{(j+1)}-R_{j+1}^{-2}\overline{b}_{-1}^{(j+1)}=0$$
$$R_{j+1}a_2^{(j)}+R_{j+1}^{-3}\overline{b}_{-2}^{(j)}-R_{j+1}a_2^{(j+1)}-R_{j+1}^{-3}\overline{b}_{-2}^{(j+1)}=0$$
$$3R_{j+1}^{2}a_3^{(j)}+R_{j+1}^{-2}\overline{a}_{-1}^{(j)}+b_1^{(j)}-3R_{j+1}^{2}a_3^{(j+1)}-R_{j+1}^{-2}\overline{a}_{-1}^{(j+1)}-b_1^{(j+1)}=0$$

$$R_{j+1}^{2}a_3^{(j)}-R_{j+1}^{-2}\overline{a}_{-1}^{(j)}+R_{j+1}^{-4}\overline{b}_{-3}^{(j)}-R_{j+1}^{2}a_3^{(j+1)}+R_{j+1}^{-2}\overline{a}_{-1}^{(j+1)}-R_{j+1}^{-4}\overline{b}_{-3}^{(j+1)}=0\qquad (j=1,2,...,n-1)$$

$$\left.\begin{aligned}&kR_{j+1}^{k-1}a_{k}^{(j)}+R_{j+1}^{-(k-1)}\overline{a}_{-(k-2)}^{(j)}+R_{j+1}^{k-3}b_{k-2}^{(j)}\\&\quad -kR_{j+1}^{k-1}a_{k}^{(j+1)}-R_{j+1}^{-(k-1)}\overline{a}_{-(k-2)}^{(j+1)}-R_{j+1}^{k-3}b_{k-2}^{(j+1)}=0\\&R_{j+1}^{k-1}a_{k}^{(j)}-(k-2)R_{j+1}^{-(k-1)}\overline{a}_{-(k-2)}^{(j)}+R_{j+1}^{-(k+1)}\overline{b}_{-k}^{(j)}\\&\quad -R_{j+1}^{k-1}a_{k}^{(j+1)}+(k-2)R_{j+1}^{-(k-1)}\overline{a}_{-(k-2)}^{(j+1)}-R_{j+1}^{-(k+1)}\overline{b}_{-k}^{(j+1)}=0\end{aligned}\right\},\ (k=4,5,...)\qquad (13)$$

where $\alpha_1^{(j)}$ is the real part of $a_1^{(j)}$.

Due to the condition for the same displacements of facing points of the *j*- and (*j*+1)-ring, because of perfect matching of the layers:

$$2\frac{\mu_2}{\mu_1}R_2^2 a_2^{(1)} - b_0^{(2)} - 2R_2^2 a_2^{(2)} = 0$$

$$\frac{\mu_{j+1}}{\mu_j}\left(b_0^{(j)} + 2R_{j+1}^2 a_2^{(j)}\right) - b_0^{(j+1)} - 2R_{j+1}^2 a_2^{(j+1)} = 0, \qquad \left(j = 2,3,...,n-1\right)$$

$$\left.\begin{aligned}
&\frac{\mu_{j+1}}{\mu_j}\left[\left(\kappa_j - 1\right)R_{j+1}\alpha_1^{(j)} - R_{j+1}^{-1}\overline{b}_{-1}^{(j)}\right] - \left(\kappa_{j+1} - 1\right)R_{j+1}\alpha_1^{(j+1)} + R_{j+1}^{-1}\overline{b}_{-1}^{(j+1)} = 0\\
&\frac{\mu_{j+1}}{\mu_j}\left(\kappa_j R_{j+1}^2 a_2^{(j)} - R_{j+1}^{-2}\overline{b}_{-2}^{(j)}\right) - \kappa_{j+1}R_{j+1}^2 a_2^{(j+1)} + R_{j+1}^{-2}\overline{b}_{-2}^{(j+1)} = 0\\
&\frac{\mu_{j+1}}{\mu_j}\left(3R_{j+1}^3 a_3^{(j)} - \kappa_j R_{j+1}^{-1}\overline{a}_{-1}^{(j)} + R_{j+1}b_1^{(j)}\right) - 3R_{j+1}^3 a_3^{(j+1)} + \kappa_{j+1}R_{j+1}^{-1}\overline{a}_{-1}^{(j+1)} - R_{j+1}b_1^{(j+1)} = 0\\
&\frac{\mu_{j+1}}{\mu_j}\left(\kappa_j R_{j+1}^3 a_3^{(j)} + R_{j+1}^{-1}\overline{a}_{-1}^{(j)} - R_{j+1}^{-3}\overline{b}_{-3}^{(j)}\right) - \kappa_{j+1}R_{j+1}^3 a_3^{(j+1)} - R_{j+1}^{-1}\overline{a}_{-1}^{(j+1)} + R_{j+1}^{-3}\overline{b}_{-3}^{(j+1)} = 0\\
&\left.\begin{aligned}
&\frac{\mu_{j+1}}{\mu_j}\left(kR_{j+1}^k a_k^{(j)} - \kappa_j R_{j+1}^{-(k-2)}\overline{a}_{-(k-2)}^{(j)} + R_{j+1}^{k-2}b_{k-2}^{(j)}\right)\\
&\qquad - kR_{j+1}^k a_k^{(j+1)} + \kappa_{j+1}R_{j+1}^{-(k-2)}\overline{a}_{-(k-2)}^{(j+1)} - R_{j+1}^{k-2}b_{k-2}^{(j+1)} = 0\\
&\frac{\mu_{j+1}}{\mu_j}\left[\kappa_j R_{j+1}^k a_k^{(j)} + \left(k-2\right)R_{j+1}^{-(k-2)}\overline{a}_{-(k-2)}^{(j)} - R_{j+1}^{-k}\overline{b}_{-k}^{(j)}\right]\\
&\qquad - \kappa_{j+1}R_{j+1}^k a_k^{(j+1)} - \left(k-2\right)R_{j+1}^{-(k-2)}\overline{a}_{-(k-2)}^{(j+1)} + R_{j+1}^{-k}\overline{b}_{-k}^{(j+1)} = 0
\end{aligned}\right\}, \left(k = 4,5,...\right)
\end{aligned}\right\} \left(j = 1,2,...,n-1\right) \tag{14}$$

Properly rearrangement of Eqs.(11-14), yields the following linear systems of equations for the determination of $a_k^{(j)}$ and $b_k^{(j)}$, for any specific number n of constituent rings:

$$2\alpha_1^{(1)} + R_1^{-2}\overline{b}_{-1}^{(1)} = -p_I$$

$$2\alpha_1^{(n)} + R_{n+1}^{-2}\overline{b}_{-1}^{(n)} = -p_E - \frac{P_c}{\pi}\left(2\omega_o - \frac{2\omega_o - \sin 2\omega_o}{2\sin^2\omega_o}\right) \tag{15}$$

$$\left.\begin{aligned}
&2\alpha_1^{(j)} + R_{j+1}^{-2}\overline{b}_{-1}^{(j)} - 2\alpha_1^{(j+1)} - R_{j+1}^{-2}\overline{b}_{-1}^{(j+1)} = 0\\
&\frac{\mu_{j+1}}{\mu_j}\left[\left(\kappa_j - 1\right)R_{j+1}\alpha_1^{(j)} - R_{j+1}^{-1}\overline{b}_{-1}^{(j)}\right] - \left(\kappa_{j+1} - 1\right)R_{j+1}\alpha_1^{(j+1)} + R_{j+1}^{-1}\overline{b}_{-1}^{(j+1)} = 0
\end{aligned}\right\}, \left(j = 1,2,...,n-1\right)$$

$$2\frac{\mu_2}{\mu_1}R_2^2 a_2^{(1)} - b_0^{(2)} - 2R_2^2 a_2^{(2)} = 0$$

$$\frac{\mu_{j+1}}{\mu_j}\left(b_0^{(j)} + 2R_{j+1}^2 a_2^{(j)}\right) - b_0^{(j+1)} - 2R_{j+1}^2 a_2^{(j+1)} = 0, \qquad \left(j = 2,3,...,n-1\right)$$

$$R_1 a_2^{(1)} + R_1^{-3}\overline{b}_{-2}^{(1)} = 0$$

$$R_{n+1} a_2^{(n)} + R_{n+1}^{-3}\overline{b}_{-2}^{(n)} = 0$$

$$\left.\begin{aligned} R_{j+1}a_2^{(j)} + R_{j+1}^{-3}\overline{b}_{-2}^{(j)} - R_{j+1}a_2^{(j+1)} - R_{j+1}^{-3}\overline{b}_{-2}^{(j+1)} = 0 \\ \frac{\mu_{j+1}}{\mu_j}\left(\kappa_j R_{j+1}^2 a_2^{(j)} - R_{j+1}^{-2}\overline{b}_{-2}^{(j)}\right) - \kappa_{j+1}R_{j+1}^2 a_2^{(j+1)} + R_{j+1}^{-2}\overline{b}_{-2}^{(j+1)} = 0 \end{aligned}\right\}, \ \left(j = 1,2,...,n-1\right) \tag{16}$$

(where, obviously, all coefficients appearing in Eqs.(16) are zero)

$$3R_1^2 a_3^{(1)} + R_1^{-2}\overline{a}_{-1}^{(1)} + b_1^{(1)} = 0$$

$$R_1^2 a_3^{(1)} - R_1^{-2}\overline{a}_{-1}^{(1)} + R_1^{-4}\overline{b}_{-3}^{(1)} = 0$$

$$3R_{n+1}^2 a_3^{(n)} + R_{n+1}^{-2}\overline{a}_{-1}^{(n)} + b_1^{(n)} = \frac{P_c}{\pi}\left[\sin 2\omega_o - \frac{1}{2\sin^2\omega_o}\left(\sin 2\omega_o - \omega_o - \frac{\sin 2\omega_o \cos 2\omega_o}{2}\right)\right]e^{-i2\phi_o}$$

$$R_{n+1}^2 a_3^{(n)} - R_{n+1}^{-2}\overline{a}_{-1}^{(n)} + R_{n+1}^{-4}\overline{b}_{-3}^{(n)} = \frac{-P_c}{3\pi}\left[\sin 2\omega_o - \frac{1}{2\sin^2\omega_o}\left(\sin 2\omega_o - \omega_o - \frac{\sin 2\omega_o \cos 2\omega_o}{2}\right)\right]e^{-i2\phi_o}$$

$$\left.\begin{aligned} 3R_{j+1}^2 a_3^{(j)} + R_{j+1}^{-2}\overline{a}_{-1}^{(j)} + b_1^{(j)} - 3R_{j+1}^2 a_3^{(j+1)} - R_{j+1}^{-2}\overline{a}_{-1}^{(j+1)} - b_1^{(j+1)} = 0 \\ R_{j+1}^2 a_3^{(j)} - R_{j+1}^{-2}\overline{a}_{-1}^{(j)} + R_{j+1}^{-4}\overline{b}_{-3}^{(j)} - R_{j+1}^2 a_3^{(j+1)} + R_{j+1}^{-2}\overline{a}_{-1}^{(j+1)} - R_{j+1}^{-4}\overline{b}_{-3}^{(j+1)} = 0 \\ \frac{\mu_{j+1}}{\mu_j}\left(3R_{j+1}^3 a_3^{(j)} - \kappa_j R_{j+1}^{-1}\overline{a}_{-1}^{(j)} + R_{j+1}b_1^{(j)}\right) - 3R_{j+1}^3 a_3^{(j+1)} + \kappa_{j+1}R_{j+1}^{-1}\overline{a}_{-1}^{(j+1)} - R_{j+1}b_1^{(j+1)} = 0 \\ \frac{\mu_{j+1}}{\mu_j}\left(\kappa_j R_{j+1}^3 a_3^{(j)} + R_{j+1}^{-1}\overline{a}_{-1}^{(j)} - R_{j+1}^{-3}\overline{b}_{-3}^{(j)}\right) - \kappa_{j+1}R_{j+1}^3 a_3^{(j+1)} - R_{j+1}^{-1}\overline{a}_{-1}^{(j+1)} + R_{j+1}^{-3}\overline{b}_{-3}^{(j+1)} = 0 \end{aligned}\right\}, \left(j = 1,2,...,n-1\right) \tag{17}$$

$$k\mathrm{R}_1^{k-1}a_k^{(1)}+\mathrm{R}_1^{-(k-1)}\overline{a}_{-(k-2)}^{(1)}+\mathrm{R}_1^{k-3}b_{k-2}^{(1)}=0$$
$$\mathrm{R}_1^{k-1}a_k^{(1)}-(k-2)\mathrm{R}_1^{-(k-1)}\overline{a}_{-(k-2)}^{(1)}+\mathrm{R}_1^{-(k+1)}\overline{b}_{-k}^{(1)}=0,\qquad (k=4,5,...)$$

$$(k-2)\left(k\mathrm{R}_{n+1}^{k-1}a_k^{(n)}+\mathrm{R}_{n+1}^{-(k-1)}\overline{a}_{-(k-2)}^{(n)}+\mathrm{R}_{n+1}^{k-3}b_{k-2}^{(n)}\right)=\frac{P_c}{\pi}\left\{\frac{\sin(k-1)\omega_o}{k-1}-\frac{1}{2\sin^2\omega_o}\left[\frac{\sin(k-1)\omega_o}{k-1}\right.\right.$$
$$\left.\left.+\frac{(k-1)\cos 2\omega_o\sin(k-1)\omega_o-2\sin 2\omega_o\cos(k-1)\omega_o}{4-(k-1)^2}\right]\right\}\left(1-\mathrm{e}^{-\mathrm{i}k\pi}\right)\mathrm{e}^{-\mathrm{i}(k-1)\phi_o}$$

$$k\left[\mathrm{R}_{n+1}^{k-1}a_k^{(n)}-(k-2)\mathrm{R}_{n+1}^{-(k-1)}\overline{a}_{-(k-2)}^{(n)}+\mathrm{R}_{n+1}^{-(k+1)}\overline{b}_{-k}^{(n)}\right]=\frac{-P_c}{\pi}\left\{\frac{\sin(k-1)\omega_o}{k-1}-\frac{1}{2\sin^2\omega_o}\left[\frac{\sin(k-1)\omega_o}{k-1}\right.\right.$$
$$\left.\left.+\frac{(k-1)\cos 2\omega_o\sin(k-1)\omega_o-2\sin 2\omega_o\cos(k-1)\omega_o}{4-(k-1)^2}\right]\right\}\left(1-\mathrm{e}^{-\mathrm{i}k\pi}\right)\mathrm{e}^{-\mathrm{i}(k-1)\phi_o}$$

$$\left.\begin{aligned}
&k\mathrm{R}_{j+1}^{k-1}a_k^{(j)}+\mathrm{R}_{j+1}^{-(k-1)}\overline{a}_{-(k-2)}^{(j)}+\mathrm{R}_{j+1}^{k-3}b_{k-2}^{(j)}\\
&\qquad-k\mathrm{R}_{j+1}^{k-1}a_k^{(j+1)}-\mathrm{R}_{j+1}^{-(k-1)}\overline{a}_{-(k-2)}^{(j+1)}-\mathrm{R}_{j+1}^{k-3}b_{k-2}^{(j+1)}=0\\
&\mathrm{R}_{j+1}^{k-1}a_k^{(j)}-(k-2)\mathrm{R}_{j+1}^{-(k-1)}\overline{a}_{-(k-2)}^{(j)}+\mathrm{R}_{j+1}^{-(k+1)}\overline{b}_{-k}^{(j)}\\
&\qquad-\mathrm{R}_{j+1}^{k-1}a_k^{(j+1)}+(k-2)\mathrm{R}_{j+1}^{-(k-1)}\overline{a}_{-(k-2)}^{(j+1)}-\mathrm{R}_{j+1}^{-(k+1)}\overline{b}_{-k}^{(j+1)}=0\\
&\frac{\mu_{j+1}}{\mu_j}\left(k\mathrm{R}_{j+1}^{k}a_k^{(j)}-\kappa_j\mathrm{R}_{j+1}^{-(k-2)}\overline{a}_{-(k-2)}^{(j)}+\mathrm{R}_{j+1}^{k-2}b_{k-2}^{(j)}\right)\\
&\qquad-k\mathrm{R}_{j+1}^{k}a_k^{(j+1)}+\kappa_{j+1}\mathrm{R}_{j+1}^{-(k-2)}\overline{a}_{-(k-2)}^{(j+1)}-\mathrm{R}_{j+1}^{k-2}b_{k-2}^{(j+1)}=0\\
&\frac{\mu_{j+1}}{\mu_j}\left[\kappa_j\mathrm{R}_{j+1}^{k}a_k^{(j)}+(k-2)\mathrm{R}_{j+1}^{-(k-2)}\overline{a}_{-(k-2)}^{(j)}-\mathrm{R}_{j+1}^{-k}\overline{b}_{-k}^{(j)}\right]\\
&\qquad-\kappa_{j+1}\mathrm{R}_{j+1}^{k}a_k^{(j+1)}-(k-2)\mathrm{R}_{j+1}^{-(k-2)}\overline{a}_{-(k-2)}^{(j+1)}+\mathrm{R}_{j+1}^{-k}\overline{b}_{-k}^{(j+1)}=0
\end{aligned}\right\},(j=1,2,...,n-1)\qquad(18)$$
$$(k=4,5,...)$$

For the $13n-1$ unknowns appearing in Eqs.(15-18), i.e., for $\left\{\alpha_1^{(1)},\alpha_1^{(2)},...,\alpha_1^{(n)}\right\}$, $\left\{a_2^{(1)},a_2^{(2)},...,a_2^{(n)}\right\}$, $\left\{a_3^{(1)},a_3^{(2)},...,a_3^{(n)}\right\}$, $\left\{\overline{a}_{-1}^{(1)},\overline{a}_{-1}^{(2)},...,\overline{a}_{-1}^{(n)}\right\}$, $\left\{a_k^{(1)},a_k^{(2)},...,a_k^{(n)}\right\}$, $\left\{\overline{a}_{-(k-2)}^{(1)},\overline{a}_{-(k-2)}^{(2)},...,\overline{a}_{-(k-2)}^{(n)}\right\}$, $\left\{b_0^{(2)},b_0^{(3)},...,b_0^{(n)}\right\}$, $\left\{b_1^{(1)},b_1^{(2)},...,b_1^{(n)}\right\}$, $\left\{\overline{b}_{-1}^{(1)},\overline{b}_{-1}^{(2)},...,\overline{b}_{-1}^{(n)}\right\}$, $\left\{\overline{b}_{-2}^{(1)},\overline{b}_{-2}^{(2)},...,\overline{b}_{-2}^{(n)}\right\}$, $\left\{\overline{b}_{-3}^{(1)},\overline{b}_{-3}^{(2)},...,\overline{b}_{-3}^{(n)}\right\}$, $\left\{b_{k-2}^{(1)},b_{k-2}^{(2)},...,b_{k-2}^{(n)}\right\}$ and $\left\{\overline{b}_{-k}^{(1)},\overline{b}_{-k}^{(2)},...,\overline{b}_{-k}^{(n)}\right\}$, there, indeed, exists a number of $13n-1$ equations, as expected and thus the problem has a solution. In other words, Eqs.(15), (16), (17) and (18) comprise $2n$, $3n-1$, $4n$ and $4n$ equations, respectively, i.e., a total sum of $13n-1$. Thus, $a_k^{(j)}$ and $b_k^{(j)}$ are indeed obtainable from Eqs.(15-18), and in this context $\varphi_j(z)$ and $\psi_j(z)$ can be recapitulated as follows:

$$\varphi_j(z)=\alpha_1^{(j)}z+a_3^{(j)}z^3+\sum_{k=5,7,9,...}a_k^{(j)}z^k+a_{-1}^{(j)}z^{-1}+\sum_{k=5,7,9,...}a_{-(k-2)}^{(j)}z^{-(k-2)},\qquad(j=1,2,...,n)\qquad(19)$$

$$\psi_j(z)=b_1^{(j)}z+\sum_{k=5,7,9,\ldots}b_{k-2}^{(j)}z^{k-2}+b_{-1}^{(j)}z^{-1}+b_{-3}^{(j)}z^{-3}+\sum_{k=5,7,9,\ldots}b_{-k}^{(j)}z^{-k},\qquad (j=1,2,\ldots,n) \tag{20}$$

where 'even' terms are missing since are all zero.
Before concluding it should be mentioned that:

(a) by setting p_I=0 in the first of Eqs.(15), the present formulae [Eqs.(15-20)] provide the solution in case internal uniform pressure is zero and the multi-layered ring is only under the action of external uniform pressure p_E and external parabolic pressure $p(\theta)$ (along two finite arcs of its outer periphery, antisymmetric with respect to x-axis),
(b) by setting p_E=0 in the second of Eqs.(15), the present formulae [Eqs.(15-20)] provide the solution in case external uniform pressure is zero and the multi-layered ring is only under the action of internal uniform pressure p_I and external parabolic pressure $p(\theta)$,
(c) by setting p_I=0 in the first of Eqs.(15) and p_E=0 in the second of Eqs.(15), the present formulae [Eqs.(15-20)] provide the solution in the case the multi-layered ring is only under the action of external parabolic pressure $p(\theta)$,
(d) by setting P_c=0 in Eqs.(15, 17 and 18), the present formulae [Eqs.(15-20)] provide the solution in the case external parabolic pressure is zero and the multi-layered ring is only under the action of internal uniform pressure p_I and external uniform pressure p_E,
(e) by setting P_c=0 in Eqs.(15, 17 and 18) and p_I=0 in the first of Eqs.(15), the present formulae [Eqs.(15-20)] provide the solution in the case internal uniform and external parabolic pressure are zero and the multi-layered ring is only under the action of externally imposed pressure p_E and
(f) by setting P_c=0 in Eqs.(15, 17 and 18) and p_E=0 in the second of Eqs.(15), the present formulae [Eqs.(15-20)] provide the solution in the case external uniform and parabolic pressure are zero and the multi-layered ring is only under the action of internal uniform pressure p_I.

Particularly, in all last three cases (d, e, f), i.e., when only uniform pressure over one or both the two boundaries (internal and external) of the multi-layered ring is present, the complex potentials are significantly simplified to:

$$\varphi_j(z)=\alpha_1^{(j)}z,\quad \psi_j(z)=\frac{b_{-1}^{(j)}}{z},\qquad (j=1,2,\ldots,n) \tag{21}$$

where $\alpha_1^{(j)}\in\mathbb{R}$ and $b_{-1}^{(j)}$ are now just provided by only Eqs.(15), for $P_c=0$, and for: $p_I\neq 0$, $p_E\neq 0$ in case (d), $p_I=0$, $p_E\neq 0$ in case (e) and $p_I\neq 0$, $p_E=0$ in case (f).

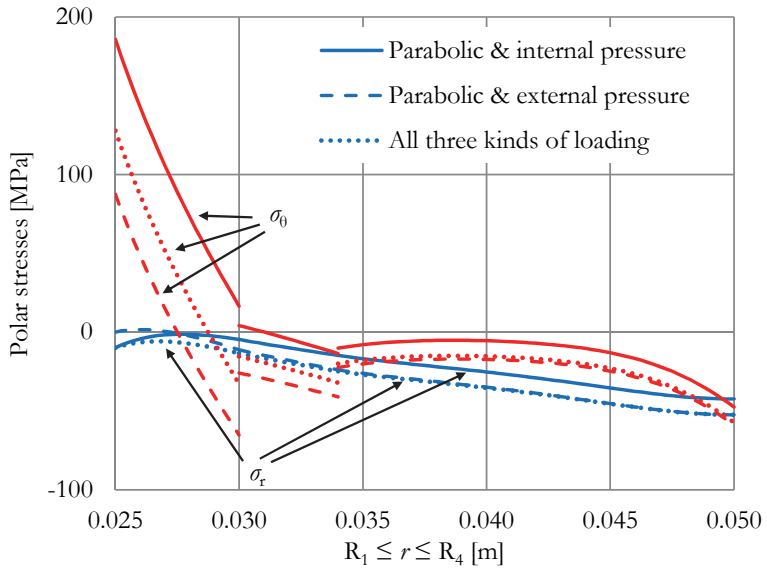

Figure 2: Distribution of stresses along the diameter corresponding to the symmetry axis of the parabolic load, for three loading schemes. Internal pressure=External pressure=10 MPa, P_{frame}=5 kN, ω_o=10°, P_c=43.1 MPa, n=3. Composite ring's thickness w=0.01 m. Inner ring (1): $R_1\le r\le R_2$, R_1=0.025 m, R_2=0.030 m, E_1=30 GPa, ν_1=0.25. Intermediate ring (2): $R_2\le r\le R_3$, R_2=0.030 m, R_3=0.034 m, E_2=10 GPa, ν_2=0.30. Outer ring (3): $R_3\le r\le R_4$, R_3=0.034 m, R_4=0.050 m, E_3=3 GPa, ν_2=0.35).

In order to demonstrate the capabilities of the solution introduced, the distribution of the radial and tangential stresses along the diameter corresponding to the symmetry axis of the parabolic load, is plotted in Fig.2, for three combinations of the constituent loading schemes, i.e., parabolic distribution of radial stresses and uniform internal pressure, parabolic distribution of radial stresses and uniform external pressure, and finally all three schemes simultaneously. The discontinuity of the distribution of transverse stress at the interfaces of the rings is the main characteristic of the plots. As it was expected, this discontinuity is stronger for the case of simultaneous action of the parabolic distribution and external uniform pressure.

NUMERICAL ANALYSIS - APPLICATION FOR n=3 CONSTITUENT RINGS

As a next step, a parametric numerical analysis was decided to be carried out, in order to explore the influence of various factors on the displacement- and stress-fields developed in a multi-layered ring. The ring with three layers under plane strain conditions was decided to be considered, due to its increased practical interest. The principal advantage of the numerical scheme is that it models the "multi-layered ring - jaw" complex (as an integrated elastic system) rather than the isolated ring. Before the main numerical study, the model was properly validated as it is described in next section.

Construction and validation of the reference numerical model

For the proper validation of the numerical model advantage was, initially, taken of the analytic solution for the most complex loading case, i.e., the partial parabolic pressure. For symmetry reasons (materials and geometry) only a quarter of the ring-jaw complex ($0^o \le \theta \le 90^o$) was constructed with the aid of ANSYS software. The geometry of the reference model is shown in Fig.3. For the radii of the layers it holds that R_j=25, 30, 34, 50 mm, for $1 \le j \le 4$. All three interfaces (i.e., between the constituent rings and between the jaw and the outer ring) were taken into account.

The model was meshed using the PLANE182 element. Contact elements (CONTA172 and TARGE169) were used to model the interfaces. The interfaces between the successive rings were considered as mutually bonded without separation. A very small (tending to zero) value was assigned to the coefficient of friction at the interface between the jaw and the external surface of the outer ring, in order to minimize (eliminate) friction stresses. This assumption was dictated by the fact that the analytic solution, described in the previous section, considers an isolated ring under exclusively radial stresses without any friction stresses at all.

The analysis performed was linearly elastic. The moduli of elasticity and the Poisson's ratios assigned to each one of the rings were E_j=30, 10, 3 GPa and ν_j=0.25, 0.30, 0.35, respectively, for $1 \le j \le 3$. The jaw was considered to be made of steel (E_{jaw}=210 GPa and ν_{jaw}=0.30).

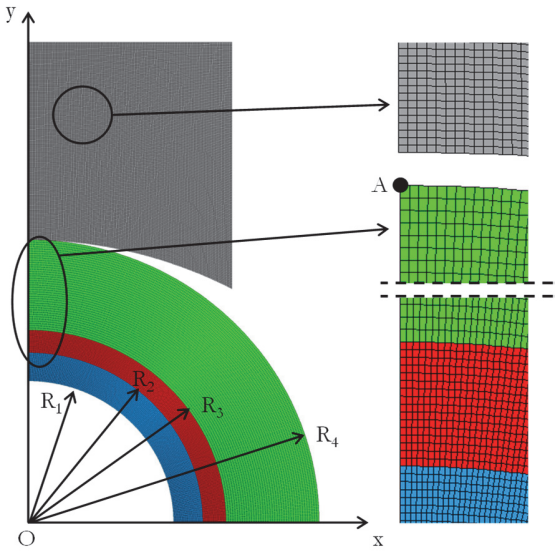

Figure 3: The reference numerical model and detailed views of the finally adopted mesh.

Due to the model's symmetry the following boundary conditions were adopted:

i. The motion along the y-axis (loading axis) of all the nodes of the lower line of the ring was restricted.

ii. All the nodes of the left (vertical) line of the ring as well as the nodes of both sides of the jaw were restricted of shifting horizontally (i.e., normally to the loading axis).
iii. A uniform vertical displacement on the nodes of the upper line of the jaw was imposed.

The optimum element size for the meshing of the model was chosen based on a proper convergence analysis. The variation of the polar stresses developed along "Path 0", i.e., the outer periphery of the outermost ring, and especially around the position where the major differences are observed is plotted in Fig.4a. The embedded graph corresponds to the stresses along the whole length of "Path 0". In addition, the total stress applied on point A (see Fig.3) is plotted in Fig.4b. Both graphs indicate that convergence is satisfactory for about 20000 elements. In order to obtain more accurate results (and given that the CPU-time consumption is not prohibitive), a number of about 38000 elements was chosen for the final meshing.

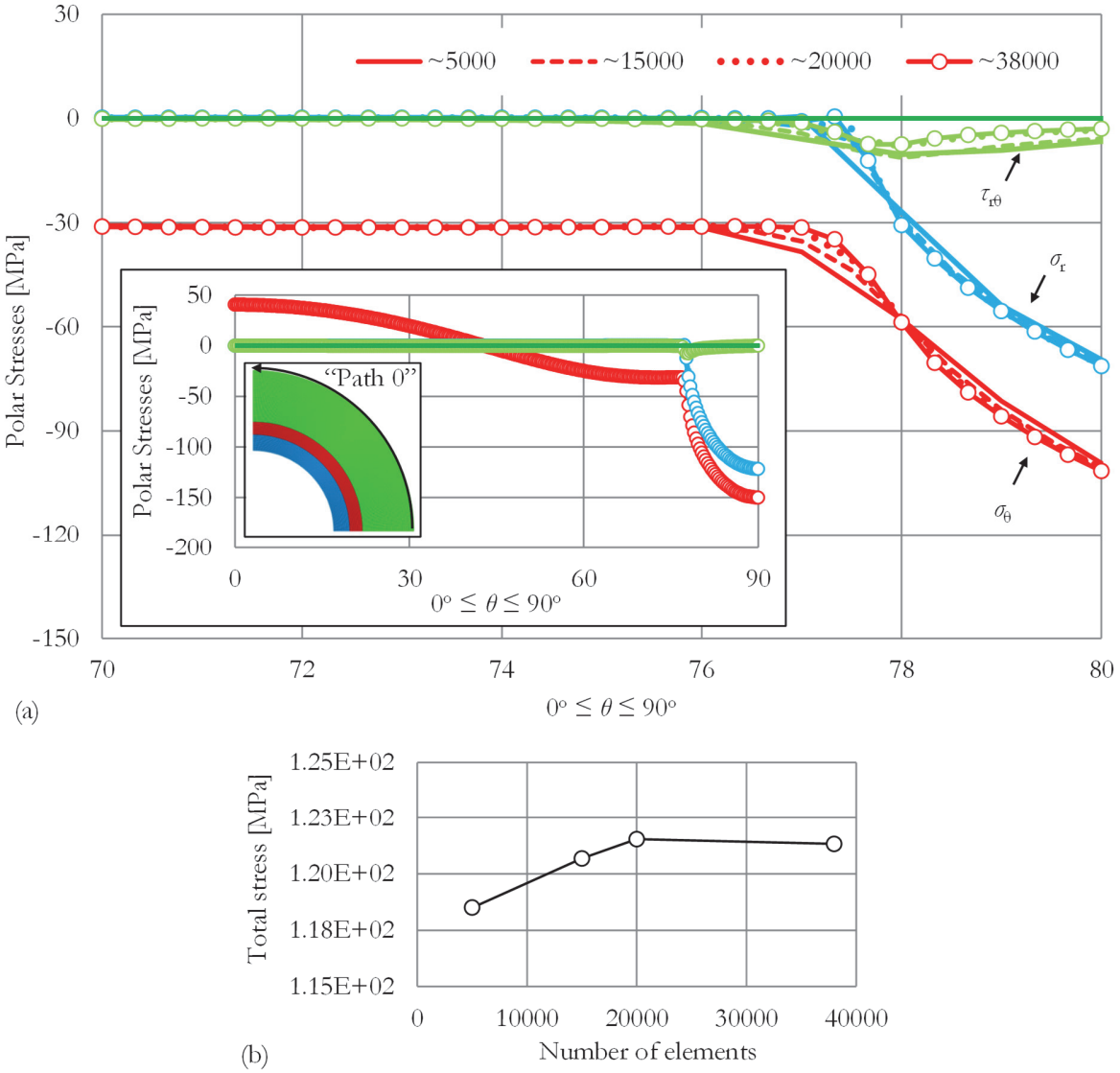

Figure 4: (a) The variation of the polar stresses developed along "Path 0" (the embedded graph corresponds to the whole length of "Path 0") and (b) the total stress applied on point A (see Fig.3) for various numbers of elements.

Before proceeding to the parametric study, the numerical model was used to check the assumption of the analytic solution concerning the parabolic distribution of radial stresses along the loaded arc of the ring. This was considered absolutely necessary because the specific assumption is based on the solution of a different problem, i.e., that of the "*compact* disc - jaw" contact problem [5] and therefore adopting a similar distribution for the "*ring* - jaw" problem appears perhaps somehow arbitrary. In this context, the vertical displacement of the upper node (point A in Fig.3) of the ring (which is, in fact, the only point of the ring in contact with the jaw before the onset of loading) was determined according to the analytic

solution described in previous section, assuming now that ω_o is not arbitrarily prescribed (as it was considered in Eqs.(1)), but it is rather provided, together with P_o, by the relevant compact disc-jaw contact problem [5].Then a uniform displacement was applied at the steel jaw (simulating in fact the load exerted by the loading frame during the laboratory experiments with the device suggested by ISRM for the standardized Brazilian-disc test), the magnitude of which was determined by demanding that it should result to a vertical displacement of point A equal to the respective one provided by the analytic solution. The results of the numerical analysis for the distribution of pressure along the common contact arc, developed at the ring-jaw interface are plotted in Fig.5, in conjunction with the parabolic pressure applied on the ring during the theoretical solution. It is seen from this figure that the two distributions are in relatively good agreement, despite some differences concerning their amplitude (equal to about 140 MPa for the analytic solution and 122 MPa for the numerical one) and also their flatness (the numerically obtained distribution appears somehow flatter). These differences should be expected, given that the parabolic distribution is an approximation of the actual "cyclic" distribution [5, 6] (developed during the contact of two elastic cylindrical bodies), which was adopted in an attempt to achieve closed-form analytic expressions for the distribution of stresses a displacements all over the disc [7, 8]. (It is here recalled, that for the actual "cyclic" distribution analytic expressions for the stress field cannot be straightforwardly obtained [5]).

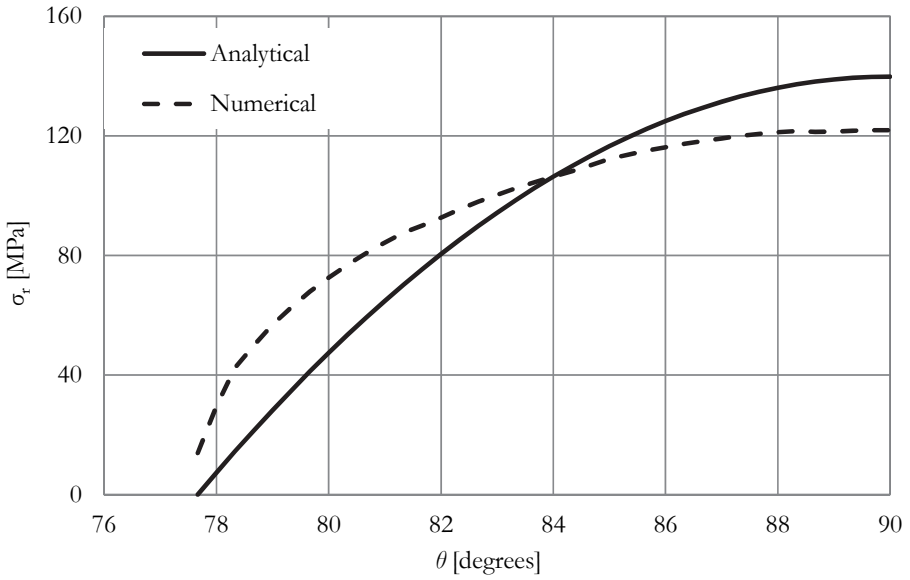

Figure 5: The applied pressure applied on the ring based on both the analytical and the numerical analysis.

Besides the above mentioned slight differences, it is quite astonishing that the analytic and the numerical approaches provide almost identical results for the "total" pressure applied on the ring indicating the static equivalency of the two solutions. Even more astonishing is the fact that the length of the contact arcs obtained by the two solutions (numerical and analytic) is again almost identical: The contact arc $2\omega_o$ determined from the numerical model equals to 24.67° while the respective one of the analytical solution is equal to 24.59°. The same excellent agreement was observed, also, for the variation of displacements and stresses along strategic paths of the model, as it can be seen, for example, in Fig.6, in which analytical versus numerical results concerning the vertical displacement (Fig.6a) and the polar stresses (Fig.6b) are plotted for "Path 1", i.e., along the diameter corresponding to the axis of loading symmetry. The differences observed are quite marginal. For example, for the displacements, the difference does not exceed 4% (Fig.6a) while for the polar stresses the differences are almost tending to zero (Fig.6b).

As an additional validation step, results of the numerical analysis were compared against the respective ones analytically obtained, also, for some combinations of the three loading schemes considered (parabolic pressure, external uniform pressure and internal uniform pressure). For this specific step the jaw was removed and the multi-layered ring was modeled as an isolated elastic body (for convenience). The following loading schemes were imposed on the ring:

Case 1: Pressure was applied on the nodes of the outer perimeter of the outermost ring along a contact length $2\omega_o$ which was assumed equal to 20°. The parabolic pressure variation corresponds to a statically equivalent force equal to 5 kN applied by the loading frame.

Case 2: Internal pressure equal to 10 MPa was applied on all nodes along the inner perimeter of the three-layered ring.

Case 3: External pressure equal to 10 MPa was applied on all nodes along the outer perimeter of the three-layered ring.

Case 4: Combination of Cases 1 and 2.
Case 5: Combination of Cases 1 and 3.
Case 6: All three types of loading, i.e., combination of Cases 1, 2, 3.
The normal polar stresses (both radial and transverse) obtained by the numerical model for all six loading cases mentioned above are presented in Fig.7 in juxtaposition to the respective analytical results. The plots are realized, as in Fig.6, along the diameter corresponding to the symmetry axis of the loading distribution. It is clear that the correlation between analytic and numerical results is quite satisfactory, for both stresses and for all loading schemes without any exception.

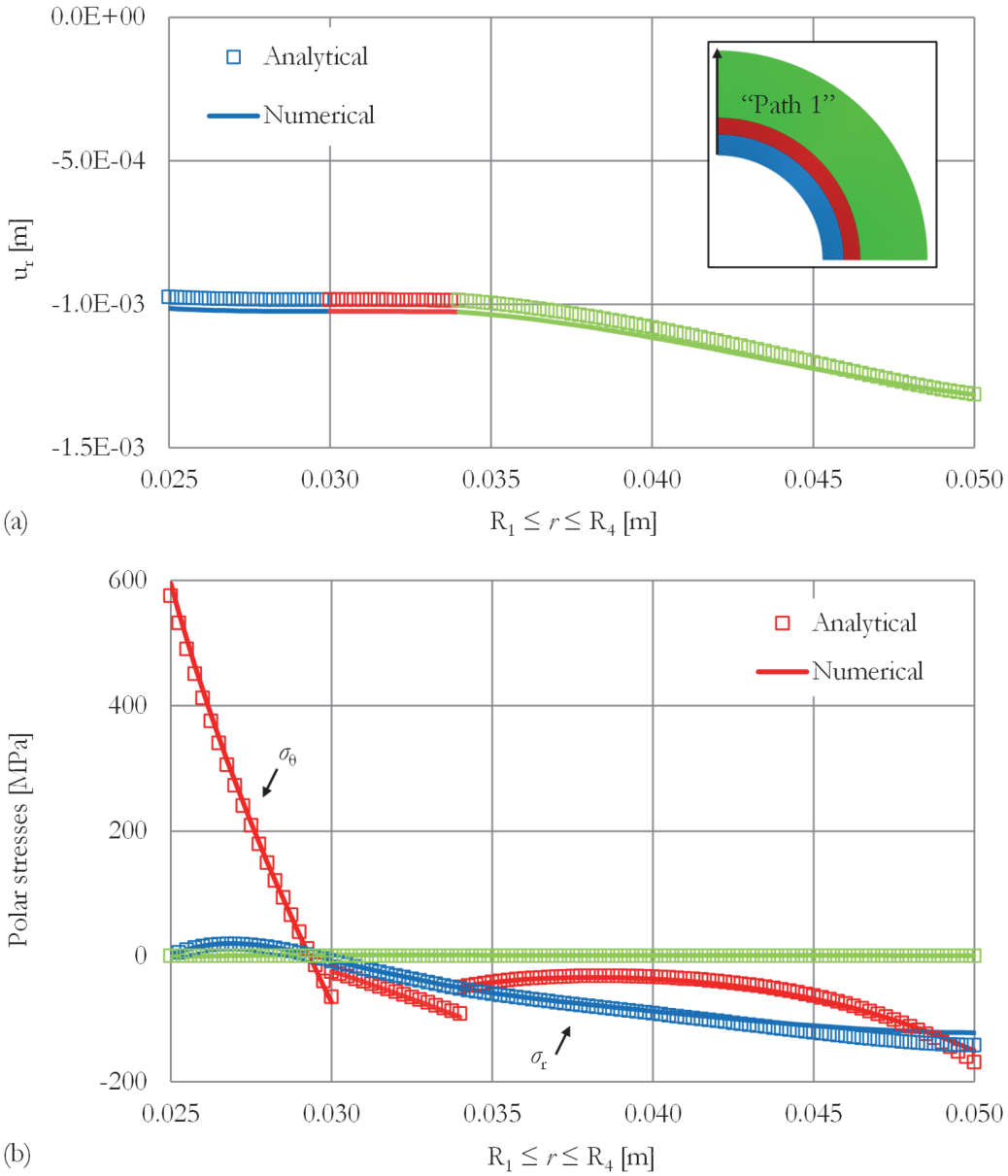

Figure 6: Analytical vs. numerical results for the (a) vertical displacement and (b) the polar stresses developed along "Path 1".

Recapitulating the data of the validation procedure, it can be definitely concluded that the numerical model approaches the analytic solution in an excellent manner. Therefore, it is safe for the model to be used for a thorough parametric analysis of the role of the (quite a few) factors, which are expected to crucially affect the overall mechanical response of the multi-layered ring, in case it is subjected to various combinations of the three constituent loading schemes considered (internal and external pressure and parabolic variation of radial stresses). Moreover, the results of the present section, besides validating the numerical model, indicated that the actual stress distribution along the contact arc at the ring-jaw interface is

rather insensitive to whether the disc squeezed between the ISRM jaws is compact or hollow, i.e., ring (either it is homogeneous or it consists of successive layers with different mechanical properties), at least for low to moderate values of the externally applied load and provided relatively thick-walled rings are considered.

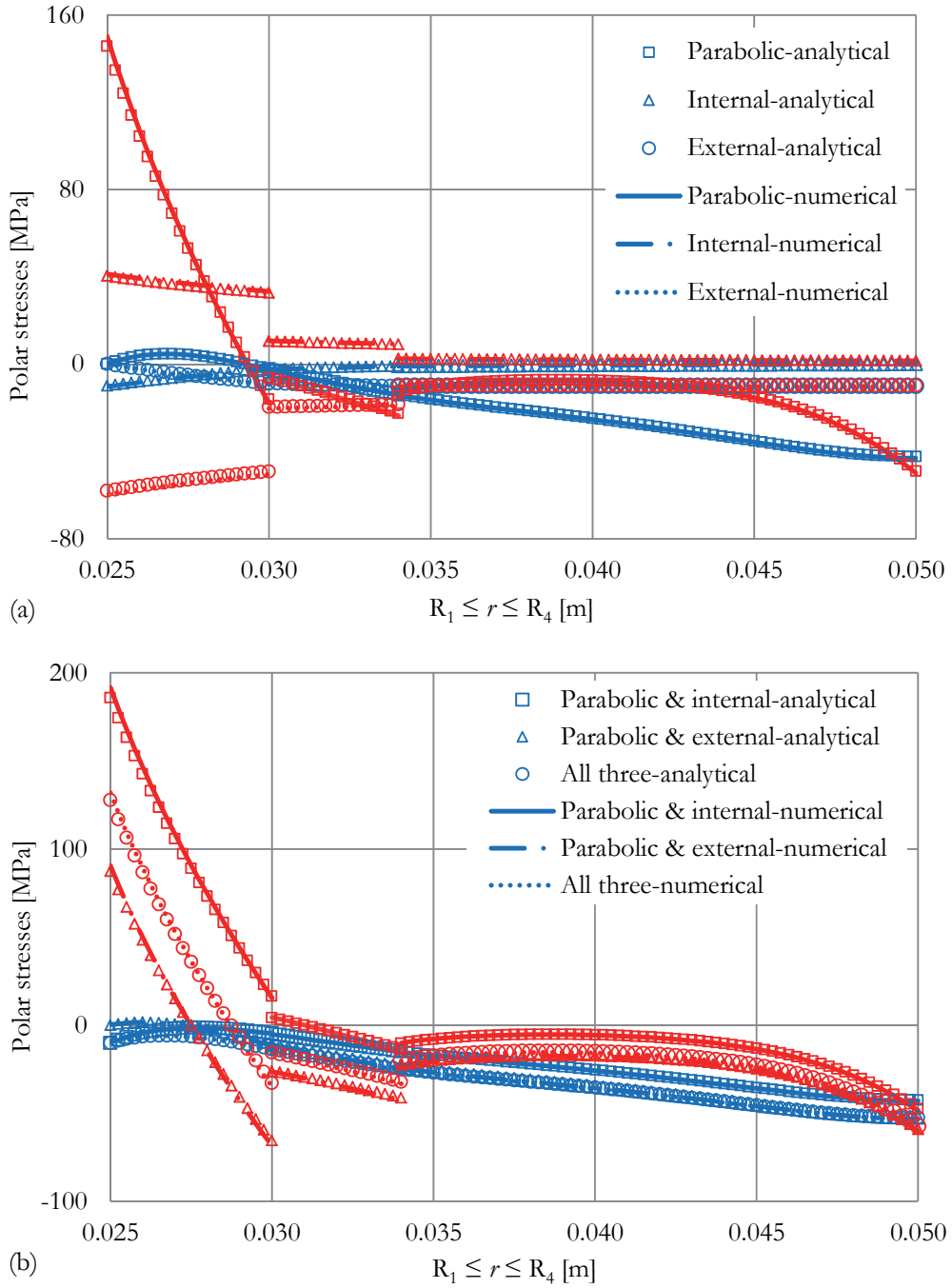

Figure 7: Analytical vs. numerical results for (a) simple and (b) complex loading schemes. Blue lines correspond to radial stress while red ones correspond to transverse stress.

Parametric numerical analysis

The as above exhaustively validated numerical model is now used for a parametric analysis. In this direction, a series of new models was constructed for the most complicated loading constituent, i.e., the parabolic pressure. Three parameters were taken into account in the present study, the influence of which is expected to be more crucial. These parameters are:

a. The modulus of elasticity of the intermediate ring, E_2.
b. The thickness of the intermediate ring, $t_2=R_3-R_2$, keeping the ring's outer diameter constant, i.e., increasing t_2 results to decrease of the thickness of the outermost ring, $t_3=R_4-R_3$.
c. The contact length, or equivalently the length of the loaded arc, $2\omega_o$, assuming that the overall externally imposed load is kept constant. In this case the jaw was not taken into account. Concerning the distribution of the pressure applied along each contact arc, it was determined by taking advantage of Eqs.(1).

The numerical values assigned to each one of the three parameters studied are summarized in Tab. 1. In addition, the variation of the applied pressure for the values considered for the length of the half contact arc ω_o is plotted in Fig.8. As it is expected, by decreasing the length of the loaded arc (while keeping the overall load constant) the amplitude of the distribution increases, leading to increased stress concentration in the immediate vicinity of the loaded arc, which in turn increases the possibility for premature failure in this region of the ring. This aspect should be carefully taken into account in case the external layer of the ring is made of relatively brittle materials.

Parameter	Values					
E_2 [GPa]	5.0	7.5	12.5	15.0	17.5	20.0
t_2 [mm]	1	2	3	5	6	
ω_o [deg]	1	3	5	7	9	11

Table 1: The numerical values assigned to each parameter.

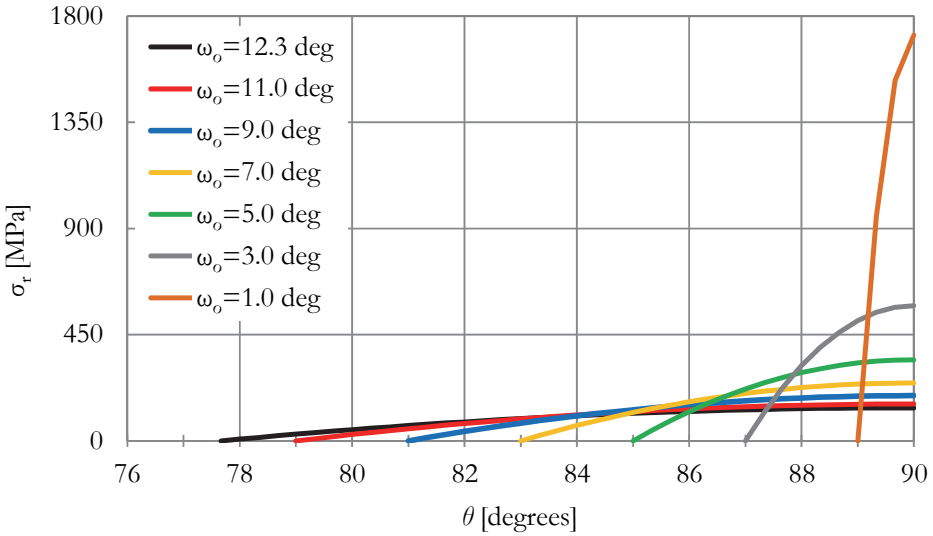

Figure 8: The variation of the pressure applied on the ring for various ω_o-values.

RESULTS AND DISCUSSION

The influence of the elastic modulus of the intermediate ring, E_2

The displacement along the loading axis (i.e., y-axis) developed all over the ring's area is presented in Fig.9a for the reference model. Its variation along y-axis for various E_2 values is exhibited in Fig.9b. It is interesting to observe that, although the values of E_2 vary within a relatively wide range (from -50% to +100% of the respective value of the reference model), the displacements along y-axis are more or less insensitive to this variation. The maximum difference does not exceed 3% and it is observed for E_2=20 GPa.

On the contrary, the stresses developed in the ring are much more sensitive to the changes of E_2. To enlighten this point (and considering that the polar reference system is much more convenient for the specific application), the variation of the transverse stress (σ_θ) along the loaded diameter is plotted in Fig.10 for all E_2 values studied. It is seen that the influence of E_2 is very strong, especially at the interface points between the constituent rings. As it is perhaps expected, the "stress jump"

is amplified as the difference of the modulus of elasticity of ring 2 from the elastic modulus of the adjacent ring increases. Therefore, the variation of σ_θ from ring 1 (innermost) to ring 2 (intermediate) is smoother when E_2=20 GPa while from ring 2 to ring 3 (outermost) the variation is smoother when E_2=5 GPa. It is also noted that σ_θ is negative all along rings 2, 3 (along the specific path) for all E_2 values studied, while it changes sign somewhere along ring 1.

The variation of the polar stresses developed along the interfaces is quite interesting. For the interface between rings 1, 2 and more specifically along the outer periphery of ring 1 (Fig.11a), σ_θ is affected more severely. When the value of E_2 is between the elastic moduli of the two surrounding rings, the variation of σ_θ is again very smooth with small variations. For E_2<10 GPa the transverse stress becomes larger as θ increases while the opposite is true for E_2>10 GPa. It is also seen from the same figure that the values of $\sigma_{r\theta}$ developed along the interface are of the same order of magnitude with σ_θ.

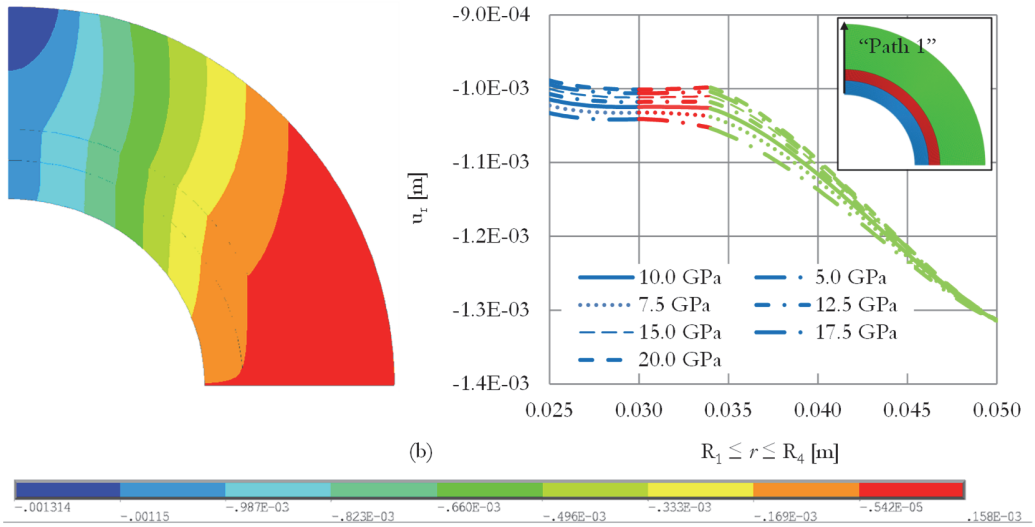

Figure 9: (a) The distribution of the u_y component of the displacement field in [m]. (b) The variation of u_y along "Path 1" for various values of the elastic modulus of the intermediate ring (E_2). The colours of the lines of the graph are in agreement to the colour code of the embedded figure.

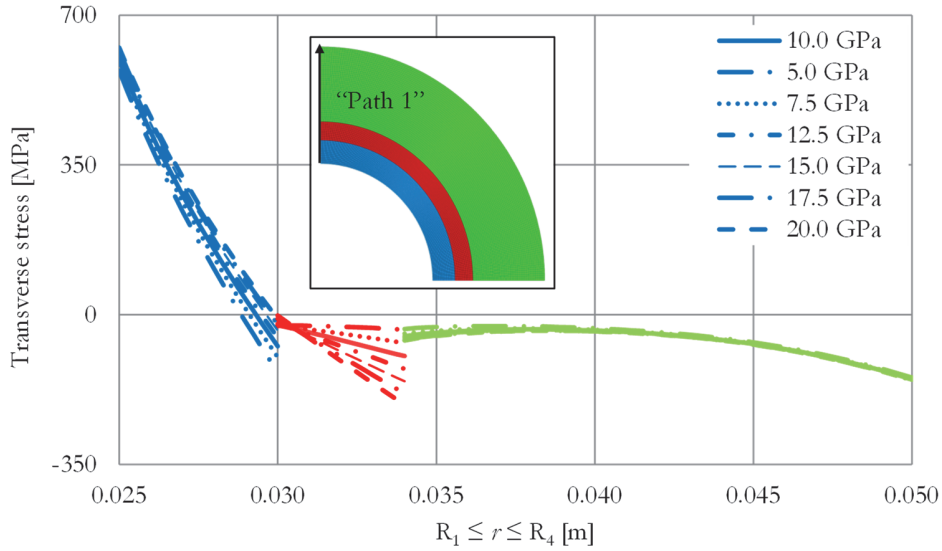

Figure 10: The transverse stress along "Path 1" for various values of the elastic modules, E_2, of the intermediate ring. The colours of the lines of the graph are in agreement to the colour code of the embedded figure.

As the modulus of elasticity of ring 2 increases, $\sigma_{t\theta}$ also increases, attaining its maximum value when θ~65°. The radial stress also attains its maximum value when θ is equal to about 65°, although a slight "move" to a lower value of θ is observed as E_2 increases. It is also to be noted that the changes of σ_r are not significant all along the outer periphery of ring 1.
The variation of stresses along the inner periphery of ring 3 (interface between rings 2 and 3) is plotted in Fig.11b. It is clear that the variation of both radial and shear stresses is qualitatively similar to the respective one along the outer periphery of ring 1 but their magnitudes are lower. The radial stress attains its maximum value when θ is equal to about 60° and the differences are mainly detected when θ varies from about 75° to 90°. Concerning the shear stress, it attains its maximum value when θ~70°. In addition, it seems that the exact position of the maximum shear stress "moves" slightly to larger θ values with increasing E_2. On the other hand, the variation of the transverse stress is monotonous all along the specific path, contrary to what it was observed along the outer periphery of ring 1.

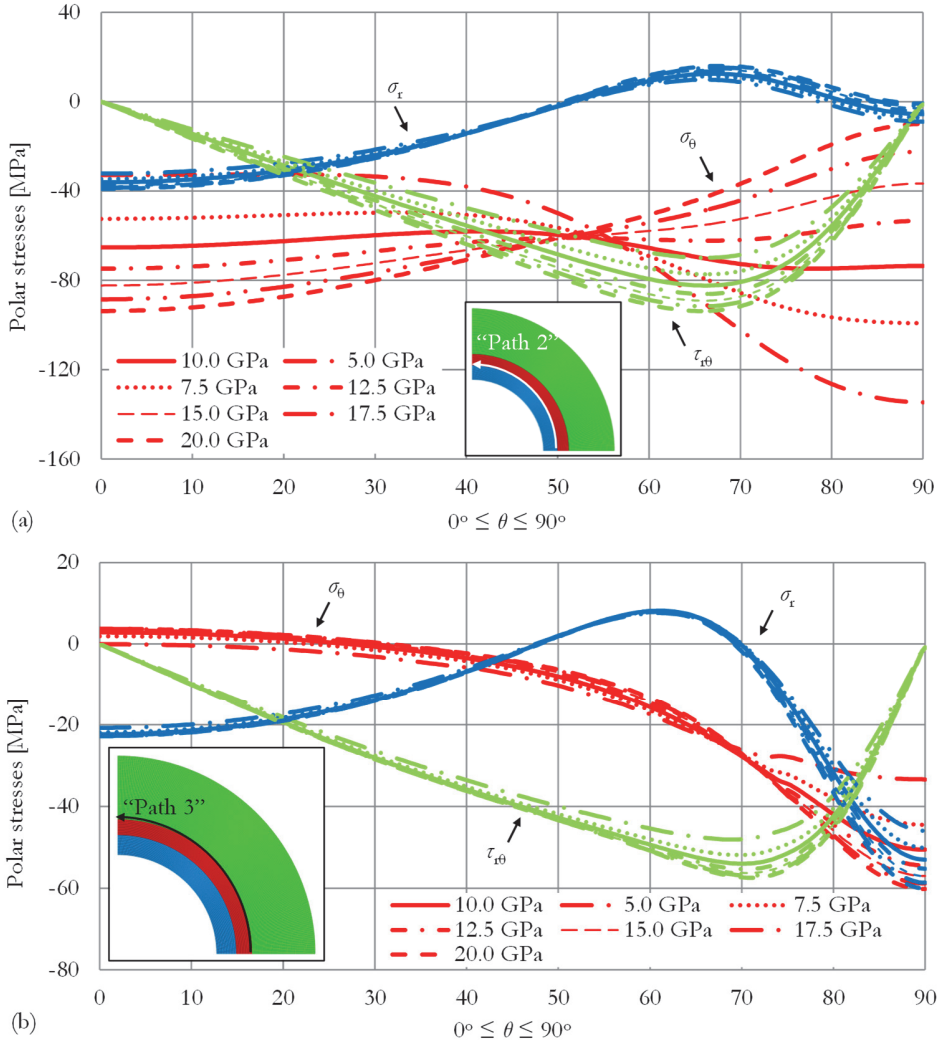

Figure 11: (a) The variation of the polar stresses along "Path 2" (outer periphery of the innermost ring) for various E_2-values. (b) The variation of the polar stresses along "Path 3" (inner periphery of the outermost ring) for various E_2-values.

The influence of the thickness of the intermediate ring, t_2

The effect of the thickness of the intermediate ring on the variation of stresses along the outer periphery of ring 1 (Fig.12a) is very similar to the one presented in Fig.11a (where the parameter studied was the modulus of elasticity of ring 2) both qualitatively and quantitatively. For t_2=4 mm (reference model) the variation of σ_θ is again smoother. For t_2<4 mm σ_θ increases with increasing θ while for t_2>4 mm σ_θ increases with decreasing θ. The shear stress, on the other hand, increases continuously with increasing t_2 and its maximum value is again detected around θ~65° independently of the values of t_2 considered here. Increase of t_2 leads also to increase of the radial stress developed. Again its maximum value seems to "move" slightly towards larger θ-value as t_2 increases.

The variation of stresses along the inner periphery of ring 3 is exhibited in Fig.12b and it is similar to the respective one in Fig.11b. However, and despite this qualitative similarity, the thickness of the intermediate ring affects more the stress field along the inner periphery of the outermost ring 3. The differences are generally larger, especially around θ=0° and θ=90°. This is true for both radial and transverse stresses. On the contrary, the shear stress attains its maximum value at θ~65° when t_2=1 mm while as t_2 increases the maximum shear stress appears at slightly larger values of θ.

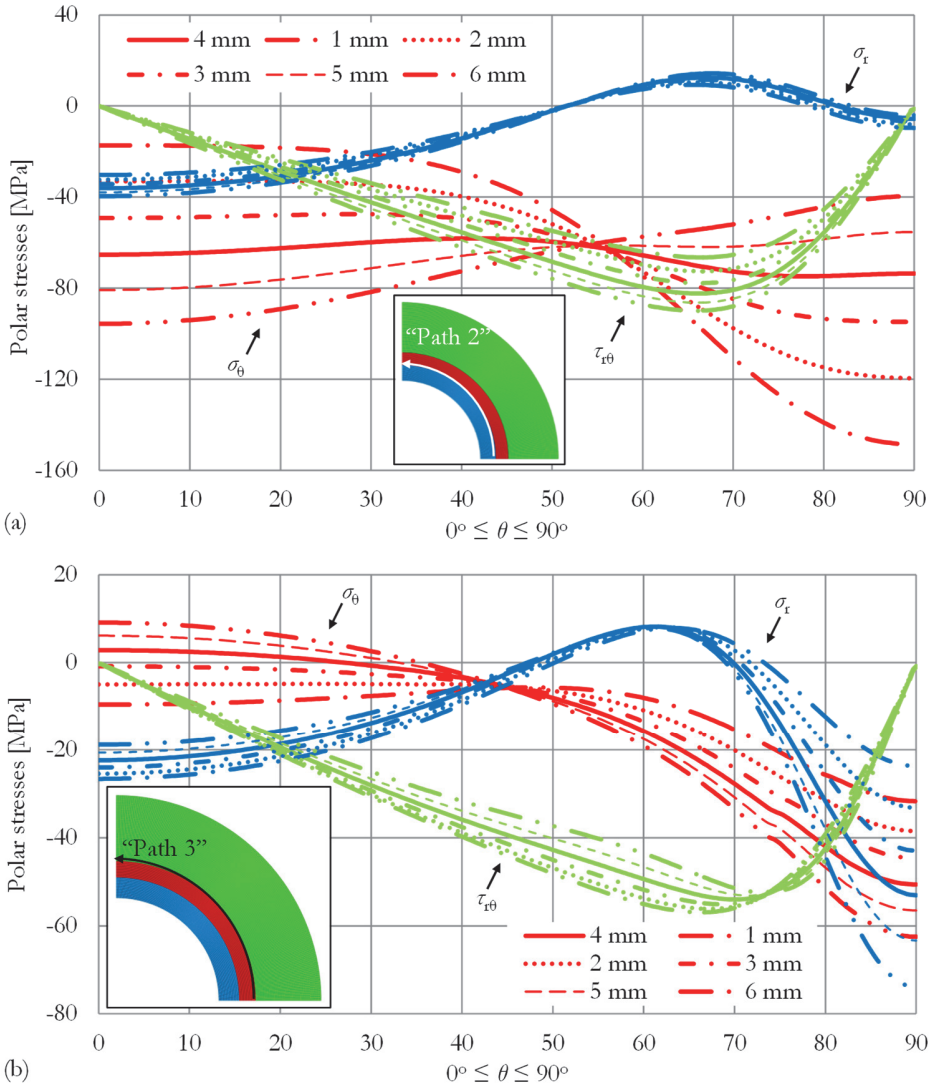

Figure 12: The variation of the polar stresses developed along (a) "Path 2" - outer periphery of innermost ring and (b) "Path 3" - inner periphery of outermost ring for various values assigned to the thickness of the intermediate ring (t_2).

Another interesting point is that the contact length between the outermost ring and the jaw, as well as the pressure applied along it, are only slightly influenced by the thickness of the intermediate ring, as it can be seen in Fig.13. The lower t_2 is, the smaller the contact length is (i.e., for t_2=1 mm, $2\omega_o$=23.34° while for t_2=6 mm, $2\omega_o$=24.67°) and the lower the maximum pressure applied on the ring is (keeping the externally applied displacement on the jaw constant).

The role of the contact length, $2\omega_o$

Keeping the "total" pressure applied constant and at the same time narrowing the contact length ω_o, results to interesting changes of the polar stresses developed along the interfaces. It is recalled here that the specific parameter is studied for an isolated ring rather than the ring-jaw complex. Therefore the contact length for the reference model is here set equal to that obtained during the validation procedure, which was equal to $2\omega_o$=24.60°.

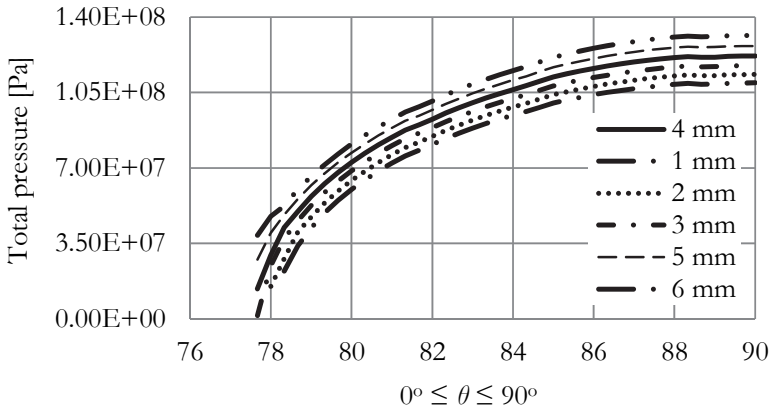

Figure 13: The variation of the total pressure applied on the ring for various t_2-values.

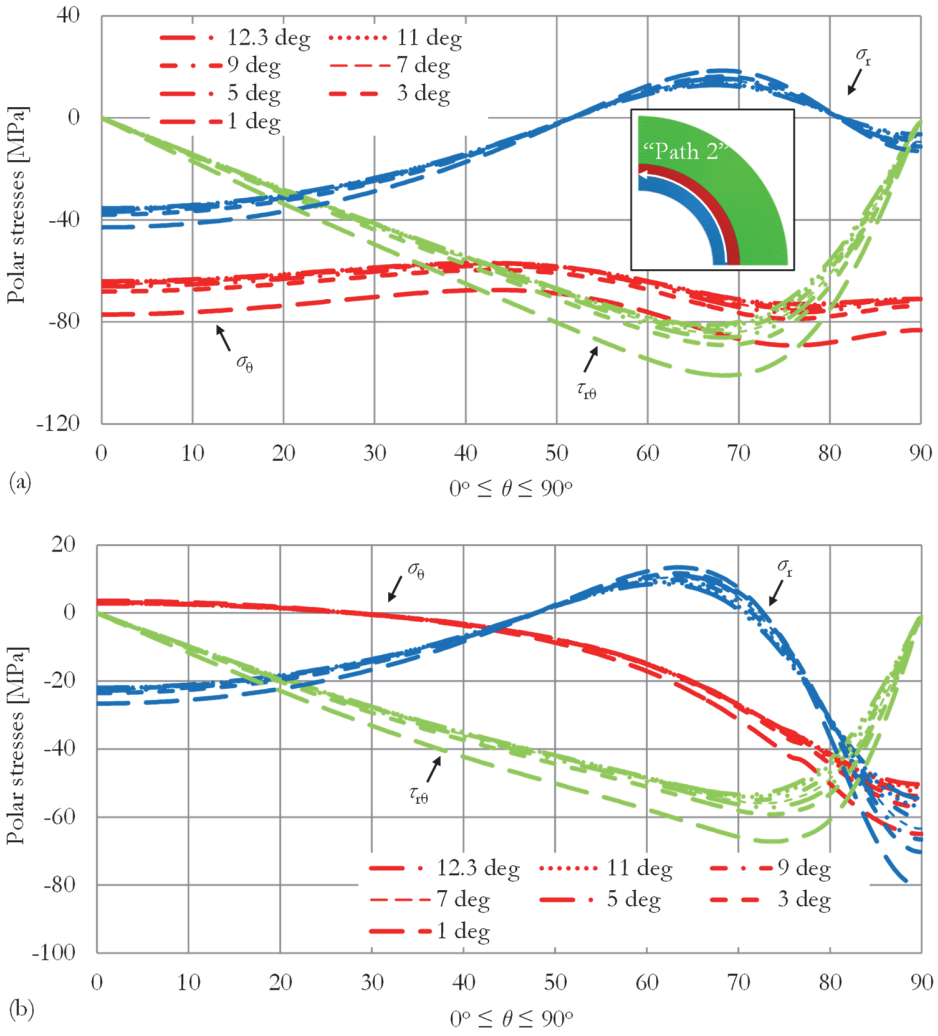

Figure 14: The variation of the polar stresses developed along (a) "Path 2" - outer periphery of innermost ring and (b) "Path 3" - inner periphery of outermost ring for various values assigned to the half contact length (ω_o).

Indeed, along the outer periphery of ring 1 (Fig.14a) the transverse stress σ_θ seems to be almost independent of the contact length for $\omega_o \geq 5^o$. The changes are noticeable only for $\omega_o < 5^o$ and the respective variations are almost similar to the aforementioned ones (attaining of course larger values). The same is more or less true concerning the shear stress. As the contact length becomes narrower, the shear stress increases (the changes are larger as ω_o decreases) attaining its maximum value at about $\theta \sim 70^o$. Similar conclusions are drawn, also, for the variation of the radial stresses.
The variation of the transverse stress σ_θ along the inner periphery of ring 3 is exhibited in Fig.14b. As ω_o decreases the changes of σ_θ are more pronounced and the maximum difference recorded is equal to about 15% for $\omega_o=3^o$ (in comparison to the reference model for which $\omega_o=12.33^o$). In case $\omega_o=1^o$, almost half of the periphery is affected and the difference now reaches about 30%. The radial stress is also strongly affected, reaching 50% larger value at $\theta=90^o$ when $\omega_o=1°$ compared to the respective stress when $\omega_o=12.33^o$. Concerning the shear stress, it is again larger as ω_o decreases attaining its maximum value around $\theta=70^o$.

CONCLUSIONS

An analytic solution for the mechanical response of a multi-layered ring under a combined loading scheme, including both uniform internal and external pressure and also parabolic distribution of radial stresses along two finite arcs of its external periphery was introduced. The solution was obtained in series form with the aid of Savin's pioneering approach for the infinite plate with a hole strengthened by rings. The main advantage of the analytic procedure described is that it is capable of providing the full-field stress- and displacement-fields for any combination of the three constituent loading schemes considered. As an application the three-layered ring was studied due to its increased practical importance.
In order for a closed form full-field solution to be achieved, some critical assumptions were adopted, besides the familiar ones related to the linearity, homogeneity and isotropy of the ring's constituent materials. These assumptions are related to the ideal bonding between the ring's successive layers, the absence of any kind of friction and the distribution of radial stresses along the loaded arcs, which was considered of parabolic nature, in accordance with the respective distribution for an intact disc compressed between the jaws suggested by ISRM for the implementation of the Brazilian-disc test.
The analytic solution was used to validate a flexible numerical model, in the direction of implementing thorough parametric studies. The advantage of the numerical model was the fact that it considered the ring and the jaw as a system of elastic bodies in equilibrium, approaching experimental reality in a much more accurate manner. The model was exhaustively validated taking advantage of the analytic results. During the validation process it was concluded that the actual stress distribution along the contact arc at the ring-jaw interface is more or less independent of some crucial geometric characteristics. In fact, it was proven that the specific distribution in case the body compressed between the ISRM jaws is intact (disc) does not exhibit significant differences compared to the respective distribution for a body weakened by the presence of a circular hole (irrespectively of whether it is a homogeneous ring or a ring consisting of successive layers with different mechanical properties). In general, the assumptions adopted during the formulation of the analytic problem for the loading scheme of the isolated ring were in excellent agreement with the conditions along the ring-jaw contact arc obtained by the numerical study of the ring-jaw complex.
The parametric study revealed quite a few interesting aspects concerning the influence of three critical parameters on the stress- and displacement-fields developed in the multi-layered ring. Generally speaking, this influence is of complicated, non-monotonous nature, rendering further parametric analysis with simultaneous variation of these parameters unavoidable.

REFERENCES

[1] Markides, Ch.F, Pasiou, E.D., Kourkoulis, S.K., The multi-layered ring under parabolic pressure, Engineering Transactions, 64(4) (2016) 433-440.
[2] ISRM, Suggested methods for determining tensile strength of rock materials, International Journal of Rock Mechanics and Mining Sciences and Geomechanics Abstracts, 15(3) (1978) 99–103.
[3] Savin, G.N., Stress concentration around holes, Pergamon Press, Oxford (1961).
[4] Muskhelishvili, N.I., Some basic problems of the mathematical theory of elasticity, 4th edition, P. Noordhoff Groningen, The Netherlands (1963).
[5] Kourkoulis, S.K., Markides, Ch.F., Chatzistergos, P.E., The standardized Brazilian disc test as a contact problem, International Journal of Rock Mechanics and Mining Sciences, 57 (2012) 132-141.

[6] Timoshenko, S.P., Goodier, J.N., Theory of elasticity, McGraw-Hill, New York (1970).
[7] Markides, Ch.F., Kourkoulis, S.K., The stress field in a standardized Brazilian disc: The influence of the loading type acting on the actual contact length, Rock Mechanics and Rock Engineering, 45(2) (2012) 145-158.
[8] Kourkoulis, S.K., Markides, Ch.F., Chatzistergos, P.E., The Brazilian disc under parabolically varying load: Theoretical and experimental study of the displacement field, International Journal of Solids and Structures, 49(7-8) (2012) 959-972.

Earthquake design for controlled structures

Nikos G. Pnevmatikos
Technological Educational Institution of Athens, Greece
pnevma@teiath.gr

George A. Papagiannopoulos
University of Patras, Greece
gpapagia@upatras.gr

George D. Hatzigeorgiou
Hellenic Open University, Greece
hatzigeorgiou@eap.gr

ABSTRACT. An alternative design philosophy, for structures equipped with control devices, capable to resist an expected earthquake while remaining in the elastic range, is described. The idea is that a portion of the earthquake loading is undertaken by the control system and the remaining by the structure which is designed to resist elastically. The earthquake forces assuming elastic behavior (elastic forces) and elastoplastic behavior (design forces) are first calculated according to the codes. The required control forces are calculated as the difference from elastic to design forces. The maximum value of capacity of control devices is then compared to the required control force. If the capacity of the control devices is larger than the required control force then the control devices are accepted and installed in the structure and the structure is designed according to the design forces. If the capacity is smaller than the required control force then a scale factor, α, reducing the elastic forces to new design forces is calculated. The structure is redesigned and devices are installed. The proposed procedure ensures that the structure behaves elastically (without damage) for the expected earthquake at no additional cost, excluding that of buying and installing the control devices.

KEYWORDS. Response spectrum analysis; Structural control; Earthquake engineering.

Citation: Pnevmatikos N., Papagiannopoulos G., Hatzigeorgiou G., Earthquake design for controlled structures, Frattura ed Integrità Strutturale, 40 (2017) 129-136.

Received: 05.12.2016
Accepted: 13.03.2017
Published: 01.04.2017

INTRODUCTION

Over the past few decades various control algorithms and control devices have been developed, modified and investigated by various groups of researchers. The works of Yao, 1975, Housner et al., 1994, Kobori et al., 1998, and Soong 1998 are representative [1-4]. There have been some attempts to connect the control forces with the

design codes. Yang et al. 2003 [5] suggested the maximum control force to be a percentage of the building weight, while Cai et al., 1997, [6] give this force as a portion of the seismic force. Lee et al., 2004, [7] determined the upper limit of control force based on the response spectrum of the external earthquake.
During the past years the design philosophy of new structure was to design stiff structures with high strength to resist the earthquake in the elastic range. After that the design philosophy moves one step further. Using the ductility of the material, structures were designed to resist lower level of earthquake forces within the elastic range but to have adequate ductility in order to face the attack of stronger earthquakes and prevent them from collapse. This drives to lighter structures compared to the previous structures and more economical. However, the capacity design and the reinforcement details increased the cost. Taking in account the cost of repair of the retrofitting of structure, after a strong earthquake, the design of ductile structures should be under consideration.
The design philosophy proposed here is to use control devices installed in the structure and provide a reservoir of strength, stiffness or damping, necessary for preventing the structure from damage when an expected earthquake will occur. Thus, the control system will drive the structure to behave in the elastic range when it is attacked by the expected earthquake and no damages will occur. As far as the cost is concerned, it is possible to achieve substantial savings by avoiding retrofit of structure during the lifetime of structure and utilize these savings for installing a control system. A systematic procedure to achieve the above objective is proposed in this work.

DESIGN PROCEDURE FOR STRUCTURES EQUIPPED WITH A CONTROL SYSTEM

The evolution of the design philosophy of structures passes through different stages. Fist the engineers design stiff and massive structures in order to behave elastically during the expected earthquake. As years passed and damages were observed after earthquakes the design philosophy was moved from the resistance of structure to energy dissipation capacity of the structural elements and design of structures with an overall ductile behavior. This drives engineers to perform capacity design for structures. This philosophy is nowadays included in all current design regulations. However, observing the damages to the structures that were designed with the latter philosophy and making calculations, the repair cost of the capacity design emerged and came into consideration. The answer to the previous consideration is the new and proposed design philosophy where the structure is oriented to capacity design equipped with control devices that will absorb a portion of seismic energy induced to the structure and as a result to keep the structure in the elastic range. The three design philosophies are depicted in Fig. 1. The proposed design procedure for the spectrum is calculated in such a way that one portion of earthquake forces is taken by the structure and the remaining ones are taken by the control devices.

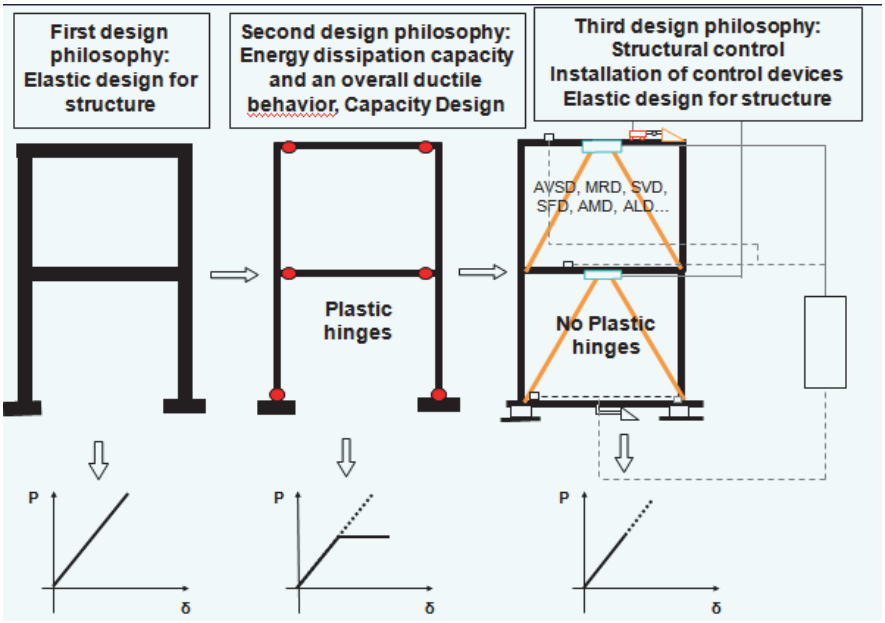

Figure 1: The three design philosophies of design of structures.

Initially, the controlled structure is designed based on a design spectrum provided by the pertinent code (Eurocodes) with a specific level of ductility. The required control forces that will take a portion of earthquake forces are calculated as the difference from forces obtained from the elastic spectrum to those obtained from the design spectrum. The maximum value of capacity of the control devices is compared with the required control force. If the capacity of the control devices is larger than the required control force then the control devices are accepted and installed into the structure. If the capacity is smaller than the required control force then a control device with larger capacity should be chosen or more devices per floor should be installed

In case the maximum available control device capacity is smaller than the required control force, or, there is a limitation to the number of control devices, then using an iterative procedure, a scale factor, α, higher than the value 1/q that reduces the elastic response spectrum is calculated. The structure is redesigned based on the new reduced spectrum by scale factor, a, and then the devices are installed into the structure. The flow chart of the procedure is shown in Fig. 2 with a solid line.

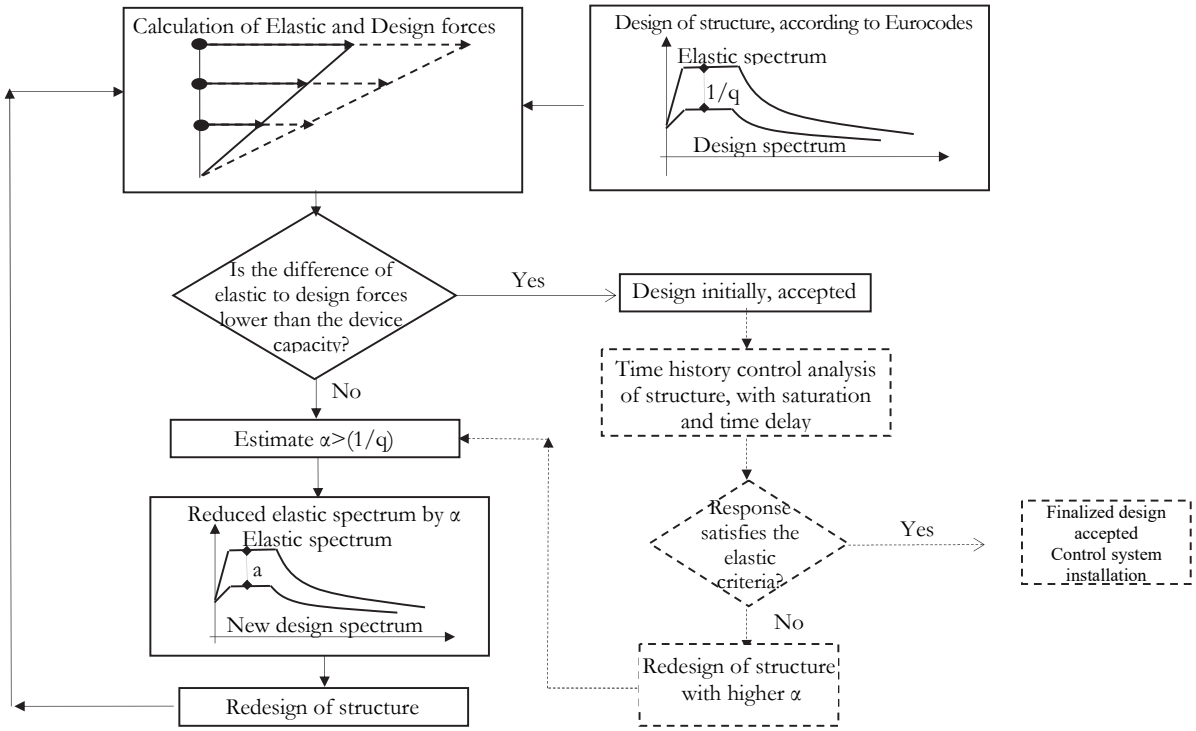

Figure 2: The flow chart of the proposed design procedure.

Estimation of scale factor, a.

From the elastic seismic forces and the maximum capacity of the control device a scale factor α is obtained and applied on the elastic spectrum. Knowing the mass and initial stiffness of the structure the eigenmodes Φ_i, eigenperiods T_i or eigenfrequencies f_i and the corresponding damping ratios ξ_i of the uncontrolled system are obtained.

The participation factor ψ_i, and elastic seismic forces $F_{q,el,i}$ for the i^{th} eigenmode are given as:

$$\psi_i = \frac{\mathbf{\Phi}_i^T \mathbf{M} \mathbf{E}}{\mathbf{\Phi}_i^T \mathbf{M} \mathbf{\Phi}_i}, \quad i=1,...,n \tag{1}$$

$$\mathbf{F}_{q,el,i} = \mathbf{M}\mathbf{\Phi}_i \psi_i S_{e,i}(T_i, \xi_i), \quad i=1,...,n \tag{2}$$

where E is the direction matrix for the earthquake and $S_{e,i}(T_i, \xi_i)$ is the elastic spectral acceleration. The maximum elastic seismic forces $F_{q,e}$ for each degree of freedom are obtained combining the Square Root of Sum Squares method (SRSS) the elastic seismic forces from each eigenmode, thus:

$$\mathbf{F}_{q,e}=\sqrt{\sum_{i}^{n}\mathbf{F}_{q,e,i}^{2}} \tag{3}$$

If $F_{d,max}$ is the maximum control device capacity (maximum possible control force), then the maximum control force that can be applied on the system is:

$$\mathbf{F}_{d,max}=\mathbf{E}_{f}F_{d,max} \tag{4}$$

where E_f is the location matrix for the control devices on the structure. Assuming that one part, up to $F_{d,max}$, of elastic seismic forces are carried by control devices, the remaining seismic forces which go directly and force the structural elements are:

$$\mathbf{F}_{q,\,new}=\begin{cases}\mathbf{F}_{q,e}-\text{sign}(\mathbf{F}_{q})\mathbf{F}_{d,max} & \text{if} \quad \left|\mathbf{F}_{q}\right|\geq\mathbf{F}_{d,max}\\ 0 & \text{if} \quad \left|\mathbf{F}_{q}\right|<\mathbf{F}_{d,max}\end{cases} \tag{5}$$

$\mathbf{F}_{q\ new}$ is a vector with n forces, where n is the degree of freedom of the system. These forces correspond to a reduced spectral acceleration. From Eq. (2) this new spectral acceleration $S_{d,i,new}(T_i, \xi_i)$, corresponding to new seismic forces, can be obtained:

$$S_{d,i,new}(T_i,\xi_i)=\frac{\left(\mathbf{M}\boldsymbol{\Phi}_{i}\right)^{-1}\mathbf{F}_{q,new}^{T}}{\psi_i}, \qquad i=1,...,n \tag{6}$$

The reduction factor α can be obtained by dividing the new spectral acceleration $S_{d,i,new}(T_i, \xi_i)$ by the corresponding initial one:

$$\alpha_i=\frac{S_{d,i,new}(T_i,\xi_i)}{S_{e,i}(T_i,\xi_i)}, \qquad i=1,...,n \tag{7}$$

The elastic spectrum is scaled using the maximum value of α_i and the structure is redesigned based on the reduced spectrum. The value of a is:

$$\alpha=\max(\alpha_i) \tag{8}$$

In order to ensure a linear behavior of the structure, dynamic control analysis is performed for a range of earthquakes (high and low frequency characteristics), with saturation control and time delay. If the response satisfies the elastic criteria, then the value of α is accepted, otherwise it is slightly increased and the above procedure is repeated. The flow chart of this procedure is shown in Fig. 2 with a dashed line.

The equation of motion of a controlled structural system with n degrees of freedom subjected to an earthquake excitation ag in the state space approach is:

$$\dot{\mathbf{X}}=\mathbf{A}\mathbf{X}+\mathbf{B}_{g}a_{g}+\mathbf{B}_{f}\mathbf{F} \tag{9}$$

The matrixes X, A, B_g, B_f are given by

$$\mathbf{X}=\begin{bmatrix}\mathbf{U}\\ \dot{\mathbf{U}}\end{bmatrix}_{2n\times1}, \quad \mathbf{A}=\begin{bmatrix}\mathbf{0} & \mathbf{I}\\ -\mathbf{M}^{-1}\mathbf{K}_{new} & -\mathbf{M}^{-1}\mathbf{C}\end{bmatrix}_{2n\times2n}, \quad \mathbf{B}_{g}=\begin{bmatrix}\mathbf{0}\\ -\mathbf{E}\end{bmatrix}_{2n\times1}, \quad \mathbf{B}_{f}=\begin{bmatrix}\mathbf{0}\\ \mathbf{M}^{-1}\mathbf{E}_{f}\end{bmatrix}_{2n\times1} \tag{10}$$

where M and C denote the mass and damping matrices of the structure, respectively, K_{new} is the new stiffness matrix of the redesigned structure, and F is the control force matrix. The control force F is determined by linear state feedback as follows:

$$\mathbf{F} = -\mathbf{G}_1\mathbf{U} - \mathbf{G}_2\dot{\mathbf{U}} = -\begin{bmatrix}\mathbf{G}_1 & \mathbf{G}_2\end{bmatrix}\begin{bmatrix}\mathbf{U} \\ \dot{\mathbf{U}}\end{bmatrix} = -\mathbf{G}\mathbf{X} \tag{11}$$

G is the gain matrix, which will be calculated by pole assignment method and according to the desired poles of the controlled system.
If the response obtained for the controlled system satisfies the design criteria, then the reduction by q or by a scale factor, α, is accepted. In this work a representative design criterion was used, that the story drift does not exceed h/300 (where h is the story height). This value does not cause member yielding. In a similar way, additional design criteria concerning the rotation and strength of structural members can be used. The above procedure was tested for a number of numerical simulations, and some representative examples are presented next.

RESULTS AND DISCUSSION

The proposed approach is demonstrated by means of numerical example where an eight-story building, described in the work of Yang et al, 1995 [7], is analyzed. Initially the elastic and design spectra are calculated based on Eurocode 8 (EC8) seismic code.
Based on those spectra and on dynamic characteristics of building the seismic forces $F_{q,i}$ for each eigenmode and their combination are calculated for both elastic and design spectrum. The seismic forces which are obtained from elastic and design spectrum and their differences are shown in Fig. 3(a). Assuming that the control devices are installed on each floor and the maximum capacity is 1000kN, following the proposed procedure the scale factor α is calculated to be equal to 0.49 or the equivalent reduction from the elastic spectrum 1-α which is equal to 51%. The elastic and design spectra and the reduced spectrum by 51% from the elastic spectrum, for which the structure will be redesigned, are illustrated in Fig. 3(b).
In order to ensure that the structure remains in the elastic range after redesigning, dynamic time control analysis history, with saturation control and time delay, for a wide range of earthquakes should be performed. The numerical simulations were performed in Simulink toolbox of Matlab software. The numerical simulation of the control scheme is described in Fig. 3(c).
The response (displacement and acceleration) of the system subjected to Athens earthquake 1999 were calculated. From the numerical results it was seen that full compensation of the displacements was achieved. According to the work of Yang et al. (2003) when one control force corresponds for each degree of freedom then complete compensation of the response can be achieved and the response state vector can be reduced to zero. Another reason that the relative displacements are near to zero is that the elastic response spectrum of the Athens earthquake are lower than the elastic spectrum that was used initially for the design procedure. The acceleration is equal to the external signal and the building behaves like executing a rigid body motion. The control forces are identical, with maximum value at 917 kN and rms value at 134 kN, because the mass of each story is the same. The storey drift between the floors was not exceeded the limit value h/300=10 mm. Time history of displacement and the acceleration from 8th floor for the controlled and uncontrolled structure is shown in Fig. 4.

SUMMARY AND CONCLUSIONS

A procedure to design a structure equipped with control devices is described. The structure is designed based on a reduced spectrum. A scale factor α which multiplies the elastic spectrum and produces a reduced spectrum is proposed. The design philosophy is that one part of seismic forces are taken by control devices and to the rest of earthquake forces taken up from the structure. The numerical results indicate that reduction of the spectrum can be achieved using control devices. The cost of repairing the post-earthquake damages of an uncontrolled structure which was design based on ductility demand can be considered as a motivation to install a control system which will keep the structure in the elastic range. The control system is acceptable if the results obtained from the dynamic control analysis

keep the structure within the elastic limit. Design criteria such as inter-story drift which shouldn't exceed a specific value that causes yielding of the structural members could be used in order to ensure elastic behavior.

(a)

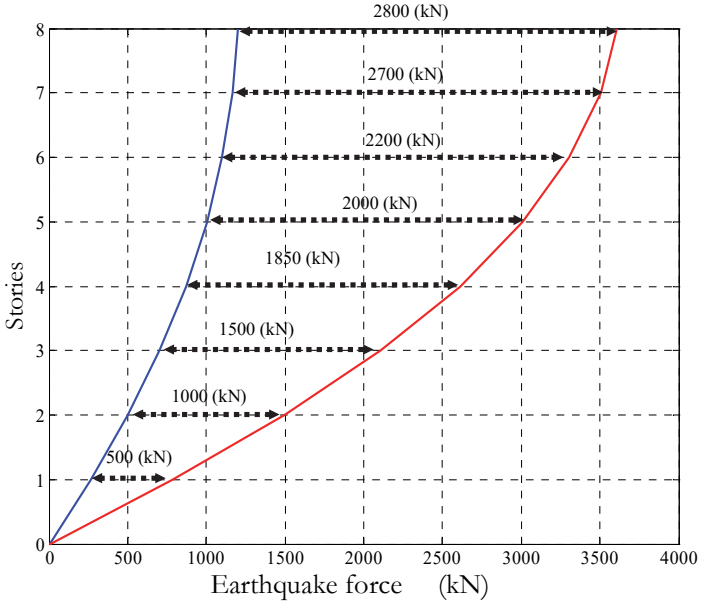

(b)

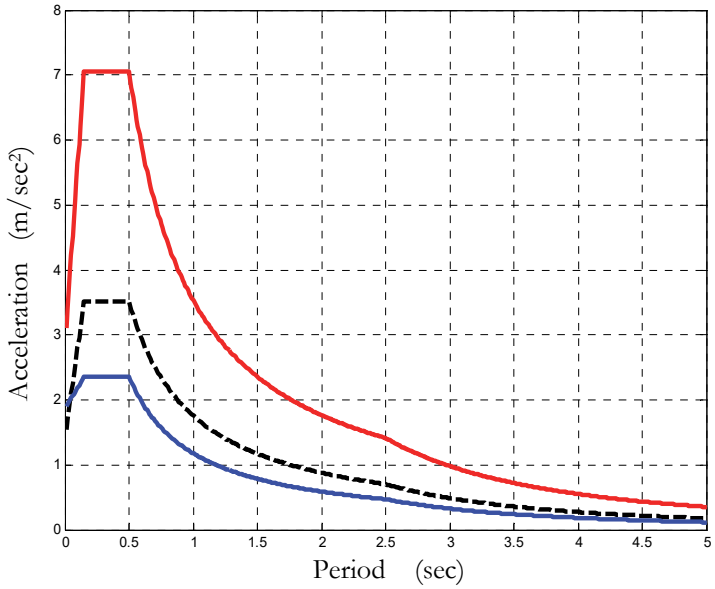

(c)

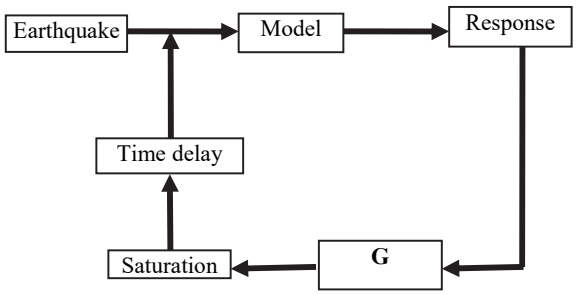

Figure 3: The difference between elastic and design forces for each story, (a), the elastic and design spectrum, (solid lines), and the reduced elastic spectrum (dash line) for the structure with control devices, (b). Model and control scheme in Simuling toolbox (c).

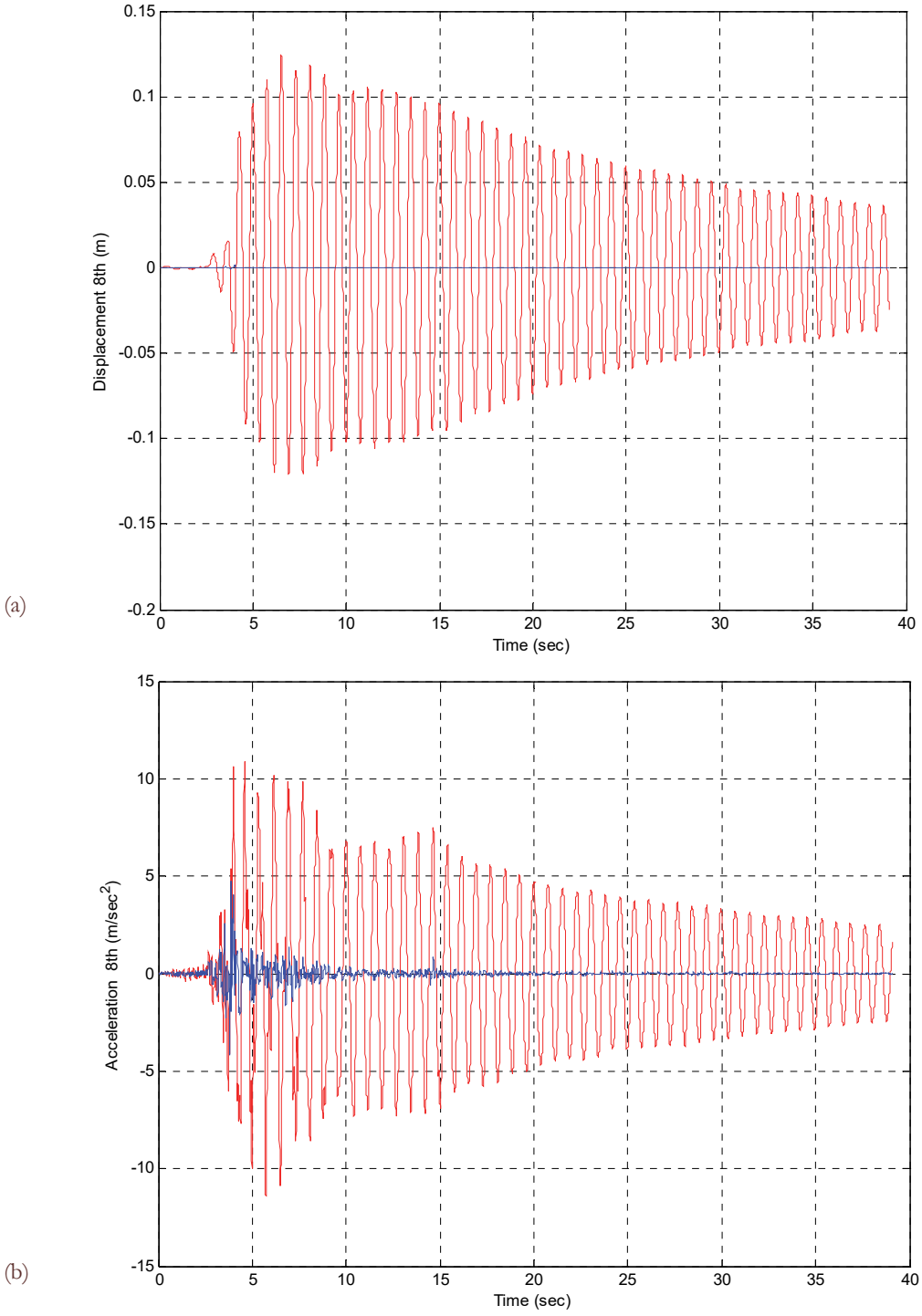

Figure 4: Displacement and the acceleration from 8th floor for the controlled and uncontrolled structure.

The proposed procedure was applied to 8-story building and the numerical results show the effectiveness of the procedure. The control system helps the structure not only to reduce the maximum response (displacements and accelerations) and keep it in the elastic range, but also to perform at much lower level than the maximum response values. This is proved by comparison of the root mean square (rms) values with the maximum values of response. The proposed design procedure seems to be an effective tool for designing controlled structures although further numerical research and experimental verification are needed. Additionally, the methodology should be applied to a space and irregular structures with significant participation of higher modes and with torsional effects.

REFERENCES

[1] Yao, J.T.P., Concepts of structural control, Journal of structural engineering ASCE, 98(7) (1972) 1567-1574.
[2] Housner, G. W., Bergman, L. A., Caughey, T. K., Chassiakos, A. G., Claus, R. O., Masri, S. F., Skelton, R. E., Soong, T. T., Spencer, Jr., B. F., and Yao, J. T. P., Structural control: Past, present and future, Journal of Engineering Mechanics, 123(9) (1997) 897–971.
[3] Kobori, T., Inoue, Y., Seto, K., Iemura, H., Nishitani, A., Procedings 2nd World Conf. on Structural Control, Kyoto, Japan, II (1998) 171-188.
[4] Soong, T.T., Active structural control: Theory and practice, Longman Scientific &Technical/Wiley London/New York, 1990.
[5] Yang, J.N., Wu, J.C., Agrawal A.K., Hsu S.Y., Sliding mode control of seismically excited linear structures, Journal of Engineering Mechanics, ASCE, 121 (2003) 1386-1390.
[6] Cai, G.P., Huang, J.Z., Sun, F., Wang, C., Modified sliding mode bang-bang control for seismically excited linear structure, Earthquake Engineering and Structural Dynamic, 29 (1997) 1647-1657.
[7] Lee, S.H., Min, K.W., Lee, Y.C., Chung, L., Improved design of sliding mode control for civil structures with saturation problem, Earthquake Engineering and Structural Dynamics, 33 (2004) 1147-1164.
[8] Yang, J.N., Wu, J.C., Agrawal, A.K., Hsu, S.Y., Sliding mode control for non linear and hysteretic structures, Journal of Engineering Mechanics ASCE, 121 (1995) 1330-1339.

S-N curve modeling method of Aluminum alloy welded joints based on the fatigue characteristics domain

Li Zou
Software Institute, Dalian Jiaotong University, Lvshun 116052, China
lizou@djtu.edu.cn

Xinhua Yang
College of Material Science and Engineering, Dalian Jiaotong University, Dalian, China
yangxhdl@foxmail.com

Jianrong Tan
Department of mechanical engineering and automation, Zhejiang University, Zhejiang, China

Yibo Sun
College of Material Science and Engineering, Dalian Jiaotong University, Dalian, China

ABSTRACT. The scatter degree of the fatigue samples is reduced when the nodal force based structural method is used for steel welded joints, while it is still high for aluminum alloy welded joints. Statistical method and rough set theory is used to fatigue analysis so that fatigue characteristic domains are determined and S-N curves are fitted. Experiment results show that fatigue life of the aluminum alloy welded joints is under the influence of some key factors and the fatigue data with the same characteristics distribute in a relatively independent area. Accordingly, a novel S-N curve modeling method of aluminum alloy welded joints based on the fatigue characteristics domain is proposed. In the proposed method, the nodal force based structural stress method is used for stress calculation and neighborhood rough set theory is used for character extraction to obtain the key factors. Then fatigue characteristics domains are divided and S-N curves are fitted on each fatigue characteristics domain instead of on the whole domain so that a set of S-N curves are obtained. Statistical results show that selection of the S-N curve for the aluminum alloy welded joints according to different fatigue characteristic domain is more accurate.

KEYWORDS. Welding; Fatigue; Structural stress; Rough set theory; S-N curve.

OPEN ACCESS

Citation: Zou., L., Yang, X., Tan, J., Sun, Y., S-N curve modeling method of Aluminum alloy welded joints based on the fatigue characteristics domain, 40 (2017) 137-148.

Received: 09.11.2016
Accepted: 10.01.2017
Published: 01.04.2017

INTRODUCTION

As a traditional processing technique, welding has been widely used in many fields, such as mechanical manufacturing, aerospace, transportation, etc. The fatigue analysis and life prediction of a welding joint are directly related to the stability and safety of the whole structure. Currently, the nominal stress method and the nodal based structural stress method are two most commonly used welding fatigue analysis and prediction methods.

The nominal stress method is the first routine way to get theoretical and experimental research in fields of engineering fatigue design, strength assessment and life prediction of welded structures. In various industry fields, its method and data has been widely standardized, and it has been maturely applied to the actual project. But because of the existence of various preconditions and regulations, choice of the S-N curves is uncertain in this method. How to accurately select the S-N curve and to calculate the stress are the most important problems which cannot be solved in this method.

The nodal force based structural stress method is a new type of fatigue life prediction technology for welded structure proposed by Dong [1]. In this method, the finite element technique is used to compute the structural stress through nodal force. Currently, the nodal force based structural stress method is one of the most striking engineering technologies for fatigue analysis of welded structures due to its mesh-insensitive hot spot stress calculation, higher fatigue life prediction accuracy and the broad applicability [2]. Dong et al. reprocessed thousands of fatigue test data of the steel welded joints in the last 50 years [3]. According to the linear regression analysis, the main S-N curve of fatigue design based on equivalent structural stress (Eq. SS) range is determined.

In this study, first of all, fatigue data of aluminum alloy welded joints is collected and the fatigue database is obtained from related literatures. Then, S-N curves are fitted based on the nodal force based structural stress and the scatter degree of fatigue data is computed. Subsequently, neighborhood rough set theory is used for knowledge reduction to find the core among the many factors which influence the fatigue life of aluminum alloy welded joints. Finally, the fatigue characteristics domain is established according to the reduction result of neighborhood rough set theory and S-N curves are fitted subsequently in each domain.

RELATED WORKS

S-N curve is the main tool to analyze and predict fatigue lifetime of a metallic material, component or structure. A large number of domestic and foreign scholars have devoted themselves to the study of the S-N curve modeling method. Monotonic test based empirical fatigue formulae and a Wholer field mathematical model is combined and a new formula for developing full range stress life curves for medium strength steels is proposed [4]. The importance of employing material specific S-N curves with appropriate stress concentration factors for special connection details and correct damage accumulation methods is highlighted. The fatigue crack growth of a double fillet weld with the existence of a semi-elliptical crack is studied [5]. The constant amplitude loading is applied where the influence of the load ratio over the fatigue life is presented. A new probabilistic model is proposed [6], where the model parameters are estimated with an EM algorithm for which the Maximisation step combines Newton-Raphson optimization method and Monte Carlo integrations. A new method that assumes linear change of scatter according to stress levels is developed in [7]. The algorithm derives from maximum likelihood estimation and general Newton's method. A study has been carried out to establish which confidence level in the estimation of the characteristic S-N curve from limited data [8].The results of the study provide a new way to optimize fatigue design whenever it is costly or time-consuming to achieve many reliable test data. A unified statistical model which can take into account any number of failure mechanisms and the possible presence of the fatigue limit is presented [9]. The adaptability of the statistical model to the S-N curves proposed in the open literature is demonstrated by qualitative numerical examples.

Generally speaking, fatigue behavior of welded components is influenced by many factors such as temperature, material type, load type, ratio and etc. Up to now, many researchers have devoted themselves to this research and initial achievements have been obtained. For example, plate thickness factor is considered and a new analytical formula of fracture toughness is proposed based on the energy theory and linear elastic mechanics [10], which would significantly reduce the calculation cycle of remaining life of structures in structural integrity assessment of welded structures. Crack initiation potential in materials containing defects is investigated numerically by focusing on defect types, size, shape, location, and residual stress influences [11]. Results show that the crack initiation potency is higher in case of serious property mismatching between matrix and defects, and higher strength materials are more sensitive to soft inclusions. Near-threshold fatigue crack growth tests are conducted at various stress ratios and different pre-cracking locations of a 25Cr2Ni2MoV welded joint by using load-shedding procedure at room temperature to investigate the transition behavior of fatigue crack growth curve [12].

Results show that there exists a transition point in the fatigue crack growth curve in the near-threshold regime, and the stress intensity range of the fatigue threshold decreases with the increasing of stress ratio.
Currently, there is still a lack of an objective and comprehensive evaluation of the great many factors which influence the fatigue life of the welded structure. To establish the mathematical model of different influence factors, neighborhood rough set theory is used to find the core factors which influence the fatigue life of the aluminum alloy welded joints based on the data itself rather than on any other prior knowledge. Fatigue characteristics domains are then determined according to the key influence factors and the S-N curves are fitted in each domain subsequently.

METHODOLOGY

Basic Principle of the Nodal Force Based Structural Stress

The normal structural stress at each node from elementary structural mechanics theory is given by

$$\sigma_s = \sigma_m + \sigma_b \tag{1}$$

$$\sigma_m = f_y / t \tag{2}$$

$$\sigma_b = 6m_x / t^2 \tag{3}$$

where $f_y = F_y / l$, $m_x = M_x / l$ is the line force and moment in the weld tow shown as Fig. 1, F_y is the nodal force, M_x is the moment around the weld toe.

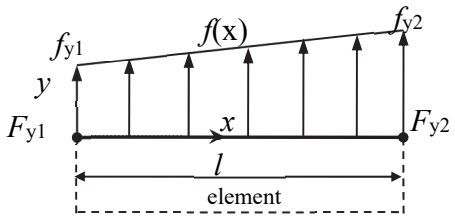

Figure 1: Definition of linear force.

Fracture mechanics is employed to estimate the fatigue life of welded joints. The stress intensity factor in crack propagation theory can be calculated as [2]:

$$\Delta K = \sqrt{t^*}[\Delta\sigma_m f_m(a/t) + \Delta\sigma_b f_b(a/t)], \tag{4}$$

where a is the crack depth, t^* is a ratio of actual thickness t to a unit thickness. $f_m(a/t)$ and $f_b(a/t)$ are membrane stress and bending stress as a function of crack growth degree respectively. According to the Paris crack growth law, the prediction of the life cycle from an infinitesimally small crack to final failure can be expressed as:

$$N = \int_{a/t=0}^{a/t=1} \frac{t^* d(a/t)}{C(M_{kn})^n (\Delta K)^m} = \frac{1}{C} t^{*1-\frac{m}{2}} (\Delta\sigma_s)^{-m} I(r), \tag{5}$$

where $M_{kn} = K / K_n$ is the notch stress magnification , K represents the total K due to both the far-field stress and the local notch stress effects and K_n represents only the far-stress contribution to the stress intensity factor. $I(r)$ is a dimensionless function of r and m is the crack growth exponent, which is set to be 3.6 in ASME [13]. A Master S-N curve can be established according to Eq. 6 based on a set of welding fatigue data. The Eq. SS can then be expressed as:

$$\Delta\sigma_\varepsilon = t^{*1-\frac{m}{2}} (\Delta\sigma_s)^{-m} I(r) \tag{6}$$

where t^* is dimensionless the equivalent $\Delta\sigma_\varepsilon$ retains a stress unit.

Neighborhood Rough Set Theory

Founded by Pawlak, rough set theory [14] aims to find the inner links of the massive, imprecise, incomplete and uncertain data, it has become an important tool to study granular computing theory nowadays [15]. However, the tradition rough set just works in discrete spaces and it can't deal directly with the numerical data that widely existed in the practical application. When dealing with the numerical data, discretization is first done to transform the numerical value into the symbol value [16, 17]. This transformation inevitably brings about information loss and the computing results usually depend largely on the effect of discretization algorithm. To deal with this problem, a neighborhood rough set model is proposed based on the definitions of δ neighborhood and neighborhood relations in metric spaces [18, 19]. Several foundation definition of neighborhood rough set theory including $\delta-neighborhood$, lower and upper approximations, dependency degree, significance of the attribute, reduction and core are first introduced here.

Definition 1 $\delta-neighborhood$

U is a non-empty finite set in the real number space, $\forall x_i \in U$, the δ -neighborhood of xi is defined as

$$\delta(x_i)=\{x\in U,\Delta(x,x_i)\le\delta\} \tag{7}$$

where Δ is a metric function, $\forall x_1,x_2,x_3\in U$, it satisfied $\Delta(x_1,x_2)>0$, $\Delta(x_1,x_2)=0$ if and only if $x_1=x_2$, $\Delta(x_1,x_2)=\Delta(x_2,x_1)$ and $\Delta(x_1,x_3)\le\Delta(x_1,x_2)+\Delta(x_2,x_3)$. The family of neighborhood granules $\{\delta(x_i)\,|\,x_i\in U\}$ forms an element granule system for a given metric space $<U,\Delta>$. We have $\forall x_i\in U,\delta(x_i)\neq\phi$ and $\bigcup_{x\in U}\delta(x)=U$. A neighborhood relation N can be written as a relation matrix $M(N)=(r_{ij})_{n\times n}$, where $r_{ij}=1$ if $x_j\in\delta(x_i)$ or $r_{ij}=0$ otherwise.

Definition 2 Lower and upper approximations

The lower and upper approximations of X in terms of relation N for a given $<U,N>$ are defined as

$$\underline{N}X=\{x_i\,|\,\delta(x_i)\subseteq X,x_i\in U\}, \tag{8}$$

$$\overline{N}X=\{x_i\,|\,\delta(x_i)\cap X\neq\phi,x_i\in U\}, \tag{9}$$

The boundary region of X is

$$BNX=\overline{N}X-\underline{N}X, \tag{10}$$

Definition 3 Dependency degree

The dependency degree of the decision attribute D to the condition attribute B is defined as

$$\gamma_B(D)=\frac{|\underline{N}_BD|}{|U|}, \tag{11}$$

It is obvious that $0\le\gamma_B(D)\le1$. If $\gamma_B(D)=1$, we say D completely depend on B otherwise D is γ -depend on B.

Definition 4 Significance of the attribute

Given a neighborhood decision table $<U,C,D,V,f>$, B⊆C,a∈C-B, the significance of a to B is defined as

$$SIG(a,B,D)=\gamma_{B\cup a}(D)-\gamma_B(D), \tag{12}$$

Definition 5 Reduction

Given a neighborhood decision table $<U,C,D,V,f>$, B⊆C, we say the subset of attributes B is a reduction of C if $\gamma_B(D)=\gamma_C(D)$ and $\forall b\in B,\gamma_B(D)>\gamma_{B-b}(D)$.

Definition 6 Core

Given a neighborhood decision table $<U,C,D,V,f>$, all reductions consist of $B_1,B_2,\ldots B_n$, the core of is defined as $core=\bigcap_{i=1}^{n} B_i$.

A kind of forward greedy reduction algorithm is used for the neighborhood decision table in this work, as is shown in the following Fig. 2, where ε is the threshold of the significance of attribute and its value is close to 0.

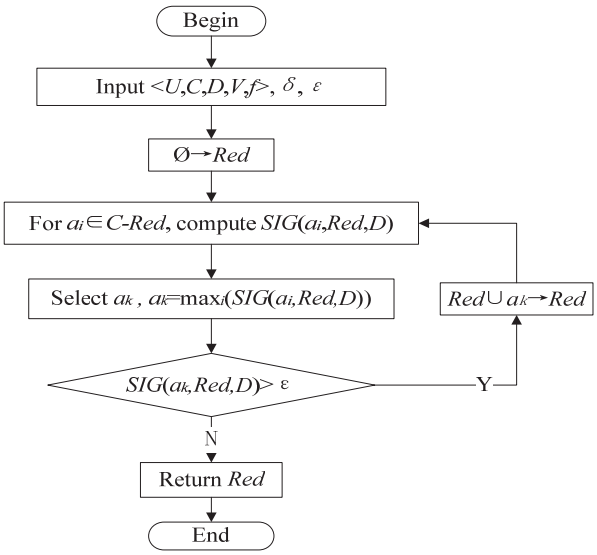

Figure 2: Reduction algorithm.

Three Types of Fatigue Stress-life Relations

Up to now, there are three types of mathematical expressions to describe the S-N curve, including Basquin [20], Langer [21] and three parameters stress-life model [22]. Among which, Basquin model is the most commonly used form, as is shown as

$$S^m N = C, \tag{13}$$

where, m and C are constants related to material types. Take logarithm on both sides, we get

$$\lg S = A + B\lg N \tag{14}$$

where， $A=\lg C/m$， $B=-1/m$.

Besides Basquin model, Langer model and the three parameters model are the other two models commonly used for fatigue analysis. The Langer model is shown as Eqs. (15) and the three parameters stress-life model is shown as Eqs. (16).

$$e^{mS} N = C \tag{15}$$

$$(S-S_f)^m N = C \tag{16}$$

In this work, three types of the fatigue stress-life relations are all used for S-N curve fitting of the aluminum alloy welded joints. Then, statistical results of the three relations are compared and the best one is selected.

NOVEL S-N CURVE MODELING METHOD

Establishment of Fatigue Database

After a review of relevant literature [23, 24], fatigue data of aluminum alloy welded joints is collected and fatigue database is built up. The total number of samples in the database is 64, and *S-N* curves are fitted on basis of these samples. Totally, there are four types of welding methods including MIG, GMAW, TIG and Manual Arc, five kinds

of material types including 5083H11, AlMg4MnCr,AlMgSi1,NP5/6 and HP30, four kinds of plate thicknesses including 10*mm*,2.5*mm*,3*mm* and 4.8*mm*, three kinds of *Ratio* including 0, 0.1 and 0.5, two kinds of load types including 4B and T, three types of joint types including TJ:p, LJ_DS:p, and SJ_DS:p. Limited to the space, only part of the experiment data is shown as below in Tab.1. It only includes fatigue data of crack initiation from weld toe, excludes that from weld and base metal.

Material type	Welding method	Thickness (*mm*)	Ratio	Load type	Joint type	Nominal stress (*MPa*)	Eq.structural stress range (*MPa*)	Life Cycles
5083H11	MIG	10	0.1	4B	TJ:p	120	161	62700
5083H11	MIG	10	0.5	4B	TJ:p	90	121	213750
AlMg4MnCr	GMAW	2.5	0.1	T	LJ_SS:p	45	174	31260
AlMg4MnCr	GMAW	2.5	0.1	T	LJ_SS:p	35	135	52040
AlMgSi1	TIG	3	0	T	LJ_DS:p	53	160	85920
AlMgSi1	TIG	3	0	T	LJ_DS:p	32	97	323460
NP5/6	Manual Arc	4.8	0	T	SJ_DS:p	46	116	188000
NP5/6	Manual Arc	4.8	0	T	SJ_DS:p	31	77	1250000
HP30	Manual Arc	4.8	0	T	SJ_DS:p	62	155	188000
					……			

Table1: Part fatigue data of the aluminum alloy welded joints.

Fitting of S-N Curves

According to the three fatigue stress-life relations mentioned in the three types of fatigue stress-life relations section, *S-N* curve fitting results using the nodal force based structural stress are obtained in Fig. 3. Comparison of goodness-of-fit statistics including *SSE*, *R-square*, *Adjusted R-square* and *RMSE* is shown in Tab. 2.

Where, sum of squares due to error measures the total deviation of the response values from the fit to the response values. It is also called the summed square of residuals and is usually labeled as *SSE*.

$$SSE = \sum_{i=1}^{n} \omega_i (y_i - \hat{y}_i)^2, \tag{17}$$

R-square is the square of the correlation between the response values and the predicted response values. It is also called the square of the multiple correlation coefficients and the coefficient of multiple determinations. *R-square* is defined as the ratio of the sum of squares of the regression (*SSR*) and the total sum of squares (*SST*). *SSR* is defined as

$$SSR = \sum_{i=1}^{n} \omega_i (\hat{y}_i - \bar{y})^2, \tag{18}$$

SST is also called the sum of squares about the mean, and is defined as

$$SST = \sum_{i=1}^{n} \omega_i (y_i - \bar{y})^2, \tag{19}$$

Where, $SST = SSR + SSE$. Given these definitions, R-square is expressed as

$$R\text{-}square = \frac{SSR}{SST} = 1 - \frac{SSE}{SST}, \tag{20}$$

R-square can take on any value between 0 and 1, with a value closer to 1 indicating that a greater proportion of variance is accounted for by the model.

The *adjusted R-square* statistic is generally the best indicator of the fit quality when you compare two models that are nested, that is, a series of models each of which adds additional coefficients to the previous model.

$$adjusted\ R\text{-}square = 1 - \frac{SSE(n-1)}{SST(\nu)}, \tag{21}$$

where the residual degrees of freedom ν is defined as the number of response values n minus the number of fitted coefficients m estimated from the response values. The *adjusted R-square* statistic can take on any value less than or equal to 1, with a value closer to 1 indicating a better fit. Negative values can occur when the model contains terms that do not help to predict the response.

Root mean squared error (*RMSE*) is also known as the fit standard error and the standard error of the regression. It is an estimate of the standard deviation of the random component in the data, and is defined as

$$RMSE = \sqrt{MSE} = \sqrt{\frac{SSE}{\nu}} \tag{22}$$

Similar with *SSE*, an *MSE* value closer to 0 indicates a fit that is more useful for prediction.

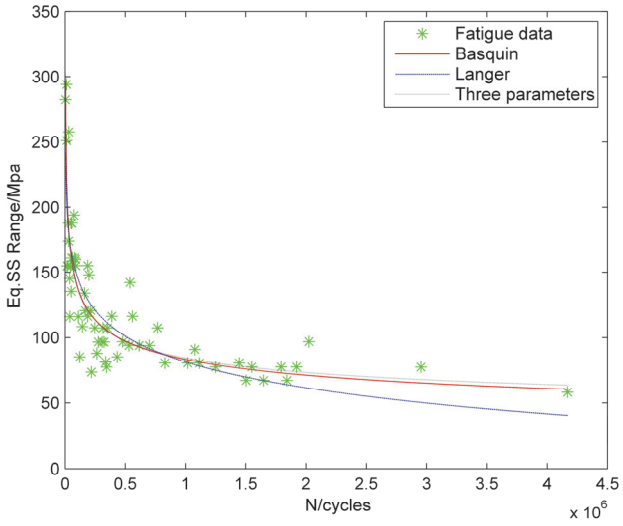

Figure 3: Fitting results of the three relations.

	Basquin	Langer	Three parameters
SSE	4.043e+04	4.853e+04	4.03e+04
R-square	0.7661	0.7192	0.7668
Adjusted R-square	0.7623	0.7147	0.7592
RMSE	25.54	27.98	25.7

Table 2: Goodness-of-fit statistics.

As could be seen from Fig. 3 and Tab. 2, the fitting effect of Langer is the worst thus it isn't suitable for this group of fatigue data. Fitting results of Basquin and three parameters are close. From the perspective of higher application security, we choose the Basquin model as the fatigue stress-life relation for this group of fatigue data of aluminum alloy welded joints. Thus in this paper, Basquin model is used and the mean *S-N* curve is fitted by the least square method based on the nodal force based structural stress according to the collected fatigue data of aluminum alloy welded joints. Scatter of fatigue data based on nominal stress and the mean *S-N* curve based on equivalent structural stress in log-log coordinates are shown in Fig. 4 and Fig.5. The goodness-of-fit statistics including *SSE, R-square, adjusted R-square* and *RMSE* by using nodal force based structural stress are shown in Tab. 3.

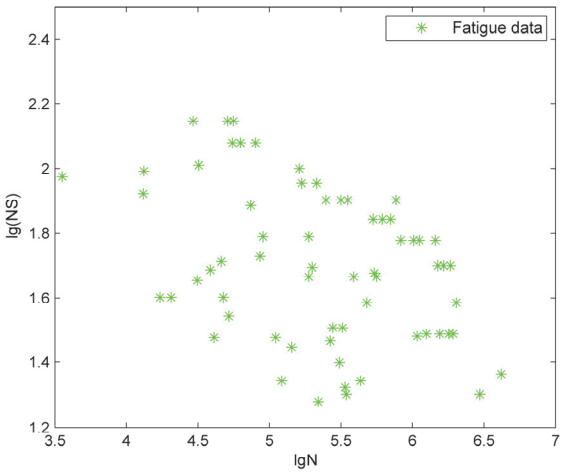

Figure 4: Fatigue data scatter based on nominal stress.

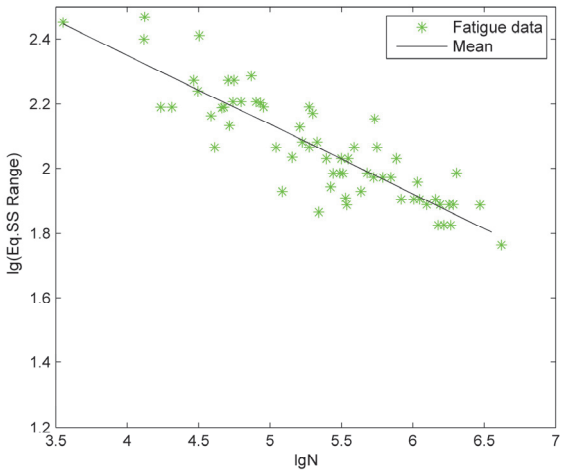

Figure 5: *S-N* curve based on Eq. SS Range.

	Mean
SSE	0.388
R-square	0.772
Adjusted R-*square*	0.7683
RMSE	0.0791

Table 3: Goodness-of-fit statistics by using Eq.SS Range.

In the Eq. SS method, the structural stress is analyzed by nodal forces approach by considering the welded toe structural stress concentration effect. The stress calculation results are insensitive to the finite element type, mesh shape and dimensions in this method, so the welded toe structural stress concentration conditions for different welded joints could be distinguished effectively. The stress parameter relevant to the fatigue lives of welds directly are defined by using the fracture mechanics and the formula for Eq.SS transformation is determined subsequently. Based on the method of stress calculation and transformation, the fatigue data of aluminum alloy welded joints are analyzed. Then the single fatigue design master *S-N* curve, which is necessarily important in the fatigue strength assessment and life prediction, is established as in Fig. 5. As could be seen from Fig. 4 and Fig. 5, the dispersion of the fatigue data has been reduced when Eq. structural stress is used compared with using nominal stress. Such problems as how to select *S-N* curves and to accurately calculate the stress existed in the nominal stress method have been overcome when the nodal force based structural stress method is used.

Features Extraction Based on Neighborhood Rough Set Theory

Besides the main stress factor, fatigue life of welded joints is also affected by other factors such as the geometry of the welded joints, material types, welding method, load type, Ratio, thickness of the plate et al.. While at present, the analysis of the related factors that influence the fatigue life of the welded joints is generally independent and the correlation between each other is rarely studied. We have tried successfully to establish the mathematical model of the influence of related factors on fatigue life by classical rough set theory [25, 26], where attribute discretization algorithm is used for the continuous attribute. Due to the use of discretization algorithm for continuous attributes inevitably causes the loss of information, in this work, neighborhood rough set theory is used to deal with the continuous attribute for features extraction, according to which fatigue characteristics domain is determined and *S-N* curve in each domain is fitted.

On basis of the fatigue database established as Tab.1, the neighborhood decision table S is built up, which could be expressed as $S=(U,C,D,V,f)$. Where U is the data set of all the aluminum alloy welded joints called the universe, $A=C\cup D$ is a non-empty finite set of attributes, C is a non-empty finite set of the factors which influence the fatigue life of the aluminum alloy welded joints called condition attributes, and D is the set of the fatigue life called decision attribute. Each attribute $a\in A$ can be viewed as a function that maps elements of U into a set V_a. The set V_a is called the value set of attribute a. In the decision table S, each row describes a solder fatigue life test sample of the aluminum alloy welded joints and each column

indicates an attribute. Considering the advantages of the nodal force based structural stress, take it as the stress factor that influence the fatigue life of the aluminum alloy welded joints in *S*. Thus the fatigue decision system *S* of the aluminum alloy welded joints is built up in this paper, where the condition attributes of *S* is C={material type(C_1), welding method(C_2), thickness(C_3,*mm*), Ratio(C_4), load type(C_5), joint type(C_6), Eq. structural stress(C_7, *MPa*)}, the decision attribute of *S* is D={*lgN*}. Part data of the decision table is shown as Tab. 4.

U	Condition attributes							Decision attributes
	C_1	C_2	C_3	C_4	C_5	C_6	C_7	D
1	5083H11	MIG	10	0.1	4B	TJ:p	161	4.7973
2	5083H11	MIG	10	0.5	4B	TJ:p	121	5.3299
3	AlMg4MnCr	GMAW	2.5	0.1	T	LJ_SS:p	174	4.4950
4	AlMg4MnCr	GMAW	2.5	0.1	T	LJ_SS:p	135	4.7163
5	AlMgSi1	TIG	3	0	T	LJ_DS:p	160	4.9341
6	AlMgSi1	TIG	3	0	T	LJ_DS:p	97	5.5098
7	NP5/6	Manual Arc	4.8	0	T	SJ_DS:p	116	5.2742
8	NP5/6	Manual Arc	4.8	0	T	SJ_DS:p	77	6.0969
9	HP30	Manual Arc	4.8	0	T	SJ_DS:p	155	5.2742
				……				

Table 4: Part data of the decision table.

In the experiment, $\delta(C_i)=STD(C_i)/\lambda$, $\lambda=2$, $\varepsilon=0.01$ .After attributes reduction, the reduction result of the neighborhood decision system of the aluminum alloy welded joints is obtained, namely{ C_1(Material type), C_4(Ratio), C_7(Eq. structural stress)}.

S-N Curve Modeling Based on Fatigue Characteristics Domain

In Eq. SS method, one master *S-N* curve is obtained at last thus the uncertain problem of *S-N* curve choice has been overcome. Compared with the nominal stress method, dispersion of the fatigue data samples in the nodal force based structural stress method has been greatly reduced. But from the design point of view, the dispersion degree of the fatigue data samples indicated by the value of *RMSE* is still relatively high, which is about 0.0791 here.

In this work, a novel *S-N* curve modeling method is put forward by using the nodal force based structural stress. In the proposed method, fatigue characteristics domains are divided on basis of the reduction result of the welding fatigue decision system obtained by using rough set granularity theory. Subsequently, *S-N* curves are fitted on each fatigue characteristics domain rather than on the whole domain. As a result, a series of *S-N* curves instead of only one master *S-N* curve are obtained at last. In the process of welding fatigue design, we should also design according to each fatigue characteristics domain rather than in the whole fatigue domain.

The fatigue characteristics domains of the aluminum alloy welded joints are determined according to the reduction result, that is, {C_1(Material type), C_4(Ratio), C_7(Eq. structural stress)} obtained by using rough set theory. All the fatigue data samples are divided into 6 series from S_1 to S_6, where S_1: { $X\in U \mid X_{C1=5083H11}$ and $X_{C4=0.1}$} $S2$: { $X\in U \mid X_{C1=5083H11}$ and $X_{C4=0.5}$} $S3$: { $X\in U \mid X_{C1=AlMg4MnCr}$ and $X_{C4=0.1}$} $S4$: { $X\in U \mid X_{C1=AlMgSi1}$ and $X_{C4=0}$} $S5$: { $X\in U \mid X_{C1=NP5/6}$ and $X_{C4=0}$} $S6$: { $X\in U \mid X_{C1=HP30}$ and $X_{C4=0}$}, among which, each series of fatigue test samples corresponds to a specific fatigue characteristics domain and the determine of the fatigue characteristics domains is shown as Fig. 6.

Fitting the *S-N* curve in each fatigue characteristics domain and 6 Mean *S-N* curves from $Mean_1$ to $Mean_6$ are obtained as is shown in Fig. 7. As could be seen from Fig. 7, fatigue data with the same characteristics scatter in a relatively independent area. For example, the scatter of green asterisk '*' which denote all the fatigue samples whose material name is 5083H11 and Ratio is 0.1 in the fatigue experiment are relatively concentrated, corresponding with characteristic domain S_1. Accordingly, the whole fatigue test samples of aluminum alloy welded joints are divided into six fatigue characteristics domains from S_1~S_6. The dispersion degree of the fatigue samples are further reduced when *S-N* curves are fitted according to each series instead of the whole fatigue samples. Six mean *S-N* curves from $Mean_1$~$Mean_6$ are obtained in the proposed method at last. The coefficients of the Basquin equation of Mean and $Mean_1$~$Mean_6$ are shown in Tab. 5.

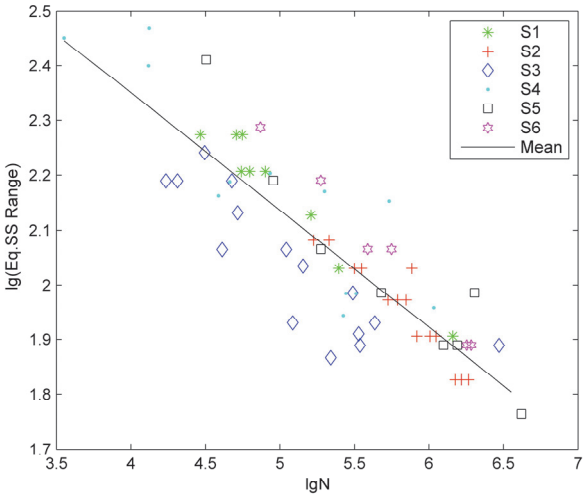

Figure 6: Determine of the fatigue characteristics domains.

	Mean	$Mean_1$	$Mean_2$	$Mean_3$	$Mean_4$	$Mean_5$	$Mean_6$
A	3.206	3.369	3.483	2.972	3.268	3.509	3.689
B	–0.2139	–0.2398	–0.2626	–0.1844	–0.2213	–0.2607	–0.2866

Table 5: Coefficients of the Basquin equation

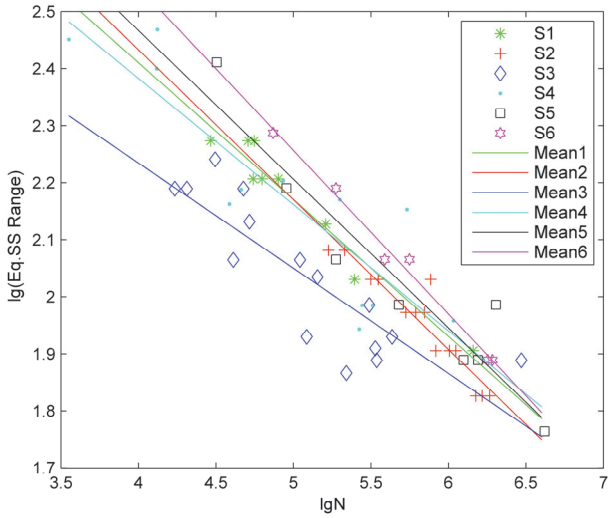

Figure 7: *S-N* curve modeling based on the fatigue characteristics domain

In the process of statistical analysis, the goodness-of-fit statistics including *SSE, R-square, adjusted R-square* and *RMSE* of $Mean_1$-$Mean_6$ are shown in Tab. 6.

	$Mean_1$	$Mean_2$	$Mean_3$	$Mean_4$	$Mean_5$	$Mean_6$
SSE	0.0068	0.0129	0.0648	0.08228	0.0291	0.0013
R-square	0.9465	0.8795	0.7263	0.7877	0.8983	0.9897
Adjusted R-square	0.9389	0.8695	0.7053	0.7665	0.8813	0.9871
RMSE	0.0312	0.0328	0.0706	0.09071	0.0696	0.0181

Table 6: Goodness-of-fit statistics of $Mean_1$-$Mean_6$.

Experiment Results and Analysis

As could be seen from Tab. 3 and Tab. 6, the values of *SSE* from $Mean_1$ to $Mean_6$ based on the fatigue characteristics domain are all smaller than that of the Mean in the whole domain. Except $Mean_3$, the value of *R-square* of $Mean_1$ to $Mean_6$ is closer to 1 than Mean in the whole domain. Each value of *Adjusted R-square* of $Mean_1$ to $Mean_6$ is closer to 1 than Mean in the whole domain. Except $Mean_4$, the value of *RMSE* of $Mean_1$ to $Mean_6$ is closer to 0 than Mean in the whole domain, which indicates that the scatter degree of the fatigue data is further reduced when fatigue characteristics domain is divided and *S-N* curves are fitted in each independent domain. Thus fatigue life prediction by using *S-N* curve modeling method based on the fatigue characteristic domains would be more accurate than that by traditional master *S-N* curve.

CONCLUSION

In this work, on one hand, nodal force based structural stress is used in the S-N curve modeling method based on the fatigue characteristics domain, thus such problems as how to accurately select the S-N curve and to calculate the stress that existed in the traditional nominal stress method have been overcome in the proposed method. The fatigue characteristics domain is determined by using rough set granularity theory, which can achieve knowledge acquisition relying only on the data itself without depending on the prior knowledge or experience knowledge.

On the other hand, the entire fatigue test samples of aluminum alloy welded joints are divided into 6 characteristics domains according to the attributes reduction result of the rough set theory, and the Mean *S-N* curves form $Mean_1$ to $Mean_6$ are fitted respectively. As could be seen from Tab. 6, the value of *SSE* which indicates the dispersion in each fatigue characteristics domain is significantly lower than that of the single master *S-N* curve obtained in the nodal force based structural stress method. Statistical analysis results show that dispersion of the fatigue data is reduced while the proposed *S-N* curve modeling method based on fatigue characteristics domain is used. Therefore, compare with the single master *S-N* curve in the nodal force based structural stress method, to determine the design *S-N* curve according to the fatigue characteristics domain is more targeted with a lower dispersion degree. Thus the fatigue calculation results will be more accurate if the proposed *S-N* curve modeling method based on the fatigue characteristics domain is used.

Future work will be concentrated on the aspects of the application of the proposed *S-N* curve modeling method based on fatigue characteristics domain in the practical engineering practice.

ACKNOWLEDGMENTS

The authors would like to thank all the reviewers for their constructive comments. This research was supported by the National Natural Science Foundation of China (51175054), Natural Science Foundation of Liaoning Province (2015020169), Dalian High Level Talent Innovation Support Plan (2016RQ053).

REFERENCES

[1] Dong, P., A structural stress definition and numerical implementation for fatigue analysis of welded joints, International Journal of Fatigue, 23 (2001) 865-876. DOI: 10.1016/S0142-1123(01)00055-X.

[2] Dong, P., Hong, J. K., Osage, D. A., et al., Master S-N curve method for fatigue evaluation of welded components, Welding Research Council Bulletin, (2002) 1-44.

[3] Dong, P., Prager, M., Osage, D., The Design Master S-N Curve in ASME Div 2 Rewrite and its Validations, Welding in the World Le Soudage Dans Le Monde, 51 (2007) 53-63. DOI:10.1007/BF03266573.

[4] Bandara, C. S., Siriwardane, S. C., Dissanayake, U. I., et al., Developing a full range S–N curve and estimating cumulative fatigue damage of steel elements, Computational Materials Science, 96 (2015) 96-101. DOI: 10.1016/j.commatsci.2014.09.009

[5] Benachour, M., Benguediab, M., Hadjoui, A., et al., Fatigue crack growth of a double fillet weld, Computational Materials Science, 44 (2008) 489-495. DOI: 10.1016/j.commatsci.2008.04.015.

[6] Fouchereau, R., Celeux, G., Pamphile, P., Probabilistic modeling of S – N curves, International Journal of Fatigue, 68 (2014) 217-223. DOI: 10.1016/j.ijfatigue.2014.04.015.

[7] Zhou, Y., Tang, X., S-N Curve Modeling for Finite Life Range under the Assumption of Linearly Changing Scatter, Sae International Journal of Materials & Manufacturing, 7 (2014) 454-464. DOI: 10.4271/2014-01-0970.

[8] Ronold, K. O., Lotsberg, I., On the estimation of characteristic S – N curves with confidence, Marine Structures, 27 (2012) 29-44. DOI: 10.1016/j.marstruc.2012.03.002.
[9] Paolino, D. S., Chiandussi, G., Rossetto, M., A unified statistical model for S-N fatigue curves: probabilistic definition, Fatigue & Fracture of Engineering Materials & Structures, 36 (2013) 187–201. DOI:10.1111/j.1460-2695.2012.01711.x
[10] Wang, P., Liu, X., Wang, Q., et al., Thickness effect on fracture toughness of A7N01P-T5 aluminum alloy, Transactions of the China Welding Institution, (2013) 45-48.(in Chinese)
[11] Zhu, M., Xuan, F., Fatigue crack initiation potential from defects in terms of local stress analysis, Chinese Journal of Mechanical Engineering, 27 (2014) 496-503.
[12] Yannan, D. U., Zhu, M., Xuan, F., Effect of Stress Ratio on the Transition Point of Fatigue Crack Growth Curve in the Near-threshold Regime of a 25Cr2Ni2MoV Steel Welded Joint, Journal of Mechanical Engineering, 51 (2015) 44-49.(in Chinese)
[13] ASME, ASME Boiler and Pressure Vessel Code Section VIII Division 2 Part 5: Design by Analysis Requirement, New York, (2007).
[14] Pawlak, Z., Rough classification, International Journal of Man-Machine Studies, 51 (1984) 469-483. DOI:10.1006/ijhc.1983.0315
[15] Wang, G. Y., Yao, Y. Y., Yu, H., A Survey on Rough Set Theory and Applications, Chinese Journal of Computers, (2009) 1229-1246. (in Chinese)
[16] Wen-Hang, L. I., Chen, S. B., Lin, T., et al., The Comparison of Discretization Method in Rough Set Based Modeling Method for Welding, Journal of Shanghai Jiaotong University, 40 (2006) 1094-1097. (in Chinese)
[17] Wen-Hang, L. I., Chen, S. B., Lin, T., et al., A Generalized Rough Set Modeling Method for Welding Process, Journal of Shanghai Jiaotong University, 12 (2007) 319-322.
[18] Hu, Q., Yu, D., Xie, Z., Neighborhood classifiers, Expert Systems with Applications An International Journal, 34 (2008) 866-876. DOI: 10.1016/j.eswa.2006.10.043.
[19] Li W., Huang Z., Jia X., et al., Neighborhood based decision-theoretic rough set models, International Journal of Approximate Reasoning, 69 (2016) 1-17. DOI: 10.1016/j.ijar.2015.11.005.
[20] Nishijima, S., Statistical Analysis of Small Sample Fatigue Data, Transactions of the Japan Society of Mechanical Engineers A, 46 (1980) 234-245.
[21] Boiler, A. S. o. M. E., Committee, P. V. ASME Boiler & Pressure Vessel Code: An Internationally Recognized Code , American Society of Mechanical Engineers, (1995).
[22] Weibull, W. Fatigue Testing and Analysis of Results. Published for Advisory Group for Aeronautical Research and Development, North Atlantic Treaty Organization, Pergamon Press, (1961).
[23] Sidhom, N., Laamouri, A., Fathallah, R., et al., Fatigue strength improvement of 5083 H11 Al-alloy T-welded joints by shot peening: experimental characterization and predictive approach, International Journal of Fatigue, 27 (2005) 729-745. .DOI: 10.1016/j.ijfatigue.2005.02.001.
[24] Beretta, S., Sala, G., A model for fatigue strength of welded lap joints, Fatigue & Fracture of Engineering Materials & Structures, 28 (2005) 257–264. DOI: 10.1111/j.1460-2695.2004.00849.x
[25] Yang, X., Deng, W., Zou, L., et al., Fatigue behaviors prediction method of welded joints based on soft computing methods, Materials Science & Engineering A, 559 (2013) 574-582. DOI: 10.1016/j.msea.2012.08.144.
[26] Yang, X. H., Zou, L., Deng, W., Fatigue life prediction for welding components based on hybrid intelligent technique, Materials Science & Engineering A, 642 (2015) 253-261. DOI: 10.1016/j.msea.2015.07.006.

A thermography-based method for fatigue behavior evaluation of coupling beam damper

Zhe Zhang
Faculty of Vehicle Engineering and Mechanics Dalian University of Technology, State Key Laboratory of Structural Analysis for Industrial Equipment, Dalian 116024, China

Jinping Ou, Dongsheng Li
Faculty of Infrastructure Engineering Dalian University of Technology, Dalian 116024, China

Shuaifang Zhang
Department of Mechanical Engineering Penn State University, State College 16802, USA

Junling Fan
Aircraft Strength Research Institute, Xi'an 710065, China
fanjunling@mail.dlut.edu.cn

ABSTRACT. Under cyclic load, local fatigue damage will occur in the metal damper widely used in the shear wall. This will deteriorate the stiffness of damper and weaken the hysteresis behaviour. The present paper proposed a new and easy method to manufacture kinds of coupling beam dampers. A thermography-based experiment was used to study the energy dissipation and damage accumulation during fatigue process of the metal damper. Based on the temperature variation related to fatigue damage process, the relationship between the plastic deformation and thermal energy dissipation was quantitatively established. Besides, the relationships between the temperature increase to damage accumulation and mechanical load were analyzed systematically.

KEYWORDS. Coupling beam damper; Hysteresis behavior; Energy dissipation; Fatigue damage.

Citation: Zhang, Z., Ou, J., Li, D., Zhang. S., Fan, J., A thermography-based method for fatigue behavior evaluation of coupling beam damper, Frattura ed Integrità Strutturale, 40 (2017) 149-161.

Received: 09.11.2016
Accepted: 21.03.2017
Published: 01.04.2017

INTRODUCTION

The coupling shear wall structure is a very common structure type due to its strong anti-lateral stiffness and great load carrying capability. Paulay et al. [1] employed the diagonal crossing reinforcement to improve the seismic resistance of the reinforcement concrete. Coull [2] used the stiffing beam on the top of the shear wall to

strengthen the structure's integrity and improve the lateral stiffness. Fortney et al. [3-4] raised the concept of changeable steel coupling beam, namely safety wire, was weakened to dissipate the energy via shear yielding and could be replaced conveniently after damage. Chung et al. [5] proposed a frictional damping device in the middle of coupling beam to decrease the response of shear wall structure under earthquake. Kim et al. [6,7] developed a compound energy-dissipation damper component by combining high-damp rubber material with two U-Shape Steel plate. Mao et al. [8] proposed a new shape memory alloy damper, which was applied as a replaceable coupling beam.

However, the existing coupling shear beam dampers are very complicate and are difficult for manufacturing. Besides, there is a lack of analysis on the failure mechanism and dissipation performance. Under this background, we proposed an easy-making shear coupling steel beam damper and also designed corresponding cyclic shear experiments to investigate the bearing capacity and energy dissipation performance. Besides, the infrared camera is used during the fatigue test process in order to record the temperature distribution and temperature change. The temperature signal then is used to analyze and evaluate the energy dissipation related to local fatigue damage. Nondestructive evaluation has been used in many areas for a long time, which includes ultrasonic nondestructive testing [9] and Infrared thermography and so on. Based on the temperature variation, infrared thermographic method is applied to determine the fatigue performance parameters in real time [10]. Temperature variation is a macro behavior of energy dissipation during fatigue process, which could reflect the energy transformation during cumulative fatigue damage process and is closely related with the evolution of interior damage [11].

Todhunter [12] studied the relationship between the temperature change and deformation. In the following 160 years, the thermos-elasticity theory was under intensive study and was improved step by step, which has been developed as a systematic theory [13]. Inglis [14] studied the relationship between fatigue and cyclic hysteresis energy, which motivated scholars to study the inner relationship between the damage evolution and the energy absorbption and dissipation during the fatigue process. As the high-speed and high-sensitivity infrared camera came out during the recent 30 years, more and more people not only paid attention on the application of nondestructive testing, but also studied the energy dissipation and thermal energy during the cyclic fatigue test to evaluate the fatigue response based on fatigue damage model and failure criteria [15-17]. Fan et al. [18,19] built the energy relationship of Miner linear cumulative damage theory based on energy dissipation theory and infrared thermography method, which could well predict the residual life of components in an easy understanding way. Zhang [20] and etc designed the coupling beam damper with Kriging surrogate model and provided a new framework to design the coupling beam dampers.

INFRARED THERMOGRAPHY AND ENERGY BALANCE

Introduction to infrared thermography

According to generalized Hooke's law, the stress-strain relationship for isotropic elastic material with thermal load is shown below:

$$\Delta\varepsilon_{ii} = \frac{1-2v}{E}\Delta\sigma_{ii} + 3\alpha\Delta T \tag{1}$$

where, $\Delta\varepsilon_{ii} = \varepsilon_{11} + \varepsilon_{22} + \varepsilon_{33}$ is the change of principle strain, $\Delta\sigma_{ii} = \sigma_{11} + \sigma_{22} + \sigma_{33}$ is the change of principle stress, a is the linear expanding coefficient, ΔT is the change of temperature, E is Young's modulus, v is poisson's ratio.

The change of temperature for elastic material under adiabatic condition follows the following rule:

$$\Delta T = -\frac{3\alpha TK\Delta\varepsilon_{ii}}{\rho C_v} \tag{2}$$

In which T is the absolute temperature, C_v is Constant Volume Specific Heat, ϱ is density, K is bulk modulus.

By substituting the equation of the relationship between Constant Volume Specific Heat (C_v) and specific heat at constant pressure (C_p): C_p-C_v=(3Eα2T)/(ϱ(1-2ν)), the following equation could be achieved:

$$\Delta T = -\frac{3\alpha T}{\rho C_v}\Delta\sigma_{ii} \tag{3}$$

Which could illustrate that there is a dynamic balance between the mechanical energy and thermal energy under adiabatic condition. The negative sign in this equation shows that the temperature would decrease when the material is under tension while the temperature would increase when the material is under compression. Thermo-elastic effect could not influence the average temperature rise on the sample surface during the fatigue process, it could only affect the temperature around the average temperature periodically, which is in accordance with the period of principle stress with a difference of the phase about 180^0.

Infrared thermography has been widely used in nondestructive testing in many materials and structures in recent years, with the advantage of large detecting area, high speed and non-contact when compared with other nondestructive testing method such as acoustic emission, magnetic-leakage nondestructive examination, X-ray and Eddy Current Testing. The theory of infrared nondestructive testing was firstly built by Carlomagno[21]. For an infinitely large plate ignoring the lateral heat flux diffusion, the heat conduction equation under the periodic heat flux of $q=I_0 e^{j\omega t}$ with only considering the heat transfer along the direction of thickness is shown below:

$$\frac{\partial T}{\partial t}=\alpha\frac{\partial^2 T}{\partial x^2} \tag{4}$$

$$\text{at}\quad x=0:-k\frac{\partial T}{\partial x}=I_0 e^{j\omega t} \tag{5}$$

In which, T is a function of temperature distribution in space and time, $a=k/(\rho c)$ is the thermal diffusion coefficient, k is the thermal conductivity coefficient, ω is angular frequency. Solving this PDE with the separation of variables, the temperature T could be expressed as a function of x and t:

$$T(x,t)=\frac{I_0}{K\sigma}e^{-\sigma x}e^{-j\omega t} \tag{6}$$

In which $\sigma=\sqrt{j\omega/a}=(1+j)\sqrt{\frac{2\omega}{a}}=(1+j)/\mu$, and $\mu=\sqrt{\frac{2a}{\omega}}$ is the diffusion length, which is also known as the damping coefficient. This equation describes the heat conduction along x under Modulation frequency control.

At least four thermographs in one period must be collected to obtain the phase φ and amplitude A, also Fourier analysis of the thermal image is necessary:

$$\varnothing=arctan\left(\frac{S_3-S_1}{S_4-S_2}\right) \tag{7}$$

$$A=\sqrt{(S_3-S_1)^2+(S_4-S_2)^2} \tag{8}$$

Since the thermal properties are different with/without damage under the periodic heat load. Non-uniform heat flux would appear and could result in different temperature amplitudes and phases according to heat conduction theory. Thus the damage could be determined based on this difference.

Infrared thermography experiment method could also monitor the temperature change in real time for structures under cyclic loading so as to find the high stress region and key region of local cumulative fatigue damage. Infrared thermography could provide efficient improvement or maintenance solutions to ensure the safety and reliability. Thus, it is significant to evaluate the safety of structure via Infrared thermography to monitor the local thermal evolution in real time, which not only could ensure the good functioning of structure but also could avoid or reduce the loss due to fatigue damage.

Energy balance during the hysteresis loading proces

Since the elasto-plastic deformation during the fatigue process is irreversible because of cumulative plastic strain energy in aspect of cumulative energy. The thermal energy dissipation evolution is similar with the evolution of temperature field with

damage in structure, so the temperature field during the fatigue process is closely related with the microstructure configuration and its nonlinear interaction with the local damage effect. As a consequence, the fatigue energy dissipation is in accordance with the regularity of thermal energy dissipation, which means that the temperature evolution could reflect the energy dissipation characteristics during the fatigue process. During the fatigue loading process, the mechanical energy, elastic strain energy, plastic energy and anelasticity damping energy are involved. . Specifically, the input energy from outside belongs to mechanical energy, which includes elastic strain energy, plastic strain energy and anelasticity damping energy. Elastic energy corresponds to the recoverable deformation of material crystal, which has no influence on damage accumulation. Anelasticity damping energy is time-related and conditionally reversible, which plays a significant role for high cycle fatigue, but it has very little influence on the total energy dissipation since plastic strain energy is the most important reason that causes damage.

Energy balance law

During the cyclic loading process, most of mechanical energy is dissipated as thermal energy into the surroundings, part of energy will stay in the material and is reflected as the transformation of microstructures. The energy balance law is shown below according to first law of thermodynamics

$$\Delta W(t) = \Delta D(t) + \Delta Q(t) + \Delta E_K(t) + \Delta E_0(t) \tag{9}$$

In which $\Delta W(t)$ is the increment of total input energy during cyclic loading process, $\Delta D(t)$ and $\Delta Q(t)$ are the increment of total storage energy and dissipation energy, respectively, $\Delta E_K(t)$ is increment of kinetic energy, which is zero under cyclic load, $\Delta E_0(t)$ is the energy dissipation increment in other forms, which is relatively very small when compared with $\Delta D(t)$ and $\Delta Q(t)$. Thermal energy dissipation and plastic strain energy during the cyclic loading process will be discussed in the following parts

Characteristics of thermal energy

Most of the mechanical energy will be transferred to thermal energy. This is the typical phenomenon of irreversibility in thermodynamics. Many researches have shown that massive thermal energy would be produced during the fatigue process. The thermal energy dissipation is caused by viscosity or interior friction, which is due to the shear deformation of crystals, specifically. Also, dislocation movement of atoms during the plastic deformation period would convert most energy into thermal energy. Thus, the temperature field caused by fatigue damage evlolution will change due to damage distribution and difference of motion for different atoms, also is partially because the thermal energy is different for different material elements. Although the ratio of thermal energy dissipation to total strain energy may be different in different cases, it is certain that thermal energy dissipation is the most important part, which plays a key role during the energy exchange of fatigue process. The thermal energy increment during the cyclic loading is shown below:

$$\Delta Q(t) = \Delta Q_q(t) + \Delta Q_h(t) \tag{10}$$

$$\Delta Q_q(t) = \rho C V \Delta T(t) \tag{11}$$

$$\Delta Q_h(t) = hA\Delta T(t) \tag{12}$$

In which $\Delta Q_q(t)$ is the increment of total interior energy of dampers at time t, $\Delta Q_h(t)$ is the convection thermal energy dissipation at time t, $\Delta T(t)$ is the average temperature rise of dampers, ρ is density, V is the working region volume, C is the specific heat, h is convection coefficient, A is the surface area of damper working zone. This paper assumes that the heat conduction between damper and loading system is negligible, the material of damper is Q235 steel, the material properties are shown in Tab. 1.

ϱ, kg/m^3	E, MPa	ν	C, Jkg^{-1}K^{-1}	h, $Jm^{-2}s^{-1}K^{-1}$	σ_b, MPa	σ_y, MPa	σ_f, MPa
7860	2.06E5	0.3	504	12.1	406	235	178

Table 1: Physical and mechanical properties of Q235 steel.

Plastic energy accumulation during the cyclic loading

By ignoring the energy dissipation such as acoustic emission, electric and magnetic energy dissipation, then Eq. (9) could be simplified as below:

$$\Delta W(t) = \Delta D(t) + \Delta Q(t) \tag{13}$$

In which $\Delta Q(t)$ is the thermal energy increment, $\Delta D(t)$ could not be got directly but could be achieved by calculating the total energy increment and thermal energy increment.

EXPERIMENTAL DESIGN AND SETUP

Sample description

The sample in this study is a steel plate with two elliptical cutouts both on top and bottom of the plate. The dimension of the sample is 280x160x5 (mm). The centers of these two elliptical holes and the major axis of the ellipse are located on the top and bottom boundary, respectively, as shown in Fig.1. Obviously, the opening area of the holes depends on the opening parameters of a and b, where a is the length of semi-major axis and b the length of minor semi-major axis. The ratio value of a/b is set as a constant of 2, while the opening areas are set different for comparison. As shown in Tab. 2, the opening ratio, defined as the ratio of the opening area to the area of the steel plate, is set as 10%, 15%, 20%, and 25% to get the final optimal opening parameter.

Specimen	*Opening ratio*	*a/mm*	*b/mm*
SPA10	10%	53.42	26.71
SPA15	15%	65.42	32.71
SPA20	20%	75.54	37.77
SPA25	25%	84.46	42.23
SPB10	10%	106.84	53.42
SPB15	15%	130.84	65.42
SPB20	20%	151.08	75.54
SPB25	25%	168.92	84.46

Table 2: Parameters of Shearing couple beam damper.

The samples are made of Q235 steel, with Young's modulus *E*=2.07e5MPa and poisson's ratio μ=0.3. Tensile test of standard sample selected in the same batch was conducted to find the actual yield strength, the constitutive model achieved in the test is shown in Fig.2.

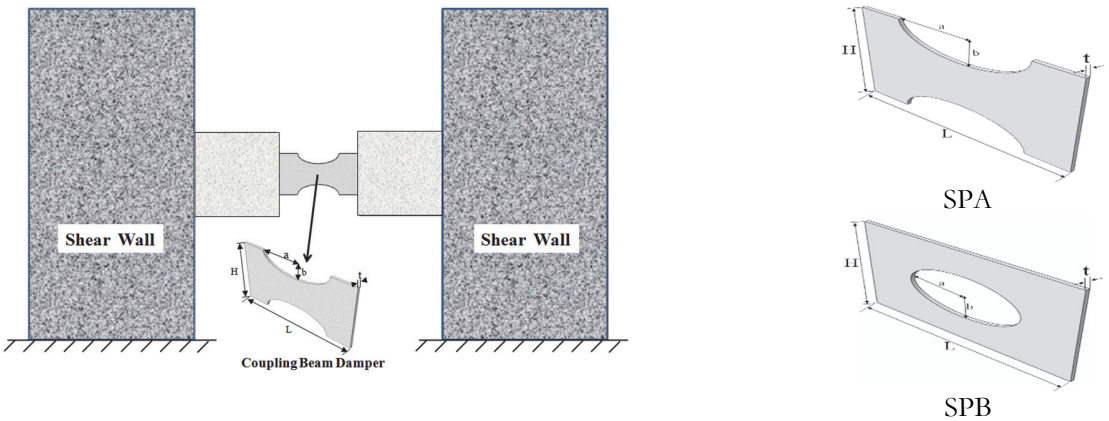

Figure 1: Coupling beam damper with top and bottom openings.

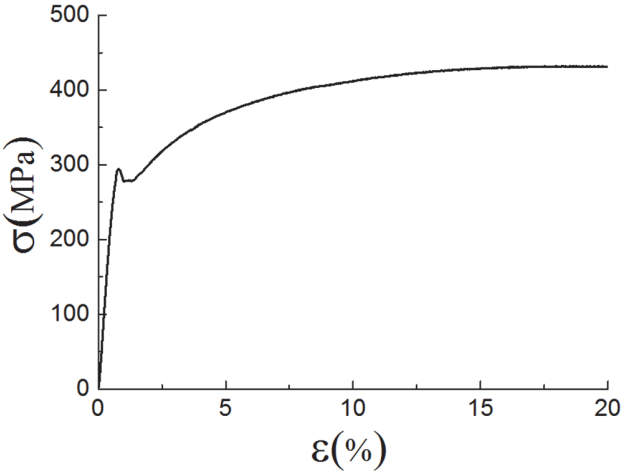

Figure 2: Material constitutive curves

Experiment setup

Experiment load and data collection system

The load was applied by MTS material test machine and controlled with displacement load, the curve of which is shown in Fig.3. The time history signal of the actual displacement load and bearing capacity was received by B&K 3050 signal collection system with the software Pulse13.0, where the sample frequency is 1kHz. The data collection system is shown in Fig. 4.

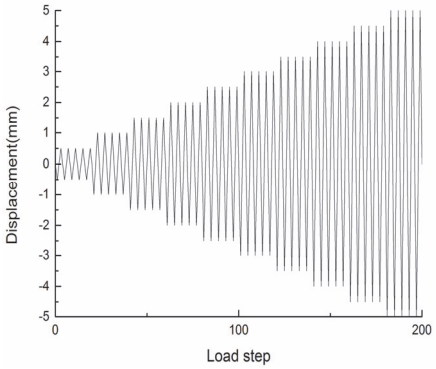

Figure 3: Displacement load curve.

Figure 4: Signal collection system.

Temperature field monitoring system

Another important parameter in this experiment is the temperature field, the Cedip Jade III Infrared camera produced by Cedip company with the technology of infraredfocal plane array was used in this experiment for temperature monitoring and collecting the temperature data. Specifically, the focal plane is composed of 320x240 InSb pixel detectors and could collect the surrounding thermal infrared radiation. The sensitivity of the infrared camera is about 0.001K at the room temperature. The temperature data collection system is shown in Fig.5. Also, the thermo sensitivity is better if the integration time is longer, which is usually set as 1.5ms. The infrared image signal process is based on time-domain averaging method to improve the resolution. Specifically, the random Gaussian noise is reduced via averaging n frames in time-domain to obtain one high quality image, which can be realized by the post-process software ALTAIR. In this experiment, the test sample is fixed with 12 high strength bolts by the sample fixture, which consists of two pairs of asymmetrical L-shape support with the layer width of 20mm, the yield strength of 235MPa and yield strength of 406MPa. Also the two pairs of fixtures are connected and fixed with 20 high-strength bolts so as to fix the sample in the center, and the top and bottom are welded with two symmetrical rod holder with a diameter of Φ 36mm, which is designed for the connection of the fixture and the load experiment system. Also the sample surface is coated with black matted paint to improve the rate of thermal radiation of the sample surface.

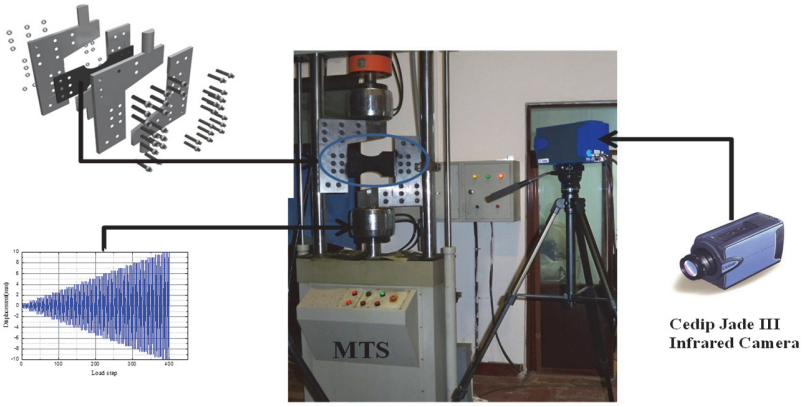

Figure 5: Load and temperature monitoring system.

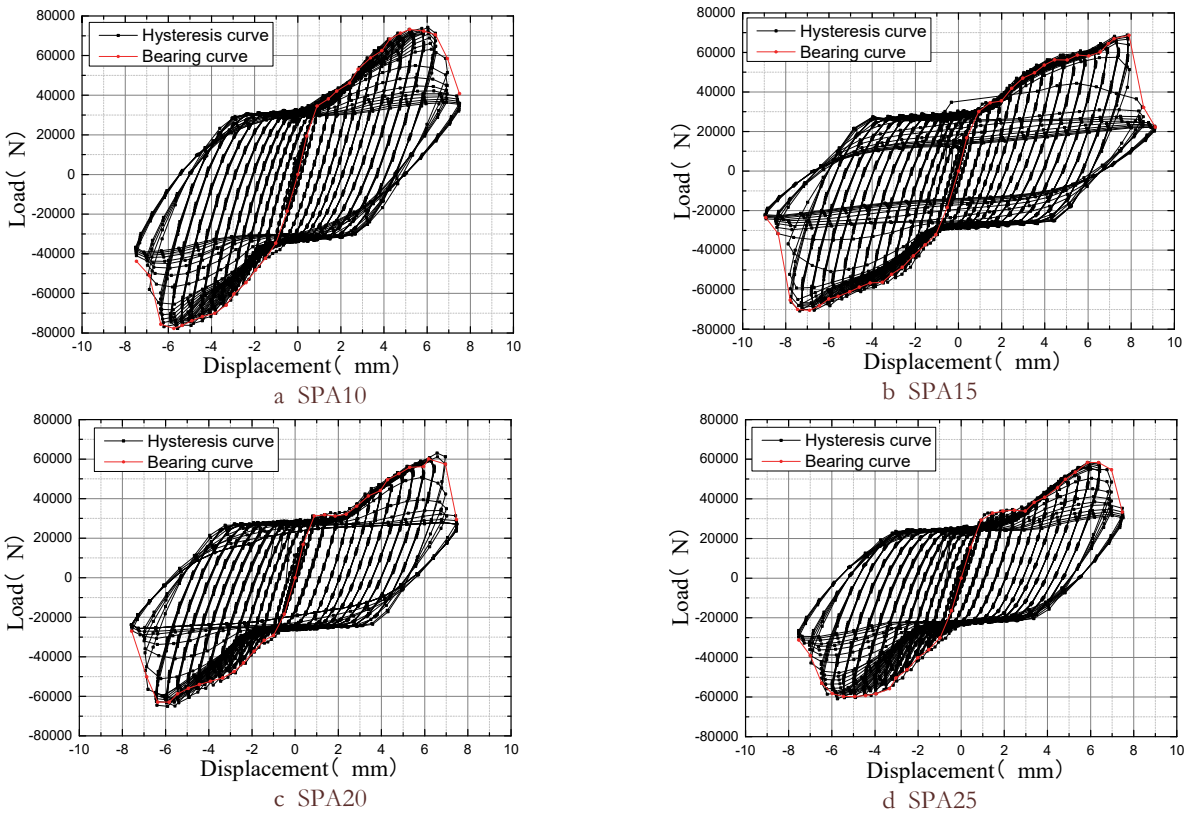

Figure 6: Hysteresis curves of dampers for SPA with different opening ratios.

RESULTS AND DISCUSSION

Hysteretic curve and the skeleton hysteresis curve

The hysteretic curve for a component or a structure is a very important and comprehensive indicator that could represent the earthquake resistance performance as well as a good judgement for structural elasto-plastic analysis. The hysteretic curves for the four different opening ratios are shown in Fig.6, in which SPwith displacement load as x-axis and bearing capacity as y-axis. As shown in this figure, all the four curves are very full as well as the stiffness degeneration (cyclic softening) occurs due to damage. Also, by comparing the four curves, we could see that the stress concentration is more and more severe while the maximum bearing capacity is becoming smaller as the opening ratio goes larger. The stiffness degeneration of damper with opening ratio of 25% is minimum in the four tests, which is because of

the high stress concentration and very low bearing capacity of such samples. In general, as the opening ratio becomes larger and larger, the stress concentration near the hole would be larger and the bearing capacity of damper would be smaller. The hysteretic curves of four different opening ratios with centered ellipse openings are shown in Fig.7, which shows that the bearing capacity and ductility would increase as the opening ratio increases. By comparing with Fig.6, we can see that the coupling beam damper with top and bottom opening is much better than the opening type of central opening under the condition of same opening ratio.

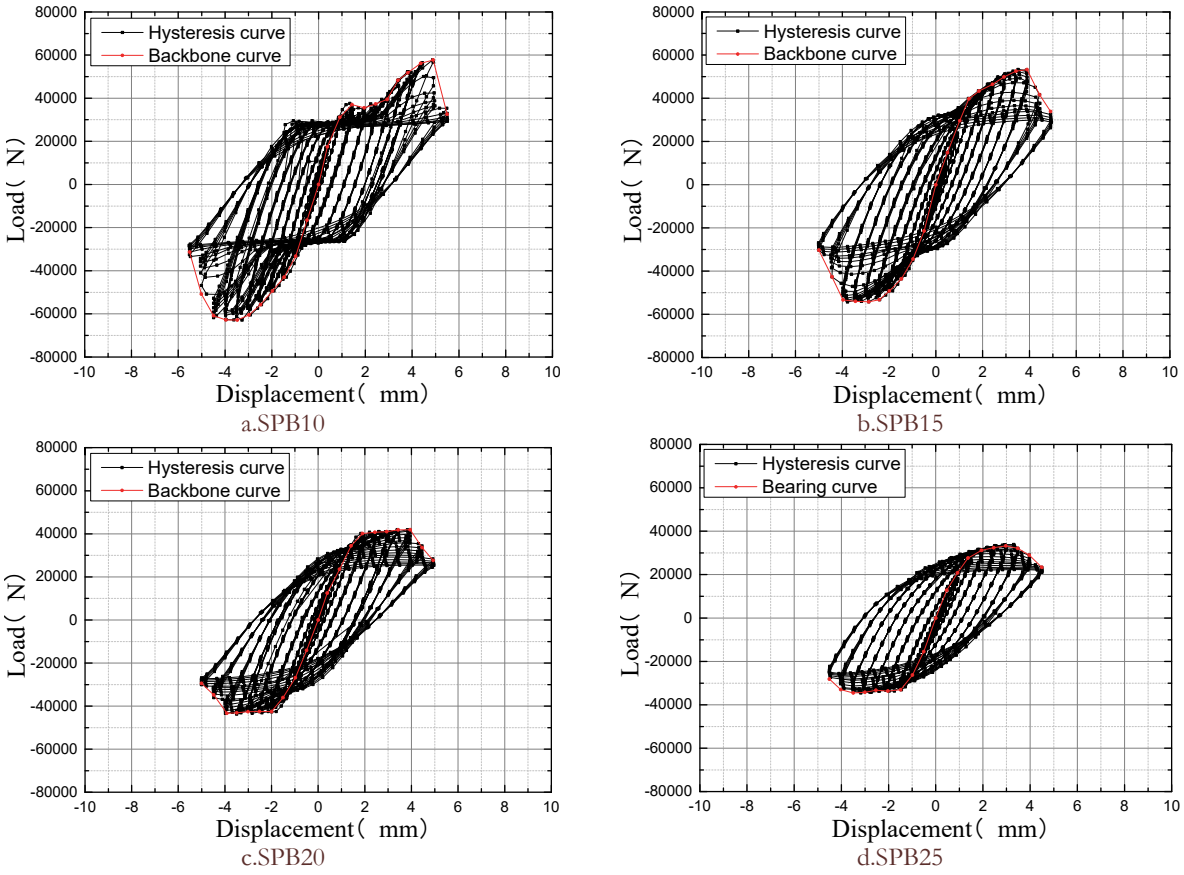

Figure 7: Hysteresis curves of dampers for SPB with different opening ratios.

Cyclic hysteresis energy

It is very important to study the variation rule of stress, strain during the cyclic loading process, the dissipation energy is usually described as the cyclic hysteresis energy, which is the area encircled by the hysteresis curve. Although the plastic deformation is not the only reason that causes the hysteresis phenomenon, which may also be caused by viscoelastic response. But plastic strain energy holds the largest part of the hysteresis energy in low-cycle tests, which means that the plastic strain energy could represent the hysteresis energy with controllable error. As shown in Eq. (14), the hysteresis energy $\Delta W(t)$ represents irreversible plastic energy during each loading and unloading cycle, which is calculated by the area surrounded by the cyclic hysteresis circle.

$$\Delta W(t) = \oint \sigma : d\varepsilon \tag{14}$$

As shown in Fig.8, the cyclic hysteresis energy under the same displacement is smaller as opening ratio becomes larger. As the displacement load goes to 7.5mm, the cumulative dissipation energy of SPA15 exceeds the cumulative energy of SPA10, which is because the plastic deformation of SPA15 is too large so as to make the stiffness degenerate late. As shown in Fig.9, SP15 performs very good hysteresis dissipation capacity. However, the accumulative dissipation energy of SPB with the opening ratio of 15% at the displacement amplitude of 4.5mm is similar with, but did not exceed SPB10

(opening ratio of 10%). As shown in Fig. 8, the dissipation energy of SPA would increase as the opening ratio decreases, which also shows that the energy dissipation performance is much better than SPB.

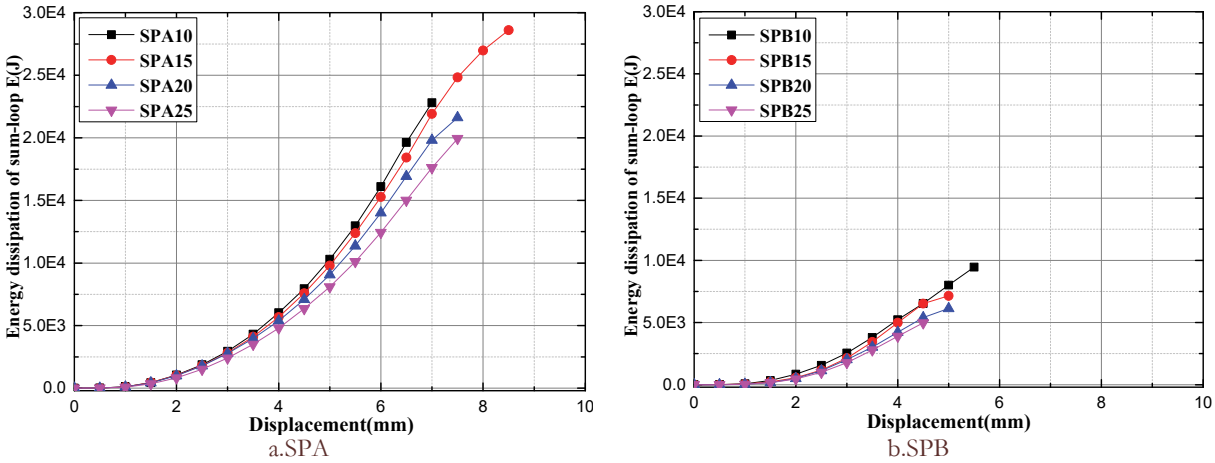

a.SPA b.SPB

Figure 8: Dissipation capacity comparison of different opening types of dampers with different opening ratios.

Relationship between skeleton hysteresis curve and temperature rise

A big percentage of energy absorbed from outside is dissipated as thermal energy during the irreversible process of fatigue, the amount of heat dissipation during the process is influenced by many factors, such as the load type, stress level, sample size, surface treatment status and surrounding temperatures. Thus the heat dissipation could reflect the energy dissipation during the process of fatigue, in other words, studying the heat dissipation could help study the law of energy dissipation of fatigue.

The thermal energy produced during the deformation of materials is the product accompanied with the evolution of crystal microstructure, and it is not related with the damage revolution process. But the change of temperature field due to heat dissipation could reflect and monitor the evolution process of microstructure flaws and the plastic deformation of crack tip. The amount of heat dissipation could reflect the difference during different damage processes and also reflect the irreversibility of material fatigue damage.

The relationship between the mechanical performance and average temperature rise for dampers with four different opening ratios is shown in Fig. 9. As shown in the figure, the temperature field for the sample was taken by the Infrared camera at the peak load displacement of 1mm and 6mm, the inflection point of temperature rise almost corresponds to the yield point of skeleton hysteresis curve, which indicates that the heat energy during the elastic period is much less while the temperature rise increases suddenly after the yield point and would keep increasing during the stiffness degeneration period. Also the local temperature rise is much higher with higher opening ratio for the same displacement load. For the specific dampers, the highest local temperature rise locates near the holding position of the sample for SPA10 and SPA15, while SPA20 and SPA25 happens near the openings, which indicates that the local plastic yield is the key to induce the average temperature rise of the whole plate.

Also, the temperature rise of SP10 is less than the three other dampers, and the yield point is not very obvious, which is caused by the warping effect that results in the out-of-plane of the center in the damper during the experiment. This is because there is elastic deformation along the direction perpendicular to the neutral layer, the temperature rise near the sample holding position is much higher than the opening location of the plate, so the local temperature rise was not obvious and the steel damper did not yield yet. The total work due to load provided such energy that caused the out-of-plane and could increase the total hysteresis dissipation energy. The out-of-plane deformation, instead of damage, caused the stiffness degeneration along the loading direction. In contrast, the out-of-plane phenomenon is not very obvious due to large opening ratio, so damage is the main reason that causes stiffness degeneration so as that the temperature rise is higher. The change of thermal energy for the four dampers is shown in Fig. 9, in which Fig. 9a and b shows the thermal dissipation energy and thermal convective energy during the experiment. In Fig.9, the blue line is the temperature signal; the green line is the energy dissipation; the orange line is the bearing capacity; and the pink line is the strength degradation of the different dampers.

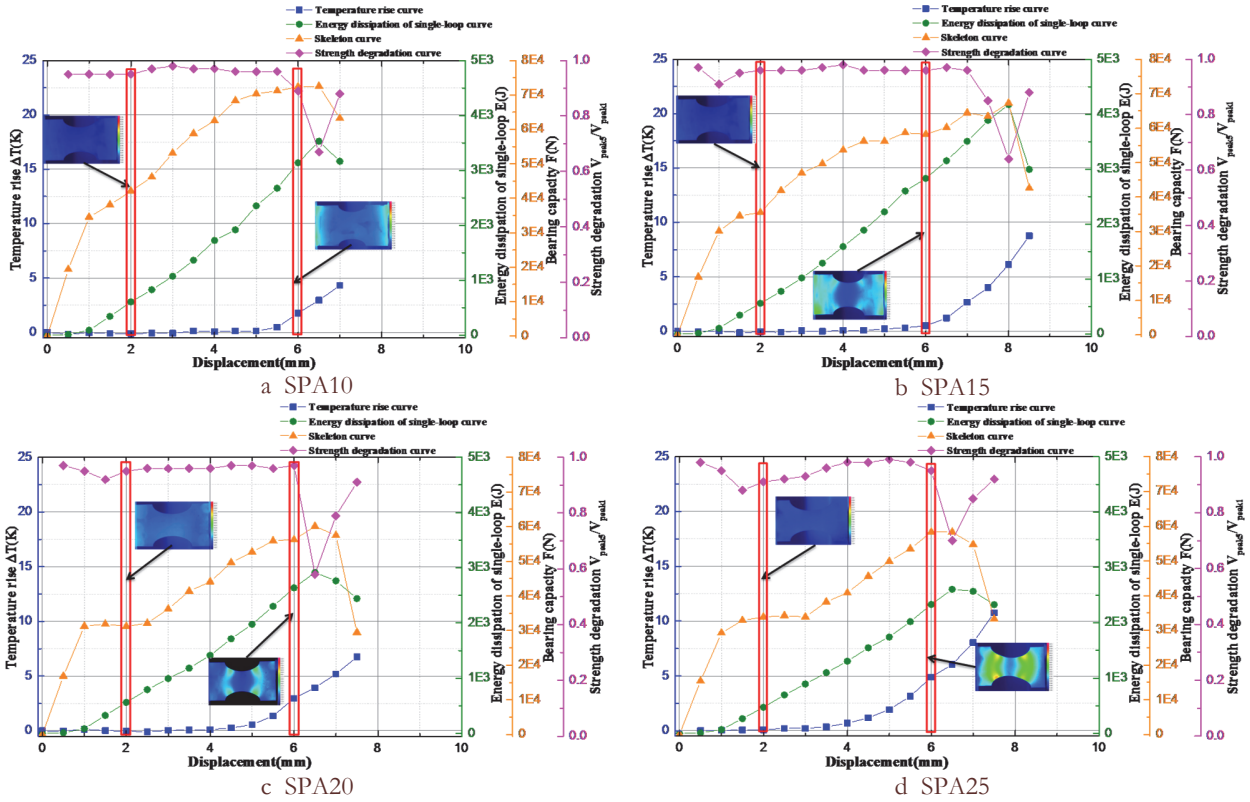

a SPA10 b SPA15

c SPA20 d SPA25

Figure 9: The relationship between the mechanical performance and average temperature rise for dampers of SPA with four different opening ratios.

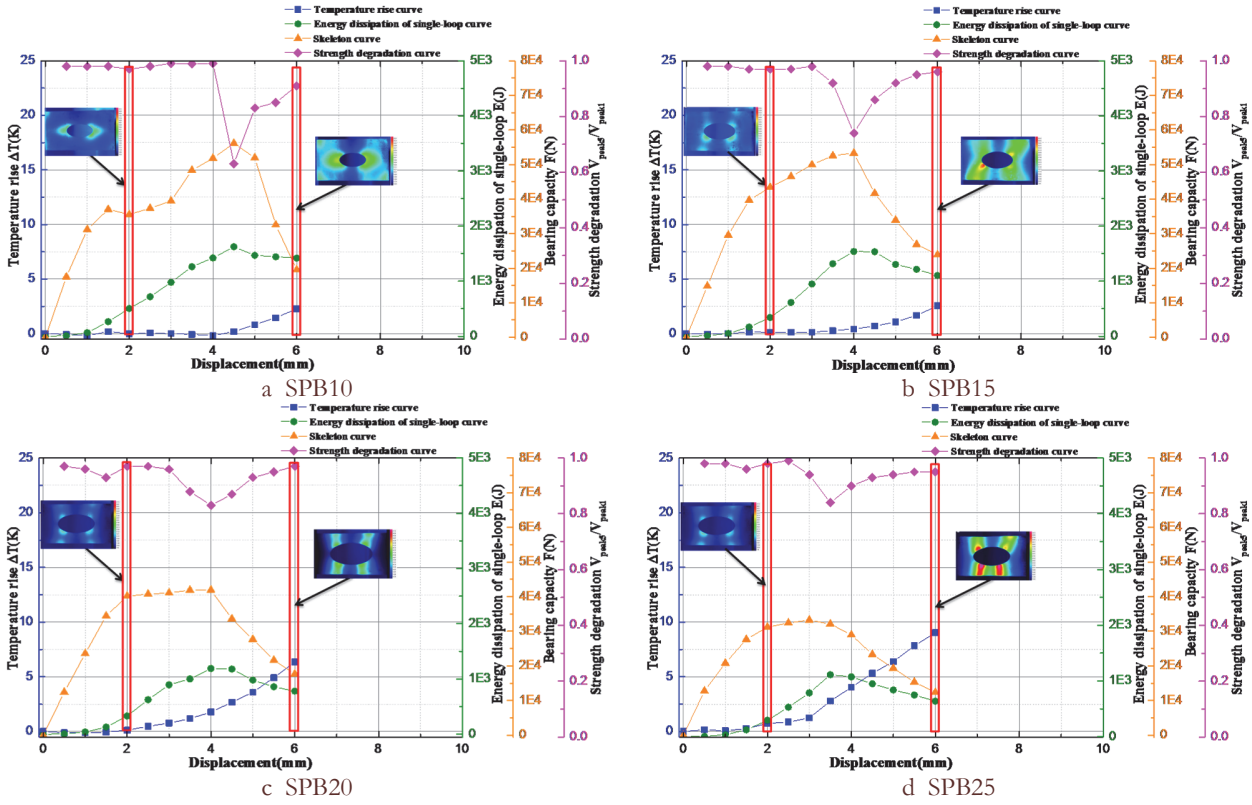

a SPB10 b SPB15

c SPB20 d SPB25

Figure 10: The relationship between the mechanical performance and average temperature rise for dampers of SPB with four different opening ratios.

The thermal energy variation for SPB with different opening ratios during the hysteresis loading process is compared in Fig. 10, in which Fig.10a and Fig. 10b show the thermal dissipation energy based on Heat characterization formula and the thermal convection energy variation trend during the hysteresis process. Similarly, Similarly, In Fig.10, the blue line is the temperature signal; the green line is the energy dissipation; the orange line is the bearing capacity; and the pink line is the strength degradation of the different dampers. From which we could see that the yield point for SPB would appear much earlier than in SPA under the case of same opening ratio. Similarly, the inflection point of temperature rise corresponds with the yielding point of the skeleton curve. Also, the local temperature would have a larger rise as the opening ratio increases under the same maximum displacement load, and the location with larger temperature rise would transfer from two fixture sides to the central opening. And the temperature rise happens earlier for larger opening ratio, and the local stress concentration would induce the obvious improvement of average temperature rise. The hysteresis dissipation energy performance behaves much better with smaller opening ratio, for which the temperature rise is not very obvious even if reaching the yielding point, this is because that the bearing capacity would decrease due to out-of-plane of the specimen instead of local damage. By comparing Fig.9 and Fig. 10, we can see that SPA behaves much better in hysteresis energy dissipation performance than SPB.

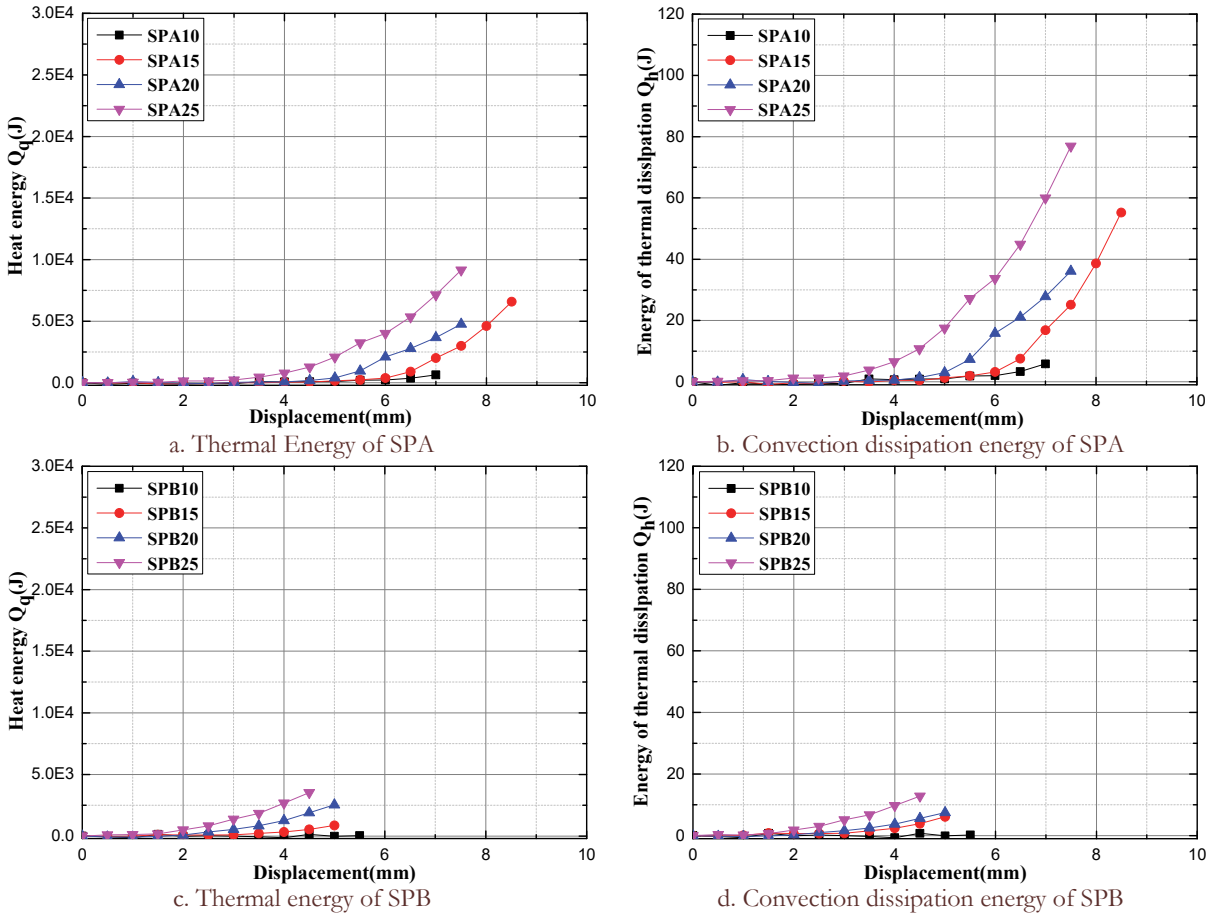

a. Thermal Energy of SPA

b. Convection dissipation energy of SPA

c. Thermal energy of SPB

d. Convection dissipation energy of SPB

Figure 11: The change of thermal energy during the hysteresis loading.

As shown in Fig.11, the average temperature rise changes earlier and earlier as the opening ratio increases. The thermal energy and convection energy could be calculated according to the temperature rise. The maximum of $\Delta Q(t)$ for SP25 is about 12500J, which holds almost 53% of $\Delta W(t)$. Thus, $\Delta Q(t)$ holds a really significant percentage of $\Delta W(t)$ during the low-cycle hysteresis loading process.

Plastic Energy

Fig.12 shows the plastic damage energy based on the energy conservation law. As can be seen from this figure, the inflection point of thermal dissipation energy would happen earlier as the opening ratio increases, the thermal dissipation

energy and the thermal convection energy is larger and larger as the opening ratio increases with the same displacement load. Also, the thermal energy due to thermal dissipation and convection holds a very large percentage of the total work, which indicates that the thermal energy is very important in plastic deformation and local damage deformation for coupling beam damper during low cycle fatigue test. Moreover, the plastic energy also holds a large part of the total energy. In sum, under the same displacement load, as the opening ratio increases, the bearing capacity and the hysteresis energy would decrease, while the ratio of thermal energy would increase.

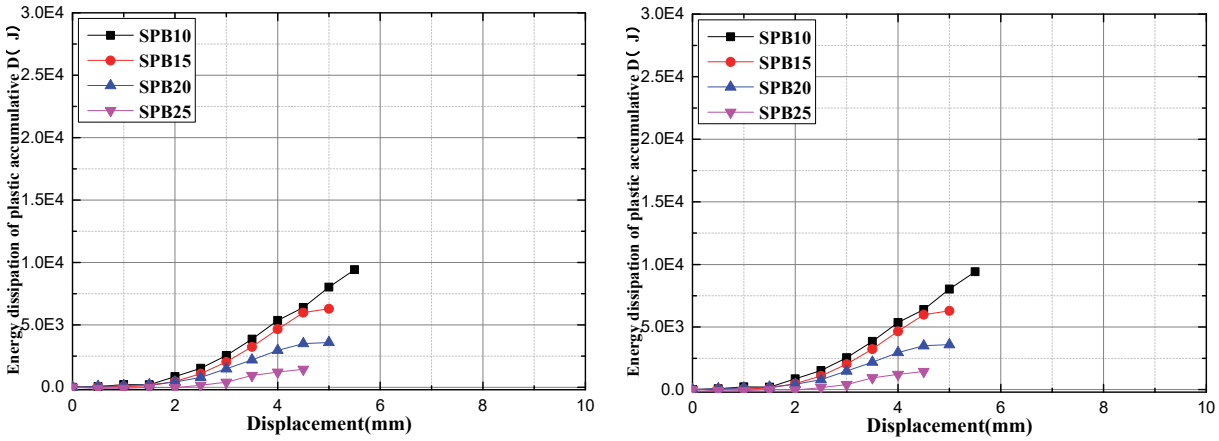

a. SPA b. SPB

Figure 12: Plastic dissipation energy of SPA and SPB during the cyclic loading process.

Conclusion

Based on the traditional hysteresis experiments of metal dampers, and by applying Infrared thermal camera to compare the temperature rise of two different kinds of coupling beam dampers during the experiments. The plastic damage energy and the relationship between different energies could be achieved according to energy balance equation, and the following conclusions could be achieved:

1. Based on the metal damper of SPA, out-of-plane phenomenon would appear easily for smaller opening ratio during the hysteresis process so as to cause the degeneration of stiffness along the loading direction under the case of not obvious yield.
2. With the same opening ratio and same displacement load condition, the hysteresis energy dissipation performance of SPA is much better than SPB.
3. The opening ratio could influence the temperature rise. Specifically, the rapid temperature rise would appear earlier for larger opening ratio.
4. During the hysteresis process of metal beam damper, the thermal energy is produced along the plastic damage and holds a very important part of total energy. The plastic energy is an important factor that deduces fatigue damage and irreversible change of microstructure. A large part of plastic deformation energy would appear in the type of thermal energy so that the temperature rises which in turn reflects microstructure evolution.

Acknowledgements

We would like to thank the financial supports of the National Natural Science Foundation of China (No.91315301-12 and No.51601175).

References

[1] Paulay, T., Simulated seismic loading of spandrel beams. Journal of the Structural Division, ASCE97 (ST9) (1971)

2407-2419.

[2] Choo, B.S., Coull, A., Stiffening of laterally loaded coupled shear walls on elastic foundations, Building and Environment, 4(19) (1984) 251-256.

[3] Chung, H. S., Moon, B. W., Lee, S. K., Seismic performance of friction dampers using flexure of RC shear wall system, Structural Design of Tall & Special Buildings, 18(7) (2009) 807-822.

[4] Rassati, G. A., Fortney, P. J, Shahrooz, B. M., Performance evaluation of innovative hybrid coupled core wall systems, American Society of Civil Engineers, (396) (2011) 479-492.

[5] Fortney, P. J., Shahrooz, B. M., Rassati, G. A., The next generation of coupling beams, Composite Construction in Steel and Concrete, V. ASCE (2014) 619-630.

[6] Kim, H. J., Choi, K. S., Oh, S. H., Comparative study on seismic performance of conventional RC coupling beams and hybrid energy dissipative coupling beams used for RC shear walls, 15WCEE, Lisbon, Portugal, (2012) 2254.

[7] Oh, S. H., Choi, K. Y., Kim, H. J., Experimental validation on dynamic response of RC shear wall systems coupled with hybrid energy dissipative devices, 15WCEE, Lisbon, Portugal, (2012) 1422.

[8] Mao, C., Dong, J., Li, H., Seismic performance of RC shear wall structure with novel shape memory alloy dampers in coupling beams, Society of Photo-Optical Instrumentation Engineers (SPIE) Conference Series, (2012) 304-320.

[9] Li D, Zhang S, Yang W, Zhang W. Corrosion monitoring and evaluation of reinforced concrete structures utilizing the ultrasonic guided wave technique. International Journal of Distributed Sensor Networks, 10(2) (2014) 827130.

[10] La Rosa, G., Risitano, A., Thermographic methodology for the rapid determination of the fatigue limit of materials and mechanical components, International Journal of Fatigue, 22 (2000) 65-73.

[11] Junling, F., Qiang, G., Yanguang, Z., Stress analysis and fatigue behavior assessment of components with defect based on FEM and Lock-in thermography, Journal of Materials Engineering (8) (2015) 62-71. (in Chinese)

[12] Todhunter, I., Pearson, K., History of the theory of elasticity and of the strength of materials, Cambridge: Cambridge University Press, (1886) 291-364.

[13] Dulieu-Barton, J. M., Stanley, P., Development and applications of thermoelastic stress analysis, The Journal of Strain Analysis for Engineering Design, 33(2) (1998) 93-104.

[14] Inglis, N. P., Hysteresis and fatigue of Wohler rotating cantilever specimen, The Metallurgist, 1(1) (1927) 23-27.

[15] Luong, M. P., Fatigue limit evaluation of metals using an infrared thermographic method, Mechanics of Materials, 28(1-4) (1998) 155-163

[16] Fargione, G., Geraci, A., La Rosa, G., Rapid determination of the fatigue curve by the thermographic method [J]. International Journal of Fatigue, 24(1) (2002) 11-19.

[17] Curà, F., Curti, G., Sesana R. A new iteration method for the thermographic determination of fatigue limit in steels. International Journal of Fatigue, 27(4) (2005) 453-459.

[18] Junling, F., Xinglin, G., Yanguang, Z., Predictions of S-N curve and residual life of welded joints by quantitative thermographic method, Journal of Materials Engineering, (12) (2011) 29-33. (in Chinese).

[19] Junling, F., Xinglin, G., Chengwei, W., Effect of heat treatments on fatigue properties of FV520B steel using infrared thermography, Chinese Journal of Materials Research, 26(1) (2012) 61-67. (in Chinese).

[20] Zhang Z, Ou J, Li D, Zhang S. Optimization Design of Coupling Beam Metal Damper in Shear Wall Structures. Applied Sciences. 7(2) (2017) 137.

[21] Carlomagno, G. M., Berardi, P. G., Unsteady thermotopography in non-destructive testing, C. Warren, ed. Proceedings of the III infrared Information Exchange, St. Louis/ USA.

Multiaxial elastoplastic cyclic loading of austenitic 316L steel

V. Mazánová, J. Polák, V. Škorík, T. Kruml
Institute of Physics of Materials, Academy of Sciences of the Czech Republic
mazanova@ipm.cz
*polak@ipm.cz, http://orcid.org/*0000-0002-0457-4680
skorik@ipm.cz
*kruml@ipm.cz, http://orcid.org/*0000-0002-8855-1709

ABSTRACT. Cyclic stress-strain response and fatigue damage character has been investigated in austenitic stainless steel 316L. Hollow cylindrical specimens have been cyclically deformed in combined tension-compression and torsion under constant strain rate condition and different constant strain and shear strain amplitudes. In-phase and 90° out-of-phase cyclic straining was applied and the stress response has been monitored. Cyclic hardening/softening curves were assessed in both channels. Cyclic softening followed for higher strain amplitudes by long-term cyclic hardening was observed. Cyclic stress-strain curves were determined. Study of the surface damage in fractured specimens revealed the types and directions of principal cracks and the sources of fatigue crack initiation in slip bands.

KEYWORDS. Multiaxial cyclic loading; 316L steel; Cyclic stress-strain curve; Crack initiation.

Citation: Mazánová, V., Polák, J., Škorík, V., Kruml, T., Multiaxial elastoplastic cyclic loading of austenitic 316L steel, Frattura ed Integrità Strutturale, 40 (2017) 162-169.

Received: 09.01.2016
Accepted: 10.02.2017
Published: 01.04.2017

INTRODUCTION

Cyclic plastic response and damage evolution in elastoplastic cyclic loading of stainless steels, specifically 316L steel, has been studied mostly in tension-compression (see e.g.[1, 2]) but also in torsion [3] and less frequently in multiaxial loading [4, 5]. Characteristic feature of cyclic plastic straining of 316L steel at room and depressed temperatures is the localization of the cyclic plastic strain. The localization of the cyclic strain into persistent slip bands (PSBs) influences its cyclic plastic response and results in formation of persistent slip markings (PSMs) in which fatigue cracks initiate.

The subject of the present contribution is to extend the study of the cyclic plastic response and early fatigue damage to tubular specimens of 316L austenitic steel subjected to cyclic tension-compression and torsion biaxial cyclic loading. Simultaneously the early stages of the fatigue damage in the form of PSMs and initiation of fatigue cracks under in-phase and 90°out-of phase straining are reported.

EXPERIMENTAL

The material studied was commercial AISI 316L stainless steel supplied by Thyssen in the form of a round bar of 20 mm in diameter. Its chemical composition (in wt.%) was as follows: 0.017 C, 1.60 Mn, 0.497 Si, 0.029 P, 0.027 S, 16.70 Cr, 10.1 Ni, 2.03 Mo, 0.031 Ca and 0.078 N. The bar was hot rolled; $\sigma_{0.2}$ = 295 MPa. The microstructure was formed by equiaxed austenite grains with the average austenite grain size was 80 μm and some delta ferrite bands. The hollow cylindrical specimens with dimensions shown in Fig. 1 were machined from the round bars. No heat treatment was applied after the machining.

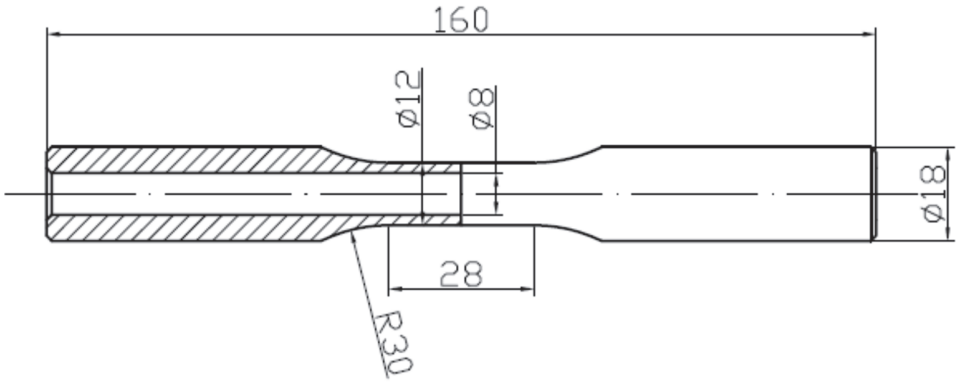

Figure 1: Geometry of the hollow cylindrical specimen

The gauge section was mechanically and electrolytically polished in order to achieve perfect surface for observation of the surface relief. All tests were performed in an electrohydraulic axial–torsion computer controlled MTS testing system. Combined axial-torsion extensometer was used to measure and control axial and shear strain. The tests were conducted under fully-reversed straining (R = -1) both in tension-compression and in torsion with constant strain rate. Axial strain rate was $5x10^{-3}$ s^{-1} and the shear strain rate on the specimen surface was equivalent to the axial strain rate. The strain in the middle diameter of the specimen is reported. Plastic strain was evaluated by subtracting the elastic component from the total strain.

Since the fatigue behaviour of the material has been already thoroughly studied in axial testing [1, 6, 7] we have performed torsion tests and in phase and 90° out-of-phase biaxial tension-compression-torsion tests. The biaxial tests are reported here.

Surface relief and fatigue crack initiation was studied on cracked specimens using optical microscope, SEM observations and FIB cutting. The surface of the specimen was inspected in FEG-SEM Lyra 3 XMU (TESCAN) equipped with focused ion beam (FIB). In order to protect the surface of the fatigued specimen from the ions during the production of surface craters the area of observation containing the PSMs was first covered by the thin sheet of platinum using electron deposition and later thicker layer was applied using ion deposition. Sectioning using FIB was performed perpendicular to the surface and nearly perpendicular to the direction of PSMs. Final cutting was performed with small intensity to achieve smooth perpendicular surface. The cuts were imaged in secondary electrons under inclination of about 35 degrees. The effect of inclination was compensated in all images of the cuts.

RESULTS

Stress-strain response

Hysteresis loops were recorded during cycling in both channels (uniaxial and torsion). Fig. 2 shows typical shapes of hysteresis loops during in-phase cycling and 90° out-of-phase cycling. Appreciable softening is apparent in in-phase cycling. Much higher stress response has been registered in 90° out-of-phase cycling at approximately the same plastic strain amplitude. Specific shape of the hysteresis loop in 90°out-of phase straining is due to reversion of the strain rate direction in both channels.

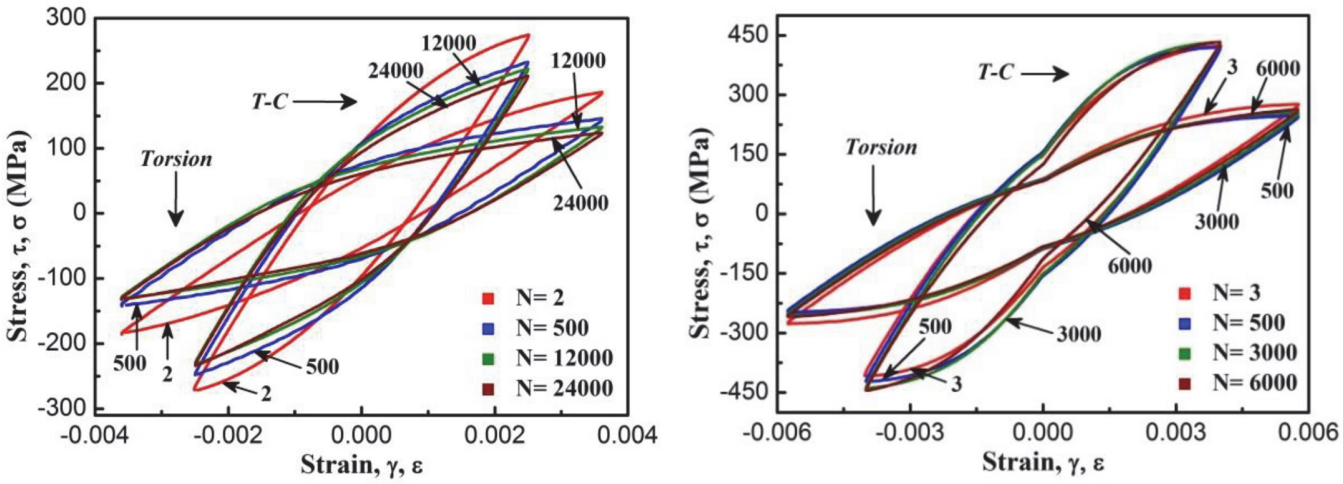

(a) (b)

Figure 2: Hysteresis loops in (a) in-phase cycling (b) 90° out-of-phase cycling.

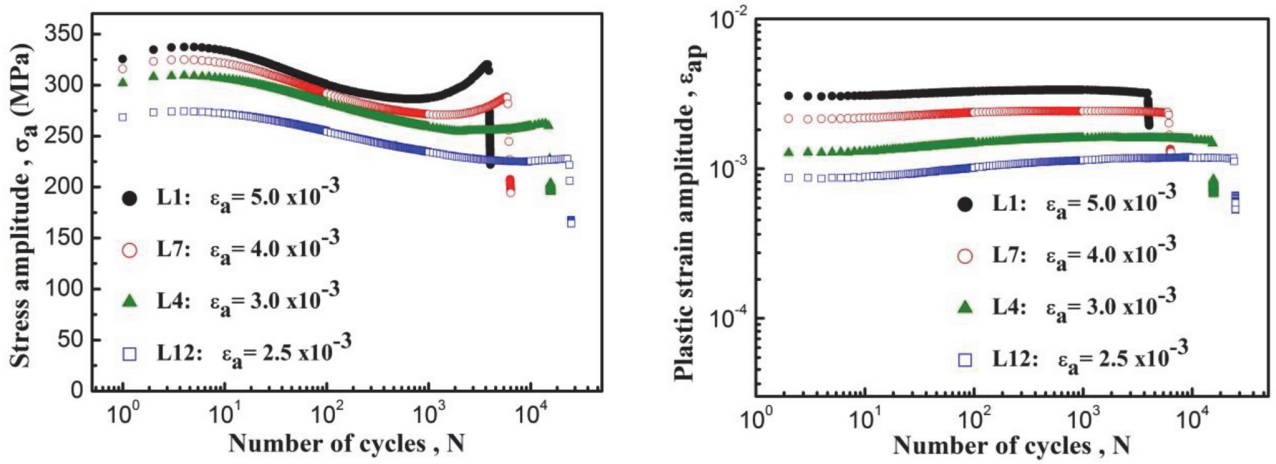

(a) (b)

Figure 3: Cyclic hardening/softening curves during in-phase cycling: (a) uniaxial stress amplitude vs. number of cycles, (b) plastic strain amplitude vs. number of cycles.

Figs 3 and 4 show in more detail the cyclic hardening and softening behavior. Except the very few initial cycles both tension-compression stress amplitude (Fig. 3a) and shear stress amplitude (Fig. 4a) decrease initially rapidly and either stabilize for the lowest strain amplitude or start to increase again towards the end of fatigue life.

During 90°out-of-phase cycling only small changes of the stress and plastic strain amplitude during fatigue life are found (Fig. 5). Early cyclic hardening is followed by mild softening for small strain amplitudes and hardening for high strain amplitudes both in tension-compression and in torsion. The level of the stress amplitude is considerably higher than in in-phase cycling.

The cyclic stress-strain curves have been plotted in Fig. 7 for in-phase and 90° out-of-phase cycling. The equivalent stress and plastic strain amplitudes in in-phase straining were calculated using von Misses relations

$$\sigma_{a,eq} = \sqrt{\left(\sigma_a^2 + 3\tau_a^2\right)} \tag{1}$$

$$\varepsilon_{a,eq} = \sqrt{\left(\varepsilon_a^2 + \frac{\gamma_a^2}{3}\right)} \tag{2}$$

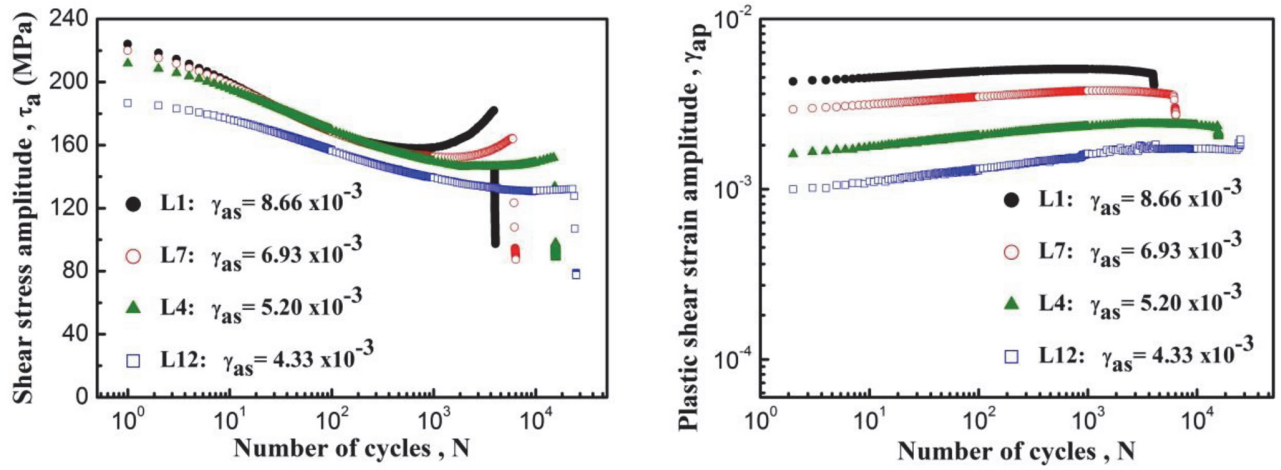

(a) (b)

Figure 4: Cyclic hardening/softening curves in in-phase cycling: (a) shear stress amplitude vs. number of cycles, (b) plastic shear strain amplitude vs. number of cycles.

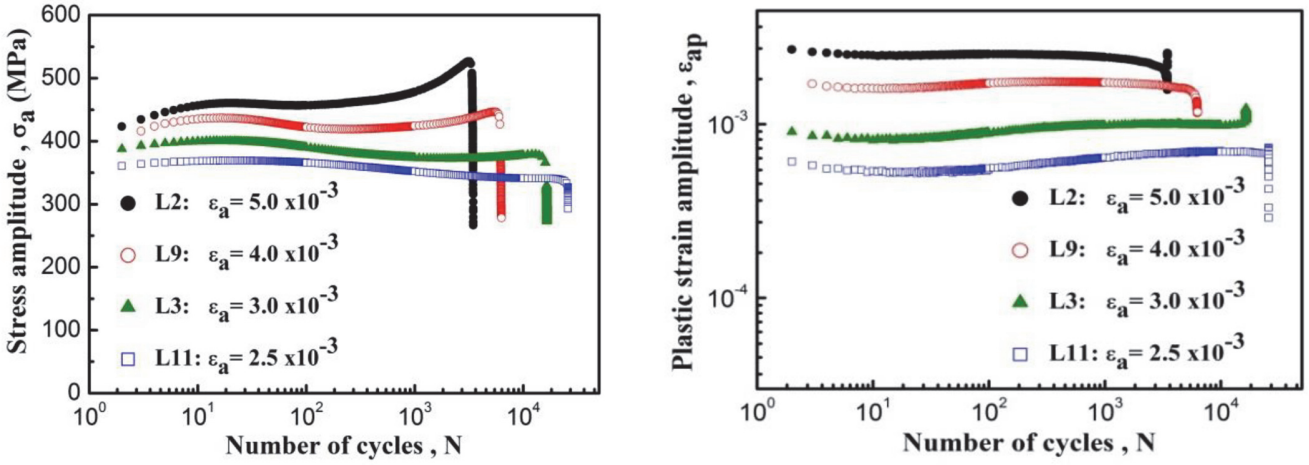

(a) (b)

Figure 5: Cyclic hardening/softening curves during 90°out-of-phase cycling: (a) uniaxial stress amplitude vs. number of cycles, (b) plastic strain amplitude vs. number of cycles.

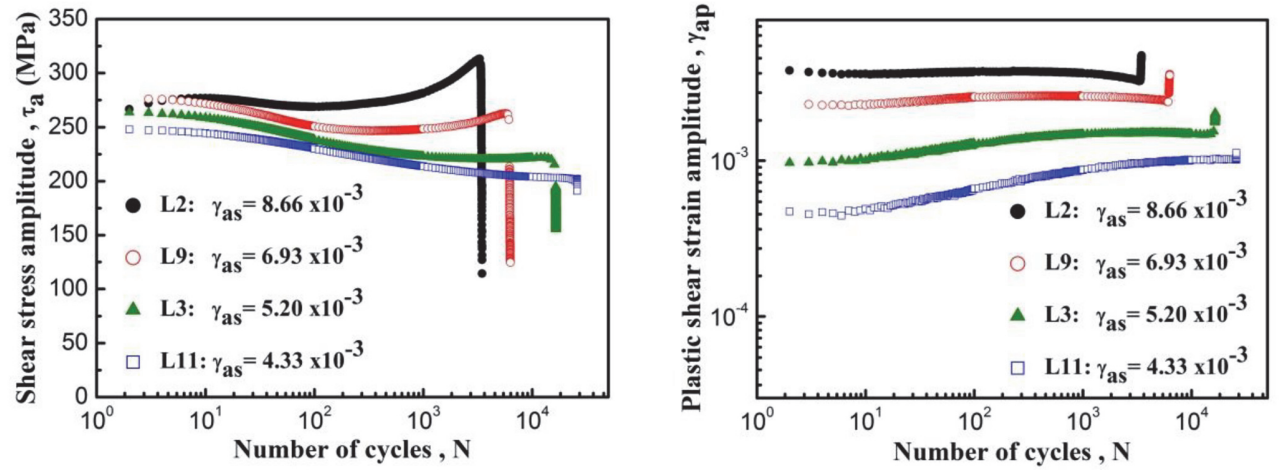

(a) (b)

Figure 6: Cyclic hardening/softening curves in 90°out-of-phase cycling: (a) shear stress amplitude vs. number of cycles, (b) plastic shear strain amplitude vs. number of cycles.

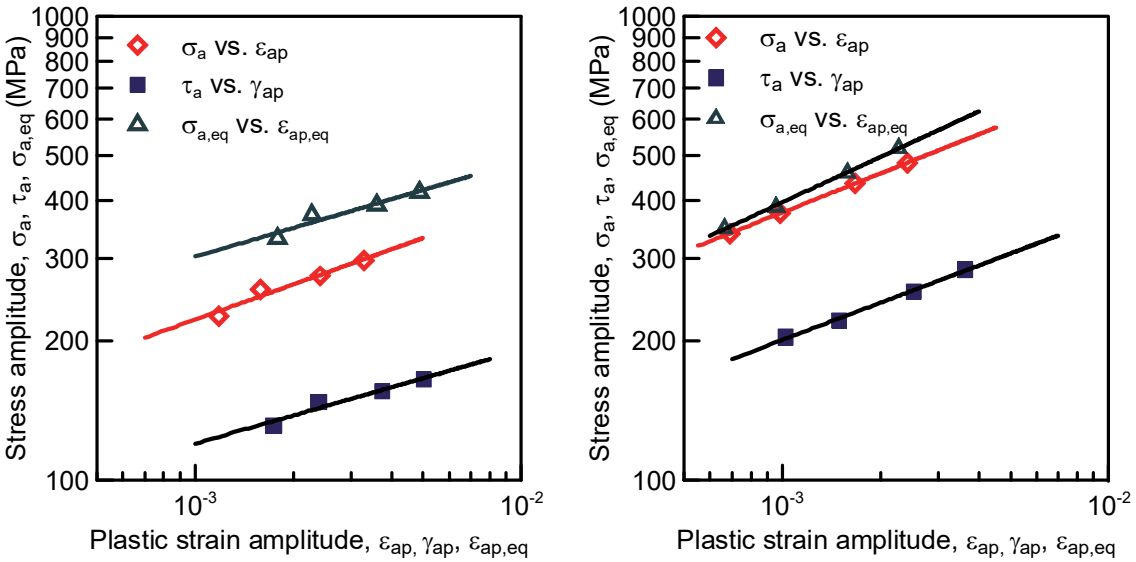

Figure 7: Cyclic stress-strain curves in biaxial cycling: (a) in-phase cycling, (b) out-of-phase cycling.

and equivalent plastic strain amplitude was evaluated using equation

$$\varepsilon_{a,eq,p} = \varepsilon_{a,eq} - \frac{\sigma_{a,eq}}{E_{eff}} \quad \sigma_a = K'\varepsilon_{ap}^{n'} \tag{3}$$

In 90° out-of-phase loading equivalent stress amplitude was evaluated using Eq. (1) but instead of using shear stress amplitude the shear stress corresponding to peak value of the axial stress was used. Equivalent strain amplitude was equal to the tension-compression strain amplitude. The effective modulus E_{eff} =190 GPa was used.
Cyclic stress-strain curve in equivalent stress and strain in in-phase straining lies above the cyclic stress-strain curve corresponding to tension-compression but has approximately the same slope. In 90°out-of-phase straining the cyclic stress-strain curve is only slightly above the cyclic stress-strain curve corresponding to tension-compression. All curves could be well approximated by the power law

$$\sigma_a = K'\varepsilon_{ap}^{n'} \tag{4}$$

The parameters of all cyclic stress-strain curves determined using least square fitting shows Tab. 1.

Type of loading	Tens.-comp. stress		Torsion stress		Equivalent stress	
	K′ (MPa)	n′	K′ (MPa)	n′	K′ (MPa)	n′
in-phase	1262	0.251	483	0.202	1258	0.206
90° out-of-phase	2604	0.279	1261	0.266	3758	0.325

Table 1: Parameters of the cyclic stress-strain curves

Early fatigue damage

Fractured specimens were studied in optical and scanning electron microscope. Multiple secondary cracks developed during the fatigue life in addition to the principal crack. The majority of larger cracks were inclined approximately 45 degrees to the specimen axis. The central part of one of these macroscopic cracks is shown in Fig. 8a. It is evident that the crack path is rugged since the crack microscopically often follows crystallographic planes.

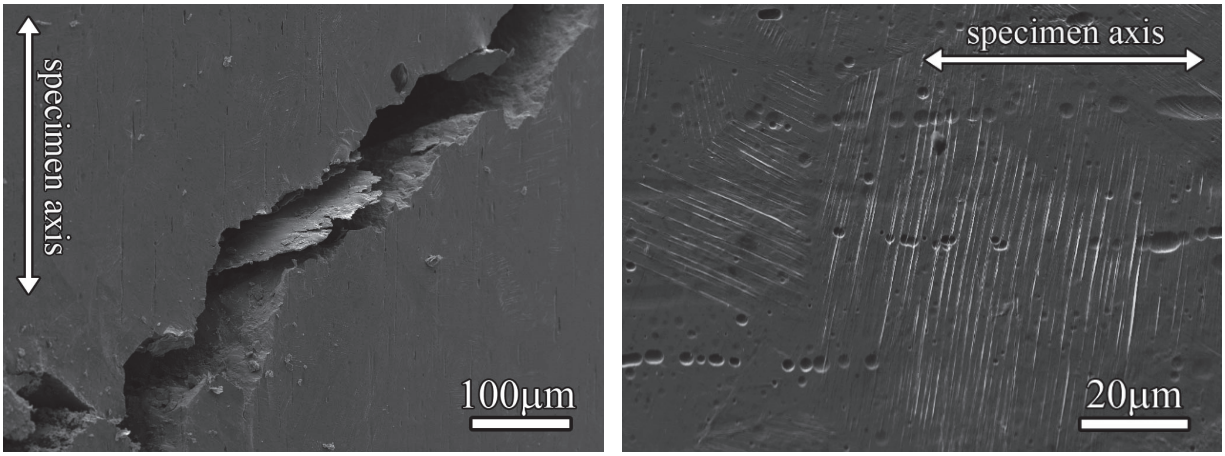

(a) (b)

Figure 8: Surface of the specimen cycled in-phase cyclic straining to fracture: (a) central part of the macroscopic crack, (b) parallel PSMs in surface grains.

We were interested in the early stages of the damage i.e. the initiation of the cracks. Fig. 8b shows the surface with grains covered by a system of PSMs. No clear crack is apparent from this picture. Also high resolution image did not allow to distinguish extrusions-intrusions and cracks. FIB cut performed on the area covered by a platinum layer reveals the shapes of extrusions and intrusions and the presence of a deep crack starting from one of the intrusions (Fig. 9a). Fig 9b shows the details of the surface relief in the location of the cut revealing several cracks starting from intrusions.

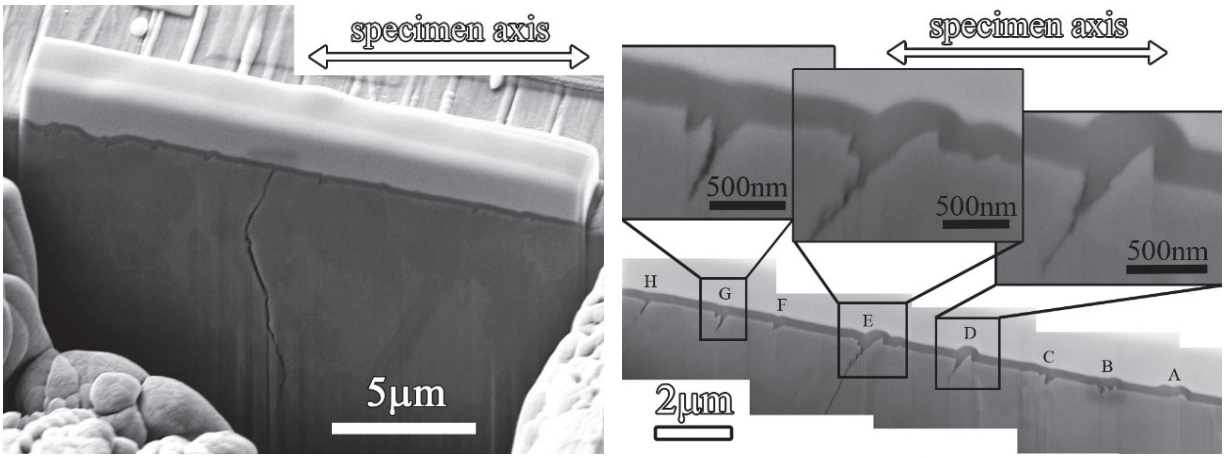

(a) (b)

Figure 9: Surface profile of PSMs produced by in-phase cycling: (a) FIB cut, (b) details of the surface profile.

Similar surface cracking and initiation of fatigue cracks was found in out-of-phase cyclic straining. Fig. 10a shows typical secondary crack and Fig. 10b the area with the PSMs. The image of the surface profile extracted from the FIB cut perpendicular to the direction of the PSMs is inserted in the picture. PSMs consist mostly of extrusions but PSMs B, E and F have also an intrusion which runs parallel to the extrusion.

Discussion

Cyclic plastic response of 316L steel in in-phase biaxial loading is close to that in uniaxial tension-compression loading [1, 6-8]. Cyclic hardening/softening curves which show long-term softening followed by cyclic hardening at higher strain amplitudes are nearly identical with those measured by Hong et al. [8] in tension-compression. Cyclic hardening/softening curves in 90° out-of-phase cycling are similar but are shifted to higher stress amplitudes.

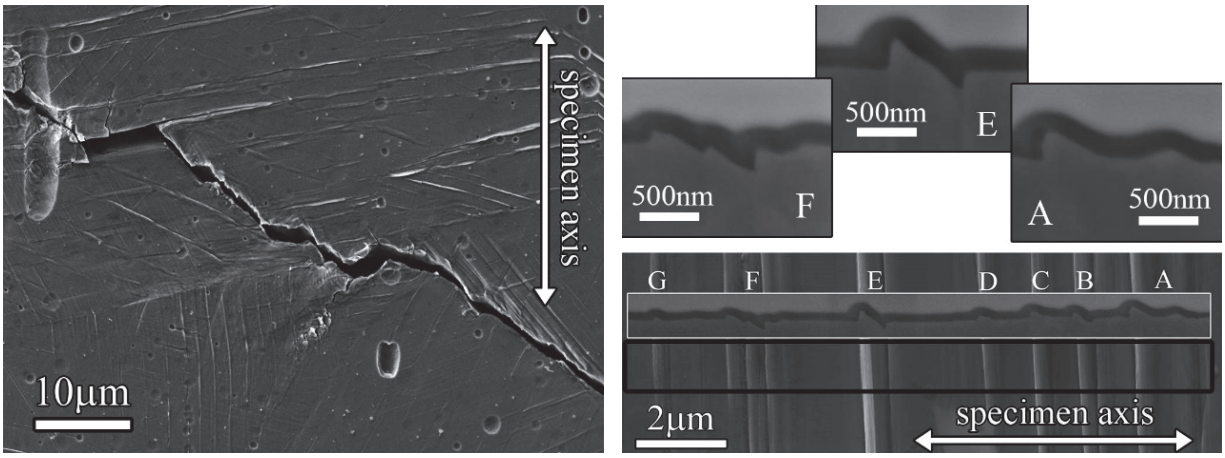

(a) (b)

Figure 10: Surface of the specimen cycled in 90°out-of phase straining to fracture: (a) central part of the secondary macroscopic crack, (b) PSMs in a grain and their profiles.

Cyclic stress-strain curves were plotted both for both individual channels and in equivalent stress and strain. Equivalent strain could be defined easily for in-phase straining. For 90° out-of-phase (diamond) straining the strain amplitude is reasonably well given by the tension-compression strain amplitude. However, the strain direction in a cycle changes and the strain path is more complicated. The cyclic stress-strain curve in equivalent stress and strain defined above lies above the cyclic stress-strain curves corresponding to tension-compression and torsion and has slightly higher slope.
Comparison of the equivalent cyclic stress-strain curves for in-phase and for 90° out-of-phase straining shows that due to the complicated strain path in 90° out-of-phase cycling the cyclic stress-strain curve is well above that of in in-phase straining. It is also apparent from Tab. 1 where the parameters of all cyclic stress-strain curves are listed.
The study of the surface of the specimens subjected to biaxial cyclic straining revealed general trend of the cracking in low cycle fatigue domain and also the early damage induced by in-phase and in 90° out-of-phase cycling. Macroscopic cracks grow at the angle around 45° to the specimen axis.
The initial stages of fatigue damage were studied in more detail. The study of the PSMs and small secondary cracks on the surface of the specimen revealed the profile of persistent slip markings consisting of extrusions and intrusions. Intrusions represent crack-like surface defect with high stress concentration factor. Fatigue cracks start from intrusions and grow along primary slip plane, usually on the boundary between the PSB and the matrix. This mechanism is the same as observed in uniaxial cyclic loading [2].

ACKNOWLEDGEMENT

The present work was conducted in the frame of IPMinfra supported through project No. LM2015069 and the project CEITEC 2020 No. LQ1601 of MEYS. The support by the project RVO: 68081723 and grants 13-23652S and 15-08826S of GACR is gratefully acknowledged.

REFERENCES

[1] Alain, R., Violan, P., Mendez, J., Low cycle fatigue behavior in vacuum of a 316L type austenitic stainless steel between 20 and 600 degrees C .1. Fatigue resistance and cyclic behavior, Mater. Sci. Eng., A 229 (1997) 87-94
[2] Man, J., Valtr, M., Petrenec, M., et al., AFM and SEM-FEG study on fundamental mechanisms leading to fatigue crack initiation, Int. J. Fatigue, 76 (2015) 11-18; DOI 10.1016/j.ijfatigue.2014.09.019.
[3] Wang, Y., Kimura, H., Akiniva, Y., et al., EBSD-AFM Hybrid analysis of crack initiation in stainless steel under fatigue loading, Key Eng. Mater., 340-341 (2007) 531-536.
[4] Jacquelin, B., Hourlier, F., Pineau, A., Crack Initiation under Low-Cycle Multiaxial Fatigue in Type-316l Stainless-Steel, J. Press. Vess.-T. ASME, 105 (1983) 138-143.

[5] Shamsaei, N., Fatemi, A., Socie, D.F., Multiaxial fatigue evaluation using discriminating strain paths, Int. J. Fatigue, 33 (2011) 597-609; 10.1016/j.ijfatigue.2010.11.002.
[6] Polák, J., Obrtlik, K., Hajek, M., Cyclic Plasticity in Type 316L Austenitic Stainless-Steel, Fatigue Fract. Eng. Mater., 17 (1994) 773-782.
[7] Pham, M.S., Holdsworth, S.R., Janssens, K.G.F., Mazza, E., Dislocation structure evolution and its effects on cyclic deformation response of AISI 316L stainless steel, Mater. Sci. Eng. A, 528 (2011) 3261-3269; 10.1016/j.msea.2011.01.015.
[8] Hong, S.G., Lee, S.B., Byun, T.S., Temperature effect on the low-cycle fatigue behavior of type 316L stainless steel: Cyclic non-stabilization and an invariable fatigue parameter, Mater. Sci. Eng. A, 457 (2007) 139-147; 10.1016/j.msea.2006.12.035.